

SEASON 6GSNS

SEASON

Self-Managed Sustainable High-Capacity Optical Networks

This project is supported by the SNS Joint Undertaken through the European Union's Horizon RIA research and innovation programme under grant agreement No. 101096120

Deliverable D3.3

The SEASON solution for data plane infrastructure

Editor L. Rapp (ADTRAN)

Contributors CNIT, CTTC, ADTRAN, UC3M, HHI, TIM, SSSA, INF-P, INF-G, WEST, ACC, ERI

Version 2

Date December 31, 2025

Distribution PUBLIC (PU)

© SEASON (Horizon-JU-SNS-2022 Project: 101096120)

Dissemination Level	Public

DISCLAIMER

This document contains information which is proprietary to the SEASON consortium members that is subject to the rights and obligations and to the terms and conditions applicable to the Grant Agreement number 101096120. The action of the SEASON consortium members is funded by the European Commission.

Neither this document nor the information contained herein shall be used, copied, duplicated, reproduced, modified, or communicated by any means to any third party, in whole or in parts, except with prior written consent of the SEASON consortium members. In such case, an acknowledgement of the authors of the document and all applicable portions of the copyright notice must be clearly referenced. In the event of infringement, the consortium members reserve the right to take any legal action it deems appropriate.

This document reflects only the authors' view and does not necessarily reflect the view of the European Commission. Neither the SEASON consortium members as a whole, nor a certain SEASON consortium member warrant that the information contained in this document is suitable for use, nor that the use of the information is accurate or free from risk, and accepts no liability for loss or damage suffered by any person using this information.

The information in this document is provided as is and no guarantee or warranty is given that the information is fit for any particular purpose. The user thereof uses the information at its sole risk and liability.

REVISION HISTORY

Revision	*Date*	*Responsible*	*Comment*
1.0	*Jun 24, 2025*	*D. Schneider*	*First draft*
1.1	*Jul 10, 2025*	*All*	*Contributions by Partners*
1.2	*Sept 3, 2025*	*D. Schneider / A. Napoli*	*Review*
2	*Dec 6, 2025*	*A. Napoli*	*Review and addition of last material*
3	*Jan 19, 2026*	*A. Napoli, C. Pinho*	*Quality check*

LIST OF AUTHORS

Partner	***Name Surname***
ADTRAN	*Lutz Rapp, Dominic Schneider*
CNIT	*Filippo Cugini, Andrea Sgambelluri*
CTTC	*Laia Nadal, Ramon Casellas, Josep Maria Fàbrega, Francisco Javier Vílchez, Ricardo Martínez, Luca Vettori, Carlos Hernández, Michela Svaluto Moreolo*
INF-G	*Mohammad M. Hosseini, Antonio Napoli, Carlos Castro, Giuseppe Parisi, Pablo Torres-Ferrera*
INF-P	*Cátia Pinho, André Souza, João Pedro*
HHI	*Abdelrahmane Moawad, Juan Moreno Morrone, Laurenz Ebner, Behnam Shariati, Johannes K. Fischer*
WEST	*Andrea Marotta, Carlo Centofanti, Alex Piccioni, Stefano Tennina*
SSSA	*Nicola Sambo, Piero Castoldi*
ACC	*Stephen Parker, Simon Pryor*
TIM	*Marco Quagliotti, Mauro Agus*
UC3M	*Jose Alberto Hernandez, Farhad Arpanaei*
ERI	*Gianluca Gambari*
FIB	*Roberto Mercinelli, Annachiara Pagano, Emilio Riccardi, Anna Chiado' Piat*

EXECUTIVE SUMMARY

The deliverable D3.3, “The SEASON Solution for Data Plane Infrastructure”, describes the final work conducted in Work Package 3 (WP3) and consolidates the results achieved in the development and the validation of advanced data plane technologies within the SEASON project. This deliverable builds upon the earlier stages documented in D3.1 and D3.2 and finalizes WP3’s contributions toward SEASON’s overarching goal: enabling self-managed, sustainable, and high-capacity optical networks suited for the demands of future 6G-era applications and infrastructures.

WP3 has operated at the core of SEASON’s technology innovation stream, responsible for investigating, modelling, developing, prototyping, and validating the data plane subsystems and components that underpin the SEASON network architecture (as defined in WP2 and verified in WP5). The work has progressed along a structured and multi-phase approach, where conceptual designs and simulations have evolved into tangible prototypes and experimental validations in conjunction with WP4 and WP5. Key achievements include:

- **Finalization of the SEASON Data Plane Prototypes**
- **Mid- and Long-Term Solution Mapping and Architectural Cohesion**
- **Demonstration and Experimental Validation**
- **Advanced Modelling and Optimization of Optical Networks**

D3.3 offers a comprehensive account of these achievements, summarizing the technological contributions, presenting the final suite of data plane prototypes, and documenting experimental and integration activities that validate their functionality and performance in real-world scenarios. It also provides a clear mapping of each innovation to SEASON’s architecture, objectives, and Key Performance Indicators (KPIs), ensuring traceability and relevance across the project lifecycle.

1 Introduction 9

2 SEASON solutions, data plane prototypes overview and KPIs achievement report 14

2.1 SEASON Solutions 15
2.1.1 Mid-term solutions 15
2.1.2 Long-Term Solutions 16

2.2 SEASON prototypes/assets 18

2.3 SEASON demos and experiments mapping 21

2.4 Topic Clustering from SEASON Project Innovative Solutions 21

2.5 Project KPIs related to WP3 24
2.5.1 KPI 2.1: Increase the available bandwidth of the fiber. 24
2.5.2 KPI 2.2: 50% CAPEX reduction 24
2.5.3 KPI 3.1: Design and implement flexible and modular MBoSDM node 25
2.5.4 KPI 3.2: MBoSDM transceivers able to increase the capacity of SoA transceivers 26
2.5.5 KPI 3.3: Optimized DSP for metro/core coherent applications 26
2.5.6 KPI 4.2: >50% contribution in energy saving 27
2.5.7 KPI 4.3: 400Gb/s RAN fronthaul ports capacity. 27
2.5.8 KPI 4.4: High accuracy profile for IEEE 1588-2019 28
2.5.9 KPI 5.1: Achieve sub-km (<500 m) and sub-dB (<0.5) resolution 28
2.5.10 KPI 5.2: Performance improvement achievable with an optical spectrum analyzer 28
2.5.11 KPI 5.3: OTDR Interrogator for latency / position measurement 29
2.5.12 KPI 5.4: Applicability of modulation format insensitive optical signal-to-noise ratio 30
2.5.13 KPI 7.3: Configuration of the MBoSDM node prototype agents for simple operations 30

3 Application of SEASON Key Achievement for Self-Managed Scalable Sustainable High-Capacity Optical Networks 32

3.1 Application 1: Next generation mobile fronthaul for B5g/6G 33

3.2 Application 2: Dynamic traffic allocation 34

3.3 Application 3: Flexible optical aggregation 34

4 SEASON Data plane prototypes 36

4.1 MBoSDM node prototype (C3.1) 36
4.1.1 Description 36
4.1.2 Interfaces 38
4.1.3 KPI assessment 40

4.2 Multi-granular Optical Node Prototype (C3.2) 41
4.2.1 Description 41
4.2.2 Interfaces 42
4.2.3 KPI assessment 42

4.3 Spatial PON Node (C3.3) 44
4.3.1 Description 44
4.3.2 Interfaces 45
4.3.3 Status 45
4.3.4 KPI assessment 46

4.4 MB(oSDM) S-BVT prototype (C3.4) 47
4.4.1 Description 47
4.4.2 Interfaces 49
4.4.3 KPI assessment 50
4.5 DSP RX-based monitoring (C3.5) 50
4.5.1 Description 50
4.5.2 Interfaces 51
4.5.3 KPI assessment 52
4.6 Multiband amplifier (C3.6) - ensuring availability by predictive maintenance applied to optical amplifiers 53
4.6.1 Description 53
4.6.2 Interfaces 54
4.6.3 KPI assessment 54
4.7 Monitoring system and telemetry (C3.7) 56
4.7.1 Description 56
4.7.2 Interfaces 58
4.7.3 KPI assessment 58
4.8 Research activities on Pluggable amplifiers (Related C3.8) 60
4.8.1 Description 60
4.8.2 Interfaces 63
4.8.3 KPI assessment 63
4.9 Research Activities on SmartNIC with coherent pluggable (C3.9) 64
4.9.1 Description 64
4.9.2 Interfaces 65
4.9.3 KPI assessment 66
5 SEASON Optical Network Architecture: Modeling and E2E Design 67
5.1 Robust Optimization of SEASON's Filterless Optical Networks with Physical Layer Uncertainties (related to C3.10, C3.11) 67
5.2 SEASON Multi-Layer Aggregation: Optical and Electronic Domains (related to C3.10, C3.11) 70
5.2.1 Optical aggregation enabled by P2MP and DSCM 71
5.2.2 Results for QoT estimation 72
5.3 Crosstalk analysis in MBoSDM Optical Networks with programmable transceivers (related to C3.1 and C3.4) 74
5.4 Impact of Inter–Core Loss and Gain Equalization on Transmission Performance in SEASON Multi–Core Systems (related to C3.1, C3.4) 76
5.4.1 Scenario and theoretical model 77
5.4.2 Setup of the testbed 80
5.4.3 Experimental results and discussion 81
5.5 Planning Practices for MBoSDM Ultra-High-Capacity Networks 83
5.5.1 Introduction 83
5.5.2 Simulation framework and scenario 83
5.5.3 Physical layer impairments and performance modeling 84
5.5.4 Results and discussion 85

5.6 End-to-end latency model for IPoWDM with coherent pluggables beyond 400 Gb/s (related to C3.8, C3.10, C3.11) 89
5.6.1 Coherent pluggable transceivers evolution 90
5.6.2 Latency analysis of IPoWDM architectures build with coherent pluggables 91
5.6.3 Methodology and simulation framework 91
5.6.4 Results 93

5.7 SEASON Framework for Metro-access flexible integration (related to C3.9, C3.10, C3.11) 95
5.7.1 Motivation and architecture 95
5.7.2 Flexible central office 96

5.8 Performance and Transient Resiliency Comparison of S- and E-band Upgrades of a C+L-band System (related to C3.2) 97
5.8.1 Simulation Setup 98
5.8.2 Power Optimization 99
5.8.3 Network Simulations 99
5.8.4 Results and Discussion 100
5.8.5 Conclusions 103

5.9 Simulation and Modeling of C+L+S Multiband Optical Transmission for SEASON OCATA Time Domain Digital Twin (related to C3.2) 103
5.9.1 Overview 103
5.9.2 Efficient MB Simulation for Dataset Generation 104
5.9.3 Machine-Learning Models for Constellation-Based QoT Prediction 105
5.9.4 Conclusions 107

5.10 Creating and Tuning Multiband Optical Transmission Digital Twin Lightpath Models (related to C3.2) 107
5.10.1 Introduction 107
5.10.2 OCATA Constellation Modelling and QoT Estimation 108
5.10.3 Lightpath Model Composition and Tuning 108
5.10.4 Results and Discussion 108

5.11 Optical performance model of Multi-Band Transport Systems with up to 24 THz of Transmission Bandwidth (related to C3.2) 110
5.11.1 Simulation Setup 111
5.11.2 System Modelling and Power Optimization 112
5.11.3 Optimization Results 113
5.11.4 Conclusions 114

6 SEASON Optical Subsystems Developed 115

6.1 Programmable MBoSDM transceiver (related to C3.1 and C3.3) 115

6.2 MBoSDM node prototype (related to C3.1 and C3.3) 118

6.3 Node multi-band & SDM 120

7 SEASON Optical Transport Infrastructure for (beyond 5G) Front/Mid-haul and Access 123

7.1 Cost-Effective Optical Ring Architecture with Automated EDFA Optimization (related to C3.8) 123
7.1.1 P2MP Bidirectional Transmission 124

7.2 Mid-haul for 6G railway and Highway exploiting smart NIC (related to C3.9) 126

8 Optical Monitoring and Power Efficiency in SEASON Network Architecture..... 130

8.1 Need for improved network monitoring (related to C3.7)..... 130

8.2 Power efficiency enabled by DSCM (related to C3.10 and C3.11) 131

8.3 Enhancing monitoring capabilities in MB networks (related to C3.2, C3.6, and C3.7) 132

8.4 Longitudinal power monitoring LPM (related to C3.5, C3.6 and C3.7)..... 135

8.5 Digital Signal Processing – Group Velocity Dispersion (related to C3.5) 138

8.6 Transceiver Count Reduction in Filterless Metro-Aggregation Networks Using DSCM (related to C3.11)..... 141

8.7 Power Consumption Considerations of Coherent Transceivers in Filterless Point-to-Multipoint Metro-Aggregation Networks with Digital Subcarrier Multiplexing (related to C3.10 and C3.11)..... 145

8.8 Resilient Anomaly Detection in Fiber Networks: ML for Multi-Threat Identification via Polarization Monitoring (related to C3.6 and C3.7) 153

8.8.1 Sensing Mechanism and Experimental Setup 153
8.8.2 Simultaneous Events 154
8.8.3 Vibration Monitoring..... 155
8.8.4 Machine-Learning Framework 156
8.8.5 Results and Performance Evaluation 156
8.8.6 Robustness to Noise..... 157
8.8.7 Conclusions 158

9 Conclusions..... 159

10 Glossary..... 161

11 References 165

1 INTRODUCTION

The development of SEASON project prototypes and studies, as described in this Deliverable D3.3, are deeply rooted in the requirements and architectures specified in WP2 [D2.1-24] and validated through techno-economic analyses performed in WP2 [D2.2-25, D2.3-25]. The SEASON high-level data plane architecture is designed to meet future network demands with two distinct time frames: medium-term (by 2028) and long-term (by 2032 and beyond). Each period is defined by its own set of technological solutions and requirements, driving the selection and validation of innovations in the data plane.

Key Achievements and relevant Contributions from WP3 include:

1. Finalization of the SEASON Data Plane Prototypes

Nine physical prototypes were developed in the project, each targeting a specific SEASON innovation. These include:

- Multiband over Space Division Multiplexing (MBoSDM) switching nodes and Sliceable-Bandwidth Variable Transponder/Transceivers (S-BVTs);
- Smart Network Interface Cards (NICs) and Data Processing Units (DPUs) for midhaul applications and edge computing;
- Digital Subcarrier Multiplexing (DSCM) point-to-multipoint (P2MP) coherent transmission over single and dual fibers;
- Spatial Passive Optical Networks (PON) nodes and filterless metro-access architectures;
- Integrated monitoring and telemetry systems, including digital signal processing (DSP)-based Rx monitoring and predictive maintenance frameworks.

Each prototype has been mapped to either mid-term or long-term SEASON solutions and is linked to defined parts of the data plane reference architecture (e.g., Edge Central Offices (COs), Cloud COs, Access Nodes), clearly demonstrating applicability and modular integration potential.

2. Mid- and Long-Term Solution Mapping and Architectural Cohesion

The deliverable synthesizes the evolution from conceptual SEASON solutions (as defined in D2.1) to their practical instantiation and integration in WP3. Both the mid-term (4-year) and long-term (8+ year) pathways are covered, with a well-defined correspondence between architectural segments (Access-Metro, Metro-Backbone) and technology building blocks.

Importantly, the mapping ensures that each data plane innovation contributes directly to at least one of SEASON's targeted KPIs – such as increasing fiber capacity utilization, reducing energy consumption, improving scalability through modular design, and enabling support for 6G and artificial intelligence (AI)-driven service demands.

3. Demonstration and Experimental Validation

The technologies developed in WP3 have been integrated and validated in several laboratory environments and in two initial planned system-level demonstrations (in Berlin at HHI) and in L'Aquila at WEST/UNIVAQ). These demonstrations reflect different deployment perspectives:

- **Demo 1 (Berlin, HHI)** focused on extended-reality (XR) services over mobile access, showcasing access-metro innovations including spatial division multiplexing passive optical network (SDM-PON), 5G radio access network (RAN), and digital subcarrier multiplexing (DSCM) technologies.
- **Demo 2 (L'Aquila, WEST/UNIVAQ)** highlighted an operator-centric end-to-end deployment, covering Access to Backbone segments and validating SEASON's multiband MBoSDM solutions.

In addition to the two initially planned SEASON demos, two new ones were added thanks to the support and in-kind contributions of the partners involved.

- **Demo 3 (Madrid, Telefonica)** presents dynamic service provisioning in a disaggregated Internet Protocol over wavelength division multiplexing (IPoWDM) network using DSCM-based P2MP XR coherent pluggables. A hierarchical software defined network (SDN) controller architecture discovers resources, configures the optical layer, and establishes services automatically. Commercial routers and whiteboxes with 400G/100G pluggables are interconnected through optical splitters. The orchestrator assigns frequencies, configures channels, and activates digital subcarrier-based services on demand. The experiment validates feasibility and measures control-plane performance and sets the required latency. A recorded version of the demo was streamed during OFC 2025 at the Nokia (INF-G) booth. The video has been made available also on the YouTube channel.
- **Demo 4 (Torino, Fibercop)** metro and access integration. This demo is hosted at Fibercop Lab in Torino, and it is a joint experiment with UnivAQ, WEST, CNIT, CTTC and INF-G. It demonstrates the coexistence over the same single-fiber Access Network infrastructure of legacy 10-Gigabit PON (XG-PON) services and high-end Metro services, based on P2MP XR technology, dynamically provisioned and carried transparently from the Metro segment network. The results of the activity will be shared with the multi-source agreement (MSA) open XR optics forum as part of the dissemination and standardization activities within the WP6.

These validations provide tangible evidence of the maturity and interoperability of SEASON components and their capability to address realistic network scenarios.

4. Advanced Modelling and Optimization of Optical Networks

D3.3 also reports on advanced modelling and optimization techniques applied to SEASON architecture. Next generation will be considerably more complex and will require extensive work to optimize for them and to guarantee their operation under several circumstances. This research includes, among others, the following topics:

- **Robust and Adaptive Optical Network Modeling:** Novel robust optimization (RO) and adjustable robust optimization (ARO) models that account for physical layer uncertainties, enabling resilient design of filterless optical networks.
- **End-to-End Latency Modeling:** Simulation-based latency assessment of IPoWDM architectures using high-speed coherent pluggables, demonstrating near-deterministic performance suitable for time-sensitive 6G services.
- **Energy and Cost Efficiency Trade-offs:** In-depth analysis of optical versus electronic aggregation at metro edges, validating DSCM as a viable low-power alternative to traditional router-based aggregation.

These numerical studies provide the theoretical underpinning for various of the architectural choices and serve to de-risk the adoption of emerging technologies in complex network environments. Furthermore, the latter provides a tool for establishing the conditions that, if satisfied, can deliver energy saving by deploying P2MP coherent transceiver with respect to point-to-point (P2P) ones.

5. Integration with Control, Management, and Telemetry Systems

A key aspect of D3.3 is its alignment with WP4, ensuring that data plane innovations are not developed in isolation but are embedded within a broader ecosystem of programmable control, telemetry, and automation mechanisms. Several prototypes (e.g., predictive maintenance systems, DSP-based monitoring) interface directly with WP4 systems, enabling self-managed capabilities and laying the foundation for automation and closed-loop network operation, in line with the goals of WP5.

6. Contributions to SEASON KPIs and Horizon Europe Objectives

Throughout the deliverable, clear links are made between individual innovations and SEASON's defined KPIs:

- **KPI 1 – Fiber capacity enhancement:** Achieved through multiband and space-division multiplexing.
- **KPI 2 – Energy efficiency improvement:** Enabled by flexible DSCM transceivers, optical aggregation, removal of transponders, and dynamic bandwidth allocation.
- **KPI 3 – Cost-effective scalability:** Delivered via whiteboxes, coherent pluggables, and filterless OLS architectures.
- **KPI 4 – Programmability and monitoring:** Supported by DSP-based telemetry and adaptive monitoring frameworks.

By addressing these KPIs, SEASON contributes directly to the objectives of the SNS JU and Horizon Europe, particularly in the areas of sustainable digital infrastructure, open and disaggregated network solutions, and enabling technologies for 6G. This topic is fully covered in Section 2.5.

The structure of the following sections is as follows.

Section 2, SEASON Solutions and Data Plane Prototypes, offers a comprehensive overview of SEASON data plane solutions, mapped to both medium-term and long-term network architectural targets. It presents the final suite of data plane prototypes, highlighting their integration with control, management, and monitoring systems, and shows their mapping against the high-level SEASON network architecture. The section also introduces the demonstrations and experiments validating the developed solutions and their practical deployment across various network segments. This section also reports an accurate description of the project outcomes in terms of KPIs and their achievements.

Section 3, Data Plane Prototypes – State of the Art and Innovative Aspects of the Developed Components, Subsystems and Systems, catalogues and describes the physical prototypes, components, and subsystems developed in SEASON, detailing their capabilities, addressed technical challenges, and mapping to project solutions and KPIs. Benchmark results and validation reports are included for each prototype, showing integration potential and readiness for experimental demonstrations and real-world deployments.

Section 4, Self-Managed Scalable Sustainable High-Capacity Optical Networks, discusses the future perspectives for fully self-managed, scalable, and sustainable optical networks, drawing on lessons learned from prototype integration, automation mechanisms, and closed-loop operation enabled by advanced control and telemetry. It emphasizes the convergence of programmable data plane technologies with intelligent network management and operational autonomy, marking the project's roadmap toward truly autonomous networking.

Section 5, Modelling and End-to-End (E2E) Design of Optical Networks, details the advanced modelling and simulation activities that support robust and scalable network design, including filterless architectures, optical aggregation, and latency analysis for coherent pluggables. It covers optimization models accounting for physical layer uncertainties, crosstalk analysis in multi-band SDM networks, energy and cost efficiency assessments, and transmission modelling of multi-core and multi-band systems. These theoretical studies underpin key architectural choices and inform the prototype implementation strategies.

Section 6, Optical Subsystems, is focused on device-level advances. It examines the design and experimental validation of optical subsystems such as programmable MBoSDM transceivers and switching nodes. It assesses node architectures for high-capacity and scalable switching, including multi-band transmission and digital twin modelling. Key differences and complementarities among prototypes are discussed, supported by experimental results that guide subsystem integration in future network deployments.

Section 7, Front/Mid-haul and Access Beyond 5G, addresses the development and evaluation of advanced transport solutions for front-haul, mid-haul, and access domains, with a view toward 6G and beyond. Topics include bidirectional P2MP transmission architectures, smart NICs/DPUs for mid-haul scenarios such as railways and highways, and flexible PON architectures for spatial aggregation and efficient connectivity. The emphasis is on cost-effective, power-efficient, and scalable solutions enabling next-generation service delivery.

Section 8, Optical Monitoring and Power Efficiency, demonstrates innovations in network monitoring and energy efficiency, presenting longitudinal power monitoring (LPM), advanced DSP-based Rx solutions, predictive maintenance, and machine-learning-powered anomaly detection. The section quantifies energy consumption savings achieved through digital subcarrier multiplexing (DSCM) and optical aggregation, illustrating approaches to transceiver reduction, cost savings, and the dual use of fiber infrastructure for both transmission and sensing.

Finally, Section 9, Conclusions, synthesizes the overall findings and key achievements of D3.3, aligning technical progress with SEASON objectives and KPIs. It highlights the contribution of developed prototypes, experimental validations, and modelling efforts in advancing the state-of-the-art toward self-managed, high-capacity, and sustainable optical data plane networks designed to support future 6G service ecosystems.

2 SEASON SOLUTIONS, DATA PLANE PROTOTYPES OVERVIEW AND KPIS ACHIEVEMENT REPORT

The SEASON project proposes a set of data plane technologies, the so-called SEASON solutions, to be applied to the high-level network data plane architecture as defined in deliverable D2.1 [D2.1-24].

SEASON's high-level data plane architecture is segmented into two domains, access-metro and backbone, and the architecture has been specified for two timeframes, the medium-term solution (MTS) with a horizon of ~4 years from now and the long-term solution (LTS) with an application target of 8 years and beyond from now. The SEASON solutions have been defined and mapped on both network architecture domains (access-metro and backbone) for the two target timeframes (4 and 8+ years).

The first part of the section is dedicated to summarizing the solutions proposed by the SEASON project and to listing the data plane prototypes developed in the project to make the implementation of these solutions possible. It also mentions the experiments (including the two demos) that demonstrate the viability of the SEASON solutions, use the related data plane prototypes developed in WP3 and the developments of WP4 regarding the control plane, telemetry architecture and SW. A second part of the section is dedicated to the KPIs achievement report.

In section 2.1, the SEASON data plane solutions for the MTS and LTS, as reported in the previous deliverable D3.2 [D3.2-24], are briefly summarized. Both solutions served as inspiration for the data plane prototypes developed in WP3 and are the references of the two main demos. The additional demos added in the last period of the project and other experimental activities focused on specific aspects performed in the project.

Section 2.2 presents the final versions of data plane prototypes which integrate some of them with other components (essentially WP4 control, management and monitoring systems and related SW) and a view of their mapping to SEASON's high-level network architecture are provided. With respect the nine relevant data plane prototypes presented in D3.2, two new ones have been added which have been developed in the last period of the project.

For completeness and considering that many prototypes are integrated in the demonstrations, in section 2.3 the mapping of the demos created in the project within the WP5 on network architecture has also been displayed.

Section 2.4 serves as a synthetic and additional overview of the project results and research topics clustering. This allows the SEASON project research and development activities to be grouped into just five macro topic clusters. Each topic cluster is linked to prototypes and to the document sections and references in which the cluster topic is developed.

Finally, section 2.5 reports the status of achievement of the KPIs addressed in WP3 as it is at the end of the WP3 working period (M32, August 2025).

2.1 SEASON SOLUTIONS

In this subsection the solutions identified by the SEASON project are reported in a concise form for the medium- and long-term, separately. Their applications in relation to the various network architecture segments are also highlighted.

2.1.1 Mid-term solutions

Concerning the mid-term period (timeframes within 4 years) the solutions proposed by SEASON Project are the following ones.

MTS-1 ROADM-free IPoWDM Networks and use of Whiteboxes with Pluggable Transceivers: an architecture based on IPoWDM nodes eliminating the use of ROADMs (i.e., packet-optical switches/routers equipped with coherent pluggable transceivers) that allows a cost-effective, low-latency, and simplified network. Open, modular L2/L3 switches supporting up to 800G pluggable modules promote vendor-agnostic flexibility and scalability. It involves mainly Access-Metro segment, but it can be applied also in the Backbone. This solution is discussed in Sections 4.8 and 5.6, where IPoWDM architectures with coherent pluggables and related latency and performance aspects are analyzed.

MTS-2 DPUs and Smart NICs: deployment of 800G-capable Data Processing Units (DPUs) and Smart NICs for traffic acceleration and monitoring at the Edge and Far Edge. Servers equipped with such smart and high data rate cards support Telco and AI service functions in the Access-Metro segment. Further details on this solution are provided in Sections 4.9 and 7.2, which describe the SmartNIC/PDU prototype and its application in mid-haul transport scenarios for 6G.

MTS-3 DSCM-Based Coherent Transceivers (P2P/P2MP): a technology enabling point to multipoint networking, allowing 400/800 Gb/s transmission and supports fronthaul at rates of 100 Gb/s and higher. Use of Bidirectional (BiDi) single-wavelength single-fiber single-laser transmission is possible thanks to interleaved in frequency of subcarrier or intelligent optical power management of the individual subcarrier to mitigate reflections. This technology optimizes bandwidth, reduces power consumption and latency by removing components (e.g., optical-electronic-optical conversion), increases spectral efficiency and reduces use of fiber (in BiDi mode) in the Access-Metro segment. his solution is addressed throughout Sections 4.7, 5.1–5.2, 5.6, and 8.2–8.7, where DSCM XR devices, optical aggregation, end-to-end performance analysis, and power-efficiency benefits are extensively evaluated. **This solution has been awarded as one of the top 10 key achievements of the year from the SNS organization.**

MTS-4 50G PON and Coherent/WDM PON: aggregates traffic efficiently using passive optical networks (PONs) scaling up the data rate and introducing coherent transmission and wavelength multiplexing, which boosts fiber capacity and access scalability in the access-metro segment. Details on this solution are presented in Section 4.3, which describes the Spatial PON prototype, and in Section 7, where PON-based access–metro integration scenarios are analyzed.

MTS-5 Pure Filterless/Hybrid OLS: enhances spectrum usage and power efficiency using flexible Optical Line Systems (OLS) supporting P2MP and P2P architectures with DSCM transceivers and multicarrier modulation (MCM) technologies, which are applied in the Access-Metro domain to provide high-capacity and flexible transmission. This solution is analyzed in Sections 5.1–5.5, which cover filterless architectures, multilayer aggregation, physical-layer impairments, planning practices, and ultra-high-capacity multiband deployments.

MTS-6 Exploitation of MB Transceivers (e.g., MBoSDM S-BVT): extended use of transceivers operating in the C+L-bands, with potential extension to the S-band. Used in the backbone and potentially also in the access-metro segment (metro core, in particular), to increase the capacity and make the network scalable. This solution is treated in Sections 6.1 and in the modeling studies of Sections 5.3, 5.4, and 5.8, which evaluate multiband transceiver scalability, crosstalk, and spectral expansion strategies.

MTS-7 Multigranular MBoSDM Switching Nodes: exploitation of MBoSDM Switching Nodes (C+L+ (possibly) S-band) to increase capacity, enable smooth scalability, and achieve high flexibility of the optical transport infrastructure, altogether. Used in both the access-metro and backbone segments, but traffic requirements demanding their use more likely in the backbone. The developments related to this solution are described in Sections 6.2 and 6.3, along with the multiband SDM modeling activities reported in Sections 5.3–5.5.

MTS-8 Advanced Monitoring Systems: advanced monitoring solutions based on fast fault and anomaly localization techniques (e.g., use data of DSP). Applied to nodes from both access-metro and backbone segments. This solution is covered in Sections 6.1–6.3, which present DSP-based and predictive-maintenance monitoring prototypes, and in Sections 8.1–8.5, where advanced optical monitoring functions and telemetry enhancements are investigated.

MTS-9 Radio mobile access based on the O-RAN architecture. Open, virtualized and disaggregated solutions for the RAN, enabling functionalities expected in 5G Advanced system (3GPP Releases 18 and 19), concerns network architecture, SW and transport solutions for X-Haul traffic. Mapped to the access-metro segment. This solution is discussed primarily in Section 7.2, which presents the transport and mid-haul innovations enabling O-RAN deployments and future 6G support.

2.1.2 Long-Term Solutions

For the long-term period (timeframe 8 years and beyond) the following list presents the SEASON solutions that are, in most cases, enhancements of ones defined for the medium-term.

LTS-1 Next-Generation Whiteboxes and Pluggable Transceivers: medium-term systems evolutions towards higher rates (up to 2 Tb/s), higher integration, smaller form factor, and lower power. Applied in access-metro in Far Edge and Edge COs, to handle both telco and service functions, such as data-intensive AI tasks. Further details on this long-term evolution are presented in Sections 4.8 and 5.6, where next-generation coherent pluggables and their impact on IPoWDM architectures and end-to-end performance are assessed.

LTS-2 Evolved DPUs: use of interfaces capable of handling data rates of 800G or higher, up to 2 Tb/s. Used in access-metro segment to support virtualization and networking of 6G RAN but also provide the computational power needed for running advanced service functions. This solution is addressed in Sections 4.9 and 7.2, which examine advanced SmartNIC/DPU architectures and their applicability in future high-capacity mid-haul and access–metro scenarios.

LTS-3 Coherent/WDM/SDM PON Deployment: A further step ahead with PON used in the access-metro domain to cope with traffic demand growth from FFTX access points (residential, business and radio mobile, with aggregated data rate on a single PON tree up to 400 Gb/s). The long-term evolution of coherent and SDM-based PON systems is discussed in Sections 4.3 and 7, where spatial PON architectures and advanced access–metro integration schemes are analyzed.

LTS-4 Enhanced DSCM-Based Transceivers: advanced DSCM coherent optics for high-performance and flexible transport (P2MP networking) with total single device rates up to 2.4 Tb/s (maximum data rate applies for hubs, leaves data rates are lower). Applications in access-metro segment to carry X-haul traffic or aggregation and transport of traffic exchanged by Far Edge and Edge COs. This evolution of DSCM coherent systems is treated in Sections 4.7, 5.1–5.2, and 8.2–8.7, where their scalability, aggregation capabilities, and power-efficiency advantages are evaluated.

LTS-5 Fully Meshed Coherent Fronthaul: Use of coherent "lite" (low cost) transceivers at ≥ 400 Gb/s for front-haul (FH) application (with 6G)**.** Use in the access-metro from mobile radio stations to Far Edge or Edge Cos where vDU functions are placed, according to 6G-ready Open-Cloud-RAN architecture. The concepts behind fully meshed coherent fronthaul are explored in Section 7.2, in the context of next-generation front-/mid-haul architectures supporting 6G-ready O-RAN deployments.

LTS-6 Full MB(oSDM) S-BVT Exploitation: extended capabilities to operate beyond the C+L band and achieve aggregated bit rates of 1 Tb/s and higher, potentially scaling up to 10 Tb/s by means of using additional bands (beyond C+L+S-bands considered for mid-term). Potential application on both access-metro and backbone, but more likely for the backbone as data rate achievable by these devices are extremely high. The long-term exploitation of multi-band S-BVT technology is examined in Sections 6.1, 5.3, 5.4, and 5.8, which analyze extended-band transmission, crosstalk effects, and multi-Tb/s scalability.

LTS-7 Advanced MBoSDM Switching Nodes: equipment enabling full granularity switching (band, wavelength, space) and extended MB use (beyond C+L+S) to support ultra-high-capacity networks. Application is in the backbone segment. Further details on this solution are reported in Sections 6.2 and 6.3, as well as in Sections 5.3–5.5, which study multigranular switching, spatial–spectral routing, and ultra-high-capacity SDM architectures.

LTS-8 Predictive Maintenance for MB amplifiers: MB amplifiers will enable the amplification of signals across multiple bands beyond C+L. Predictive Maintenance improves existing monitoring processes and reduces the network downtime. Multiband amplifiers will be deployed within both the access-metro and backbone segments, according to the strategy for the introduction

of MB systems (i.e., MoSDM nodes and transceivers/transponders) in each segment. This solution is detailed in Sections 6.1–6.3 and 8.1–8.5, which describe DSP-based monitoring, predictive-maintenance frameworks, and advanced telemetry for multiband amplification systems.

LTS-9 Advanced O-RAN-Based RAN: Further developments of radio access based on the O-RAN architecture supporting double Split, 2 (MH) and 7.2 (FH), in 6G perspective. Integration of O-RAN architecture facilitating optimized deployment of vDU and vCU functions in the Access metro segment. The long-term evolution of O-RAN-based mobile access is discussed in Section 7.2, which examines 6G-oriented mid-/front-haul architectures and their integration with SEASON's transport innovations.

2.2 SEASON PROTOTYPES/ASSETS

The updated list of data plane prototypes/assets in their final version is reported in detail in Section 4, shortly listed in Table 2.2-1. The table summarizes all the data plane prototypes developed in the SEASON project and includes the prototype code, a brief description of the prototype, the leading partner involved in prototype development, the solution of mid- or long-term addressed by the prototype and the experiment or demo in which the prototype was tested, are the data reported in columns of the table. Please note that not all the SEASON solutions are addressed by data plane prototype as some solutions involve aspects connected to control, management, telemetry, which regards SW architecture and coding developed in WP4. Figure 2.2-1 illustrates the mapping of the prototypes for the long-term version of the data plane architecture. The figure is meant to illustrate in which parts of the architecture (which segment, which central office category, which equipment) the prototypes would be used.

Table 2.2-1: SEASON data plane prototypes.

Prototype/ Asset	Short Description	Owner partner	SEASON solution addressed	Experiment or demo
C3.1	MBoSDM node	CTTC	MTS-7	CTTC lab
C3.2	Multigranular node	HHI	LTS-7	Demo 1
C3.3	Spatial PON node	WEST	MTS-4, LTS-3	Demo 2
C3.4	MBoSDM S-BVT	CTTC	MTS-6, LTS-6	CTTC lab
C3.5	DSP Rx based monitoring	HHI	LTS-8	HHI lab
C3.6	Predictive maintenance for Multi-Band Amplifiers	ADTRAN	MTS-8	ADTRAN lab
C3.7	Monitoring & Telemetry system	ADTRAN	MTS-8	HHI and CTTC labs
C3.8	Pluggable amplifier	ERI	MTS-1	ERI lab
C3.9	Smart NIC / PDU with coherent pluggable	CNIT	MTS-2, LTS-2	CNIT lab
C3.10	Dynamic service allocation	TEF & INF-G	MTS-3	Demo 3
C3.11	Access-Metro integration	FIB, CNIT, WEST, INF-G	MTS-3/4, LTS-4/5	Demo 4

Prototypes C3.1 (MBoSDM node) and C3.4 (MBOSDM S-BVT) are described in sec 7.1 and 7.4 of D3.2 respectively, and the typical application of both could be in the core part of access-metro segment as highlighted in Figure 2.2-1. Specifically, these prototypes can be employed in Edge COs when traffic growth will require capacities not supported by C-band or C+L bands only. In this document improvements in both prototypes are reported. For C3.1 (section 6.2) further optimization of the switching device has been implemented to include spectral switching granularity in the L-band. For C3.4 (section 6.1) further transmission assessment has been performed to evaluate the transceiver scalability capabilities towards enabling multi Tb/s transmission. Both prototypes are extensively experimented in CTTC labs.

Prototype C3.2 (Multigranular Node) is described in sec 7.2 of D2.3 and a summary of prototype characteristics with results of the last validation report is included in section 6.3 of this deliverable. It is similar to prototype C3.1, but for its intrinsic characteristics the typical application is in the backbone as shown in Figure 2.2-1, specifically in Cloud CO where huge amount of traffic belonging to many different flows must be flexibly handled. This prototype is employed in Demo 1 (Berlin Demo) in the multi-band core network part.

Prototype C3.3 (Spatial PON node) is described in Section 7.3 of D3.2 and it has not been further developed in the last period of the project. The mapping of the prototype is in the access-metro part as equipment connected to physical OLTs from one side and with multicore (or bundle of) fibers on the other towards user OTNs. Prototype C3.3 is used in Demo 2 (L'Aquila Demo).

Prototype C3.5 (DSP Rx based monitoring) is described on section 7.5 of D3.2 and additional development are included in Section 4.5. It can be applied everywhere the transceivers with this additional capability are used (backbone and access-metro) to monitor the state of the transmission over the network. Prototype C3.5 has been developed and tested in ADTRAN lab.

Prototype C3.6 (Predictive Maintenance (PdM) framework for Multi-Band Amplifiers) is described in section 7.6 of D2.3. As it is a framework combining anomaly detection, prognosis, and diagnosis applied to multiband amplifiers, it can be applied everywhere multiband amplifiers are deployed, so both access metro and backbone. PdM prototype developed and experimented in HHI labs and the fine-tuning for the use on multiband amplifier is forecasted for Q3 2025.

Prototype C3.7 (Monitoring & Telemetry systems) is described in section 7.7 of D3.2 and enhancements of last period are reported in section 8. It is applicable in all parts of the network, from the access-metro to the backbone. It is not a single prototype but a set of solutions: how to enhance monitoring capability, longitudinal optical monitoring, DSP monitoring (covered by prototype C3.5), ML base anomaly detection. They are described in dedicated subsection of section 8 and they are developed and experimented in HHI, ADRTRAN and CTTC labs.

Prototype C3.8 (Pluggable amplifier-amplifier gain control) is described extensively in section 7.8 of D3.2. No further development is achieved in last period of the project. Prototype concerns an algorithm to appropriately adjust the amplifier gain in a ring without additional monitoring equipment.

Prototype C3.9 (Smart NIC/PDU with coherent pluggable) is described extensively in subsection 7.9 of D3.2. A development of the prototype has been achieved with an experiment emulating the use of PDU as card of a system (server) used to support Mid-Haul traffic transportation in a O-RAN architecture, as reported in subsection 7.2. The prototype is used in the access-metro part of the network and has been experimented in CNIT lab.

Prototype C3.10 was not included in D3.2 as it is a new prototype developed in the last period of the project. It concerns the dynamic service allocation for DSCM XR systems, and it is linked to an additional experimental Demo, the Demo 3 designed and performed within a collaboration between TID, CTTC and NOKIA-G.

Prototype C3.11, like C3.10, was developed in the final phase of the project and was not described in D3.2. It is a solution for integrating access and metro segments that applies the solutions proposed in SEASON. The prototype was developed by Fibercop in collaboration with CNIT and WEST, with the support of NOKIA-G, and is based on the architecture described in section 5.7. The prototype is tested in Demo 4 and documented in the final deliverable of WP5.

The prototype implementations demonstrate progressive evolution from individual component validation (C3.1-C3.4) to integrated system demonstrations (C3.10-C3.11), supporting both laboratory validation and real-world deployment scenarios through Demo 1-4 configurations.

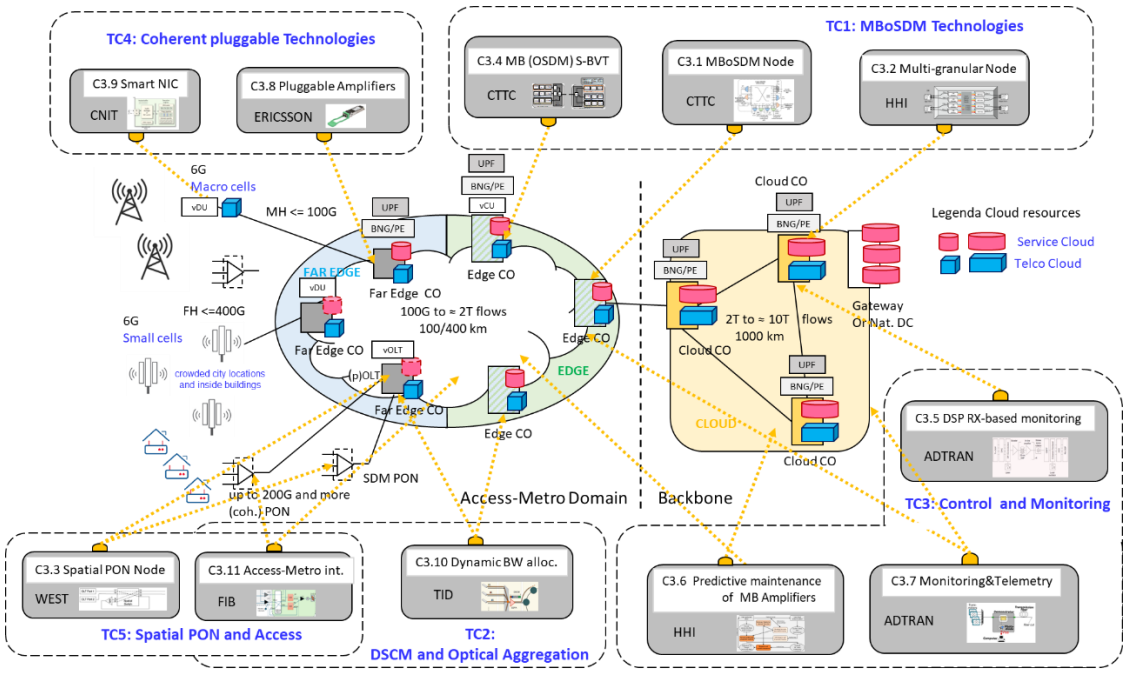

Figure 2.2-1: Prototypes mapping on Data plane architecture with Topic Clustering highlighted.

2.3 SEASON DEMOS AND EXPERIMENTS MAPPING

Figure 2.3-1 is an attempt to map the two main project demos, Berlin and L'Aquila, plus the two additional ones, Demo 3 and Demo 4, onto the long-term SEASON architecture. As it can be seen, Demo 1, which is oriented towards services (particularly on extended reality – XR - provided over mobile access), involves the access-metro segment and the related systems and equipment (5G RAN and core, SDM-PON, metro network), while Demo 2, oriented towards an operator's vision, concerns all network segments, from access to the backbone, without focusing on particular services but demonstrating the feasibility of SEASON MBoSDM solutions with an end-to-end vision. Both Demo 3 and Demo 4 involve use of DSCM XR devices and has been devoted to demonstrating the capability of dynamic bandwidth allocation and integration with ODN to achieve a full access-metro integration and infrastructure (fiber) sharing.

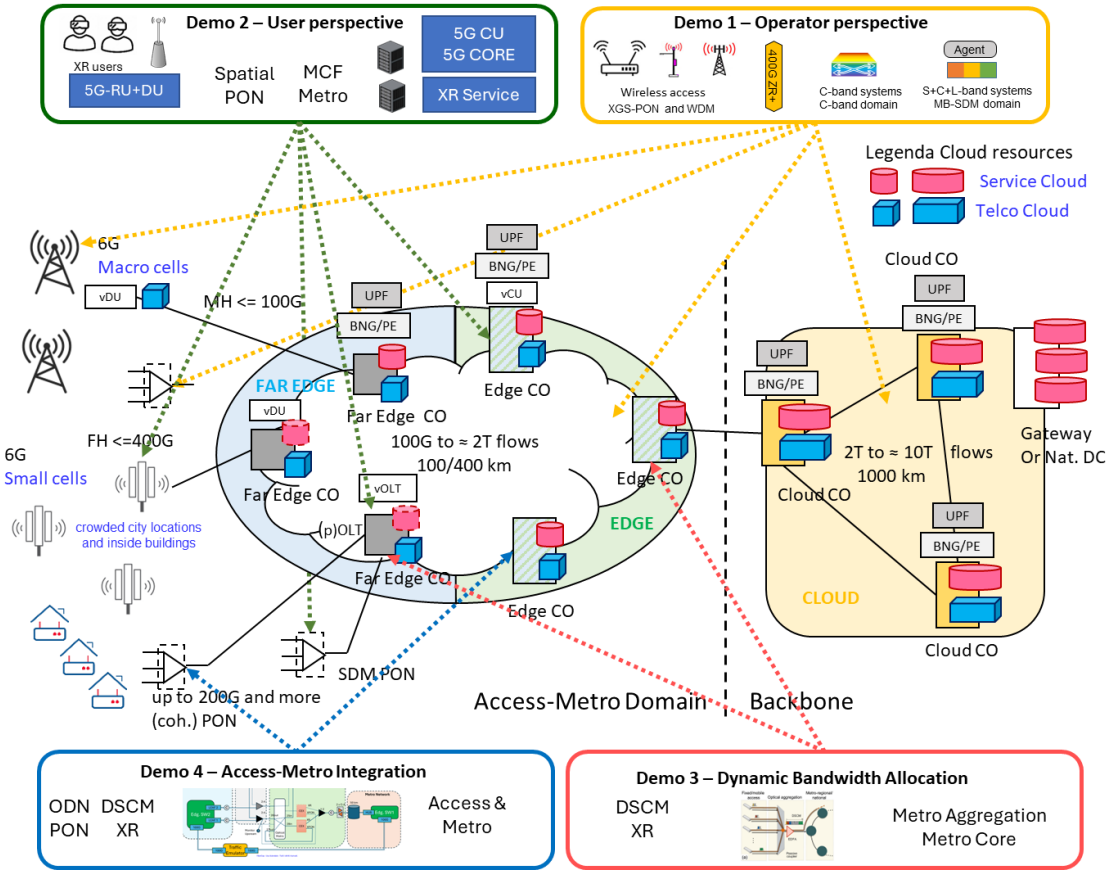

Figure 2.3-1: Experiments (demos) mapping on long-term data plane architecture.

2.4 TOPIC CLUSTERING FROM SEASON PROJECT INNOVATIVE SOLUTIONS

Analyzing the innovation solutions items listed in Section 2.2, it is possible to cluster the study objects and prototyping activities of SEASON project into five main Topic Clusters. Clustering is

focused on WP3 activities, i.e., on data plane aspects, so it does not cover the project in its entirety, although control (WP4) and integration (WP5) aspects are also partially involved. The five topic clusters are listed below along with the relevant elements involved in each of them, for the medium and long term separately.

Topic Cluster 1 - TC1: Multi-Band over Space Division Multiplexing (MBoSDM) Technologies

- Medium-term Solutions (2.1.1):
  - Multi-band switching nodes for S, C, L bands.
  - Sliceable bandwidth/bit rate variable transceivers (S-BVT)
  - Multigranular switching architectures.
  - Filterless network designs reducing OEO conversions.
- Long-term Solutions (2.1.2):
  - Spatial division multiplexing with multi-core fibers (19-core MCF)
- Ultra-high capacity systems achieving 2.4-3.6 Pbs switching capacities.
  - Multi-core/multi-mode fiber systems

Topic Cluster 2 - TC2: Digital Subcarrier Multiplexing and Optical Aggregation

- Medium-term Solutions:
  - Digital subcarrier-based multiplexing (DSCM) for P2MP transceivers
  - Optical aggregation for energy savings
  - Horseshoe-and-spur topology implementations.
- Long-term Solutions:
  - Dynamic bandwidth allocation systems
  - Access-metro integration with fiber sharing
  - P2MP coherent systems for fronthaul/midhaul

Topic Cluster 3: TC3: Advanced Network Control and Monitoring

- Medium-term Solutions:
  - DSP-based monitoring systems
  - Predictive maintenance for amplifiers
  - Telemetry systems for network monitoring
- Long-term Solutions:
  - SDN control plane integration
  - Software-defined control systems
  - Real-time traffic adaptation mechanisms

Topic Cluster 4: TC4: Coherent Pluggable and Amplification Technologies

- Medium-term Solutions:
    - 800ZR and 800G OpenZR modules
    - Pluggable amplifier systems
  - Coherent pluggable transceivers for white-box devices
- Long-term Solutions:
  - 1600ZR/3200ZR standard alignment systems

- Low-power DSP architectures with frequency domain filtering
- Multi-band amplifier systems

Topic Cluster 5 - TC5: Spatial PON and Access Network Solutions

- Medium-term Solutions:
  - Spatial PON nodes for aggregation/disaggregation
  - Smart NIC PDU with coherent pluggables
- Long-term Solutions:
  - Full access-metro integration
  - Infrastructure fiber sharing mechanisms.

The following comprehensive mapping table relates the five Topic clusters to the prototypes, to the sections of this document describing the related studies carried out and, in the last column, the references, among which there are many articles published in the top journals in the field.

Table 2.4-1: Comprehensive Mapping Table.

TC1: MBoSDM Technologies		
Related Prototypes	**Relevant Sections**	**Related References**
C3.1 (MBoSDM node), C3.2 (Multigranular node), C3.4 (MBoSDM S-BVT)	Section 5 (5.3: Crosstalk, 5.4: MCF performance, 5.5: Ultra-high-capacity planning) Section 6 (6.1: S-BVT improvements, 6.2–6.3: switching nodes)	[Moh25], [Cas25], plus references in Section 5 & 6
TC2: DSCM and Optical Aggregation		
Related Prototypes	**Relevant Sections**	**Related References**
C3.10 (Dynamic BW allocation), C3.11 (Access-Metro integration)	Section 5 (5.1–5.2: filterless & aggregation, 5.6: IPoWDM latency, 5.7: Flexible CO framework) Section 8 (8.2–8.7: power efficiency, transceiver reduction, anomaly detection)	[Moh25], [Case25]
TC3: Network Control and Monitoring		
Related Prototypes	**Relevant Sections**	**Related References**
C3.5 (DSP Rx-based monitoring), C3.6 (Predictive maintenance for MB Amplifiers), C3.7 (Monitoring Telemetry)	Section 4 (4.5–4.7: monitoring systems) Section 8 (8.1–8.5: DSP monitoring, LPM, predictive maintenance)	Monitoring + DSP publications cited in Sections 4 & 8
TC4: Coherent Pluggable Technologies		
Related Prototypes	**Relevant Sections**	**Related References**
C3.8 (Pluggable amplifier), C3.9 (Smart NIC PDU)	Section 4.8 (pluggable amplifier) Section 4.9 (SmartNIC PDU) Section 5.6 (IPoWDM coherent pluggables)	References in Sections 4.8, 4.9, 5.6

TC5: Spatial PON and Access		
Related Prototypes	**Relevant Sections**	**Related References**
C3.3 (Spatial PON node), C3.11 (Access-Metro integration)	Section 4.3 (Spatial PON) Section 5 (Access-metro integration models) Section 7 (front/mid-haul and access systems)	PON and access-metro references in Sections 4, 5, 7

2.5 PROJECT KPIS RELATED TO WP3

2.5.1 KPI 2.1: Increase the available bandwidth of the fiber.

Increase the available bandwidth of the fiber from actual C-band (~35 nm) to O, E, S, L, U bands (~415 nm) that, together with the usage of SDM, e.g., with >10 fibers / cores, will make the available bandwidth to grow by a factor ×120.

Achieved (see Deliverable D2.3 for details)

The actual increase in available bandwidth is influenced by several factors, including transmission distance, signal impairments, and the number of active channels. Early studies indicate that this increase can be effectively achieved by combining multiband (MB) transmission with spatial division multiplexing (SDM).

The 120× capacity enhancement targeted by KPI 2.2 is primarily enabled by SDM, especially through the deployment of multiple parallel fibers (a more practical solution in the medium term) and multicore fibers (expected to be more viable in the long term). Reaching this level of enhancement typically requires around 20 to 30 parallel multiband systems or cores.

A comprehensive techno-economic evaluation of the solutions capable of supporting this capacity increase is presented in Deliverable D2.3, supported by the studies and frameworks discussed in this document.

Section 5 provides an in-depth analysis of the technologies that enable increased fiber bandwidth. Specifically, Sections 5.3 and 5.4 examine the impact of cross-talk between parallel cores within a fiber (an effect that could constrain the number of usable cores and is critical to understanding the limitations of future SDM systems using multicore fibers). Sections 5.8 and 5.11 present transmission models and compare the optical performance of various multiband systems with spectral occupation up to 24 THz.

2.5.2 KPI 2.2: 50% CAPEX reduction

50% CAPEX reduction by (1) designing an architecture that jointly leverages on parallel fibers (where fiber resources are abundant), multiple bands (where fiber resources are scarce), and multi-core fibers (where fibers are not present, e.g., for cell densification); (2) limiting intermediate aggregation in routers thanks to the ultra-high capacity of MBoSDM and by

exploiting smart coherent pluggable to remove aggregation layers and unnecessary O/E/O conversions.

Achieved (see Deliverable D2.3 for details). Several studies described in this deliverable served as basis for the techno-economic analysis presented in deliverable D2.3 that validates this KPI. The modeling of the transmission and evaluation of the performance of multiband systems (described in sections 5.5, 5.8 and 5.11) helped to select the bands that are more suited for future deployments and should be used on the techno-economic studies related to (1).

2.5.3 KPI 3.1: Design and implement flexible and modular MBoSDM node

Design and implement flexible and modular MBoSDM node prototypes able to switch/add/drop channels in at least 3 different bands (e.g., S, C, L) in an SDM/MCF fiber infrastructure featuring up to 10 fibers/cores, able to cope with switching capacities scalable up to between 2.4-3.6 Pb/s (considering a 4-degree node with 50% local add/drop and depending on the number of used bands and SDM cores/fibers) [SRIA, mid-term evo ~2028], by approaching (fractional) space-wavelength flexible architectures [Ma15].

Achieved. In deliverable [D3.2-24], initial discussion has been included related to the achievement of this KPI. There, different node architectures were presented and evaluated for high-capacity, MBoSDM optical networks. These advanced node architectures, based on spatial optical cross-connects (S-OXCs) or MB wavelength-selective switches (WSS), provide advanced switching capabilities and trade-off flexibility/performance versus cost/complexity. Although these architectures are not yet commercially available, they can be built with mature components such as band pass filters (BPF), fan-in/fan-out devices, OXCs, or WSS operating in a single or double band (C+L). Each degree of these switches can handle up to several hundred Tb/s, and a node with a degree greater than four can easily achieve an overall switching capacity in the Pb/s range. In deliverable [D2.3-25], discussion on node traffic capacities is performed considering the reference backbone network topology proposed in section 5.2.2 of SEASON deliverable D2.1. To support the development of a scalable infrastructure that meets these high switching capacities, SEASON has developed and implemented two prototypes (C3.1 and C3.2, detailed in section 7), which enable both spatial (core, fiber) and spectral (wavelength/band) switching. These prototypes are designed to switch, add, and drop channels across at least three different bands (C+S+L) within an SDM infrastructure, aligning closely with the KPI requirements. Section 4.1 demonstrates the transmission of three slices of the MB(oSDM) S-BVT prototype at 41.3 Gb/s (C-band), 45.4 Gb/s (L-band), and 34 Gb/s (S-band) over 25 km of MCF. This multiband flow is switched using the three-degree node prototype component C3.1 (Section 7), which enables both band (S+C+L) and core switching, employing a 19-core MCF with two cores connected to the prototype. Leveraging the full S+C+L spectral range over a 19-core MCF can significantly boost total capacity. Under this setup, 350 channels at 25 GHz (S-band), 175 channels at 25 GHz (C-band), and 150 channels at 50 GHz (L-band) can envision a total capacity of 28.2 Tb/s. When extending to the spatial dimension of the 19-core MCF, 0.5 Pb/s can be

envisioned. For higher-degree node configurations, target KPI switching capacities between 2.4 Pb/s and 3.6 Pb/s would be enabled.

2.5.4 KPI 3.2: MBoSDM transceivers able to increase the capacity of SoA transceivers

MBoSDM transceivers able to increase the capacity of SoA transceivers [Nad22] up to 2× - 4× by exploiting enhanced wavelength/space dimensions while enabling appropriate slice/band/core/fiber selection according to the network path.

Achieved. In Section 4.1, capacity upgrades scenarios with MB and SDM are presented and evaluated towards targeting this KPI. The required capacity scaling up to 2x – 4x could be envisioned by expanding transmission into S-, C, and L-bands and introducing SDM for additional spatial paths. In this regard, programable MB(oSDM) sliceable bandwidth/bit rate variable transceiver prototype (S-BVT), proposed in SEASON (component C3.4 described in section 7), supports flexible, sliceable bandwidth allocation across S-, C- and L-bands, providing scalability, improved network utilization and appropriate slice/band/core/fiber selection according to the network path. The prototype can be dynamically reconfigured using software-defined networking (SDN) agents, which control and adjust the programmable transceiver components and other reconfigurable devices according to network requirements and demand. This flexible transceiver approach is fully aligned with the project's KPIs, supporting adaptable allocation of spectral and spatial resources to achieve target capacity enhancements. Experimental evaluation demonstrated in Section 4.1 and previous results in deliverable D3.2, shows that operating over the complete S+C+L band on a single core of a 19-core MCF could enable an aggregate capacity of 28.2 Tb/s, assuming 350 channels in the S-band (SSB), 175 channels in the C-band (SSB), and 150 channels in the L-band (DSB). In comparison, a state-of-the-art (SoA) C-band S-BVT populated with 175 C-band (SSB) channels would reach roughly 7 Tb/s. Therefore, using a multiband (S+C+L) approach allows for a theoretical increase in capacity by a factor of up to 4, which would further scale with the number of MCF cores. Nevertheless, expanding transmission across multiple cores and using multiple bands introduces new challenges, such as stimulated Raman scattering (SRS) and crosstalk (XT), which can affect and limit the actual capacity achieved and the scalability factor, as also indicated in section 3.3.

2.5.5 KPI 3.3: Optimized DSP for metro/core coherent applications

Optimized DSP for metro/core coherent applications, able to increase 4× data-rate, reaching up to 1.6Tb/s per port with power consumption suitable for future pluggable modules.

Achieved. The current work on optimized DSP for metro and core coherent applications is making strides toward supporting up to 1.6 Tb/s per port, aligning with the demands for future pluggable modules under the emerging 1600ZR standard. A key focus is the integration of novel low-power DSP architectures, specifically those employing frequency domain (FD) filtering for group velocity dispersion (GVD) compensation—a computationally intense task within DSP.

In Section 6.5, the FD filter architecture uses FFT and IFFT to facilitate GVD compensation by handling signal processing in the frequency domain. However, as symbol rates increase, the complexity and power demands of these DSP operations grow significantly, especially for symbol rates of 120 GBd and higher. complexity analysis quantified by non-trivial complex multiplications were shown and presented in an accepted, PTL paper which shows that up to 12% reduction for 120 GBd and up to 18% for 240 Gbd.

2.5.6 KPI 4.2: >50% contribution in energy saving

>50% contribution in energy saving via dynamic spatial channels aggregation and deactivation of unused transceivers at the OLT side basing on traffic conditions over total 70% energy saving targeted by [SRIA].

Achieved. The dynamic spatial aggregation architecture developed in SEASON effectively achieves the targeted energy efficiency improvements by dynamically activating and deactivating spatial lanes in response to real-time traffic demands. As discussed in D2.2, simulation results demonstrate an average potential energy saving of 38%, with peak savings up to 87.5%, depending on the ratio of fixed to variable power consumption and the configuration of spatial lanes. Experimental validation on a commercial PON system, characterized by a relatively high baseline power, confirmed measurable energy savings of around 4%. The lower experimental figure is primarily due to the fact that the commercial hardware used was not originally designed to support the activation/deactivation mechanisms explored within SEASON, thus limiting the achievable power variation at the transceiver. When considering the joint activation and deactivation of Radio Units (RUs) and Distributed Units (DUs) in the mobile network together with the optical access domain the overall saving increases to approximately 8% experimentally measured. Further optimization of radio equipment operation could raise the total system-level energy saving up to 19%. These results confirm the effectiveness and scalability of the proposed architecture for next-generation energy-aware optical and radio access networks.

2.5.7 KPI 4.3: 400Gb/s RAN fronthaul ports capacity.

400Gb/s RAN fronthaul ports capacity.

Achieved. Studies indicate that achieving 6G capabilities within the next five years will require increasing the bandwidth to 400 Gbps in the Fronthaul segment. This substantial bandwidth expansion underscores the growing necessity to adopt coherent optical technology for efficient data transmission. As part of the SEASON project, we have chosen to explore and implement a WDM Mesh Network in the Fronthaul segment. By incorporating 400 Gbps transceivers, this architectural approach allows us to significantly enhance network capacity while introducing greater flexibility.

Coherent pluggable 400G transceivers, based on Open ZR+ specs, face challenges like low-power output and fixed amplifier gain, impacting OSNR and receiver sensitivity. Low-power versions require fixed attenuators, affecting power budgets. High-power versions (+3 dBm) reduce these issues, enabling longer distances and supporting up to 6 nodes with 15 wavelengths and 21 dB EDFA gain. At 200 Gb/s, up to 10 nodes are feasible.

2.5.8 KPI 4.4: High accuracy profile for IEEE 1588-2019

High accuracy profile for IEEE 1588-2019 or better, evolving ±1.5 µs of LTE and Release-15 Standalone, aiming to ns with target IEEE P802.1CM A+ networks, demanding an accuracy better than 12.5 ns.

Achieved. To meet the KPI requirements, Accelleran deployed a Telecom Grandmaster (T-GM) clock within the CU server, utilizing an Intel E810 NIC card. The T-GM is synchronized using a GNSS satellite timing signal, and timing information is distributed across the IP network. This setup enables the O-DUs and O-RUs to achieve precise time and phase synchronisation with the T-GM through the PTPv2 (IEEE 1588-2019) protocol, in which timing signals are propagated from the T-GM to the Telecom Time Slave Clocks (T-TSCs) implemented in the O-DU and O-RU. In the SEASON demonstration sites, this deployment achieved timing accuracy ranging from −10.1012 ns to 11.1012 ns with a confidence level of 99.999%, thereby surpassing the KPI requirement of 12.5 ns accuracy.

2.5.9 KPI 5.1: Achieve sub-km (<500 m) and sub-dB (<0.5) resolution

Achieve sub-km (<500 m) and sub-dB (<0.5) resolution in the estimation of longitudinal fiber attenuation points and optical amplifier gain, respectively, using DSP-based monitoring scheme.

Achieved. The SEASON project aims to enhance optical network monitoring by improving the resolution and accuracy of longitudinal power profile estimation using DSP-based techniques. We used a method based on Linear Least Squares (LLS) method, achieving a higher accuracy in anomaly localization. The method was developed in [C3.5] and achieves sub-km (less than 1km) and sub-dB (0.46 dB) resolution in estimating fiber attenuation points. The detailed work was published in a JOCN paper and is reported in this deliverable under section 8.4.

2.5.10 KPI 5.2: Performance improvement achievable with an optical spectrum analyzer

Performance improvement achievable with an optical spectrum analyzer (OSA) embedded in the amplifier setup and control identified for different link designs and applications.

Achieved. Dynamic gain equalization in erbium-doped fiber amplifiers (EDFA) using adaptive gain-flattening combined with spectral measurements in each optical amplifier embedded into a link has the potential to significantly improve link performance [Rap03]. However, additional

cost introduced by the required components made this technique economically unattractive. Furthermore, an alternative technique based on a reconfiguration stage turned out to provide similar performance improvement at a lower cost. However, cost has changed significantly since wavelength configurable devices have been realized, and they are now cheaper due to their large use in modern optical networks and the progress in photonic integration. Therefore, the concept of spectral reconfigurability has been revisited in view of the multi-band technology, in particular thulium-doped fiber amplifiers (TDFA) for the S-band. Using a simplified simulation model for TDFAs developed in this project, the potential of this technology has been evaluated.

Developing a simulation model based on rate equations would have significantly exceeded the available time resources and has not been planned in this project. However, it is planned to confirm the results obtained at a later stage, once the work currently underway in another project has been completed.

2.5.11 KPI 5.3: OTDR Interrogator for latency / position measurement

OTDR Interrogator for latency/position measurement with 4 ns / < 1 meter accuracy respectively.

Achieved. The D-OTDR system has been designed to meet KPI 5.3 by enabling precise latency and position measurements in fiber-optic transport networks without service disruption. It achieves 4-ns latency resolution and sub-meter spatial accuracy through a fully digital approach, avoiding high-power analog pulses and traffic interruption typical of traditional OTDR. Using complementary Golay coded sequences at low optical power on reserved out-of-band wavelengths (1610–1630 nm), the system applies correlation-based processing to reconstruct event timing with 2-ns resolution, mapping to approximately 20 cm spatial precision. The architecture integrates an FPGA for sequence generation and timestamping with an SFP transceiver housing the laser, AGC receiver, and optical circulator, enabling one-ended activation without remote equipment. Continuous in-service monitoring identifies discontinuities, connectors, micro-bends, and severe faults with high timing fidelity, reducing MTTD and MTTL. Unidirectional latency measurement is supported via out-of-band filtering and timing anchors, ensuring compatibility with live traffic. Operational features include a detection range up to 52 km, low power consumption (~1 W), and absence of dead zones or saturation, eliminating launch fibers. Long coded sequences and robust correlation deliver high SNR for timing extraction, guaranteeing KPI 5.3 targets of 4-ns latency granularity and position accuracy below 1 meter. An extended technical description of the D-OTDR system is provided in Deliverable D5.3. Overall, D-OTDR offers scalable, accurate diagnostics for next-generation optical networks.

2.5.12 KPI 5.4: Applicability of modulation format insensitive optical signal-to-noise ratio

Applicability of modulation format insensitive optical signal-to-noise ratio (OSNR) measurement techniques in different scenarios determined, sources of inaccuracy identified, impact of signal distortions worked out.

Achieved. Spectral correlation has been shown to be a promising technique for monitoring signal quality in agile, disaggregated and open networks [Rap21]. In particular, it has been shown that the technique is able to capture the impact of all major propagation impairments in a standard single mode fiber. However, the measurement results also revealed that the measurement parameter reacts with different sensitivity to the different impairments. Therefore, it has been concluded that aligning the sensitivity of the measurement parameter should be further investigated for getting a universally usable GSNR value for characterizing link quality.

For this purpose, further investigations including additional postprocessing of the measurement results have been conducted in order to get a better alignment of the sensitivities. In fact, differences in the sensitivities to different effects could be reduced, but the achievements are not sufficient for qualifying as a universal tool for estimated link quality.

In summary, the KPI has been achieved in that the applicability of the *modulation format insensitive optical signal-to-noise ratio (OSNR) measurement techniques in different scenarios has determined and effects leading to increased inaccuracy have been identified. In particular, the impact of signal distortions has been pointed out.*

Building on this, it would be desirable to develop a technology that reduces the influence of the mentioned effects on the results. Initial work in this direction has been undertaken, and improvements have been achieved. However, further improvements going significantly beyond this KPI were not possible within the available project-related effort.

2.5.13 KPI 7.3: Configuration of the MBoSDM node prototype agents for simple operations

***Configuration of the MBoSDM node prototype agents for simple operations from the SDN control plane of O(100ms*).**

Achieved. The activity is related to the integration of the MBoSDM node prototype with the SDN control plane and related agents. A detailed explanation for the assessment of this KPI is provided in deliverable D5.3 and D5.2. There the control plane delay/latency for the MBoSDM node prototype was evaluated based on the time required for the SDN controller to send configuration commands using the NETCONF protocol and the defined YANG data models for the node. Under a LAN-like control plane scenario, the SDN controller successfully executed SDM

cross-connections and multiband (e.g., L+S) cross-connections within the target constraint of **O(100 ms)**, measuring a latency of 75.19ms**.**

3 APPLICATION OF SEASON KEY ACHIEVEMENT FOR SELF-MANAGED SCALABLE SUSTAINABLE HIGH-CAPACITY OPTICAL NETWORKS

This section translates the key technical achievements and data plane prototypes presented in Section 2 into representative application scenarios. The applications discussed here illustrate how the WP3-developed technologies (detailed in Sections 4–7) can be combined to support concrete deployment contexts aligned with SEASON KPIs and system-level demonstrations.

In this section, we present a possible path towards truly self-managed, scalable, sustainable, and high-capacity optical networks, as introduced in [Cas25, Fer25, Nap25]. In this context, we summarize key SEASON achievements, discuss the importance of the work carried out within the project, and provide an outlook on the evolution of optical fiber communication systems based on some of our key results. Building on these findings, we outline the different architectures and applications, devices, solutions, and tools required to deploy optical networks capable of guaranteeing the necessary scalability while ensuring full sustainability and flexibility.

Central to the SEASON solution are the S-BVTs, which, in principle, can be tuned to operate over MB and multi-core systems and can be also employed to realize P2MP configurations if needed. We then illustrate several applications based on P2MP S-BVTs in scenarios such as metro-aggregation optical networks, passive optical networks and radio access networks, highlighting the benefits offered by this approach in enabling sustainable, scalable, and flexible optical infrastructures. Furthermore, we address the growing impact of AI, ML, and beyond-5G technologies on traffic patterns and network requirements.

In modern metro-access networks, Internet Protocol data traffic is increasingly hub-and-spoke (H&S), highly dynamic, and shaped by heterogeneous patterns. While Intensity Modulation Direct Detection (IMDD) systems are reaching their limits even in short-reach scenarios, coherent transmission is emerging as a strong candidate to provide the necessary reach, spectral efficiency, scalability, and manageability demanded by new applications. The motivation for developing truly scalable, sustainable, and flexible optical networks is therefore strongly linked to sustainability goals, encompassing optimized power consumption and architectures, software-configurable operation that adapts to real traffic, seamless migration from low-speed to high-speed regimes [Cas24], improved spectral efficiency, and architectural simplification through the elimination of unnecessary OEO conversions, thus reducing required hardware [Cast25].

In SEASON, we propose using coherent P2MP enabled by DSCM to cope with H&S traffic patterns. The approach is rooted in digital communication, taking the spectrum and the digital transceiver as fundamental building blocks. Concepts such as 1.6T ZR+ and DSCM are being considered in several conferences and industrial events, while the overall objective is to solve or simplify issues across multiple network segments. This includes less transceiver, energy saving

– dynamic, PON overlay – compatible, and intergenerational compatibility, and – possibly – less router interfaces.

Hereafter, we consider a selected list of applications to explain how DSCM-based P2MP transceivers can enable scalability, sustainability, and flexibility.

3.1 APPLICATION 1: NEXT GENERATION MOBILE FRONTHAUL FOR B5G/6G

The first considered application focuses on next generation mobile fronthaul, and it is reported in next Section 7, where a P2P link for front-hauling applicable to B5G/6G deployment is illustrated. Crucial factors for the upcoming mobile transport include: (i) high-speed TRXs; (ii) BiDi transmission over a single fiber to support latency-critical B5G/6G applications [Tar24]; and (iii) simplified hardware to eliminate costly dual-laser setups such as in [Aca24]. To avoid a dual-laser, a single-laser-wavelength transmission (visualized in Figure 3.1-1 (b, c)) could be considered. However, as shown in [Cav24, Fer24], this configuration might suffer from high penalties due to distributed Rayleigh backscattering and discrete reflections from components, which become particularly detrimental when upstream (US) and downstream (DS) share the same wavelength [Fer24]. Figure 3.1-1 (d, e) illustrates an alternative method using DSCM, maintaining a single-laser -wavelength by interleaving digital subcarriers (DSCs) for both US and DS in the frequency domain [Ras19]. We have shown that this configuration, based on DSCM, reduces the penalty caused by reflection to almost zero [Fer24] as the flexibility introduced by the DSCM enable to use different DSCs for the DS and US. An additional benefit of DSCM for mobile transport is the ability to provide US and DS capacities symmetrically or asymmetrically according to the conditions of traffic varying over time. This has been investigated and reported in [Fer25], where DSCM-based transceivers enable the BiDi transmission in half mode, and if optimized, they can also enable full mode for some or all DSCs. A brute-force optimization of the individual power of the DSCs has been also carried out.

This application is enabled by the DSCM-based coherent transceivers (C3.4), Smart NIC/DPU solutions (C3.9), and access–metro integration prototype (C3.11), as detailed in Sections 4.4, 4.9, and 7.2.

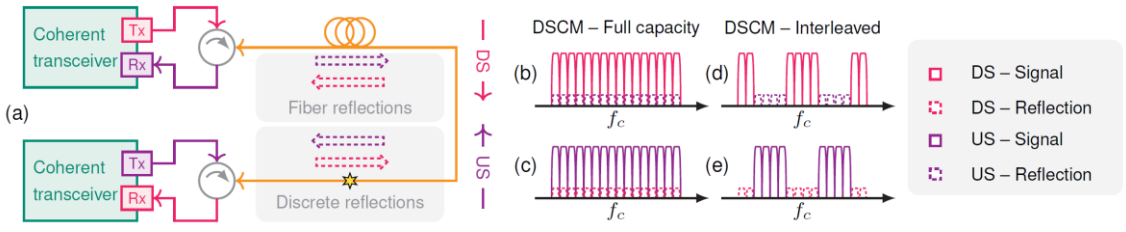

Figure 3.1-1: Bidirectional transmission over single fiber single laser single wavelength and reflection mitigation using DSCM. Reflections are caused by fiber because of the distributed Rayleigh backscattering and of the discrete components such as circulators.

3.2 APPLICATION 2: DYNAMIC TRAFFIC ALLOCATION

The second considered scenario that we address offers two primary advantages: capacity re-utilization [Her23] and energy efficiency [Cas25]. In [Her23], we introduced traffic clustering using DSCM to facilitate more efficient utilization of the spectrum. In [Cas24], we showed that the spectrum of the network could be better used during low traffic at night. Thanks to the flexibility provided by the DSCs, this is possible by reallocating spectrum for new services, like a fiber-as-a-service approach and reduces network power consumption by modifying the operational parameters of coherent DSCM TRXs (e.g., turning off idle DSCs) [Cas24, Cas25]. Figure 3.2-1 below shows the static allocated capacity of 100G SC TRXs (green) and the dynamic one of 100G P2MP units (violet), with the dashed black line depicting the variations in daily traffic.

The described dynamic traffic allocation relies on the dynamic service allocation prototype (C3.10) and the control/telemetry integration described in Sections 5.7 and 8.

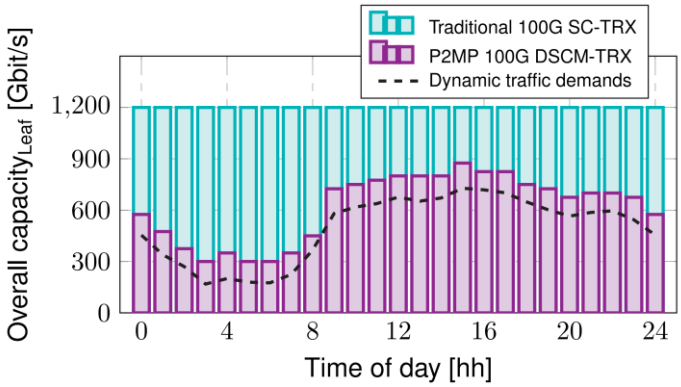

Figure 3.2-1: Exemplary of daily traffic variation and provisioned.

3.3 APPLICATION 3: FLEXIBLE OPTICAL AGGREGATION

The flexibility enabled by DSCM-based coherent pluggable can considerably simplify the design of complex horseshoe networks [Cas23]. Figure 3.3-1 (a, b) illustrates an example of a horseshoe network provided by Telecom Italia Mobile (TIM) that mimics existing urban network topologies. In this analysis, for simplicity, the leaf nodes (circles) are connected to a single hub (square). Thanks to P2MP TRX, we can aggregate multiple horseshoes at the hub, thus reducing the hardware needed and improving scalability. In Figure 3.3-1 (a), we do not aggregate the two horseshoes, so we need one hub TRX per segment (2×400G), while in Figure 3.3-1 (b) both horseshoes can be served by a single high-capacity TRX. The optical aggregation can be carried out as long as there are DSCs available, and the minimum OSNR is above the required threshold. In case the number of DSCs increases above the available, then a new highspeed TRX will be needed. It is important to stress that for P2P TRX, the number of TRXs at the hub is equivalent

to the number of lead nodes and clearly no aggregation between horseshoes would be possible. Furthermore, a switch would be needed to aggregate the traffic of the leaf nodes. In general, the higher the level of aggregation enabled by P2MP, the lower the number of TRXs needed. However, as network size increases, aggregation levels decrease because of being constrained by the network's minimum OSNR. In [Cas25], these scenarios have also been addressed in terms of energy efficiency and saving.

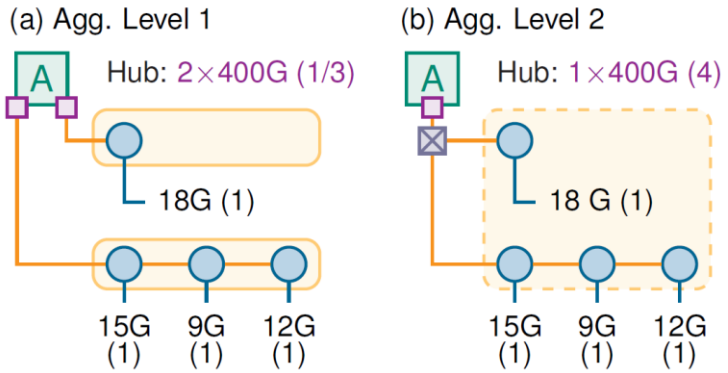

Figure 3.3-1: Two-horseshoe network configurations: (a) no aggregation (a); (b) with optical aggregation. The squares are couplers/splitters.

The energy savings achieved by DSCM and P2MP enabling all-optical traffic aggregation are investigated also in Secs. 5.2 and 8.2, at the edge between access and metro segments. Optical aggregation may save energy-hungry router interfaces strongly contributing to build sustainable networks [Cas25].

Flexible aggregation is supported by multigranular switching nodes (C3.1, C3.2) and multiband transmission technologies analyzed in Sections 5.3–5.5 and implemented in Section 6.

4 SEASON DATA PLANE PROTOTYPES

This section reports on the different WP3 components, subsystems and systems developed as innovative prototypes within the SEASON project in the final version achieved at the end of the project. In Section 2 of this document, the connection between the prototypes and SEASON's medium- and long-term innovations has been highlighted (see Table 2.2-1). Furthermore, still in section 2, the prototypes have been grouped into the following five topic clusters:

- TC1: Multi-Band over Space Division Multiplexing (MBoSDM) Technologies (C3.1, C3.2)
- TC2: Digital Subcarrier Multiplexing and Optical Aggregation
- TC3: Advanced Network Control and Monitoring
- TC4: Coherent Pluggable and Amplification Technologies
- TC5: Spatial PON and Access Network Solutions (C3.3)

The association between prototypes and thematic clusters is given in Table 2.4-1. The subsections of this chapter are dedicated to specific prototypes. Each subsection is dedicated to a single prototype that recalls the thematic cluster to which the prototype is associated and provides the final prototype report. This report specifies the project partner that developed the prototype, where it was built (a partner's lab), how it was tested (in a single partner's lab or in a joint demo), and includes a final description of the prototype, its interfaces, and the target KPIs addressed with their level of achievement. As a summary, it can be said that the development of all data plane prototypes was successfully completed, and all associated KPIs were fully achieved, as specified below individually for each prototype.

4.1 MBOSDM NODE PROTOTYPE (C3.1)

4.1.1 Description

In the framework of the SEASON project, CTTC has developed a multiband (MB) over spatial division multiplexing (SDM) switching node prototype to advance the capabilities of current node options.

Beyond the state of the art, the C3.1 prototype demonstrates, for the first time in an experimentally validated node, the joint exploitation of multiband (S+C+L) transmission and space-division multiplexing with band, wavelength- and space-selective switching capabilities. While existing solutions typically address either multiband operation or SDM independently, C3.1 integrates both dimensions within a single modular node architecture, enabling scalable Pb/s switching capacities with reduced filtering complexity.

This prototype is associated with the topic cluster TC1. The architecture is designed to support both spectral (band and wavelength) and spatial granularities to meet the capacity scaling and traffic demands of next-generation optical networks. It ensures a highly adaptable, modular, and

flexible switching paradigm with advanced capabilities suitable for evolving network environments. Spectral granularity, in terms of wavelength, is achieved using fixed- and flex-grid wavelength division multiplexing (WDM) technology, utilizing C-band 100 GHz AWG and programmable WSS devices, respectively. The WSS bandwidth and central wavelength can be adjusted with 12.5 GHz granularity within the C-band. The design includes two WSS units with 1x2 ports and two AWG units with 1x5 ports on fixed 100 GHz ITU-T C31-C35 channels to leverage WDM. The proposed MBoSDM node prototype has been optimized in the second phase of the project, as previously detailed in section 4.2. This optimization ensures increased flexibility in the spectral domain by considering wavelength granularity in the C+L-bands. MB dimension is addressed by incorporating four 1x3 MB filters operating within the S-, C-, and L-bands (two units per direction for bidirectional MB transmission). SDM is achieved by utilizing distinct spatial paths, enhancing switching capabilities, and network throughput. To this end, fan-in/-out devices are included, enabling efficient core switching with a 19-core multi-core fiber (MCF) of 25.4 km (two cores per direction). This setup ensures bidirectional SDM transmission, providing bidirectional core availability. The prototype supports core switching across four cores within the available MCF and facilitates add/drop operations. The core structure is built with an 18x18 optical matrix switch, offering multiple and dynamic switching configurations.

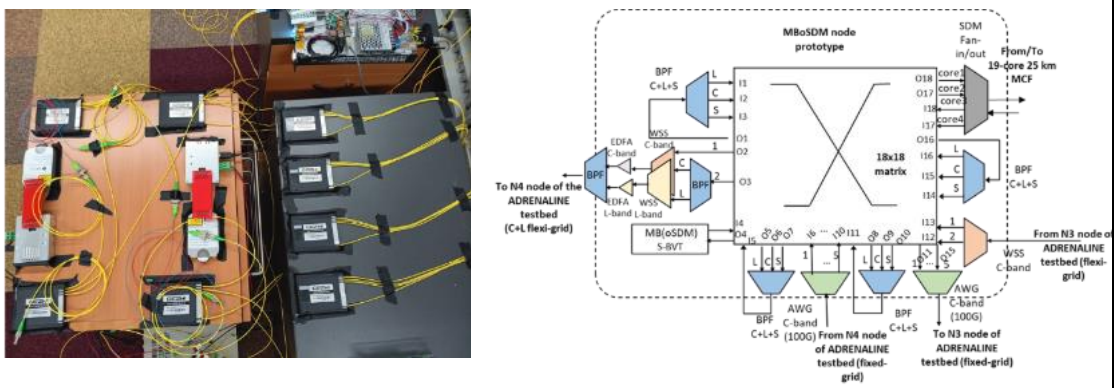

Figure 4.1-1: MBoSDM switching (a) prototype integrated in the ADRENALINE testbed and (b) architecture with the main updated building blocks.

The node prototype is integrated within the ADRENALINE testbed, establishing different path connections to two network nodes. Node programmability and flexibility are achieved using WSS devices, which allow full reconfiguration within the C-band and L-bands for flex-grid operation and optimized resource utilization, as seen in Figure 4.1-1. This design also ensures flexibility and versatility regarding exploited granularities and available resources (both spectral and spatial). Broader spectrum coverage and the use of spatial channels significantly enhance overall network capacity, flexibility, and efficiency. The node solution can be scaled to meet target capacity requirements by increasing the number of ports in the matrix and WSS modules. These capabilities create a switching solution that aligns with the anticipated demands of high-capacity and dynamic network environments.

Table 4.1-1: MBoSDM switching node prototype parameters and key features.

Parameter	Specifications
Operation bands	S-band (1460-1530 nm) C-band (1530-1565 nm) L-band (1565-1625 nm)
Operation cores	2 cores per direction
Insertion loss	< 3.2 dB
Optical power	< 20 dBm
PDL	< 0.1 dB
Switching speed	20 ms

Table 4.1-2: MBoSDM switching node key features.

Key features	Specifications
Scalability	Limited to the matrix and filters port count
Flexibility	WSS (flex- grid operation within C+L-bands) Enhanced resources and bandwidth
Programmability	WSS initial and final slices, port attenuation and switching port
Operation	MB, WDM and SDM

Table 4.1-1 and Table 4.1-2 specifies the node parameters, including main bands and cores of operation, insertion loss (IL), maximum optical power allowed, polarization-dependent loss (PDL), and switching speed.

The node prototype has been implemented, optimized and experimentally validated into a MBoSDM scenario (see Section 7.2). A final demonstration including the integration of the proposed node prototype with the control plane has been performed at CTTC. The activities are reported in deliverable D5.2.

4.1.2 Interfaces

The proposed MBoSDM node prototype can be controlled by means of an SDN agent based on NETCONF, implemented within the project (WP4). A demonstration of the integration of the node prototype with the corresponding network controller and related agents has been demonstrated and the main achievements are reported in deliverable D5.2. The MBoSDM node prototype has been abstracted to define logical, high-level operations, as detailed in the D5.1 of SEASON. Figure 4.1-2 shows the abstraction of the MBoSDM node prototype in terms of input/output ports used to define logical high-level operations that will enable the implementation of the node SDN agent. The considered node operations include: i) core switching from one core port to another core port; ii) optical band add and drop; iii) spectrum switching and iv) spectrum add and drop from/to different cores of the 19-cores MCF, the MB(oSDM) S-BVT prototype and different nodes of the ADRENALINE testbed. Additional key programmable parameters have been identified to implement low level interfaces that will enable the reconfiguration of specific node building blocks and subsystems. Specifically, the SDN agent maps the high-level operations to the configuration of the node specific elements such as matrices and WSS (in terms of initial and final slices, the switching port and configuration of

these slices, and the attenuation). Finally, Table 4.1-3 reports the different interfaces for control and management of the switching MBoSDM node.

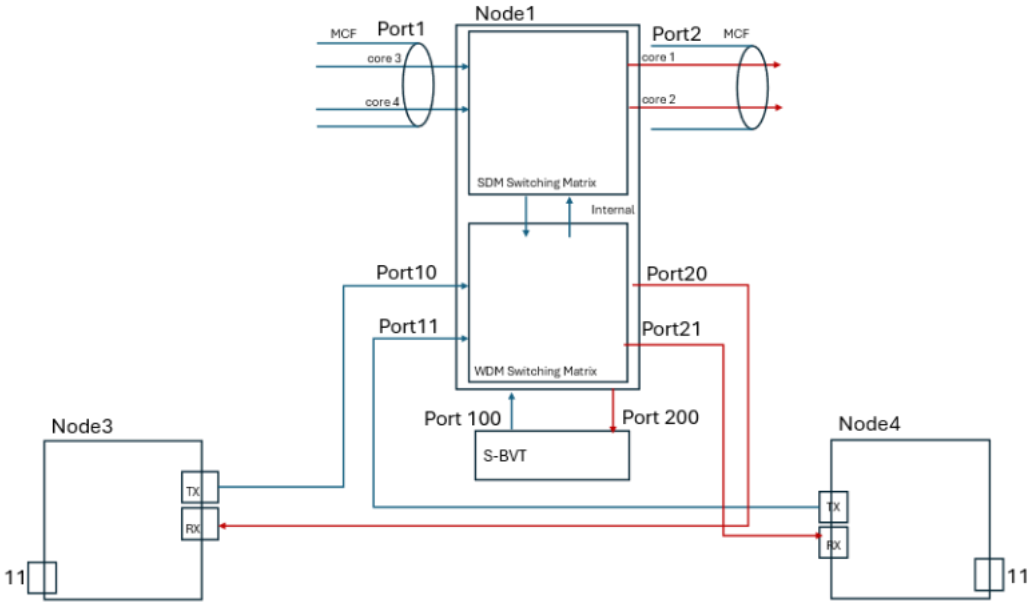

Figure 4.1-2: Abstracted view of the MBoSDM node prototype.

The snippet of Figure 4.1-3 represents the YANG data model for the MBoSDM node, which defines the structure and semantics of the configuration and operational data exchanged between the SDN controller and the node agent.

```
module: season-mbosdm-node
  +--rw node
  |  +--rw address        inet:ip-address
  |  +--rw node_id        yang:uuid
  |  +--ro ports
  |  |  +--ro port* [id]
  |  |     +--ro id           uint32
  |  |     +--ro name?        string
  |  |     +--ro direction?   season-mbosdm-types:port-direction
  |  |     +--ro type?        season-mbosdm-types:port-type
  |  +--rw connections
  |     +--rw connection* [name]
  |        +--rw name           string
  |        +--rw input_port     uint32
  |        +--rw output_port    uint32
  |        +--rw input_core     uint32
  |        +--rw output_core    uint32
  |        +--rw band?          enumeration
  |        +--rw n              int16
  |        +--rw m              uint16
  +--ro info
     +--ro software_version?   string
     +--ro hardware_version?   string
```

Figure 4.1-3: Snippet of the MBoSDM node YANG data model.

Table 4.1-3: Interfaces for control and management of the switching MBoSDM node.

S.No	Interface	Description
1	MBoSDM SDN controller	It builds on the CTTC FlexOpt SDN controller, extended to support multiple switching layers. It is developed in the framework of WP4.
2	MBoSDM node agent	It is developed using the netopeer framework and a SEASON-defined YANG model (Figure 4.1-3), enabling operations at the SDM/core and multi-band flexi-grid levels. The YANG model serves as the interface between the SDN controller and the agent, supporting Create/Read/Update/Delete (CRUD) operations on cross-connections with constraints on ports, cores, and switching layers.
2	Identification of node control operations	A set of node high-level control operations have been identified to enable suitable SDN control integration.
3	Identification of programmable elements	A set of programmable elements and reconfigurable parameters have been identified to properly map the high-level operation to the node configuration.

4.1.3 KPI assessment

The assessment of KPI 3.1 has been assessed, as detailed in section 2.5. This KPI deals with the design and implementation of modular MBoSDM node prototypes s able to switch/add/drop channels in at least 3 different bands (e.g., S, C, L) in an SDM/MCF fiber infrastructure featuring up to 10 fibers/cores, able to cope with switching capacities scalable up to between 2.4-3.6 Pb/s. The presented MBoSDM node prototype (component C3.1) enables suitable spectral (C+S+L band, wavelength) and spatial (core) switching to properly upgrade the capabilities of future optical networks in terms of capacity/bandwidth scaling. Key components are used for the node implementation, including BPFs, WSSes, AWGs and optical cross connects (OXCs). Each degree of these switches can handle up to several hundred Tb/s, and a node with a degree greater than four can easily achieve an overall switching capacity in the Pb/s range. In D3.2 and D3.3, transmission of 44 Gb/s (C-band), 35.8 Gb/s (L-band) and 39.3 Gb/s (S-band) signals have been assessed within a 19-cores MCF of 25.4 km. This MB flow is switched with the 3-degree prototype node C3.1 to assess the KPI. By populating the full S+C+L band spectra over one core of the 19-core MCF the total capacity can be suitably scaled. Specifically, with 350 channels at 25 GHz (S-band), 175 channels at 25 GHz (C-band), and 150 channels at 50 GHz (L-band), a capacity of 27 Tb/s can be achieved. By considering the 19-core MCF, which includes the spatial dimension, this capacity could be scaled up to 0.5 Pb/s. With a higher degree node, the target KPI switching capacities of 2.4-3.6 Pb/s could be envisioned.

4.2 MULTI-GRANULAR OPTICAL NODE PROTOTYPE (C3.2)

4.2.1 Description

In the framework of SEASON WP3, we designed a passive MBoSDM node prototype that is capable of band and space/fiber switching. This prototype is associated with the topic cluster TC1. The prototype is fully controllable though an SDN agent and supports selective band switching as well as add/drop functions for the S-, C-, and L-bands. The prototype is based on a fixed and static optical band-selective filter architecture combined with a fully configurable optical cross-connect (i.e., an optical matrix switch). The node functions as a hierarchical network node, providing a fast route-and-select architecture at the band level. While maintaining backward compatibility with legacy transport schemes and traditional wavelength-selective switching for each band, the prototype preserves the cost efficiency factor.

Beyond the state of the art, the C3.2 prototype extends conventional flex-grid and multigranular ROADM architectures by enabling simultaneous multi-granularity switching across multiple optical bands. While existing solutions typically support wavelength- or fiber-level granularity within a single band, C3.2 allows dynamic adaptation of the switching granularity (fiber, band, wavelength) across S, C, and L bands, addressing core-network scalability requirements that are not supported by current ROADM implementations.

The innovative design incorporates eight multiband multiplexers or splitters/combiners (MB Mux and MB Demux) and a 12×12 optical matrix switch that allows flexible band routing. So, each input fibers of the four input fibers is demultiplexed into S, C and L band via the splitters, and then those bands are fed into the 12×12 optical matrix switch, this process is reversed by the multiplexers on the other side. Additionally, monitoring ports are integrated at each input and output port for measurement devices, such as Optical Spectrum Analyzers (OSA), to ensure effective monitoring throughout the validation and operational phases of the prototype. A schematic of the node is depicted in Figure 4.2-1.

In the assembly process, each four multiplexers and four monitor couplers are integrated in a single box or chassis, so we end up with two chassis and the optical matrix switch, the assembled prototype is present in HHI laboratory (Figure 4.2-2a).

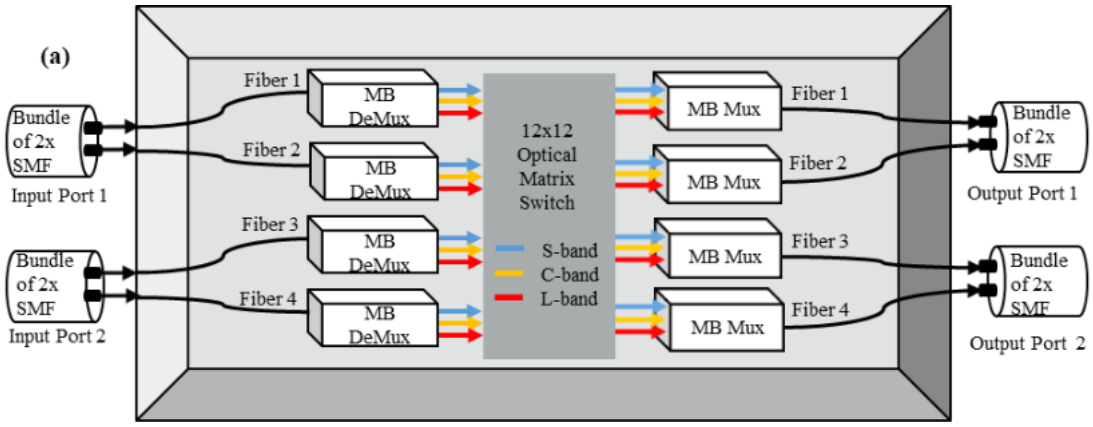

Figure 4.2-1: Multi-granular Optical Node Prototype Architecture.

4.2.2 Interfaces

The switch is fully programmable, allowing for remote operations between the multiple inputs and outputs. The integration with the control plane is taking place in WP5 and is a part of the final demo of the project. A set of high-level control operations for the nodes have been identified to enable suitable SDN control integration, in the identification process we define the input ports, output ports and the selected band/bands to enable the switching process based on the figure above, the work is also being reported in an OFC demo and will be presented in San Francisco. The Table 4.2-1 reported hereafter describes the SDN control and management for the MBoSDM node.

Table 4.2-1: Interfaces for control and management of the switching MBoSDM node.

S.No	Interface	Description
1	SDN Control	SDN agent implementation for node reconfiguration and programmability.

4.2.3 KPI assessment

The prototype was characterized by using a polarization-dependent loss analyzer (PDLA) to verify insertion loss (IL) and PDL of the multiple paths. An example of the characterization curves can be observed in Figure 4.2-2(b), where it is possible to note an average IL below 3 dB and a PDL below 0.1 dB across all bands for all pathing possibilities of the prototype. These values are also presented in Table 4.2-2 below, where the specifications of the device are summarized. The gaps observed in the transitions of the bands occur due to the overlap of the distinct transfer functions of the band-specific filters that compose the MB Mux and MB Demux. Thus, these transitional regions are out of the specification of operation of the device.

Table 4.2-2: Prototype specifications.

Parameter	Specification
Operation Bands	S-band: 1460-1522 nm C-band: 1527-1565 nm L-band: 1574-1640 nm
Insertion Loss	< 3.0 dB
PDL	< 0.1 dB

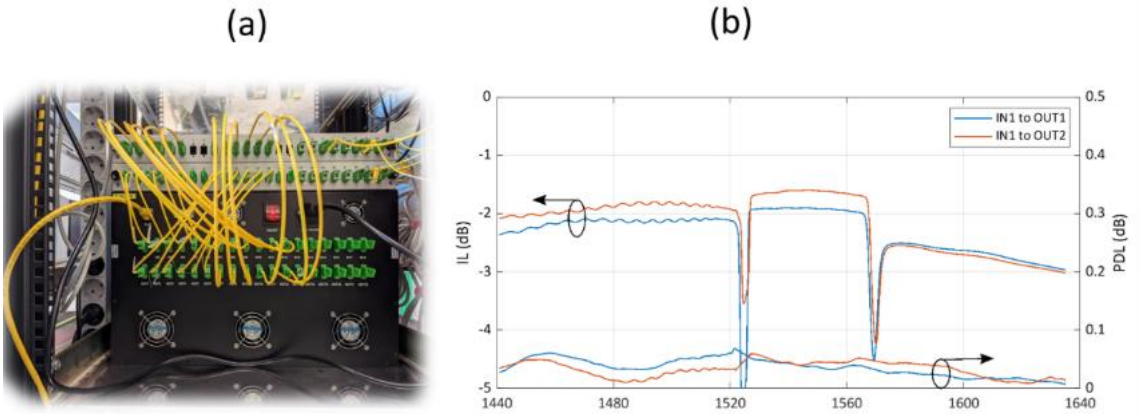

Figure 4.2-2: a) Chassis and the Optical Matrix Switch b) Example of Prototype Characteristics.

We focused on the assessment of KPI 3.1 by designing and implementing flexible and modular MBoSDM node prototypes able to switch and add/drop channels in at least three different optical bands (e.g., S, C, and L). Unlike state-of-the-art optical nodes, which typically support single-band operation and limited SDM capabilities, the proposed prototype jointly enables multiband and space-division switching within the same node architecture. The prototype was integrated with an Amplified Spontaneous Emission (ASE) input and a monitoring system consisting of an Optical Spectrum Analyzer (OSA) and an optical switch after the prototype, allowing the routing of node inputs and outputs to the OSA in order to experimentally demonstrate both fiber (SDM) and band (MB) switching capabilities. The experimental setup is shown in Figure 4.2-2.

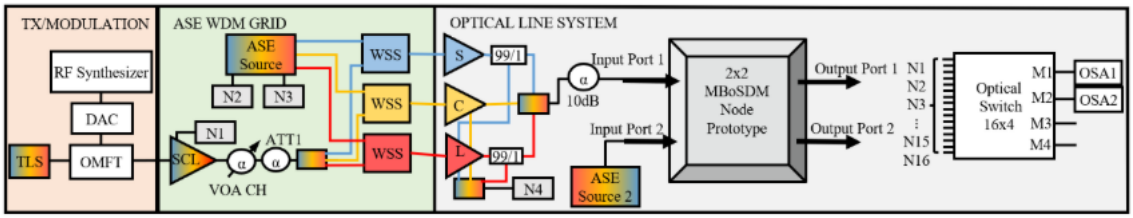

Figure 4.2-2: Node prototype test setup.

4.3 SPATIAL PON NODE (C3.3)

4.3.1 Description

In the framework of the SEASON project, a prototype of a Multicore Passive Optical Network (PON) node has been developed, showcasing an innovative and flexible architecture designed to optimize the use of multicore fiber (MCF) technology in access networks. This prototype enables efficient management of spatial lanes within the MCF, supporting dynamic traffic adaptation and energy efficiency while maintaining high network performance. This prototype is associated with the topic cluster TC5.

The Multicore PON node prototype supports multiple spatial lanes that can be dynamically aggregated or bypassed using a spatial switch, as depicted in the architecture diagram (Figure 4.3-1 (a,b,c)). The prototype architecture follows a 2 lanes configuration, where two spatial lanes can be aggregated/disaggregated over two OLT ports. The spatial switch in the architecture plays a crucial role, either bypassing the spatial lanes directly to their corresponding OLT ports (2x2 configuration, Figure 4.3-1 (b)) or directing them to a splitter/combiner for aggregation (2x1 configuration, Figure 4.3-1 (c)). The splitter/combiners are essential for realizing spatial aggregation, allowing multiple spatial lanes to be combined and efficiently transmitted over the available OLT ports.

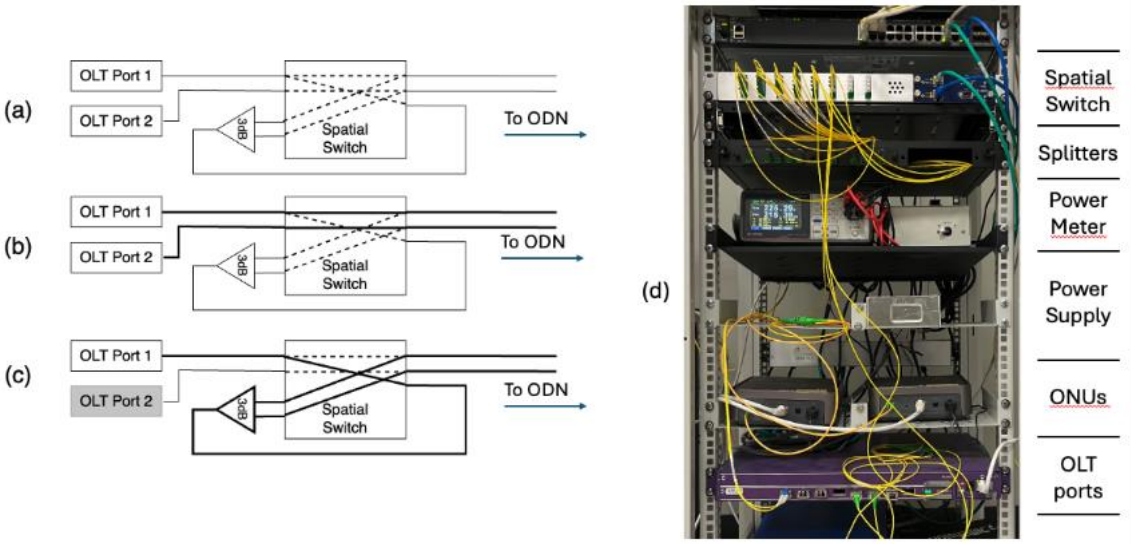

Figure 4.3-1: (a) 2 lanes spatial PON architecture; (b) 2x2 configuration; (c) 2x1 configuration; (d) Spatial PON Prototype.

In practice, the prototype is implemented with a compact and modular design, as shown in the photo of the physical setup (Figure 4.3-1 (d)). The prototype shown in the photo includes an end-to-end spatial PON system comprising several functional layers: an ONU layer, a splitting layer for realizing the ODNs and spatial aggregation, a switching layer to control spatial aggregation, and an OLT ports layer for the activation and deactivation of transceivers.

Additionally, the photo shows an energy consumption measurement device that will be used in the ongoing project for the assessment of energy savings. The prototype's modularity allows for flexible deployment in various network scenarios, accommodating different traffic demands and network configurations.

4.3.2 Interfaces

Table 4.3-1 below outlines the key interfaces supported by the Multicore PON node prototype, each playing a crucial role in the management and operation of the system. These interfaces facilitate communication between the prototype and higher-level network management systems, allowing for efficient service setup and dynamic control of network elements. The REST interface provides a north-bound communication channel for the transport orchestrator, enabling the configuration of services with specific requirements such as VLAN characterization, bandwidth allocation, and prioritization of traffic. The NETCONF PON interface allows direct interaction with the OLT ports, managing the activation and deactivation of transceivers. Additionally, the NETCONF SWITCH interface is used to control the spatial switch, handling the physical aggregation and disaggregation of spatial lanes. Each of these interfaces is integral to the prototype's functionality, ensuring flexibility and control in a complex network environment.

Table 4.3-1: Interfaces for control and management of the Spatial PON node.

S.No	Interface	Description
1	REST	This high level north-bound interface allows transport orchestrator to setup a service with specific requirements in terms of vlan characterization, bandwidth assignment, time prioritization.
2	NETCONF PON	The prototype supports NETCONF to interact with OLT ports and control port activation/deactivation.
3	NETCONF SWITCH	The prototype supports NETCONF to interact with the spatial switch and control physical aggregation/disaggregation of spatial lanes.

4.3.3 Status

The status of the spatial PON node prototype is described in Table 4.3-2.

Table 4.3-2: Status of Spatial PON node prototype.

S.No	Status	
1	Status	Realized prototype and implemented dynamic logical association of users to different OLT ports to be operated in conjunction with physical aggregation/disaggregation.

4.3.4 KPI assessment

The Multicore PON node prototype's capabilities have been evaluated by assessing its performance in different configuration settings using a controller and the management interface of the Polatis switch. These evaluations are crucial to demonstrate the dynamic adaptability of the system in managing spatial lanes and OLT ports.

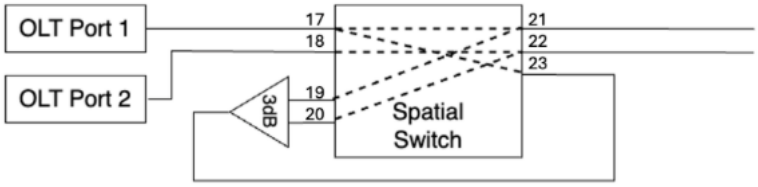

Figure 4.3-2: Two lanes setup adopted for testing.

Figure 4.3-2 shows the adopted setup for testing purpose. In the figure, port identifiers of the spatial switch are reported. Figure 4.3-3 presents the configuration of the node in a 2x2 setting. On the left side of the figure, the controller interface is shown, which is responsible for setting and managing the configuration. It displays the commands and status outputs as the 2x2 configuration is implemented. On the right side, the management interface of the Polatis switch provides a visual representation of the cross-connects, confirming that the spatial lanes are correctly routed and aggregated according to the 2x2 configuration settings. This demonstrates the successful application of the controller's commands and the switch's ability to manage the spatial lanes effectively.



Figure 4.3-3: 2×1 configuration demonstration.

Figure 4.3-4 illustrates the node configuration in a 2×1 setting. Like the first figure, the left side shows the controller interface managing the configuration process, while the right side displays the Polatis switch's management interface. In this scenario, the 2×1 configuration involves aggregating two spatial lanes into a single output, demonstrating the system's flexibility in adapting to different network demands. The visual feedback from the switch's interface confirms that the configuration is applied correctly, with the spatial lanes being managed and routed as intended.

These assessments highlight the innovative prototype's capability to dynamically adjust to different configurations, ensuring optimal network performance. The real-time monitoring and control provided by the integrated interfaces are critical for maintaining the efficiency and reliability of the system, showcasing its potential for deployment in advanced optical networks.



Figure 4.3-4: 2x2 configuration demonstration.

4.4 MB(oSDM) S-BVT PROTOTYPE (C3.4)

4.4.1 Description

A MB(oSDM) S-BVT prototype has been proposed and developed in the framework of SEASON project. This versatile and innovative solution enables us to enhance network efficiency, resilience, and sustainability [Nad23]. This transceiver prototype supports MB operation within the S, C, and L bands, offering capacity scalability. It features a flexible and adaptable structure composed of various bandwidth/bit rate variable transceivers (BVTs), which can be based on different technologies, operate beyond the C-band, and be activated or deactivated according to traffic demands and network requirements. This prototype is associated with the topic cluster TC1.

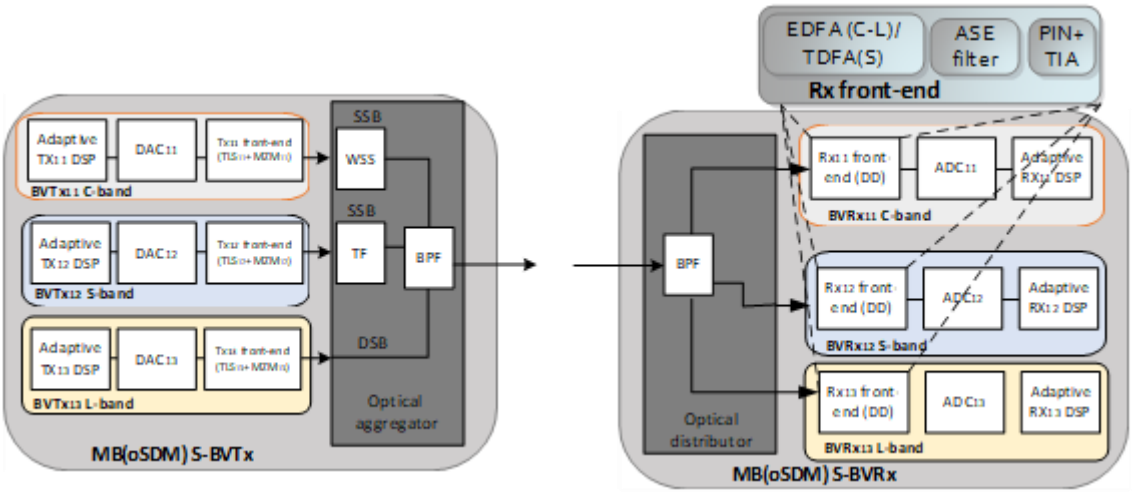

Figure 4.4-1: MB(oSDM) S-BVT prototype architecture.

Dissemination Level	Public

The proposed transceiver architecture is shown in Figure 4.4-1. A high-capacity flow is generated and distributed over the network using an optical aggregator/distributor with band-pass filters (BPFs). Additionally, programmable filters such as wavelength selective switches (WSSes) or tunable filters (TFs) can be included to perform SSB modulation, enhancing resilience against chromatic dispersion. Thanks to its modular architecture, both point-to-point (P2P) and point-to-multi-point (P2MP) connectivity are supported, reducing cost and complexity while enhancing efficiency. The sliceable architecture allows for the dynamic allocation of available MB bandwidth into smaller, manageable portions that can also be transmitted through different fiber spatial channels.

The developed prototype (see Figure 4.4-2) leverages advanced modulation formats, such as orthogonal frequency division multiplexing (OFDM), and is based on intensity modulation (IM) and direct detection (DD). Adaptive loading is implemented to further enhance overall flexibility and performance [Nad23-2]. Digital-to-analog conversion is performed using a digital-to-analog converter (DAC) operating at 64 GSa/s. Details on the implemented adaptive digital signal processing (DSP) can be found in [Nad23]. At the transmitter side, external modulation with Mach-Zehnder modulators (MZMs) and tunable laser sources (TLS) per band are adopted. An external cavity laser (ECL) is used for the S-band contribution. At the receiver side, suitable amplification options are targeted for each band based on doped fiber amplifier (xDFA) technology. Specifically, erbium DFA (EDFA) is used for the C and L bands, while thulium DFA (TDFA) is considered for the S-band. The receiver front-end also includes a filtering stage for amplified spontaneous emission (ASE) noise removal and simple PIN photodiodes. An oscilloscope operating at 100 GSa/s is used for analog-to-digital (ADC) conversion.

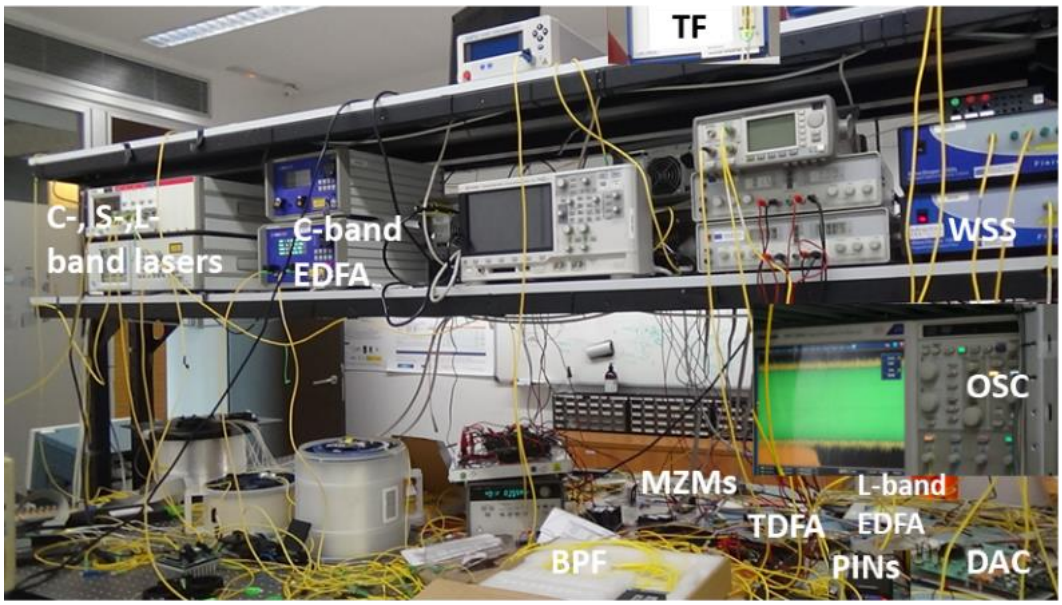

Figure 4.4-2: MB(oSDM) S-BVT prototype at CTTC premises.

The transceiver prototype has been successfully implemented and experimentally validated within an MBoSDM scenario (see Section 5.1 for updated transmission results). The transceiver

prototype has been successfully integrated with the **MB(oSDM) S-BVT agent** (developed in the framework of WP4). D5.2 reports last validation result of integration of the transceiver prototype (WP3) with the SDN control plane (WP4), and corresponding SDN agents.

4.4.2 Interfaces

The programmability and interoperability of the proposed MB(oSDM) transceiver can be facilitated by the effective implementation of open SDN agents [Nad23]. These agents reconfigure various system parameters and optical elements according to the network requirements. The SDN paradigm provides the flexibility needed to automatically satisfy the stringent and varying demands of the network. This is achieved by dynamically adjusting the transceiver components and their parameters appropriately. Specifically, the OpenConfig open data model can be implemented to suitably reconfigure the transceiver. Various programmable transceiver parameters and elements have been identified for the effective configuration and modification of the proposed MB(oSDM) S-BVT. Primarily on the transmitter side, it is possible to adjust the central frequency and power of the TLS, as well as the DAC channels. On the receiver side, the OSC can be reconfigured. Additionally, an activity related to energy-aware routing computation has started including specific and relevant power consumption attributes of the underlying transport devices (S-BVT) to extend the current TAPI Context information (see Section 4.4) [Nad24]. A summary of the interfaces and their descriptions is provided in Table 4.4-1.

Table 4.4-1: Interfaces for control and management of the MB(oSDM) S-BVT prototype.

S.No	Interface	Description
1	MB(oSDM) SDN agent	Implementation of SDN agents, based on OpenConfig, to suitable program the MB(oSDM) S-BVT. A dedicated S-BVT SDN agent has been developed, leveraging the netopeer framework to implement the NETCONF protocol and support OpenConfig Terminal Device and Platform Optical YANG models.
2	Energy-aware routing computation	Extend current TAPI Context information to include specific and relevant power consumption attributes of the MB(oSDM) S-BVT.

In the Figure 4.4-3, we report the successful reconfiguration of the three different slices of the MB(oSDM) S-BVT prototype.

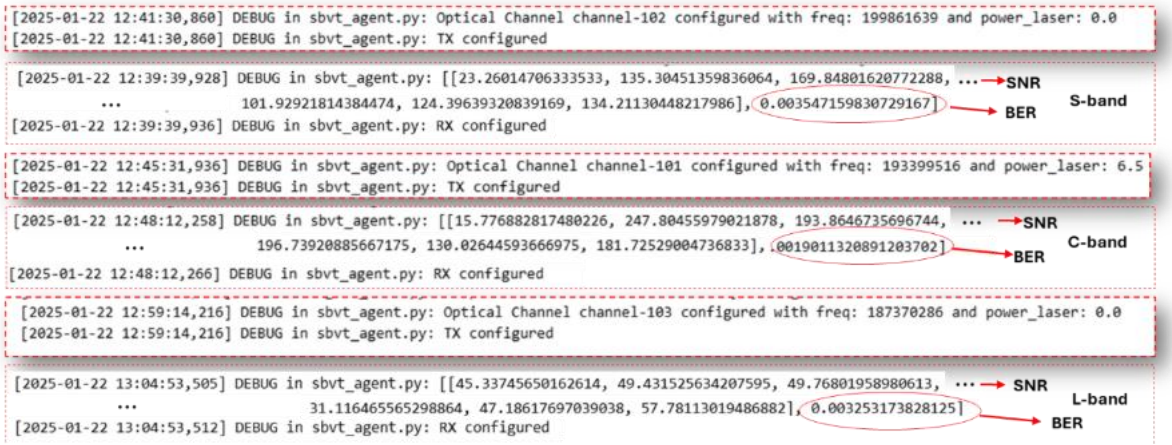

Figure 4.4-3: MB(oSDM) S-BVT reconfiguration by means of SDN agents.

4.4.3 KPI assessment

The MB(oSDM) transceiver has been experimentally assessed to validate SEASON KPI 3.2 related to the implementation of MBoSDM transceivers able to increase the capacity of SoA transceivers [Nad22] up to 2× - 4× by exploiting enhanced wavelength/space dimensions while enabling appropriate slice/band/core/fiber selection according to the network path. Specifically, MBoSDM transmission after 19-cores MCF of 25.4 km has been assessed. By leveraging SDM, the spatial dimension can also be utilized, providing new resources to further increase overall network capacity. Using a single core of the 19-core MCF and fully populating the S, C, and L bands, an aggregated capacity of 28.2 Tb/s could be envisioned after 25.4km of MCF by only considering MB transmission over 1 core. This translates to a capacity scaling factor of 4 compared to the SoA C-band transceivers, which can be further improved by including the spatial dimension. However, transmission impairments such as Raman scattering (SRS) and XT can limit the overall achieved capacity. Hence, the corresponding KPI 3.2, targeting a 2× - 4× capacity scaling factor is achieved.

4.5 DSP RX-BASED MONITORING (C3.5)

4.5.1 Description

State-of-the-art optical performance monitoring solutions typically rely on dedicated external hardware modules or optical taps, which become impractical in multiband and SDM systems due to cost, complexity, and scalability limitations.

In previous projects (i.e., B5G-OPEN), the relevance of the technique based on correlation method was realized by utilizing the proposed link tomography for two different use-cases: longitudinal power profile monitoring and anomaly detection [Sen22, Sen25]. In SEASON, the goal is to implement the Linear Least Squares (LLS) approach version of the scheme to have better accuracy in anomalies detection and localization. Figure 4.5-1 b) illustrates the Rx-DSP

processing chain employed in this work. After analog-to-digital conversion (ADC) and resampling, the signal undergoes matched filtering followed by chromatic dispersion (CD) compensation. Next, polarization demultiplexing (Pol. demux in Figure 4.5-1 b)) is applied to correct the random polarization rotations introduced during transmission. This is followed by carrier frequency recovery to compensate for any frequency offset between the transmitter laser and the local oscillator. Subsequently, blind carrier phase recovery is carried out using a blind phase search algorithm to mitigate phase noise originating from the linewidths of both the laser and the local oscillator.

Once pre-processed, the signal is duplicated into two tributaries, labeled as I and II in Figure 4.5-1 b), in preparation for the proposed Longitudinal Power Monitoring LPM scheme. The LPM extraction method used in this study follows a distinct but conceptually similar approach to that proposed by T. Sasai et al. in [Tak22]. However, it is important to note that detecting physical layer attacks is not an exclusive capability of our implementation. Rather, this functionality can be achieved using any Rx-DSP algorithm capable of visualizing optical power variations as a function of distance, such as LLS or CM.

This prototype of DSP RX-based monitoring system is associated with the topic cluster TC3.

Beyond the state of the art, the C3.5 prototype demonstrates how receiver-side DSP can be reused to perform optical performance monitoring without requiring additional optical hardware, even in multiband and space-division multiplexed transmission scenarios. This approach enables scalable, cost-effective monitoring and provides real-time performance indicators directly at the receiver, supporting fast and autonomous network control loops that are not achievable with conventional external monitoring solutions.

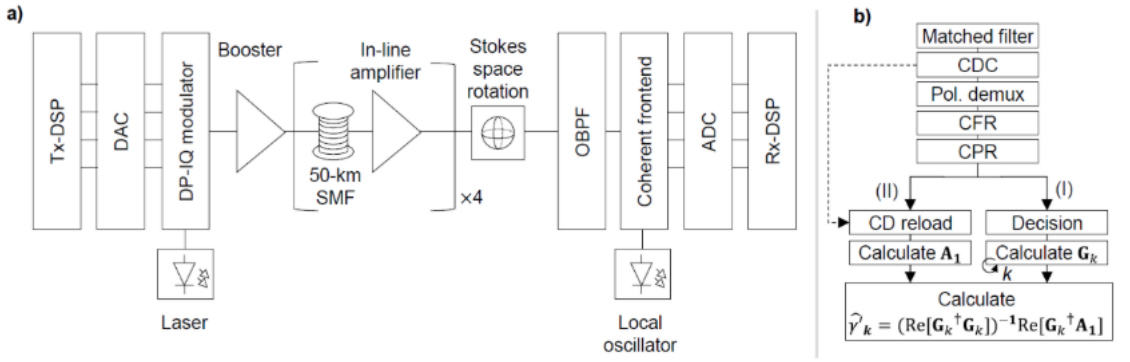

Figure 4.5-1 a) Schematic of the transmission model used in the numerical simulations of this paper. b) Rx-DSP structure based on the proposed algorithm.

4.5.2 Interfaces

The interfaces of this component are reported and described in Table 4.5-1.

Table 4.5-1: Interfaces for control and management of the DSP RX-based monitoring system prototype.

S.No	Interface	Description

1	Correlation Method	Old interface was based on the correlation method with lower resolution
2	LLS	New interface based on LLS technique pursuing a higher resolution accuracy.

4.5.3 KPI assessment

We considered in our simulation in the work, which was accepted in JOCN, KPI 5.1 validation where we seek a sub dB and sub km fault localization. The schematic of the simulation is shown in Figure 4.5-1(a) and with the help of the LPM engine that we used we achieved the results shown in Figure 4.5-2. In Figure 4.5-2(b) we can see that we could detect up to a sub dB [0.46 dB] resolution verifying part of the KPI for now. These capabilities directly support SEASON KPIs related to network automation, scalability, and energy efficiency by reducing monitoring overhead while enabling self-managed operation

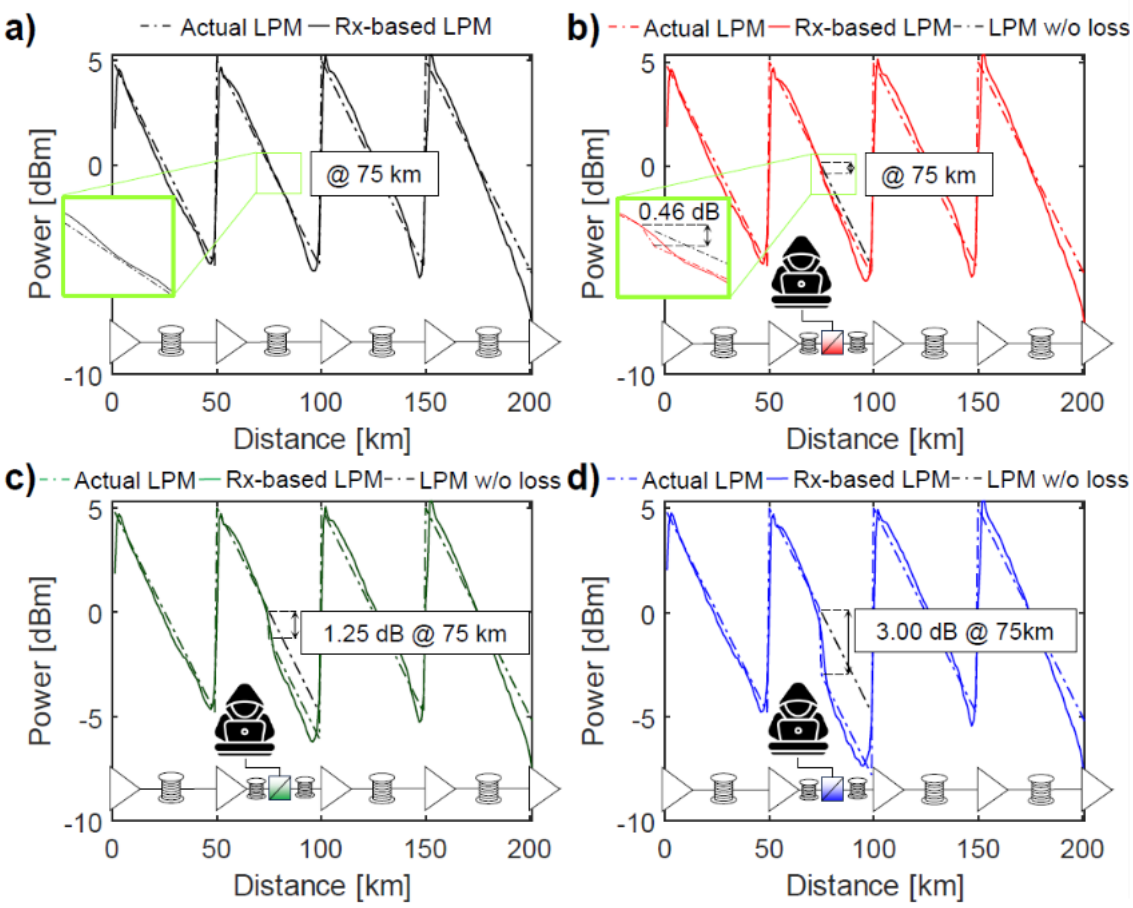

Figure 4.5-2 (a) Actual LPM vs estimated LPM. Actual LPM vs estimated LPM with emulated power drop at 75 km with a value of (b) 0.46 dB, (c) 1.25 dB, and (d) 3 dB.

4.6 MULTIBAND AMPLIFIER (C3.6) - ENSURING AVAILABILITY BY PREDICTIVE MAINTENANCE APPLIED TO OPTICAL AMPLIFIERS

4.6.1 Description

In today's digitalized society, communication is essential for various forms of communication, including messaging and social media. Telecommunication networks, such as access networks and datacenter interconnections, use long-haul optical transmission links with optical fiber amplifiers for repeatedly restoring signal power. Performance of these amplifiers is subject to ageing effects. Over time, pump lasers may degrade, requiring replacement. Various techniques have been developed to monitor pump lasers, focusing on high pump power and injection current values [Rap23]. However, these methods have weaknesses, as they only detect degradations at high pump powers. Predictive maintenance (PdM) is an essential component in Industry 4.0, combining anomaly detection, prognosis, and diagnosis into one framework. Applying PdM to optical fiber amplifiers can enhance current monitoring and reduce network downtime risk. Ever higher data transmission rates are becoming necessary, particularly because of constant technological development. One approach is to widen the bandwidth, which entails the use of multiband amplifiers. PdM for optical multiband amplifiers is therefore of great importance as the number of amplifiers in the optical network increases and consequently also the failure rate.

This prototype of DSP RX-based monitoring system is associated with the topic cluster TC3.

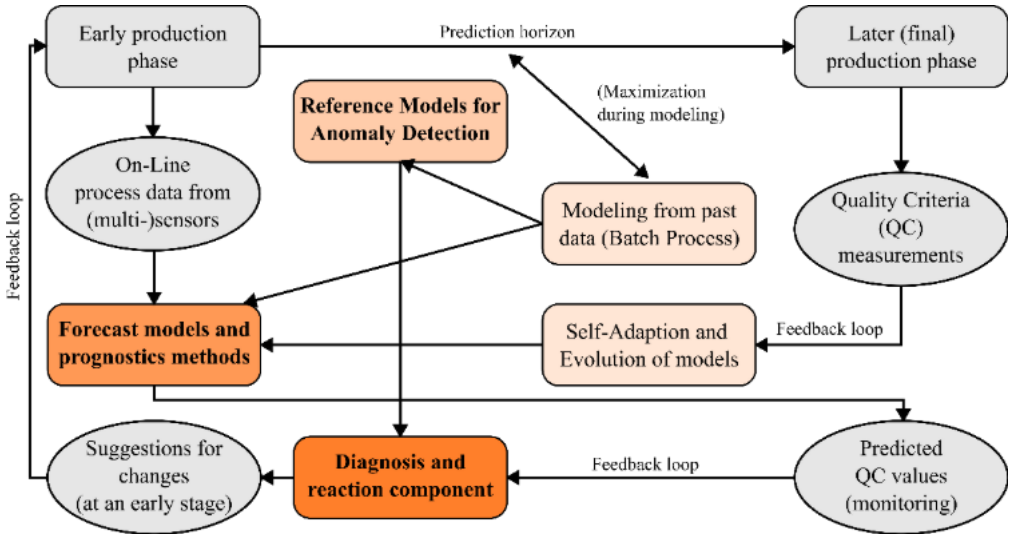

Figure 4.6-1: Generalized PdM framework [Lug19].

The PdM framework, proposed by [Lug19] and shown in Figure 4.6-1, consists of system models used for anomaly detection, prediction, forecasting, or diagnosis. These models describe system behavior under normal conditions and are adapted to the existing use case of multiband amplification. Advanced signal processing techniques are required to build robust models, which detect anomalous behavior and trigger prognosis and diagnosis components.

A PdM based prototype for improved supervision of optical fiber amplifiers has been developed, which can access high-quality historical data and monitor load and usage of components in combination with condition monitoring at the system level, and therefore enable (1) Anomaly Detection, (2) Prognosis and Forecasting and (3) Diagnosis and Fault Identification. This prototype accesses the system parameters of the multiband amplifier at defined inspection intervals and triggers the proposed PdM pipeline with subcomponents (1), (2) and (3).

4.6.2 Interfaces

The interface and its description is reported in Table 4.6-1.

Table 4.6-1: Interfaces for control and management of prototype for predictive maintenance in multiband amplifiers.

S.No	Interface	Description
1	REST	REST interface is used to acces the current state of the parameter of the amplifiers card. All subcomponents of the PdM system are merged into one large deep learning model, to minimize the model management efforts. The current version of the PdM prototype was trained on EDFA data.

4.6.3 KPI assessment

Investigations of the three subcomponents of the PdM system are presented below. Anomaly detection uses a fuzzy clustering-based method for identification of atypical behavior in time series of EDFA systems, combining fuzzy clustering procedures with entropy analysis (EA) and principal component analysis (PCA). EA is used for dynamic feature selection, reducing feature space and increasing computational performance. PCA extracts features from the raw feature space for generalization capability. Three different fuzzy clustering methods are evaluated in view of performance and generalization. The change detection framework (CDF) can detect changes in pump current time series at an early stage for arbitrary points of operation, compared to state-of-the-art predefined alarms in commercially used EDFAs. Experimental measurements of drifting pump currents show significant generalization under arbitrary operational conditions, detecting anomalies in time series with up to 4.9% drift from typical operating conditions. The algorithm can robustly detect anomalies in degenerative features and noisy data streams resembling normal operating conditions, as shown Figure 4.6-2 [Sch24]. The CDF triggers downstream models for Prognosis and Forecasting as well as Diagnosis and Fault identification.

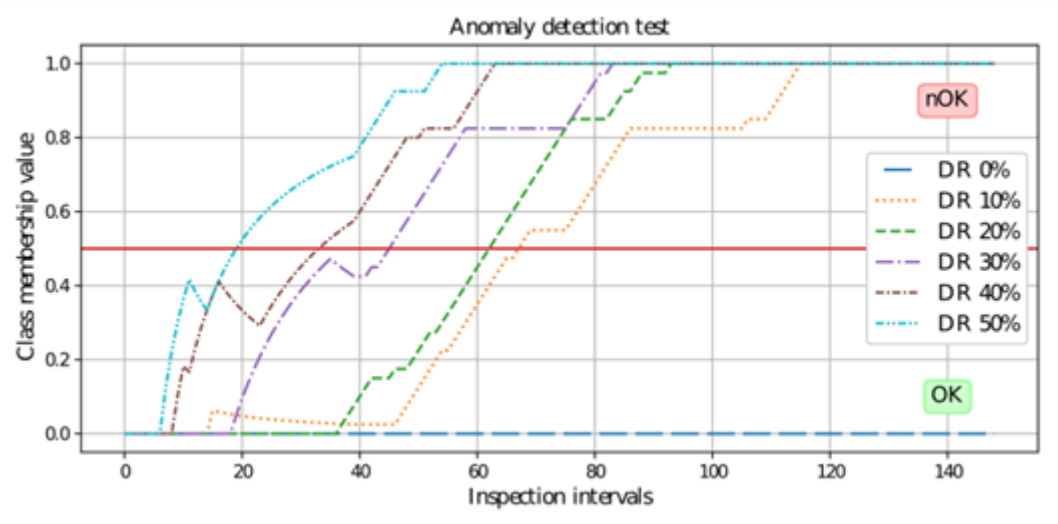

Figure 4.6-2: Anomaly identification test on different datastreams [Sch24].

Remaining is an essential parameter in predictive maintenance techniques, ensuring reliability and safety. However, modern systems operate under complex conditions, making forecasting difficult. This PdM approach uses a novel RUL prediction method called sparse low-ranked self-attention transformer (SLAT) [Sch26]. SLAT uses encoder-decoder architecture, extracting features for sensors and time steps using a self-attention mechanism. The model reduces overfitting and increases generalization. Experimental application to optical fiber amplifiers shows that SLAT outperforms state-of-the-art methods. The run to failure (RTF) plot, shown in Figure 4.6-3, demonstrates the RUL prediction capability of SLAT for different failure types and degradation scenarios.

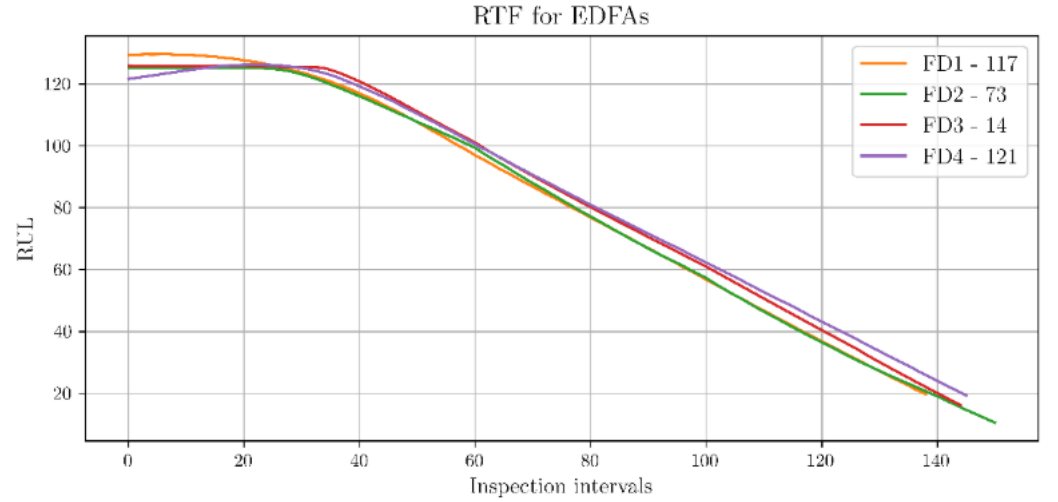

Figure 4.6-3: RTF for different faults and units of EDFAs [Sch26].

The diagnosis component of the PdM prototype focuses on identifying fault cases (FC) when system degradation has occurred, allowing for corrective measures to be initiated. Diagnosing FC is a classification task in the context of PdM, using system data at runtime. Data-driven

models have evolved from statistical models to ML algorithms, with the most efficient using the attention mechanism. Recent transformer-based models use convolutional layers for feature extraction, embedding with parallelization of three different-granulated feature maps. A novel transformer-based architecture, inverse triple-aspect self-attention transformer (ITST), is presented for diagnosing FC in optical fiber amplifiers [Sch25]. ITST uses a triple aspect self-attention mechanism in three domains, extracting time, sensor, and frequency dependencies for improved generalization and performance. Figure 4.6-4 indicates that ITST has a reliable classification capability for the FC with a worst misclassification rate of 15%, therefore the method is valid for diagnosing FC in complex systems like optical fiber amplifiers.

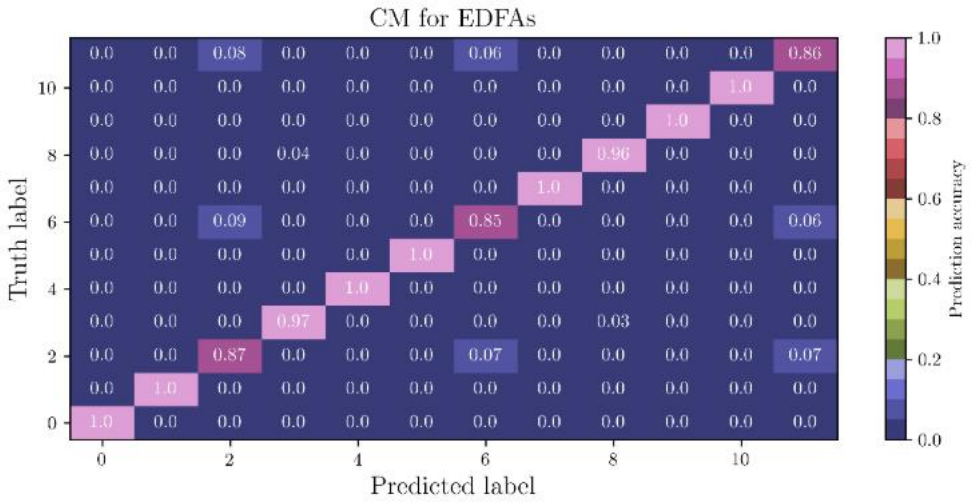

Figure 4.6-4: Confusion Matrix (CM) for FC in EDFAs [Sch25].

This evaluation of the PdM prototype on the use case of an EDFA in the C-Band showed potential for early detection of degradation processes, prediction of RUL, and diagnosis of FC in optical fiber amplifiers, increasing the availability and reliability of optical communication networks. This work laid the foundations for the generation of a PdM for multiband amplifiers. Further investigations must be carried out with regard to adaptation of the deep learning models onto amplifier working in the MB and, if necessary, extension or fine-tuning of the individual models.

4.7 MONITORING SYSTEM AND TELEMETRY (C3.7)

4.7.1 Description

Fiber-optical networks are crucial for digital transformation, but guaranteeing their permanent availability requires continuous monitoring and fault localization [Eur23]. Most fibers are buried in the ground and susceptible to damage from human activities. Traffic interruptions are often caused by excavation and rodents [Fuj01]. Power levels monitored continuously for amplifier control can be used for detecting a faulty span, thus avoiding the installation of new hardware. The exact position of the cut within a span is determined using a mobile optical time domain

reflectometer (OTDR) [Kum12]. This method saves equipment costs but delays restoration of data transmission. nsive.

Therefore, a fault localization technique that significantly reduces repair time at almost no additionalHowever, equipping networks with permanent OTDRs keeps repair time small but is expe equipment cost has been conceived and verified. Using the concept, the side of the fiber span closer to the cut is determined for reducing travel time and repair time. Thanks to low cost and in most cases anyhow available hardware, this technology can be deployed across an optical network on short notice.

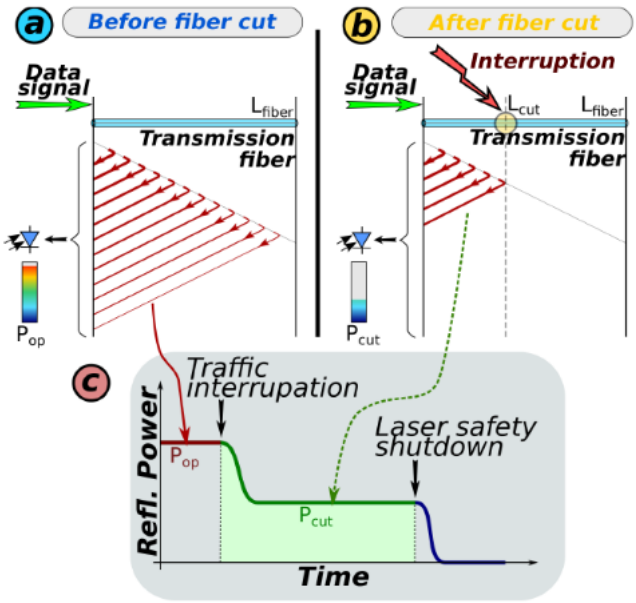

Figure 4.7-1: Reflected power a without traffic interruption and b with traffic interruption. c Evolution of reflected power over time during a fiber break.

The demonstrator set up in the laboratory uses data signals propagating in the fiber without requiring additional auxiliary lightwaves. Power components propagating back to the transmitter due to distributed reflections caused by Rayleigh backscattering are detected by a power monitor along the fiber axis. The total power measured at the fiber input represents the total power of all power components reflected from different locations over the total length of the transmission fiber, as shown in Figure 4.7-1. When the fiber is cut, the measured power drops to a smaller level, and the position of the cut can be determined from the measured reflected power and the attenuation coefficient known from system installation.

This monitoring system is a prototype associated with the topic cluster TC3.

The main goal of the invention is to provide an estimate of the location of a fiber cut at low cost. This becomes possible since the required hardware is present in almost all commercial amplifiers offering gain or output power control. In some cases, a small modification might be required, namely implementing the output monitoring capability by a 2x2-splitter in contrast to the frequently used 1x2-splitter. Since the conceived technique is to be implemented into an optical amplifier card and only requires a backward monitor comprising a splitter and a photodiode

connected to a signal processing system, the demonstrator setup comprising only components required for verifying the technique is quite simple, as illustrated in Figure 4.7-2.

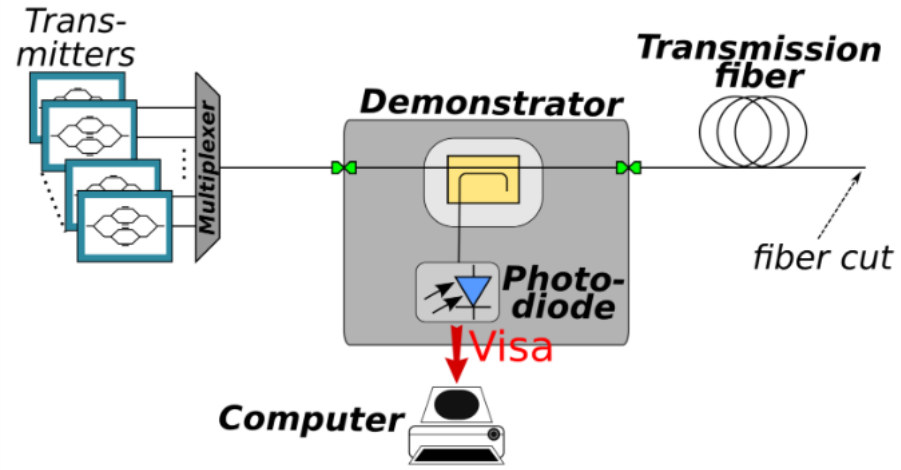

Figure 4.7-2: Demonstrator setup for demonstrating fault localization in fiber optical networks at low complexity by using optical components that are already implemented in most commercial amplifiers.

4.7.2 Interfaces

The interfaces and its description of this component is reported in Table 4.7-1.

Table 4.7-1: Interfaces for control and management of prototype for monitoring system and telemetry.

S.No	Interface	Description
1	VISA	The photodiode for power measurement is implemented in a measurement device, whereas this device is controlled remotely using a VISA interface.

4.7.3 KPI assessment

The demonstrator has been verified by launching data signals into fibers of the same type but different lengths, with attenuation coefficients of 0.19 dB/km and 0.20 dB/km. The power reflected back to the fiber input is measured and normalized to the power determined for the fiber with maximum length.

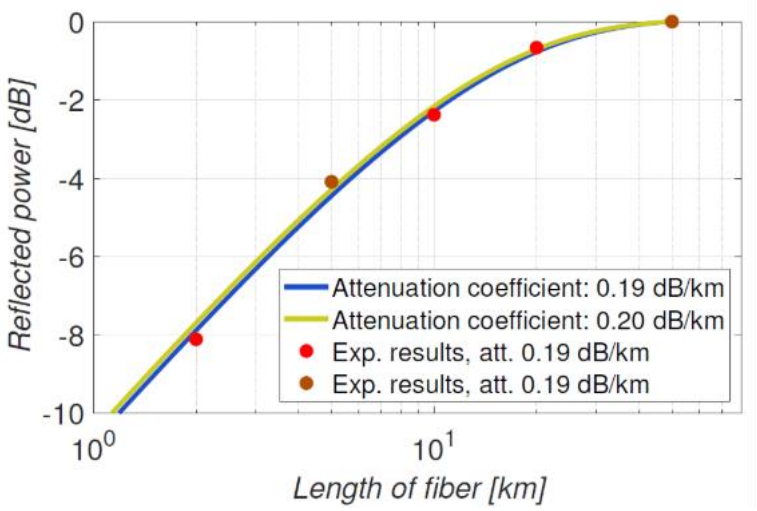

Figure 4.7-3: Experimental results showing reflected power versus fiber length.

The results in Figure 4.7-3 show an expected decrease in reflected power with decreasing fiber length. For an initial length of 60.9 km, the output of a photodetector monitoring power reflected back to the input of the fiber span is shown in Figure 4.7-4 versus time for a fiber cut. After the fiber cut, the length of the fiber segment connected to the transmit equipment is only 10.3 km, resulting in a power ratio of 61.6%.

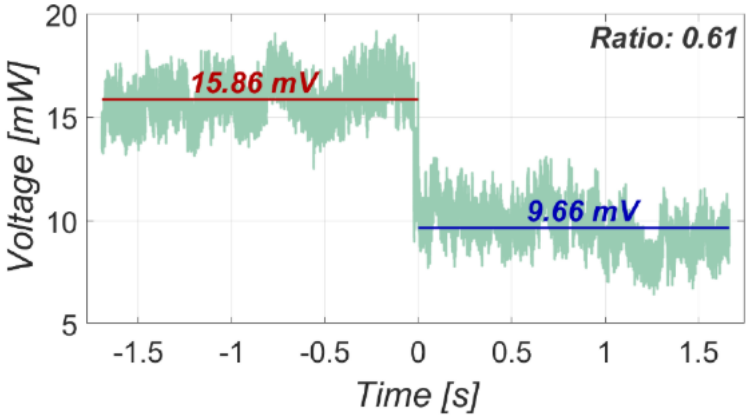

Figure 4.7-4: Output of the photodetector used for monitoring the reflected power with a power cut happening at zero on the time axis.

The demonstrator for fast fault localization in fiber optical networks is described, offering cost-effective and permanent monitoring, and ensuring high network availability by reducing repair time.

The proposed technology represents a significant advancement in enhancing the reliability and availability of optical networks. Achieving higher reliability requires comprehensive network monitoring; therefore, the cost-effective provision of appropriate monitoring devices is of critical importance. In contrast to conventional solutions, the developed approach is available at virtually no additional cost, enabling rapid and widespread deployment across the entire network.

4.8 RESEARCH ACTIVITIES ON PLUGGABLE AMPLIFIERS (RELATED C3.8)

4.8.1 Description

EDFAs integrated into pluggable modules are low-cost amplifiers used mainly for optical connections at fixed distance between datacenters. Its lack of variable gain makes it more suitable for applications with a fixed gain, where transmission conditions are established and predictable. Despite this limitation, the EDFA amplifier is advantageous in network access as it can be implemented to increase signal range without significant investment. With our architecture (Figure 4.8-1), we were able to establish an optical ring that comprises four nodes, using six channels via WDM. This ring allows the transmission of multiple signals through the same optical fiber, thus optimizing the use of existing infrastructure and increasing the overall capacity of the system.

Pluggable low-cost amplifiers are associated with the topic cluster TC4.

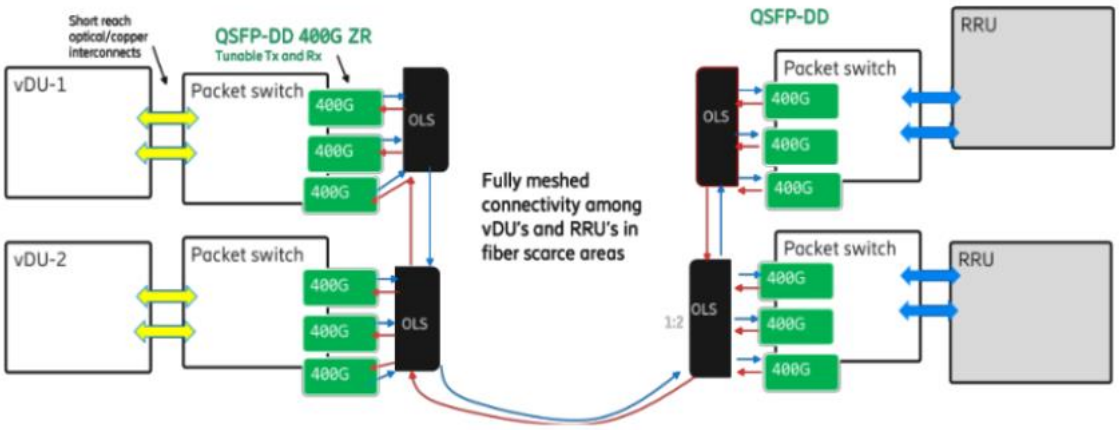

Figure 4.8-1: WDM horseshow mesh.

The network topology designed for the Fronthaul network segment presents a sophisticated infrastructure where vDUs and RRUs are seamlessly integrated with packet switches and OLS, utilizing 400G QSFP-DD transceivers to facilitate high-speed data transmission. The schematic diagram illustrates the network's core, where vDUs are connected to adjacent packet switches via short-reach optical or copper interconnects, signifying their proximity within the network. Each of these packet switches boasts 400G links to the OLS, which serves as the network's backbone, providing high-bandwidth data paths.

To optimize the network's performance in fiber-scarce regions, the OLS units are interconnected to create a fully meshed topology, extending over long distances as indicated by the 20-30km duplex fiber links that ensure bidirectional communication over a substantial reach. The network's periphery features RRUs connected to packet switches, which are in turn linked to the OLS, maintaining the consistency of the high-speed 400G connections throughout the network's

architecture. These connections form a physical ring, as shown by the red and blue lines in the diagram, which also corresponds to a logical mesh network, offering redundancy and robustness for network reliability.

A key component of the network's design is the use of QSFP-DD 400G tunable transceivers, capable of adjusting both transmission and reception parameters for long-range, high-throughput applications. This approach indicates a deliberate effort to ensure high bandwidth and adaptability for advanced telecommunications systems, such as those required by 5G networks. The entire network infrastructure is engineered for efficiency and scalability, particularly in environments with limited fiber resources, thereby maximizing network efficiency through a full mesh connectivity approach in sparsely populated areas.

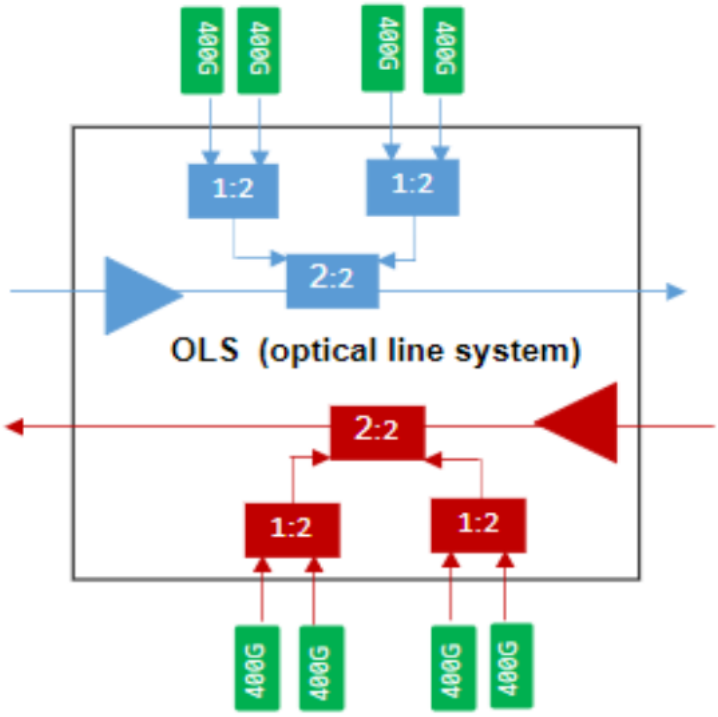

Figure 4.8-2: Filterless OADM node.

Dissemination Level	Public

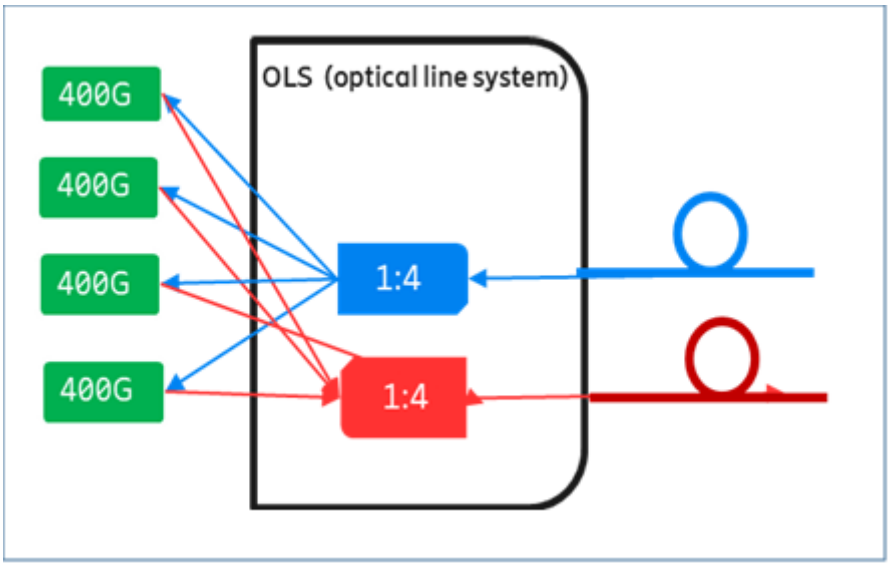

Figure 4.8-3: Filterless Terminal node.

The images depicted above (Figure 4.8-2 and Figure 4.8-3) are a zoomed-in view of an OLS, providing a detailed look at the internal configuration of the system, which includes splitters and couplers essential to support a ring topology. This close-up shows the strategic design choices made to facilitate efficient signal propagation through the network. The OLS depicted in the diagram is an integral part of the network infrastructure, with direct and non-selective splitting mechanisms indicating its reliance on simple but robust signal distribution methods. The presence of pluggable EDFAs within the system illustrates the inherent flexibility of the design, allowing for the dynamic addition or removal of channels as network demands evolve. Wavelength management is handled through precise tuning of the lasers within the 400G transceivers, ensuring the network can scale and adapt to a variety of requirements.

The system architecture, highlighted by “1:2” and “2:2” port configurations, emphasizes the system's capacity for high-speed data throughput, while interfaces labelled 400G highlight the high-capacity nature of the connections. The diagram effectively communicates the complex interaction of components within an advanced optical network, optimized not only for rapid data transfer but also to maintain signal strength and provide flexible wavelength allocation. Overall, the scheme captures the essence of a sophisticated optical network design that is both adaptable and scalable, capable of meeting the complex needs of modern high-speed data communication.

The comparative analysis table showcases the distinct capabilities of Dual and Single Amplifiers within a network system. Dual Amplifiers are designed to manage up to 8 channels, while Single Amplifiers can handle a significantly wider range, from 16 to 48 channels. Both types of amplifiers are equipped with features like AGC and APC, which provide the necessary adjustments for consistent performance, irrespective of the variations in input levels. A key differentiation is that Single Amplifiers have an added advantage of flatness control, ensuring uniform gain distribution across all channels, a feature not available in Dual Amplifiers. Furthermore, in terms of output power, Single Amplifiers have the flexibility to offer a slightly

higher range, adjustable from 15 to 17 dBm, whereas Dual Amplifiers maintain a constant output of 15 dBm. This comparison clearly outlines the functional distinctions between the two amplifier types, highlighting that Single Amplifiers offer a higher degree of control and a broader operational range, making them suitable for more demanding applications that require fine-tuned signal management and greater flexibility. Further details are reported in Table 4.8-1.

Table 4.8-1: Comparison between Dual and Single Amplifier.

	Dual Amplifier	Single Amplifier
Channels	8	16-48
AGC	Yes	Yes
APC	Yes	Yes
Flatness Controll	No	Yes
Output Power	15 dBm	15-17 dBm

4.8.2 Interfaces

The interface and its description is reported in Table 4.8-2.

Table 4.8-2: Interface for pluggable EDFA Amplifier.

S.No	Interface	Description
1	Command line	The architecture of WDM horseshoes is developed in WP3. Is design the OLS (optical line system). The OLS features splitters, couplers, and pluggable EDFAs for efficient signal distribution, supporting a ring topology. It uses precise laser tuning in 400G transceivers for scalable and adaptable wavelength management

4.8.3 KPI assessment

EDFA amplifiers are fixed gain, while being cost-effective and easy to implement; they introduce constraints on network scalability. This is because the preset gain requires that the signals have a well-defined input power to avoid over-amplification or insufficient amplification. As a result, it is often necessary to adjust the length of the optical path—for example, adding additional fiber cables to fit this fixed gain, a process that can increase the cost and complexity of the infrastructure. A significant improvement could come from the adoption of variable gain amplifiers. These devices allow for gain adaptability in response to dynamic changes in network conditions, such as changing the input power or adding new transmission channels. With the use of variable gain amplifiers, the network gains flexibility, as it is no longer necessary to adjust the length of the optical path for each specific signal. In addition, the use of a high-power transceiver that can operate at an output level of at least 0 dBm could help to increase the efficiency of the system. A high-power transmitter can compensate for line losses and interact more effectively with the amplifier.

However, the amplifiers used within the SEASON project offer gain variability but lack a flatness control system, which is essential to ensure homogeneous amplification across all channels. Without this capability, some channels may be amplified more than others, leading to suboptimal signal balance and potential transmission quality problems. To meet this challenge—and in line with KPI 8.1, which targets improved performance and reliability in multi-channel optical transport systems—it would be advisable to integrate a flatness control mechanism that automatically adjusts the gain for each channel. This ensures a consistent and reliable signal over the entire bandwidth.

4.9 RESEARCH ACTIVITIES ON SMARTNIC WITH COHERENT PLUGGABLE (C3.9)

4.9.1 Description

In the SEASON project, we propose the use of SmartNIC, also called Data Processing Unit (DPU), equipped with P2P and P2MP coherent transceivers as an innovative cost-effective *edge solution* providing converged packet, optical and computing resources in a single platform. DPUs with coherent transceivers enable reduction of telecommunication equipment (e.g., aggregation routers / gateways) with benefits in terms of latency, power consumption, and reduction of O/E/O conversions. Furthermore, they enable new and advanced optical and packet monitoring capabilities (as preliminarily investigated in D3.1 and D4.1 respectively).

Pluggable modules used in SmartNIC-DPU are associated to the topic cluster TC4.

A relevant use case of an edge node equipped with DPU encompassing coherent transceivers refers to the implementation of Distributed 5G Units (DU), as reported in Figure 4.9-1. On the left, we present the current scenario where the DU needs to be co-located with the RUs since the cell site is too far from the central office (e.g., rural areas, coverage of railways/highways). In this scenario, the cell site gateway manages only very few connections: the one from the central office to the server hosting the DU and the two/three connections towards the RUs. In SEASON, as shown in the figure on the right, we present the proposed scenario where the cell site GW is removed thanks to the use of network interface cards (NIC), equipped with P2MP coherent pluggable transceiver.

The NIC is hosted in the server running the DU. Indeed, NICs/DPUs with up to four interfaces can be also exploited to directly reach the co-located RUs. This way, the Cell Site Gateway can be avoided, with significant benefits in terms of management and reliability, power consumption and latency (one less standalone element to power on, manage, monitor, and traverse). Introduction of the DPU.

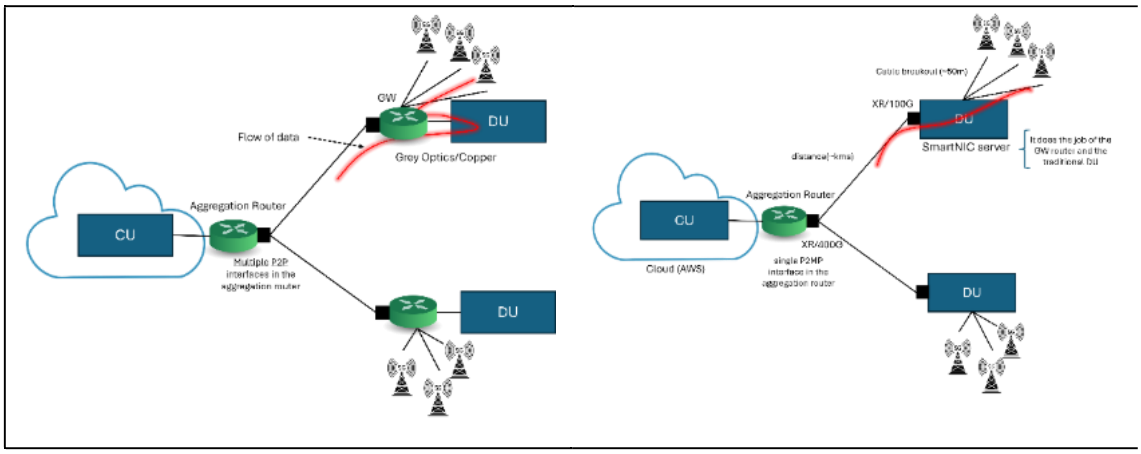

Figure 4.9-1: (left) state-of-the-art solution leveraging a standalone Cell Site Gateway router; (right) proposed approach within SEASON, eliminating – under specific conditions – the Cell Site GW.

To support this innovative scenario, SEASON is proposing as innovative component a NIC/DPU supporting coherent pluggable modules. Three main aspects need to be addressed.

The first aspect refers to the limited power provided to transceivers by current generation NICs/DPUs which does not allow power on current generation of coherent pluggable transceivers. Such limitations require technological evolution which is beyond the project scope.

The second aspect, assuming the first one is successfully addressed, refers to the proper control of the transceiver. In SEASON this latter aspect is specifically addressed. A lightweight SDN Agent has been implemented to support the configuration of the optical transceiver equipped within the DPU, enabling the configuration of output power, frequency, and operational mode. Furthermore, in the case of P2MP transceivers, additional parameters need to be considered, such as specific hub-leaf configurations of the OpenXR module. This aspect is addressed in SEASON WP4.

The third aspect, addressed by WP3 (see Section 7.2), refers to the design and implementation of the data plane technology within the NIC/DPU, using the DOCA flow solutions leveraging hardware acceleration.

4.9.2 Interfaces

Table 4.9-1: Interface for pluggable optical transceivers controlled by a DPU card.

S.No	Interface	Description
1	OpenConfig	A lightweight SDN Agent has been implemented in WP4 to support the configuration of the optical transceiver equipped within (*) the DPU. Specific parameters to be configured are the standard ones for a coherent P2P transceiver: output power, frequency, and operational mode. In the case of P2MP transceivers, additional parameters include specific hub-leaf configurations of the XR module.

(*) As of today, coherent transceivers cannot be directly inserted into DPUs due to electrical and heating constraints. For this reason, in SEASON, we insert them in packet-optical switches, but their control is performed as if they are plugged in the DPU, i.e., by software modules running within the DPU.

4.9.3 KPI assessment

The C3.9 prototype was experimentally evaluated in a representative 5G/6G testbed based on two commercial servers equipped with NVIDIA BlueField-2 DPUs operating at 100 Gb/s. The evaluation focused on the node experiencing both pass-through traffic between the TWO DPU ports as well as termination towards the host server. Accelerated VNF offloading was implemented using DOCA libraries (v2.9), enabling packet classification and forwarding to be fully offloaded in hardware. Traffic received from the central office was processed through hardware-accelerated switching and DOCA Flow pipelines, steering packets either toward local termination or pass-through interfaces without involving the DPU ARM cores. This architecture allows high-throughput processing while preserving compute resources for additional VNFs. Performance was assessed using both stateless (VIAVI) and stateful (iPerf3) traffic generators to emulate downstream traffic. The results demonstrate that the 100 G DPU sustains full line-rate throughput (up to 90 Gb/s total) for packet sizes of 512 B and above, while only a limited throughput reduction is observed for small packets (128 B) due to packet-rate processing overhead. These results confirm that C3.9 meets the targeted KPIs related to high-capacity traffic handling, efficient VNF acceleration, and scalability toward future 6G edge deployments. Further details are reported in Section 7.2.

5 SEASON OPTICAL NETWORK ARCHITECTURE: MODELING AND E2E DESIGN

5.1 ROBUST OPTIMIZATION OF SEASON'S FILTERLESS OPTICAL NETWORKS WITH PHYSICAL LAYER UNCERTAINTIES (RELATED TO C3.10, C3.11)

Designing efficient and reliable optical networks is crucial, but they are vulnerable to various factors like unpredictable traffic, performance fluctuations, measurement errors, aging, and potential failures. These uncertainties can compromise network designs if not addressed during the design phase. Traditional Deterministic Optimization (DO) methods, which often use large margins or heuristics, can ensure quality but may waste resources and do not guarantee feasibility under the worst conditions. While increased flexibility and monitoring can reduce these margins, they also add complexity and operational costs. The core challenge in optical network design lies in dealing with uncertain input data and the high dimensionality of problems, which demands computationally efficient solutions.

To overcome these challenges, techniques like Stochastic Optimization (SO) and Robust Optimization (RO) are employed when uncertainty information is available. SO, optimizes for expected outcomes using probability distributions but doesn't guarantee performance in worst-case scenarios. RO, on the other hand, focuses on optimizing for worst-case performance, ensuring reliable design across a range of uncertainties. However, basic RO can be overly conservative, assuming all parameters hit their worst-case values simultaneously [Ber03]. To address this, more advanced approaches like Γ-robustness, in SEASON, as a novel contribution, we propose to use the Adjustable Robust Optimization (ARO). ARO, which allows for decisions to be made after some uncertainties are revealed, has shown promise in operations research [Tal04] but has seen limited application in optical network design. We propose an ARO methodology using a Mixed-Integer Linear Programming (MILP) model to consider a wider range of uncertainties and compares its performance against Γ-robustness and baseline DO methods. In the studies we carried out in SEASON, ARO achieves a reliable, fully protected network with 16.6% less optimality loss compared to the DO, significantly outperforming conservative standard Robust Optimization (RO).

We exemplify DO, RO, and ARO methods using a simple linear program (LP) where only the coefficients of the variable u are uncertain as shown in Figure 5.1-1.

Deterministic Optimization (DO): This method uses only the nominal (average) values of the uncertain parameters. In our example, DO yields an objective value of 0.5. While it provides the best possible outcome if the parameters are exactly as expected, it doesn't account for any deviations.

Robust Optimization (RO): To ensure feasibility across all defined uncertainties, RO considers the worst-case scenario. This approach leads to a tighter feasible region, which, while guaranteeing a solution regardless of the uncertainty within the specified range, results in a 37%

loss in optimality compared to the DO solution. Essentially, RO prioritizes robustness over a potentially higher objective value.

Adaptive Robust Optimization (ARO): ARO offers a more sophisticated approach by allowing some decision variables to "adapt" once the uncertainty is revealed. In this case, variable v can adjust after the actual value of the uncertain parameter ξ (related to u's deviation) is known, even though u is still a "here-and-now" decision. This adaptability significantly improves the outcome, leading to a fully protected solution that incurs only a 16.6% loss in optimality compared to the DO case. This is a substantial improvement over RO's 37% loss, showcasing the benefit of adaptive decision-making. For practical purposes, v is modeled as an affine function of ξ.

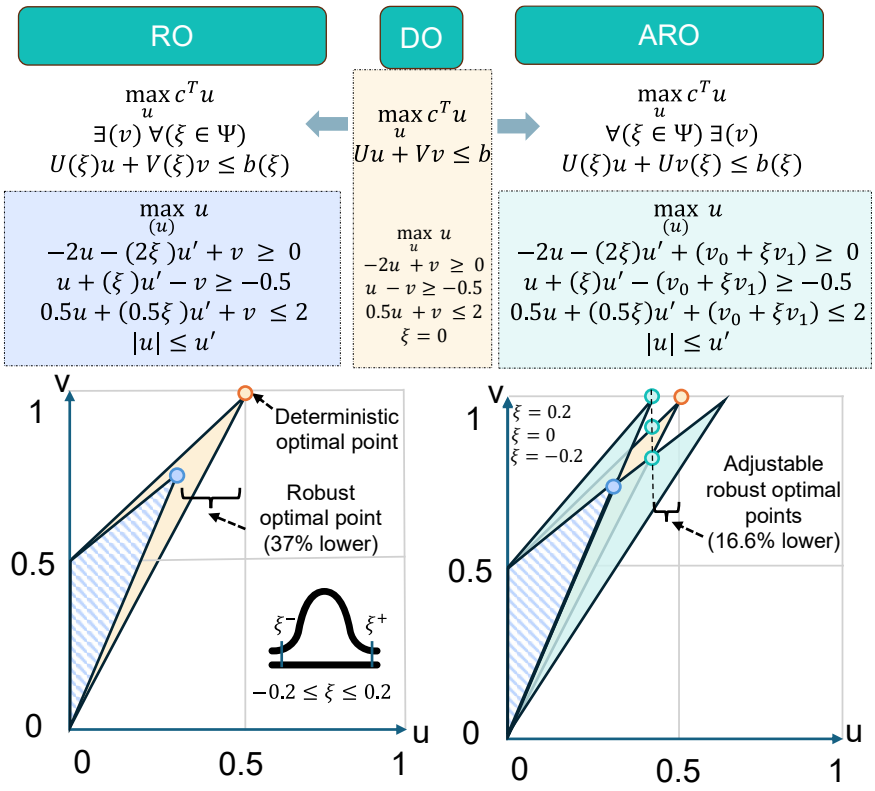

Figure 5.1-1: RO, and ARO variations of a simple 2-variable and 3-constraint DO problem.

We investigated optimization of a filterless horseshoe network in the presence of links attenuation uncertainty [Moh25]. We showed that the reliability of design can be improved at the cost of optimality loss, assuming the network configuration cannot be changed later when the uncertainty has been revealed. However, it is not always the case, and some decisions can be readjusted.

We propose a P2MP filterless horseshoe optical network designed for resilience, connecting leaf nodes to hubs as shown in Figure 5.1-2. It can be built to handle unpredictable span losses and launch power variations. The network uses single-mode fiber pairs for each link, and designers can strategically place optical amplifiers—either as "express amplifiers" before the leaf nodes or

as pre- and post-amplifiers within the hubs. A key part of the design involves selecting specific coupler ratio at each leaf node, which has defined add/drop and express losses.

The design process involves making two types of decisions:

- **"Here-and-now" choices:** These are fixed upfront and include selecting the **coupler types** for each leaf node and direction, as well as determining **amplifier locations**.
- **"Wait-and-see" choices:** These are adaptive, primarily focusing on setting the gain of the deployed amplifiers or adding more amplifiers as needed.

All these decisions are subject to critical constraints to ensure the network functions properly:

- **Transceiver sensitivity:** Signals must be strong enough for the transceivers to receive them.
- **Linear operation:** The launch power within each span must be limited to prevent signal distortion.
- **SC power imbalance:** Differences in SCs power in the upstream direction, caused by varying path losses, need to be minimized.

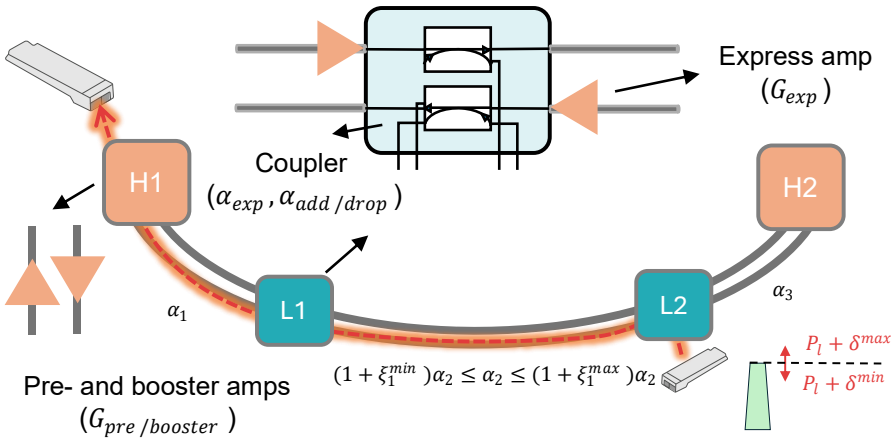

$$P_{L2\to H1} = P_l^{L2} + \alpha_{add}^{L2} + \alpha_2 + G_{exp}^{L1} + \alpha_{exp}^{L1} + \alpha_1 + G_{pre}^{H2} \ge P_s^{H1} \quad \text{(DO)}$$

$$P_l^{L2} + \alpha_{add}^{L2} + \delta\,\acute{p}_l + \alpha_2 + \xi_2\acute{\alpha}_2 + G_{exp}^{L1} + \alpha_{exp}^{L1} + \alpha_1 + \xi_1\acute{\alpha}_1 + G_{pre}^{H2} \ge P_s^{H1} \quad \text{(RO)}$$

$$P_l^{L2} + \alpha_{add}^{L2} + \alpha_2 + G_{exp}^{L1} + \alpha_{exp}^{L1} + \alpha_1 + G_{pre}^{H1} + \Gamma \min_{\xi_1,\xi_2,\delta} \{\delta\,\acute{p}_l + \xi_2\acute{\alpha}_2 + \xi_1\acute{\alpha}_1\} \ge P_s^{H1}$$

$$P_l^{L2} + \alpha_{add}^{L2} + \alpha_2 + G_{exp,0}^{L1} + \alpha_{exp}^{L1} + \alpha_1 + G_{pre}^{L1} + \delta^{min}\,\acute{p}_l + \min_{\xi_1,\xi_2,\delta} \left\{\xi_2\acute{\alpha}_2 + \xi_1\acute{\alpha}_1 + \sum_i \xi_i W_i^{L1}\right\} \ge P_s^{H1} \quad \text{(ARO)}$$

Adjustable

$$G_{exp,}^{L1} = G_{exp,0}^{L1} + \sum_i \xi_i W_i^{L1}$$

Figure 5.1-2: Two-leaf horseshoe, and a sample constraint in DO that is reformulated for RO and ARO.

This study investigates P2MP networks using 400G modules (dual-polarization 16-QAM, 16 subcarriers at 4 GBaud). The system operates under specific constraints: a minimum receiver power of -24 dBm/SC, a launch power of -12 ± 0.2 dBm/SC at leaf nodes and hubs, a nonlinearity threshold of -8 dBm/SC, and a maximum SC power imbalance of 14 dB at the hub receiver.

The research evaluated twenty 8-leaf networks, each with a typical loss of 0.24 dB/km and an average length of 12 km. To test for feasibility, link attenuation uncertainty was modeled using a uniform distribution. The study considered a range of coupler ratios, from balanced (50/50) to various unbalanced ratios (10/90 to 50/50 in 10% increments), and amplifiers with gains ranging from 10 to 30 dB.

Figure 5.1-3 illustrates how increasing uncertainty affects the number of amplifiers and power imbalance in Robust Optimization (RO) ($\Gamma = 1$) and Approximate Robust Optimization (ARO) designs, comparing balanced and unbalanced couplers. Figure 5.1-3(a) shows that RO generally requires a sharper increase in amplifiers as uncertainty grows, especially with unbalanced couplers. ARO with unbalanced couplers, however, uses significantly fewer amplifiers and handles higher uncertainty, demonstrating better performance and resilience. Figure 5.1-3(b) reveals that RO consistently results in higher SC power imbalance than ARO. Interestingly, ARO with unbalanced couplers reduces the SC power imbalance as link uncertainty increases. This is likely due to the added flexibility provided by more amplifiers.

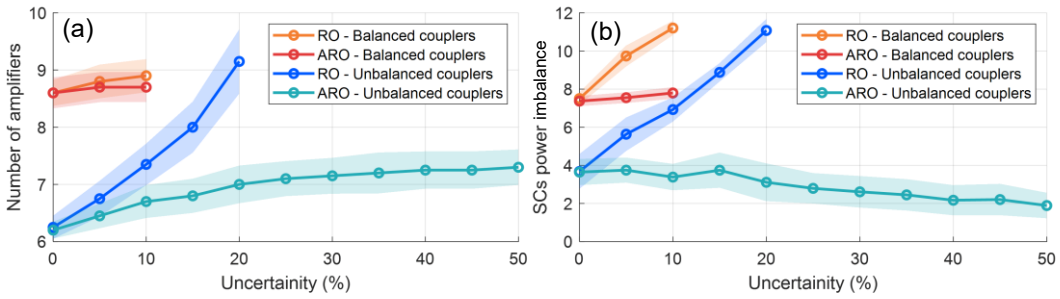

Figure 5.1-3 (a) Number of amplifiers and (b) SCs power imbalance versus uncertainty for RO and ARO methods.

In conclusion, ARO can help to have a trade-off between complexity and optimality when dealing with uncertainties in network design.

These results contribute to KPIs 2.1 and 2.2 by showing that simplified network architectures based on filterless horseshoes with P2MP end nodes can provide sufficient bandwidth to Metro-Access nodes at reduced cost and high-power efficiency.

5.2 SEASON Multi-Layer Aggregation: Optical and Electronic Domains (related to C3.10, C3.11)

Within the SEASON project, optical aggregation enabled by DSCM has been investigated as a cost- and energy-efficient solution [Cas25], e.g., for access-metro edge nodes. In this section, we will present node architectures enabling optical or electronic traffic aggregation and we will

show analysis on transmission performance. For additional studies on energy and cost efficiency, the reader may refer to Section 8 and D2.3.

Such an investigation is driven by the fact that a large contribution to the energy requirements is caused by router interfaces and by operations performed in the electronic domain (e.g., traffic aggregation). For instance, different network segments – such as access and regional – are interconnected by routers or electronic switches. At an edge node, lower-rate traffic flows are aggregated electronically and then routed in the metro-regional or national segment. Performing traffic aggregation in the optical domain may strongly reduce the energy requirements at the edge nodes.

In this work, we analyze digital sub-carrier multiplexing (DSCM) to all-optically aggregate traffic at the edge node of a metro-regional/national segment to avoid energy-hungry electronic (router) interfaces. This requires that optical flows transparently i) traverse access segments, ii) are aggregated through a passive optical coupler, iii) and then, traverse the metro-regional/national segment. The Quality of Transmission (QoT) of such flows is here estimated, resulting – as expected – in a negligible impact (about 2% in transmission performance) due to the propagation in the access segment and due to the optical traffic aggregation. This minor drawback is negligible when compared to the benefit of significantly reducing the amount of devices, which consequently considerably reduce the power consumption thanks to all-optical traffic aggregation and P2MP.

5.2.1 Optical aggregation enabled by P2MP and DSCM

DSCM offers an additional layer of multiplexing [Wel21]: i.e., the digital sub-carriers (DSCs). One of the key advantages of DSCM is the possibility of optically aggregating traffic. This may pave the way to relevant changes in traffic aggregation as illustrated in Figure 5.2-1. Here, several transceivers are associated with different access segment traffic collection points, e.g., serving traffic from optical line terminals (OLTs) collecting traffic from several passive optical networks (PONs) for fixed access, a baseband unit (BBU) or a cell site router for mobile radio site. The gathered traffic is allocated to a DSC or a subset of available DSCs. The signals flow over the access segment and then enter the passive coupler where the DSCs are aggregated all-optically. An Erbium-doped fiber amplifier (EDFA) might be needed to compensate for the loss due to the propagation from the access to the edge and for the losses due to the coupler. Finally, the aggregated signal flows within the metro-regional or national network. Such an architecture can be referred to as P2MP and it contrasts with the point-to-point (P2P) architecture reported in Figure 5.2-1.

With P2P – and electronic aggregation – each traffic flow from access is received by a dedicated transceiver at the edge; then, a router aggregates the traffic, and another (higher-rate) transceiver (maybe even installed into a transponder) generates the signal that is routed over the metro-regional/national segment. The comparison of the two architectures in Figure 5.2-1 shows that with optical aggregation: i) transceiver interfaces can be saved at the edge since

signals are by-passed and not terminated; ii) router interfaces are saved at the edge since traffic is aggregated all-optically.

In the case of optical aggregation, QoT estimation should account for i) signal propagation within the access segments, ii) the losses due to the passive coupler, and iii) the propagation within the metro-regional/national segment. DSCs originating in different access nodes are aggregated in a single DSCM signal and terminated at a single destination metro-regional/national node, where a router will distribute the sub-traffic flows to other segments.

In the next sub-section, QoT estimation results are presented for a specific network scenario.

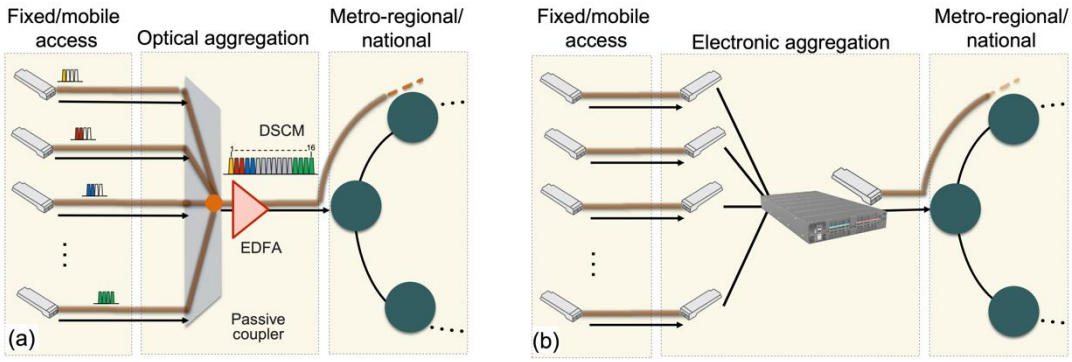

Figure 5.2-1: (a) Optical and (b) Electronic aggregation approaches.

5.2.2 Results for QoT estimation

The network scenario of Figure 5.2-2 depicts a metro-regional/national topology with links' (and spans') length sourced from SEASON D2.1 [D2.1-24]. DSCM is assumed with 16 DSCs for a maximum overall capacity of 400G per transceiver. Each metro-regional/national node serves four fixed or mobile access segment collection points with links of 10 km, allowing a maximum capacity of 100G per 10 km link. DSCs are generated in the access segments, aggregated all-optically in a metro-regional/national node, and then terminated to another metro-regional/national node, as in the illustrative example (in orange) in Figure 5.2-2.

The QoT estimation is based on optical-signal-to-noise ratio (OSNR) computation in a linear regime. OSNR is computed per path (e.g., assuming the worst wavelength channel). A fiber attenuation of 0.2 dB/km is considered; DSCs aggregation (i.e., at the coupler) is assumed to introduce a loss of 6 dB; metro-regional/national node architecture is switch&select and each node introduces 10 dB loss (5 dB per wavelength selective switch). In the edge node, an EDFA compensates for fiber attenuation within the access and for the coupler loss. Launch power is set to -1.0 dBm. Then, an EDFA is placed after each link or fiber span compensating for fiber attenuation and node loss. OSNR requirements are retrieved from the XR Optics specifications [XR-24] and are 24 dB for 400G DP-16QAM, 20 dB for 300G DP-8QAM, and 15 dB for 200G DP-QPSK. A variable number of operational margins [Chr19], ranging from 0 dB to 5 dB, are considered to account for other effects such as aging and QoT model inaccuracies. The OSNR is

computed for all routes starting from an access segment and terminating at a metro-regional/national node as in the example of Figure 5.2-2. As a benchmark, the QoT in the scenario of electronic aggregation of traffic is estimated. In this case, the OSNR is computed for all routes starting in a metro-regional/national node and terminating in different metro-regional/national nodes.

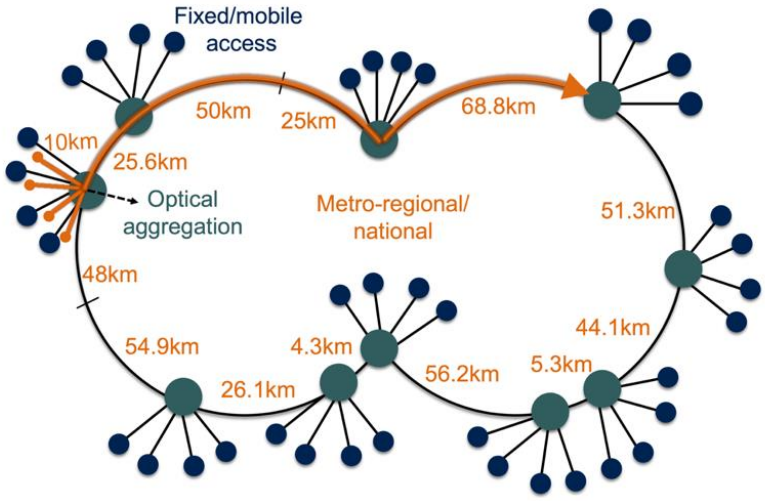

Figure 5.2-2Figure 5.2-2 Considered network scenario.

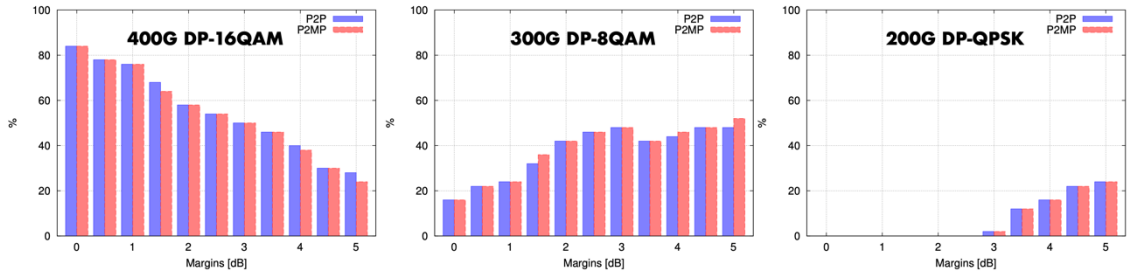

Figure 5.2-3: Percentage of routes where the most spectral-efficient modulation format is DP-16QAM, DP-8QAM, or DP-QPSK.

Figure 5.2-3 reports the percentage of routes supporting channels using the most spectral-efficient modulation format (DP-16QAM, DP-8QAM, or DP-QPSK), as a function of the operational margins. The analysis of Figure 5.2-3 shows that using P2MP (optical aggregation) or P2P (electronic aggregation) lead to similar results. Thus, having an optical by-pass (which includes the propagation from the access, the coupler loss for traffic aggregation, and the related amplification noise) has only a minimal impact on the QoT (at least in the considered scenario), so that the same most spectral efficient modulation format can be selected with P2MP or P2P. Focusing on 400G DP-16QAM, around 80% of routes support it when considering no operational margin (in both P2MP and P2P approaches). However, the percentage of routes supporting 400G DP-16QAM decreases as the margins increase since, in this case, some routes cannot reach the OSNR requirement of 24 dB. Consequently, 300G DP-8QAM should be transmitted instead. This effect is particularly clear when increasing margins up to 3 dB. If even higher operational margins are considered, some routes that were previously feasible with

8QAM modulation format become infeasible (thus, the percentage of 8QAM routes may decrease for specific operational margins) and the use of QPSK modulation format rapidly becomes necessary. Since P2MP leads to slightly worse QoT than P2P only, the difference between the two is visible for a few cases of operational margins (1.5 dB, 4 dB, and 5 dB) only. Moreover, the resulting difference in the percentage of routes supporting 400G DP-16QAM is very small (2%). Finally, 200G DP-QPSK is considered for all remaining routes, when high margins are required.

5.3 CROSSTALK ANALYSIS IN MBOSDM OPTICAL NETWORKS WITH PROGRAMMABLE TRANSCEIVERS (RELATED TO C3.1 AND C3.4)

In this section a crosstalk (XT) analysis has been performed in a MBoSDM optical network scenario. XT is a major limitation in SDM transmission over multicore fiber (MCF), as it results from unwanted coupling between adjacent cores, leading to transmission performance degradation. Hence, an experimental validation and analysis of the impact of XT using three building blocks of the SEASON MB(oSDM) S-BVT prototype enabling full S+C+L operation has been assessed over a 19-cores MCF spanning 25.4 km [Nad25]. In SEASON, we also confirmed that the L-band exhibits the highest XT, which might become the limiting factor for high-performance wavelength assignment in future MCF-based systems. More details and the architecture of the MB(o)SDM S-BVT (SEASON component C3.4) can be found in Section 7.4 of deliverable [D3.2-24].

The experimental setup for the XT assessment considers the three transmitters operating at 40 Gb/s. 4 QAM uniform modulation is considered for all the orthogonal frequency division multiplexing (OFDM) subcarriers composing a 20 GHz electrical signal. A digital-to-analog converter (DAC) with a sampling rate of 64 GSa/s performs the digital-to-analog conversion. The generated OFDM signals are externally modulated with Mach-Zehnder modulators (MZMs), biased at the quadrature point, and driven by tunable laser sources (TLs) configured at different wavelength covering the S-, C-, and L-bands. After modulation, the signals are amplified with erbium-doped fiber amplifiers (EDFAs) with fixed output power of 0 dBm (for the C- and L-bands), while a thulium-doped fiber amplifier (TDFA) is used for the S-band. The TDFA output power is maintained at 0 dBm with automatic current control by adjusting the pump currents.

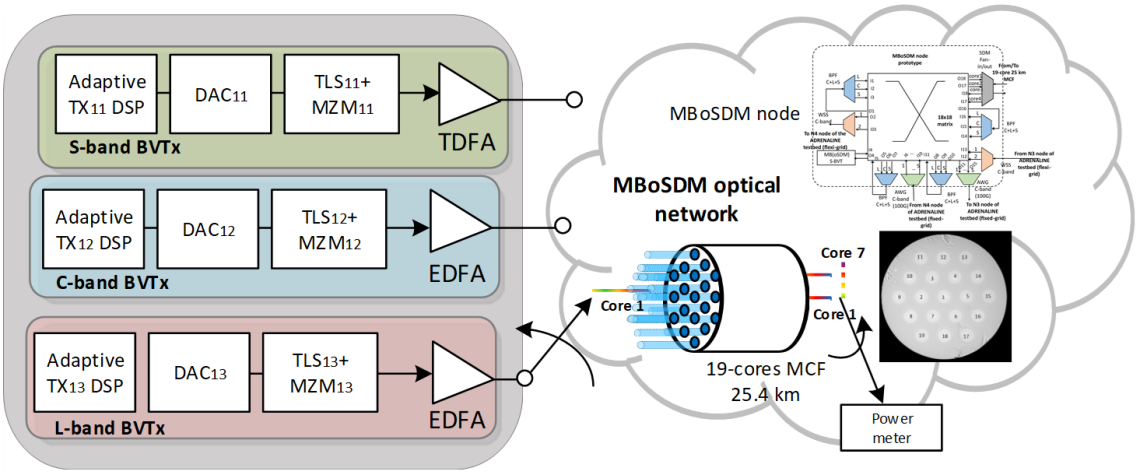

Figure 5.3-1: MBoSDM setup for XT validation including transceiver (component C3.4) and switching (component C3.1) SEASON solutions.

Each transmitter is connected to core 1 of a 25.4 km MCF of 19-cores, as seen in the setup schematic of Figure 5.3-1. Power levels at both the output core and adjacent cores (cores 2 to 7) are measured to evaluate the resulting XT, as shown in Figure 5.3-2. We have considered different wavelengths within the S-, C-, and L-bands in steps of 5 nm. According to Figure 5.3-2 the L-band exhibits the highest XT values, ranging from −24.6 dB to −21.9 dB. In the C-band, XT values range between −29.3 dB and −22.3 dB, while the S-band shows lower XT impact, with values from −38.2 dB to −28.5 dB.

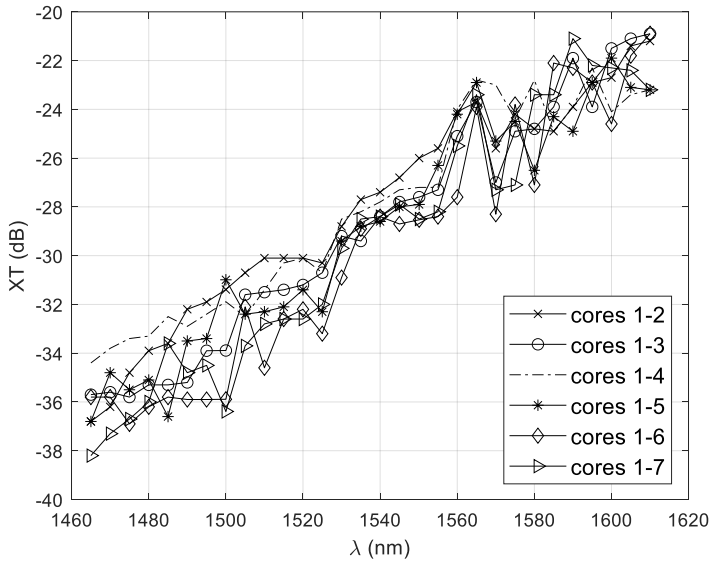

Figure 5.3-2: XT experimental results from core no. 1 to adjacent cores 2-7.

Figure 5.3-3 (a) presents simulation results based on XT equations from references [Fei14, Far24], using the MCF specifications of the experimental setup [Nad23]. In the simulations, up to six adjacent cores are populated, which leads to an increase in XT of up to 7.8 dB compared to the single-core case.

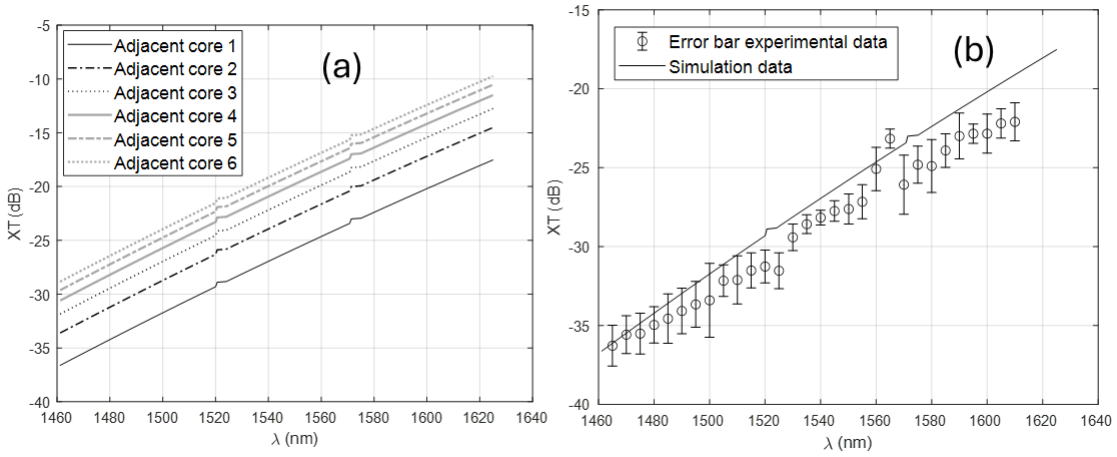

Figure 5.3-3 (a) XT simulation results considering up to 6 populated adjacent cores, and (b) simulation and experimental results comparison.

Finally, Figure 5.3-3 (b) compares simulated and experimental XT values for a configuration where only core 1 carries an OFDM signal. Both trends exhibit consistent behavior across wavelengths, validating the proposed analytical XT model that will be used in the project for further XT analysis including network studies (see Section 5.3). This information can assist an SDN control plane in making appropriate decisions, such as wavelength band selection, to ensure an efficient operation and management of the network resources, including spatial channels (cores) allocation, according to the required capacity/performance requirements.

These results are closely related to the KPIs 3.1 and 3.2 by helping to analyze the impact of XT when transmitting over MCF.

5.4 Impact of Inter–Core Loss and Gain Equalization on Transmission Performance in SEASON Multi–Core Systems (related to C3.1, C3.4)

To cope with the request for improved energy efficiency and reduced cost, future long-haul systems based on multi-core fibers (MCFs) will rely on MCF amplifiers as key elements. These objectives are mainly achieved by using multi-mode pumps in a cladding pumping scheme. Major challenges resulting from this pumping scheme are gain imbalances between the cores and transient control, since this pumping scheme does not support individual gain control in the different cores. Therefore, hybrid pumping schemes complementing the high-power multi-mode pump with single-mode pumps have been proposed. Launching the pump power emitted by each of these pumps into one core of the erbium-doped fiber (EDF) allows for independent fine tuning of the gain in each core. In view of amplifier noise figure, launching the single-mode pump power counter-directionally to the transmit signals into the cores of a MCF connected to the input of such an amplifier is a compelling alternative solution. In this configuration, gain balancing is achieved by means of distributed Raman amplification in the transmission fiber.

Stimulated Raman scattering (SRS) is a major nonlinear fiber effect limiting capacity of multi-band systems. Due to this nonlinear fiber effect, power is transferred from shorter wavelengths to longer wavelengths. In consequence, shorter wavelength channels have smaller power at the fiber end than the longer wavelength channels if all channels are launched at the same power into the fiber. The increasing power differences among the channels also affect inter-core crosstalk from one core to another core. Due to this reason, numerical investigations revealed larger crosstalk power levels at longer wavelengths as compared with shorter wavelengths. However, this does not necessarily lead to performance degradation since longer wavelength channels propagating in both cores experience similar Raman gain. Thus, the power of signals affected by crosstalk from another core is also increased. In consequence, degradation of the signal-to-interference ratio (SIR) is avoided, and the potentially detrimental effect of increased crosstalk power is cancelled out.

In contrast to the previous scenario, equalizing gain and loss among the different cores by making use of distributed SRS in the transmission fiber induces Raman gain only in the cores with higher attenuation. The impact of Raman assisted gain balancing on transmission performance caused by ICXT in a MC scenario is investigated in the following. For the analysis, a trench-assisted 7-core fiber is considered. In SEASON, we investigated the detrimental effect of Raman-assisted loss and gain equalization on XT in MCF, and experimentally quantified that Raman amplification for loss compensation increases the XT-induced OSNR penalty by ~30% (e.g., from 1.7 dB to 2.5 dB), guiding design limits for multi-span multi-core systems.

More details and references are provided in an article published in IEEE Photonics Technology Letters [Rap25].

5.4.1 Scenario and theoretical model

Increase of ICXT by Raman assisted loss equalization is explained on the basis of Figure 5.4-1. In the considered scenario, crosstalk power resulting from channels propagating in core 1 accumulates in core 2 along the fiber axis. In particular, crosstalk contributions from two positions along the fiber axis, one close to the beginning of the fiber after propagation distance L1 (left column) and one close to the fiber end at length L_2 (right column), are illustrated. For the following numerical calculations and explanations, the coupled-power theory (CPT) is used that has been shown to provide sufficiently accurate results in view of crosstalk power characterization. In the considered scenarios, signal power in the center core is not altered by the following parameter variations. In consequence, the SIR relevant in view of transmission performance reduces in the same proportion as the ICXT power increase.

For describing contributions to the total crosstalk power in core 2 at the fiber end, a mathematical model has been derived that revealed to following aspects. With identical attenuation coefficients in both cores, each position along the fiber axis contributes equally to the total crosstalk power at the fiber end. In other words, attenuation that is not experienced by a lightwave before the coupling point is present after the coupling into the other core such that the total attenuation is independent of the coupling point. However, contributions

occurring closer to the fiber input are larger if the attenuation coefficient is larger in core 1 as compared with core 2.

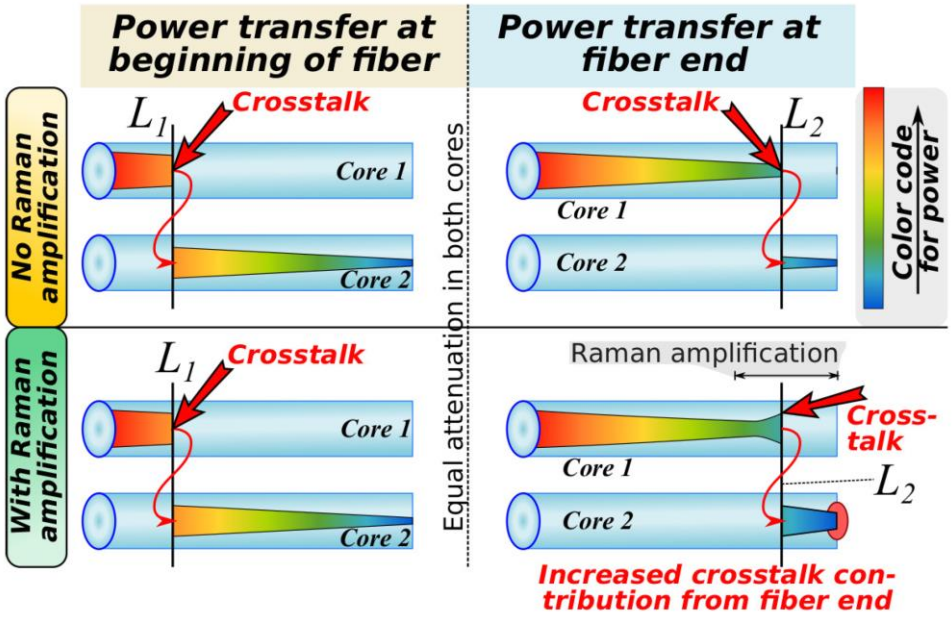

Figure 5.4-1: Schematic drawing illustrating crosstalk increase due to counterdirectional Raman amplification.

The situation changes if lightwaves propagating in core 1 experience Raman amplification close to the fiber end due to counterdirectional pumping as illustrated in the lower part of Figure 5.4-1, whereas there is no distributed amplification in core 2. Power components coupled into core 2 close to the fiber input at distance L_1 do not experience Raman gain. In contrast, power components coupling over close to the fiber end at position L_2 are enhanced such that the total crosstalk power increases with loss balancing across the cores.

In the following, crosstalk in the center core is analyzed theoretically based on a constant coupling coefficient along the fiber axis characterizing coupling from the outer cores to the center core. Total signal power in the outer cores is assumed to decay exponentially with optional amplification by counter-directional Raman amplification, as illustrated in Figure 5.4-2 for a fiber with 50 km length, an attenuation coefficient of 0.2 dB/km in the center core, and 0.3 dB/km in the outer cores. The coupling coefficient is fitted to the experimental results presented in the next section. Adjusting the Raman gain to 5 dB to compensate for the loss differences between outer cores and center core, ICXT power accumulated in the center core is represented in Figure 5.4-2 by the blue curve. For comparison purposes, ICXT power without Raman amplification is indicated by the red curve. In contrast to the other curves, the green dashed curve takes signal depletion by ICXT into account, but apparently this effect can be neglected. Power levels for ICXT are normalized to the total input power into the outer cores.

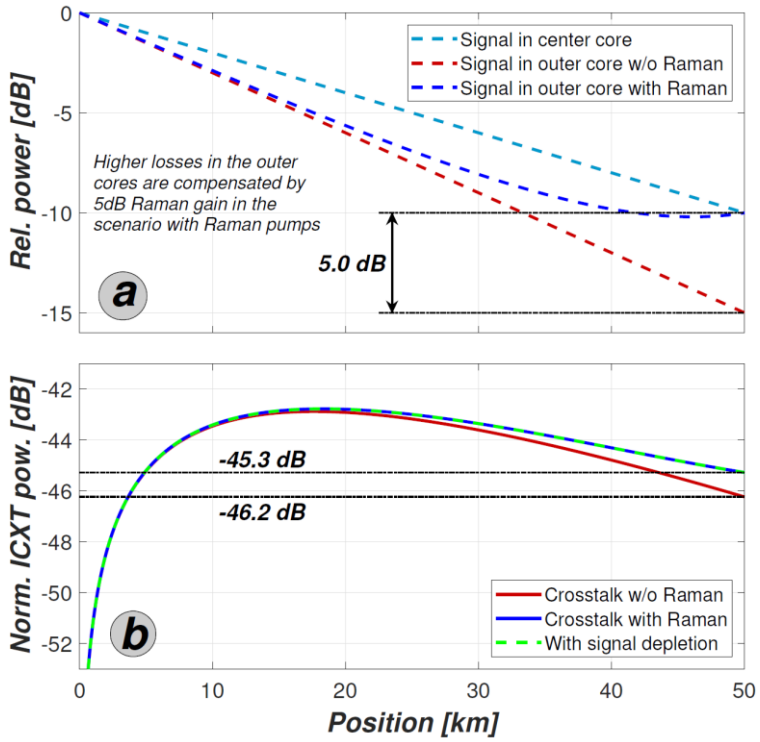

Figure 5.4-2 (a) Power distribution of signals in the center core and the outer cores (b) Accumulation of ICXT power in the center core.

The increase of ICXT power with increasing Raman gain in the outer cores is illustrated in Figure 5.4-3, revealing an ICXT reduction with increasing loss in the outer cores, wherein the legend indicates the total loss difference between outer cores and center core for each curve. As apparent from the dash-dotted line, total crosstalk power in the center core decreases with increasing attenuation difference, even when exactly compensating for the loss difference by Raman gain in the outer cores. The dashed curve in Figure 5.4-3 indicates ICXT power versus this loss difference without Raman gain. For generating the red solid curve, it has been assumed that the Raman gain in the outer cores is exactly adjusted to compensate for their higher loss. This scenario is identical with the scenario represented by the dash-dotted curve in Figure 5.4-3. In addition to the loss difference, there might be the need to compensate for gain differences between the outer cores and the center core in the optical amplifiers. Therefore, the Raman gain is further increased in steps of 1 dB with the results represented in different colors that show a further increase of ICXT with increasing Raman gain.

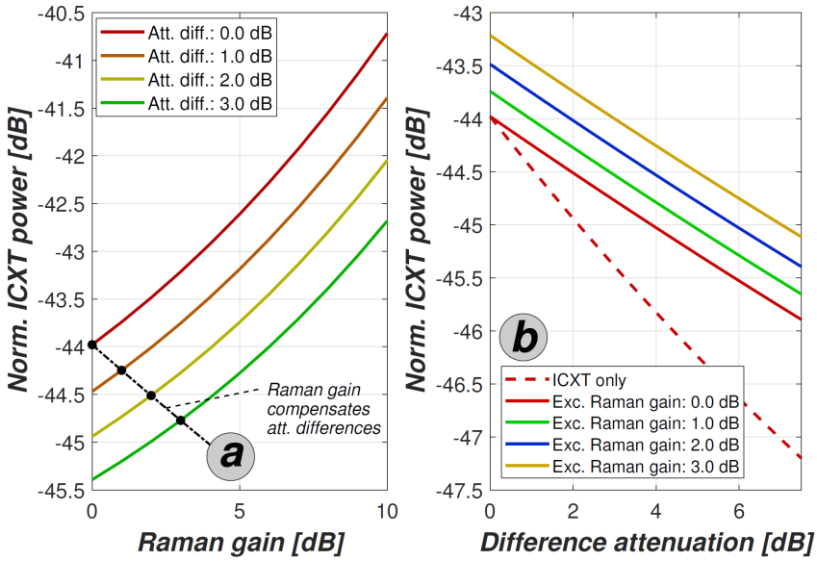

Figure 5.4-3: (a) ICXT power versus Raman gain for various attenuation differences (b) ICXT power versus attenuation difference fully compensated with Raman gain for different levels of the excess Raman gain (fiber length 50km).

5.4.2 Setup of the testbed

The experimental setup shown in Figure 5.4-4 is designed for evaluating the BER impact of counter-directional Raman amplification in individual cores of a trench-assisted MCF with seven cores and a length of 50 km. Crosstalk power measured at the output of the center core has been by 46.2 dB smaller than the equal power launched into each of the outer cores. The Raman gain is adjusted to either just compensate for insertion loss differences between the cores or for additionally balancing gain differences in the different cores of a subsequent EDFA with pump sharing used in a data communication link. The following investigations focus on ICXT accumulated in the center core, which experiences the largest ICXT.

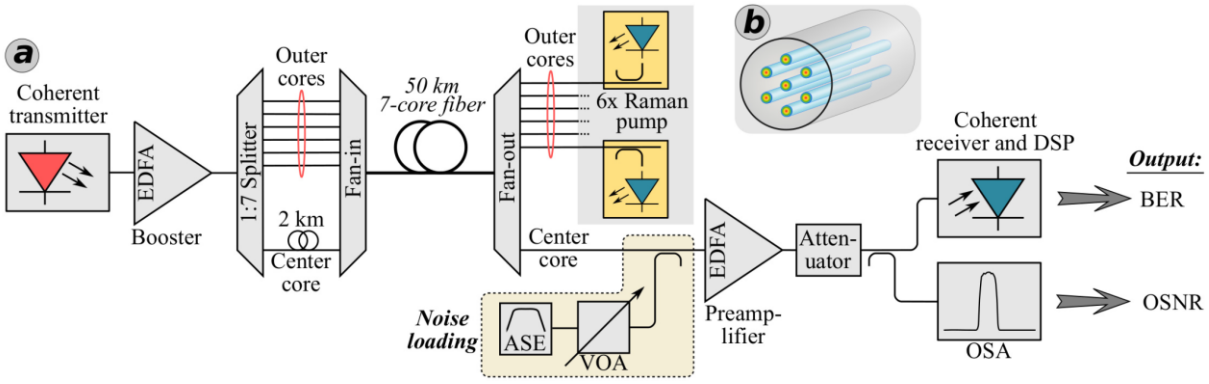

Figure 5.4-4: (a) Multi-core fiber loss and gain equalization testbed configuration, (b) 7-core fiber schematic

With the noise loading apparatus coupled to the output of the center core, the effect of ICXT on BER is demonstrated. Therefore, variable ASE power is added to the detected signal by means of an ASE source and a VOA. Before directing the output signal to the receiver and an OSA for measuring the actual OSNR, the power of the signal in the center core is increased by a

preamplifier. The following attenuator adjusts the receive power such that it is in the optimum range of the coherent receiver. After signal reconstruction with a commercial DSP, the pre-FEC BER is determined.

Different scenarios are characterized by determining BER versus OSNR. First, only the center core is connected to the fan-in device, such that no ICXT from other cores occurs. Next, the outer cores are connected to the fan-in device for revealing the impact of ICXT from all outer cores on the performance of the center core without inducing Raman gain. In a further step, the Raman pumps are switched on, and the gains are configured to compensate for loss differences of the cores, requiring an average Raman gain of 5.7 dB, with the individual Raman gains ranging from 4.4 dB to 7.0 dB in the different outer cores. In the last scenario, the Raman pumps are set to their maximum output power. In addition to the loss differences of the MCF, this scenario accounts for the gain differences of a subsequent in-line MC amplifier installed in a typical multi-core transmission link.

5.4.3 Experimental results and discussion

Measured BER values are depicted in Figure 5.4-5 versus OSNR for the four scenarios explained above. As expected, the lowest BER is obtained without ICXT and all OSNR penalties presented in the following refer to this reference case. Adding ICXT from the outer cores, the BER degrades significantly with an OSNR penalty of 1.7 dB for a BER 10^{-3} as illustrated in Figure 5.4-5 and of 0.4 dB for a BER of 10^{-2}. Activating counter-directional Raman amplification in the outer cores, the corresponding power levels at the fiber end increase in these cores, which is accompanied by an additional increase of ICXT in the center core and a further decrease of the SIR. This results in a BER increase with an additional OSNR penalty of 0.8 dB for the loss compensation case and 1.2 dB for the max. Raman gain case at a BER of 3×10^{-3}. For a BER of 10^{-2} close to the FEC threshold, this penalty amounts to 0.1 dB only. Thus, loss compensation increases the ICXT-induced OSNR penalty by around 30%, as illustrated in the inset showing the relative increase of ICXT penalty due to loss compensation versus BER. In a multi-span scenario, such small OSNR values will arise after several spans with ICXT accumulation and enhancement in several spans, such that the Raman-induced OSNR penalty becomes relevant. Dividing the BER values of the three curves with ICXT shown in Figure 5.4-6 by the respective BER values for the reference scenario at equal OSNR reveals that gain equalization by Raman amplification leads to a BER increase by 15 % at the highest OSNR of 24 dB.

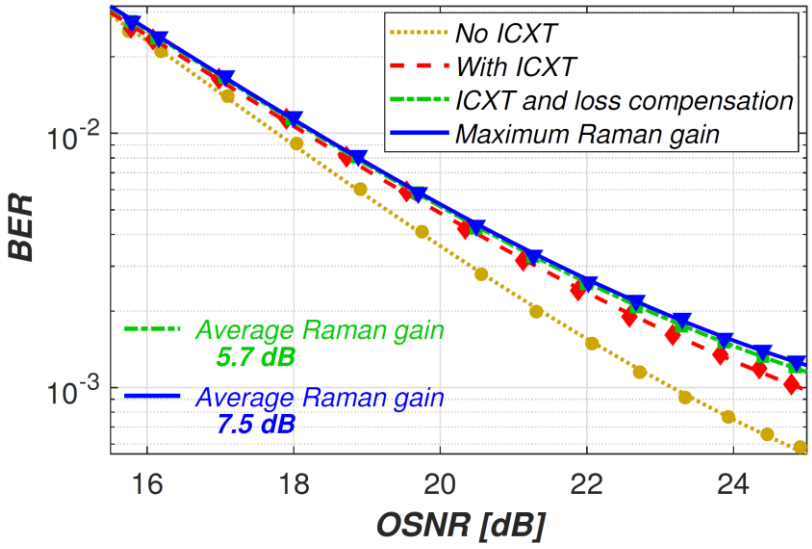

Figure 5.4-5: (a) Experimental results: BER versus OSNR for scenarios without ICXT, with ICXT and with~ICXT enhanced by different levels of Raman gain.

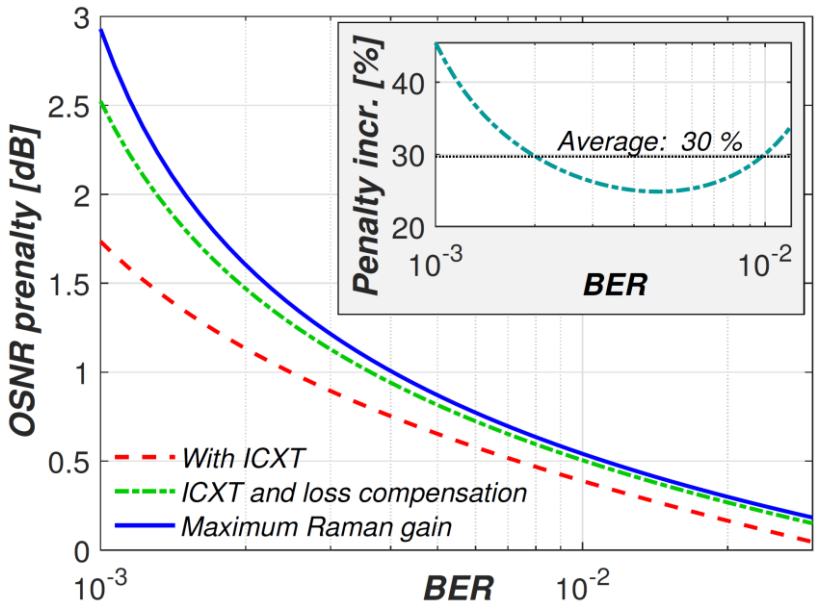

Figure 5.4-6: OSNR penalty versus BER for scenarios with XT and with XT enhanced by different levels of Raman gain (Reference for penalty: scenario without ICXT).

5.5 PLANNING PRACTICES FOR MBOSDM ULTRA-HIGH-CAPACITY NETWORKS

5.5.1 Introduction

Modern optical backbone networks face continually increasing demands driven by 5G, future 6G, large-scale cloud computing, and high-bandwidth applications such as artificial intelligence and global data center interconnects. As capacity requirements escalate, the traditional C-band spectrum is no longer sufficient. Recent advances have highlighted two complementary approaches to further increase the usable optical channel count and overall throughput: (i) spectral expansion into adjacent L- and S-bands (multi-band operation), and (ii) space division multiplexing (SDM), particularly using multi-core fibers (MCFs). The combination of these techniques—multi-band over space division multiplexing (MBoSDM)—has become a compelling architectural strategy for next-generation ultra-high-capacity networks.

However, planning practices for MBoSDM deployment are challenging due to the complex interplay of physical-layer impairments across bands and spatial dimensions. Telecom operators require robust methodology and quantitative insight into the opportunities and limitations of MBoSDM to inform migration strategies, investment, and the choice of network element technologies such as amplifiers, multiplexers, and programmable transceivers. Importantly, performance depends not only on fiber length and modulation format but also on spectral location and inter-core interactions, necessitating frequency- and core-aware design optimization.

In the context of SEASON, we developed a novel physical-layer-aware planning methodology and dynamic simulation framework to easily compare C, C+L, C+S, and C+L+S spectrum expansion strategies. We conclude that the C+L+S-band scenario provides the highest absolute throughput (up to 175% greater than C-band) and the lowest bandwidth blocking probability (BBP) under dynamic load.

5.5.2 Simulation framework and scenario

To thoroughly assess MBoSDM performance, this study establishes a detailed physical-layer-aware simulation environment. Four representative spectrum expansion scenarios are evaluated:

- C-band: 80 channels over 6 THz
- C+L-band: 160 channels over 12 THz
- C+S-band: 188 channels over 14 THz
- C+L+S-band: 268 channels over 20 THz

All scenarios employ a channel grid of 75 GHz spacing with a symbol rate of 64 GBaud, supporting adaptive modulation formats from PM-BPSK to PM-64QAM (100–600 Gbps per channel,

dependent on the GSNR achieved). The analysis is applied to a realistic long-haul topology modelled on the US backbone network, comprising 60 nodes interconnected by links with detailed band-specific fiber parameters—including frequency-dependent attenuation, chromatic dispersion, effective area, nonlinear coefficients, Raman gain spectrum, amplifier gain profile, and noise figures.

5.5.3 Physical layer impairments and performance modeling

A core contribution of this work is the advanced modeling of linear and nonlinear impairments endemic to wideband and SDM-enabled propagation. Key impairments included are:

- **Amplified Spontaneous Emission (ASE) noise:** Arising from cascaded optical amplifiers, it accumulates along the path and degrades signal quality.
- **Nonlinear Interference (NLI):** Stemming from Kerr effect nonlinearities, especially under high power, and modeled using a semi-closed form enhanced generalized Gaussian noise (EGN) model to accurately capture wideband system dynamics and the effect of inter-channel stimulated Raman scattering (ISRS).
- **Inter-core Crosstalk (ICXT):** This crosstalk, particularly prominent in strongly- or weakly-coupled MCFs, depends on core pitch, trench-assisted design, and operating frequency, and is modeled using a frequency-dependent formulation validated in previous work.
- **Transceiver noise and filter/aging penalties:** Additional degradation sources from hardware characteristics.

The aggregate quality of transmission (QoT) for any given lightpath is evaluated using the generalized signal-to-noise ratio (GSNR) metric, which quantifies the effective SNR combining all impairment contributions. This is mathematically defined as:

$$GSNR_{LP}|_{dB} = 10\log_{10}([SNR_{ASE}^{-1} + SNR_{NLI}^{-1} + SNR_{ICXT}^{-1} + SNR_{TRx}^{-1}]^{-1}) - \sigma_{Flt}|_{dB} - \sigma_{Ag}|_{dB} \quad \text{Eq. 1}$$

Where each SNR term represents the contribution of a distinct physical impairment; the filtering and system aging penalties ($\sigma_{Flt}, \sigma_{Ag}$) are also included for realism.

The key performance indicators (KPIs) targeted in this planning study are:

- Network throughput: The cumulative traffic successfully transmitted across all source-destination pairs, considering all core-to-core connection permutations.
- Spectral efficiency: Gauged as total supported bit rate per unit frequency, often normalized by the utilized spectrum.
- Bandwidth Blocking Probability (BBP): The fraction of total requested bandwidth that is blocked due to unavailability of free spectral slots, insufficient cores, or modulation format reach limitations.

For throughput and BBP calculations, the following methodology is used:

- Paths: For the 91 possible datacenter-to-datacenter (core) pairs, the three shortest paths are considered, reflecting realistic routing choices.
- Traffic modeling: Connection requests arrive according to exponential inter-arrival and holding time distributions, simulating dynamic service provisioning.
- Demand distribution: Requested traffic is uniformly distributed between 100–600 Gbps, in 100 Gbps increments.
- Simulation runs: For statistical reliability, each simulation comprises 150,000 requests (for the four-core configuration) and continues until either a 95% confidence interval is reached, or 50 simulation seeds are completed.
- Blocking calculation: BBP is determined as the total blocked bandwidth divided by the total requested bandwidth during the simulation—capturing the fundamental limits imposed by spectral, spatial, and modulation availability.

The scenarios reflect a hierarchical optical network architecture, where only the 14 principal datacenter nodes feature full add/drop capability, and the remaining nodes operate in transit mode without such functionality. This distinction is significant in evaluating routing and provisioning limitations encountered in real deployments.

5.5.4 Results and discussion

Figure 5.5-1 depicts the distribution of modulation format level (MFL) for all core-to-core connections, segmented by spectrum band. This enables network architects to visually correlate spectral position with modulation reach, informing placement strategies for high-priority or high-throughput connections. Figure 5.5-1 compares total network capacity and average blocking probability as a function of scenario, spectrum allocation, and offered load, quantifying the real-world consequences of spectrum expansion.

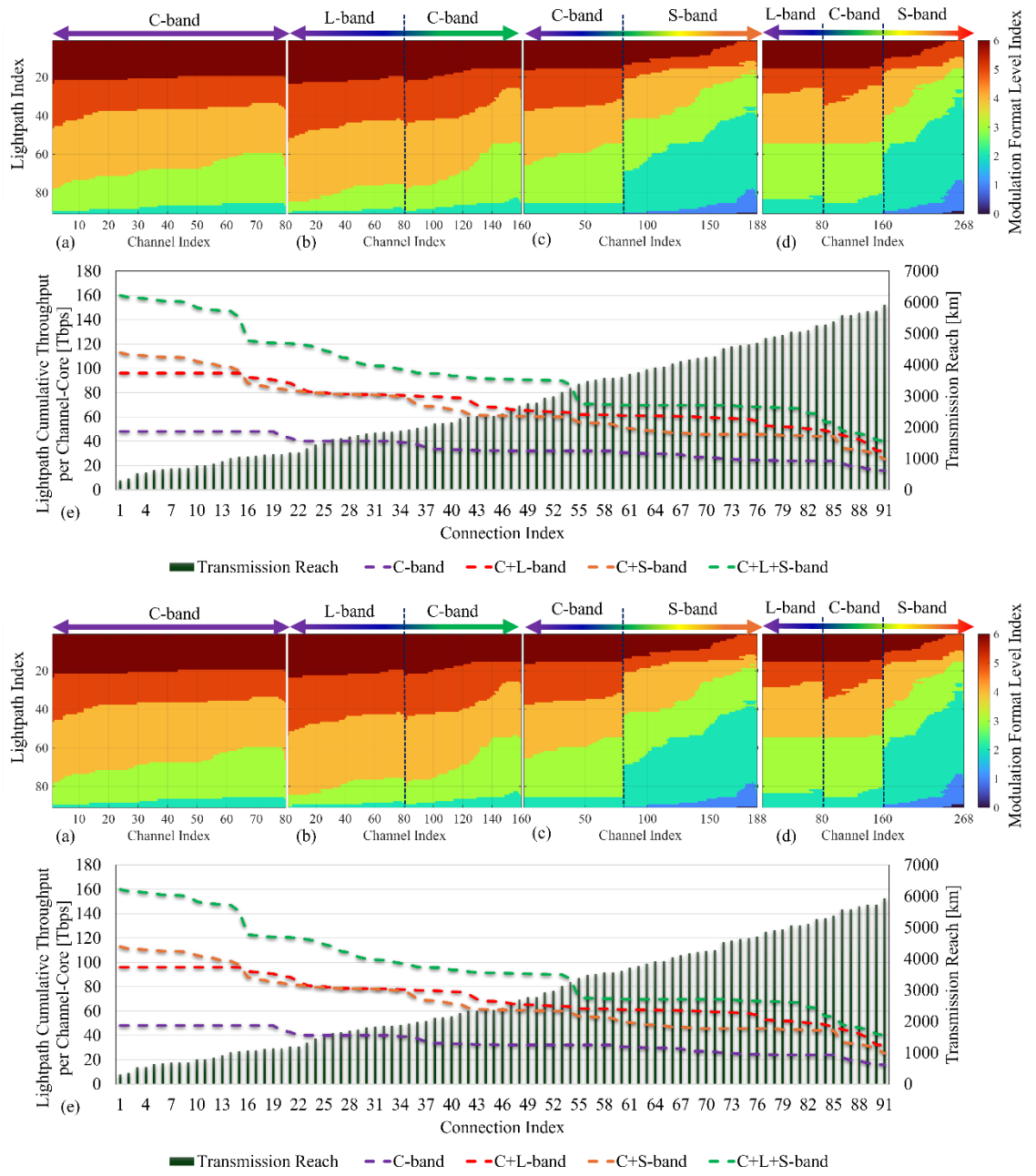

Figure 5.5-1: (Top) Modulation format level distributions per channel for each MBoSDM configuration across 91 connections. (Bottom) Cumulative bit rate distribution per connection index and the corresponding transmission distance.

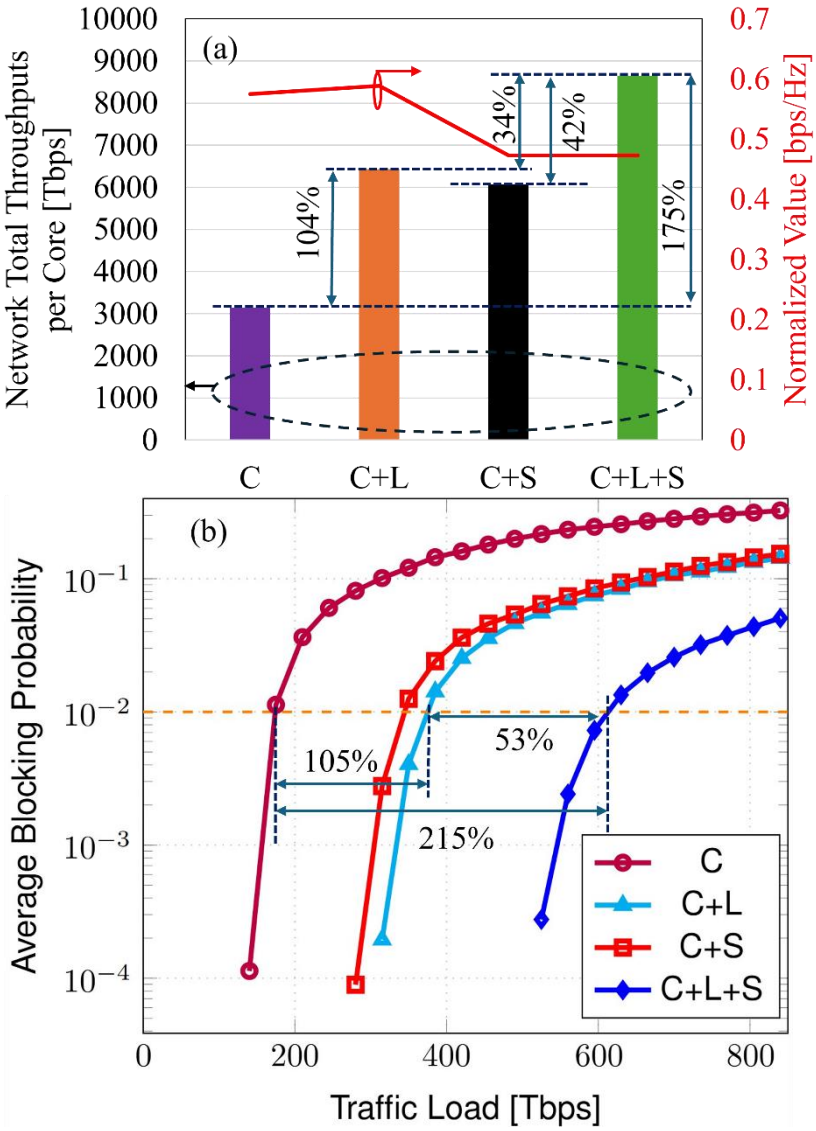

Figure 5.5-2: Network total throughput for diffident MBoSDM scenarios, (b)BBP of different solutions in L+C+S muti-band network under different traffic loads.

A central insight from the simulations concerns the distribution of modulation formats across channel index, band, and lightpath length:

- C-band and C+L-band: The modulation format profiles are relatively stable, with many core-to-core connections sustaining higher-order modulation (e.g., PM-16QAM to PM-64QAM), thanks to low loss and high-quality optical amplifiers in these bands.
- S-band (in C+S and C+L+S scenarios): Higher attenuation and increased Raman-induced power tilt result in a more pronounced degradation of signal quality, leading to the adoption of lower-modulation formats and a sharply reduced reach for high-order modulations.
- C+L+S-band: While this scenario enables the largest spectrum (20 THz, 268 channels), the GSNR distribution is the most heterogeneous. ISRS effects and inter-band power imbalances create substantial variation, with throughput gains concentrated on short

and medium-length connections (< 1000 km), as shown by the cumulative bit rate and distance distribution per channel.

The figure of merit for each spectrum expansion scenario is their total supported throughput under dynamic service request load, as well as the probability of bandwidth blocking under full-load conditions:

- C+L+S-band: Delivers up to 175% higher throughput than the C-band, 34% higher than C+L-band, and 42% more than C+S-band, validating its capacity gains for both datacenter and core backbone applications.
- Comparative performance: Although the C+S-band scenario presents more channels than C+L (188 vs 160), attenuation in the S-band and ISRS effects result in lower throughput for long-haul links; however, for sub-1000 km paths, S-band resources perform well.
- Blocking scenarios: As traffic and distance increase, especially beyond 3000 km, C+L+S experiences a sharper cumulative throughput drop due to amplified ISRS effects. Nevertheless, it shows the lowest average BBP due to expanded spectral space, outperforming both C+L and C+S under high-load regimes.

The normalized capacity per Hz, as shown on the right axis of Figure 5.5-2 (top), supports a nuanced interpretation. While the C+L+S approach offers maximum absolute throughput and minimum blocking, the C+L-band scenario provides the highest bit rate efficiency per unit bandwidth—an important consideration for operators prioritizing spectral resource utilization over raw capacity expansion.

Impact of Physical Layer Effects: The study shows that while inter-core crosstalk (ICXT) increases in the L-band (and can be a dominant factor in some SDM system configurations), for the evaluated trench-assisted weakly-coupled four-core MCF with state-of-the-art design, ICXT is not the limiting factor in wideband operation. Instead, performance is predominantly constrained by the loss coefficient, ISRS, and the amplifier noise profile. This is a significant planning insight, guiding both the selection of fiber type for multi-band use and the prioritization of amplifier and Raman gain flatness engineering over further ICXT suppression at moderate core counts.

Network Planning and Operator Guidelines: Trade-Offs and Recommendations

- Migration Path: Operators with substantial deployed C-band infrastructure may consider incremental migration to C+L-band as a risk-mitigated strategy for near-term expansion—that option already benefits from commercial deployment and robust component maturity.
- Maximum Capacity: For scenarios demanding the lowest blocking and highest overall throughput, full C+L+S deployment is favored, recognizing that additional system complexity (notably around ISRS management, component compatibility, and control plane algorithms) is also incurred.

- Short-Haul Versus Long-Haul: While spectrum expansion to S-band is beneficial for short to intermediate ranges, its use for long-haul paths is less advantageous without parallel advancements in amplification and power tilt correction.
- Efficiency Focus: Where operators prioritize maximal spectral efficiency instead of brute capacity, C+L systems appear optimal, based on normalized bit rate per Hz analysis.

The simulation workflow ensures statistically significant, reliable results through thousands of connection requests, multi-seed evaluation, and strict convergence criteria (95% confidence intervals). This methodology not only supports internal planning decisions but provides a foundation for vendor specification, standardization contributions, and regulatory submissions.

In conclusion, this study delivers a comprehensive, physical-layer-informed evaluation of best planning practices for MBoSDM networks, combining spectral (C, L, S) and spatial (four-core MCF) design options within a realistic US-backbone topology. The findings highlight that C+L+S-band expansion achieves the highest total capacity and the lowest bandwidth blocking probability, positioning it as the preferred configuration for future-proof, high-growth, core and inter-datacenter transport. It further shows that efficiency and implementation practicality favor C+L for near-term deployments, with solid performance and mature commercial support. For each scenario, physical-layer impairments must be carefully considered, with ISRS and amplifier noise presenting more significant constraints than ICXT within the studied operational regime. Finally, planning must explicitly account for the interplay between network topology, add/drop architecture, spectral properties, and core-specific impairment handling.

This study was invited for a presentation at ECOC 2025, under the title "Best Planning Practices for Ultra-High-Capacity Networks based on Multi-Band over Space Division Multiplexing", and has been further invited for a special issue at JOCN.

5.6 End-to-end latency model for IPoWDM with coherent pluggables beyond 400 Gb/s (related to C3.8, C3.10, C3.11)

Recent advancements in coherent optical technology, particularly the development of pluggable coherent transceivers operating at 400 Gb/s and above, present an opportunity to transform network architectures and improve multiple performance characteristics across various dimensions (cost, simplicity, bandwidth and latency) [Cug20]. In fact, new standards like OpenZR+ Multi-Service Agreement (MSA) have accelerated the adoption of coherent technology by producing standardized specifications for coherent pluggable transceivers operating at 400G, 800G and above, offering low cost and energy efficiency [Cug20-2, Dic24]. These transceivers can be directly integrated into high-density routers and switches, eliminating the need for separate transponder shelves and leading to simplified network nodes and architectures, and potentially enabling flatter architectures with more deterministic latency properties [Gio23, Han24].

In parallel with these technological advancements, there is increasing research interest in deterministic networks that can provide guaranteed performance characteristics. However, the

impact of high-capacity coherent transceivers on network determinism remains relatively unexplored, from a queuing theory point of view. Indeed, high-capacity transceivers dramatically reduce variable latency and jitter allowing for nearly deterministic network behaviour and performance.

We developed in SEASON, a new a simulation framework for E2E network latency in IPoWDM architectures using high-speed coherent pluggables (≥ 400 Gb/s). We demonstrated that high data rates make variable latency components (queuing/transmission) negligible, enabling near-deterministic network performance without complex scheduling.

5.6.1 Coherent pluggable transceivers evolution

The first generation of coherent optical systems emerged in the late 2000s, primarily targeting long-haul and submarine applications requiring maximum distance and capacity. These systems were complex, power-hungry, and expensive, making them suitable only for the most demanding core network applications. Over the subsequent decade, coherent technology has undergone continuous advancement, with successive generations delivering higher capacity, smaller form factors, lower power consumption, and reduced costs. In 2020, the creation of the OpenZR+ Multi-Service Agreement (MSA) aimed to produce standardized specifications for 400G coherent pluggable transceivers initially targeting Data-Center Interconnect (DCI) applications. This initiative has proven successful, with numerous manufacturers now producing interoperable 400G transceivers that meet the technical requirements while offering low cost and energy efficiency.

These 400G coherent pluggable transceivers, available in formats such as QSFP-DD and OSFP, can achieve data rates of 400 Gb/s over distances up to 120 km using Dual-Polarization 16-ary Quadrature Amplitude Modulation (DP-16QAM) at a symbol rate of 69 Gigabaud. More advanced variants like 400G ZR+ offer additional flexibility, supporting multiple modulation formats (DP-16QAM, DP-8QAM, and DP-QPSK) and enabling transmission over distances up to 500 km with amplification. The roadmap for coherent pluggables continues to evolve rapidly. In March 2025, Coherent Corp. announced general availability of their 800G coherent QSFP-DD transceiver, leveraging advanced IC-TROSA optical engine on proprietary Indium Phosphide (InP) chip technology. The industry is also preparing for the release of 1.6T (as 8×200G) and even 3.2T (as 16×200G) transceivers with similar features concerning reach, cost, energy efficiency, and programmability.

The emergence of such high-speed coherent pluggable transceivers enables new architectural approaches based on IPoWDM (IP over Wavelength Division Multiplexing) architectures where grey interfaces and the Flex-switchponder are replaced by disaggregated low-cost packet-optical boxes equipped with energy-efficient 400G ZR/ZR+ transceivers. The most disruptive approach involves removing ROADMs entirely, with packet-optical boxes connected exclusively with point-to-point coherent pluggables. This approach significantly simplifies the Optical Line System, leading to architectures that are easier to control, operate, and manage.

5.6.2 Latency analysis of IPoWDM architectures build with coherent pluggables

Network latency in optical networks consists of several components: propagation delay, transmission delay, processing delay, and queuing delay. Understanding these components is crucial for analysing the overall network performance and determinism.

Propagation delay refers to the time taken for light to travel through fiber, approximately 5µs per km in standard silica fibers (or 3.33 µs per km in hollow-core fibers). This delay component is fixed and directly proportional to the physical distance traversed.

Transmission delay is the time required to serialize a packet onto the physical medium, calculated as the packet size divided by the link capacity. For example, a 400G NIC needs approximately 30 ns to insert a 1518-byte Ethernet frame into the physical media. This latency is reduced to 15 ns at 800G, 7.6 ns at 1.6T, and just 3.8ns at 3.2T.

Processing delay occurs within network equipment and includes tasks such as Forward Error Correction (FEC) processing. For 400G coherent transceivers, FEC processing typically introduces few microseconds (1-5µs) of delay per hop. Different FEC implementations can affect both performance and latency. For instance, a concatenated RS(544,514) + BCH(126,110) FEC offers approximately 10.3dB net coding gain for 16QAM signals with a latency of about 52 ASIC clock cycles.

Finally, queuing delay is the time that packets spend waiting in buffer queues before transmission, which varies depending on network load and traffic patterns [Ala21]. This is the only variable component in the latency budget and has traditionally been the main source of latency uncertainty in networks [Bha08].

Deterministic network dimensioning aims at providing predictable and guaranteed performance characteristics, particularly in terms of latency and jitter (delay variation), if possible, with upper bounds for a large majority of packets. Such networks are essential for time-sensitive applications that require precise timing and predictable performance. As shown next, the emergence of high-capacity coherent pluggable transceivers creates new possibilities for network determinism, since at speeds of 400 Gb/s and above, queuing and transmission delays—traditionally variable components of network latency—become negligible compared to fixed components like propagation and processing delays. This fundamental shift potentially transforms the nature of network performance from probabilistic to deterministic without requiring complex schedulers or synchronization mechanisms.

5.6.3 Methodology and simulation framework

The following network scenarios aim at simulating the total latency (both fixed and variable) of different network topologies with IPoWDM architecture, that is, assuming packet-optical switches with 400G and above coherent pluggables. This architecture does not have intermediate ROADMs, and all packets have to travel hop-by-hop suffering O/E/O conversion at

each intermediate node. This has a benefit of inherent regeneration (i.e., for links below 60-80 Km no optical amplification is needed) and reduces the network complexity of multi-layer designs of IP over ROADM architectures.

In terms of latency, such IPoWDM architectures suffers from O/E/O conversion and latency additions including processing and queuing but as observed next, this is negligible at multi-Gigabit/s speeds.

Concerning fixed delay components, classical 5 μs per kilometer of silica fibers is assumed for propagation, and 4μs per hop for FEC processing in 400G coherent transceivers. Regarding transmission and queuing delays, we apply the general Kingman's equation for G/G/1 queues (see Eq. 1), which approximates the average waiting time in a queue with general arrival and service time distributions and is accurate as the network load ρ approaches 80% and above:

$$E(W_q)_{\frac{G}{G}} \approx E(X) \times \frac{\rho}{1-\rho} \times \frac{C_A^2+C_X^2}{2} \qquad \text{Eq. 1}$$
$$1$$

where $E(W_q)$ is the average waiting time in queue, $E(X)$ is the average packet service time, ρ is the link load, and C_A^2 and C_X^2 are the coefficients of variation of packet inter-arrival times and packet service times, respectively [Bha08, Kin61].

By analyzing these latency components across different transmission capacities, we can determine their relative contributions to the overall latency budget and assess how the latency characteristics of networks evolve as capacity increases.

For the simulation scenarios three different Metropolitan Area Network (MAN) topologies are considered (shown in Figure 5.6-1):

1. Tokyo MAN: A network with 24 nodes representing a medium-sized metropolitan area.
2. Milano MAN: A larger network with 53 nodes covering an extensive urban area.
3. MAN157: A large-scale topology consisting of 157 nodes and 166 links, representing complex urban network scenarios.

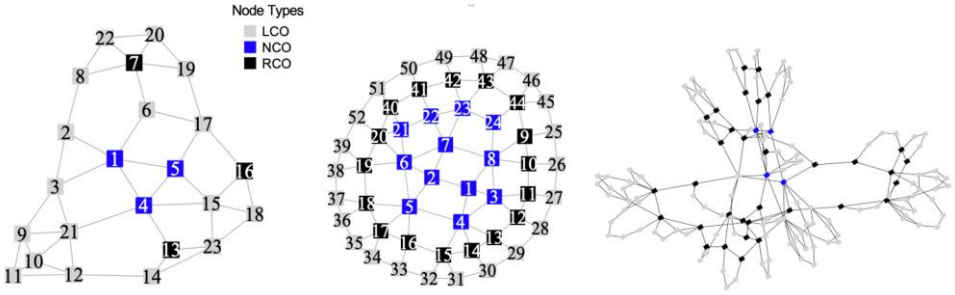

Figure 5.6-1: MAN, topologies used in evaluation: Tokyo (left), Milano (center), MAN157 (right).

Dissemination Level	Public

These networks include different types of nodes, including both Access (Grey), Metro-Access (Black), and Metro-Core (Blue) nodes simulating the classical hierarchical network architecture that most telcos follow in the design of their MANs for medium-size and large cities.

For traffic modelling, we adopted a realistic approach based on empirical observations. Traffic loads were adjusted to represent different operational scenarios: 30% for Access, 50% for Metro-Access, and 40% for Metro-Core nodes. These configurations simulate varying levels of network stress across each MAN topology.

The packet size distribution follows the empirical distribution observed at AMS-IX (Amsterdam Internet Exchange), with an average packet size of 1019 bytes and a standard deviation of 1162 bytes, resulting in a coefficient of variation of C_X^2=1.3 for service times. This distribution reflects real-world Internet traffic patterns more accurately than simplified models.

To implement our analysis, we developed a comprehensive simulation environment using the R programming language, integrating advanced open-source libraries such as igraph and simmer to model network topologies, simulate traffic flows, and analyze queuing delays. The igraph library is used to define the network topologies, including the three-MAN layouts described above. The Discrete Event Simulation (DES) library simmer enables the generation of individual packets, routing them through defined paths, and collecting delay statistics at each hop. Our simulation framework accounts for transmission, queuing, and processing FEC delays, allowing for a comprehensive evaluation of packet latency. The simulation focuses on five distinct capacities: 400G, 800G, 1.2T, 1.6T, and 3.2T, providing insights into how increasing transmission rates affect network performance.

For each simulation scenario, we collect detailed statistics on the different latency components and their contributions to the overall end-to-end delay. This includes average values, percentiles (particularly the 99th percentile for assessing worst-case performance), and statistical distributions. The simulations run for a sufficient duration to capture steady-state behavior, with multiple independent runs to ensure statistical significance. This approach allows us to analyze how increasing transmission capacities affect network performance, particularly in terms of latency determinism, across realistic network topologies and traffic conditions. The open-source nature of our simulation framework also promotes reproducibility and extensibility for future research.

5.6.4 Results

Table 5.6-1 overviews the average latency results obtained on each topology for multiple bitrates. The table shows both the queuing latency only and the total latency that includes all latency components, that is, queuing, transmission, propagation and processing. As shown, the queueing latency component is ridiculously small compared to the total latency, especially at high speeds (800G and above) and for large-size network diameters (like MAN157 whose end-to-end paths are between 10 and 20 Km).

Table 5.6-1: Average latency between Access CO and National CO for different topologies and packet-optical switches with high-speed coherent pluggables.

Tokio Topology					
Bitrate	400G	800G	1.2T	1.6T	3.2T
Queuing latency	0.27 μs	0.13 μs	0.09 μs	0.07 μs	0.03 μs
Total latency	12.62 μs	12.48 μs	12.44 μs	12.42 μs	12.38 μs
Milano Topology					
Bitrate	400G	800G	1.2T	1.6T	3.2T
Queuing latency	0.27 μs	0.13 μs	0.09 μs	0.07 μs	0.03 μs
Total latency	5.27 μs	5.15 μs	5.12 μs	5.10 μs	5.07 μs
MAN157 Topology					
Bitrate	400G	800G	1.2T	1.6T	3.2T
Queuing latency	0.32 μs	0.16 μs	0.11 μs	0.08 μs	0.04 μs
Total latency	76.51 μs	76.35 μs	76.30 μs	76.28 μs	76.24 μs

Thus, the contribution of queuing delay to total latency is almost negligible in all cases. Not only the average latency is negligible, but also the 99th delay percentile, as shown in Figure 5.6-2. This figure compares the average total latency (in red) with the worst-case latency (in blue) calculated as the upper Chebychev bound. As shown, the variable latency contribution due to queueing is negligible, since the majority of latency is due to propagation and FEC processing.

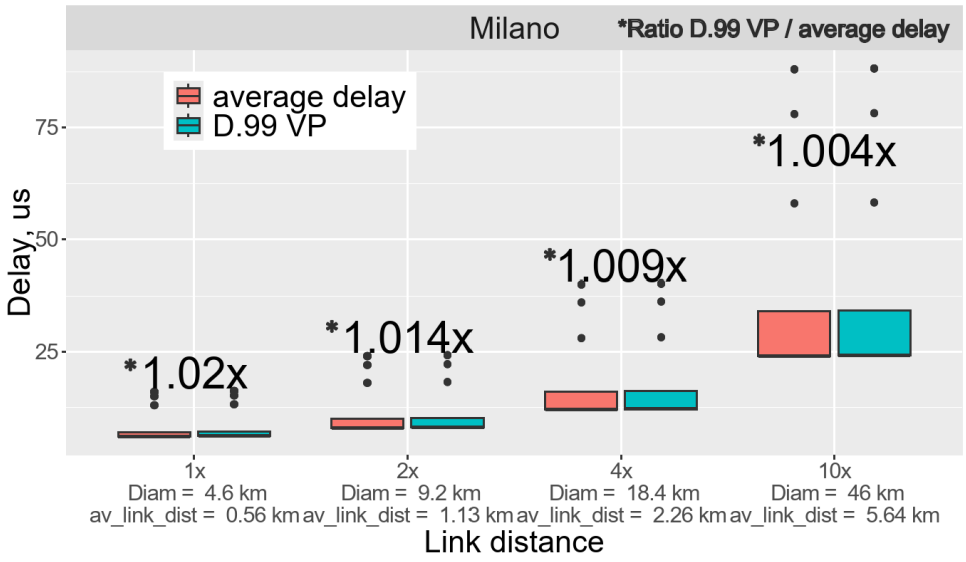

Figure 5.6-2: Comparison between average end-to-end latency and worst-case end-to-end latency for Milano topology.

5.7 SEASON FRAMEWORK FOR METRO-ACCESS FLEXIBLE INTEGRATION (RELATED TO C3.9, C3.10, C3.11)

5.7.1 Motivation and architecture

The flexible central office architecture proposed in the following subsection responds to one of the most relevant goals of SEASON project, namely the implementation of an integrated metro access network segment, able to fulfil the challenges that network operators are facing due to traffic that is continuously growing in terms of volumes and dynamicity.

Moreover, this goal is pursued also taking into account the need to minimize the cost of the physical infrastructure, by relying on high capacity longer reach working technologies (coherent DWDM transceivers) that allow the reduction of the number of central offices, and by introducing an element of flexibility in the architecture (a spatial optical matrix) that enables the implementation of a pay-as-you-grow mechanism, almost hitless in terms of disturbance of the already existing services.

The presence of the spatial optical matrix, in this innovative node architecture, enables to implement a Spatial Division Multiplexing paradigm (SDM), that presently relies on the usage of parallel fibers, but in future could also be applied to multicore fibers (MCF).

Furthermore, the proposed solution enables the on-demand adding of capabilities needed for reconfigurable and automated new services: indeed, the spatial matrix not only allows fiber switching, but introduces a new degree of flexibility thanks to on-demand amplification functions towards the access and adaptation between single and double fiber systems for point-to-point and point to multi-point services. The introduced automation reduces human intervention, with a significant improvement in the time it takes to deliver a service that involves both the access branch and the optical transport branch. All this using an optical matrix that enables flexibility with very low additional energy expenditure.

This flexibility element responds to the important requirement of keeping at minimum the power consumption of the node, also allowing to keep turned off some of the active elements of the node, and turn them on when needed, following the dynamicity of the traffic demand.

The fulfilment of these objectives requires to efficiently exploit innovative technologies that are progressively becoming available, as evolution of consolidated transmission technologies typical of the access and of the metro network segments, and to enable their coexistence in a converged and integrated metro-access infrastructure, optimizing the usage of the fibers available in the field.

More in detail, this solution proposed in SEASON define the Flexible Central Office (FCO) framework, and it enables true converged metro-access using DSCM P2MP coherent transceivers. It is based on the usage over the same fiber infrastructure of passive optical networks (PON) access transmission technology and coherent digital subcarrier multiplexing (DSCM) point to multipoint metro technology (also known as XR technology). Furthermore, this

enables coexistence and transparent transport of legacy PON and high-end Metro services over a single shared fiber, minimizing electronic conversions and maximizing flexibility.

The bidirectional transmission of DSCM channels over traditional single fiber point to multipoint Optical Distribution Network (ODN), typical of the access network segment, is enabled by the adoption of fiber optical circulators, while their coexistence with PON signals over the same optical fibers is made possible by the introduction of ad-hoc band filters named CoeXistence Elements (CEX); amplification is added when needed.

A detailed description of the node architecture is reported in the following subsection.

5.7.2 Flexible central office

This paragraph describes the architecture proposal to enable flexible provision of high end services, carried out by Coherent point to point transmission or by configurable XR subcarrier multiplexing point to multi-point transport system whose hub is located in the metro network, over the same traditional single fiber Access point to multipoint ODN (Optical Distribution Network).

This solution, thanks to the use of an optical matrix, allows to enable the provision of the high-end service by minimizing the impact on already active retail services without the need to know a priori on which ODN the need to offer this service will arise.

Figure 5.7-1 illustrates the basic scheme of the proposed architecture.

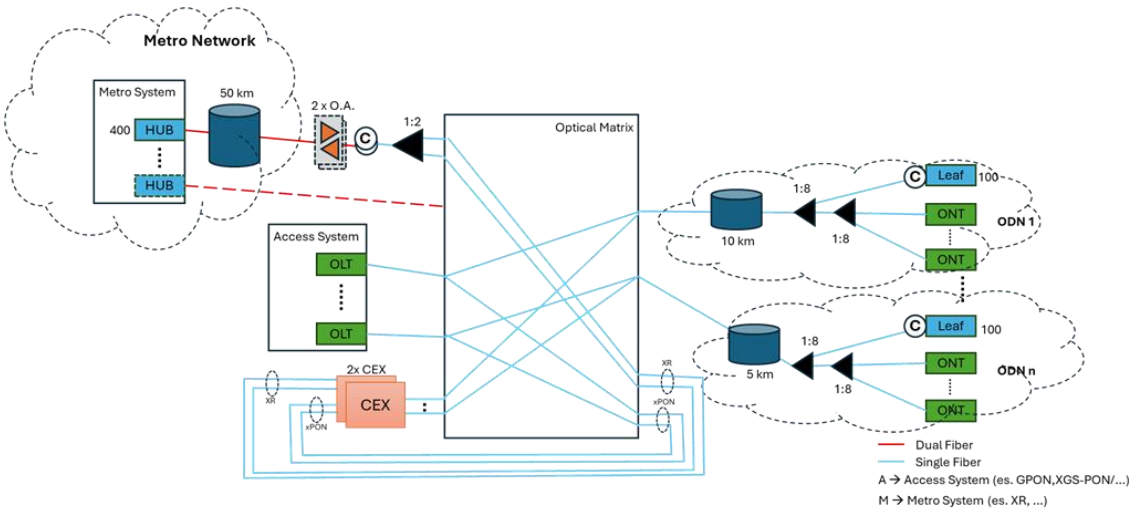

Figure 5.7-1: Flexible Central Office architecture scheme and operational principle.

As can be seen from the diagram in the figure, in addition to the optical matrix, the CEX (CoExisting Elements) have also been inserted into the reference architecture to allow the sharing of the same ODN between the traditional xPON systems and the XR systems operating in "single fiber mode" (for this purpose, the appropriate introduction of optical circulators is foreseen).

Furthermore, to comply with the power budget specifications of the XR systems, the use of optical amplifiers (Downstream/Upstream) is foreseen before the circulator both to recover the attenuation encountered in the metro network and to deal with the attenuation of the ODN network in the access network.

The operating principle of this architecture is that when a High End customer requests the service at one of the terminations of one of the ODNs underlying the optical exchange, that particular ODN is directed by means of the optical matrix towards one of the CEXs connected to the matrix so that the combined optical signal of the xPON system and the XR system are directed together towards the interested ODN.

This operation performed with the optical matrix, with an automatic and remote procedure, allows to minimize the effect of the interruption of the optical signal on the existing services, minimizing the disruption for xPON customers and reducing the OPEX of provisioning the requested high-end service, thanks to the remote configuration of the flexibility elements.

Not knowing a priori where the need may arise (on which ODN) to offer the High End service, another advantage of this architecture consists in the possibility of sharing the transmission capacity of a single multicarrier system (HUB) on different ODNs, optimizing their use with clear advantages both in terms of CAPEX (pay as you grow) and in terms of OPEX (minimizing the power consumption). This, together with the potential use of different wavelengths for Hubs in case of a strong customer demand, allows a significant safe of fibers in the primary segment of the access network.

A tradeoff design between the achieved flexibility in configuration and the number of optical matrix ports involved in the scenario is advisable according to the available link budget and the control model of the switching architecture.

5.8 Performance and Transient Resiliency Comparison of S- and E-band Upgrades of a C+L-band System (related to C3.2)

Multi-band transmission (MBT) has emerged as one promising solution to the ever-increasing demand for capacity in optical networks [Win18]. Among the potential candidates for MBT, the S-band is particularly promising because of its fiber characteristics being similar to those of the C- and L- bands. Several studies have demonstrated the benefits of incorporating the S-band into C+L systems to enhance capacity [Sem20, Ham19]. However, the expanded spectral footprint of an S+C+L-band system (exceeding 13 THz) intensifies stimulated Raman scattering (SRS)-induced power transfer between channels, posing significant challenges to service survivability and network management.

To address these issues, some researchers propose using the E-band instead of the S-band [Sam22]. By introducing a 14-THz guard band between the C+L and E bands, wavelength interdependence can be reduced, simplifying network operations. This approach, while forgoing

some spectral regions with the lowest fiber attenuation and limiting the use of Raman amplification in the C and L bands, offers potential advantages in operational stability and manageability [Sou25].

In SEASON, we use numerical simulations to explore the advantages of enhancing a C+L-band optical system by incorporating the E-band, instead of the S-band, or by implementing Raman amplification. Building upon the findings in [Sou25], we assess network performance with and without Raman amplification of C+L-, S+C+L- and E+C+L-band systems, offering new perspectives on optimizing spectral efficiency (SE) and improving the resilience of next-generation optical networks. This study is important because it provides operators with a solution based on critical real-world robustness data, and which moves beyond static capacity analysis to enable informed practical choice between kinds of ultra-wideband upgrades.

5.8.1 Simulation Setup

We assume each amplification band spans 6 THz (as shown in Table 5.8-1) and 120-GBd signals are transmitted within a 150-GHz spectral grid, resulting in 40 channels per band. We evaluate three MBT systems: C+L, S+C+L, and E+C+L. Each system can utilize up to 20 backward Raman pumps spaced by 1 THz. For the C+L-band system, Raman pumps are placed within the 199 THz to 218 THz range, while for the S+C+L-band system, they are placed between 205 THz and 224 THz. In the E+C+L-band system, all twenty Raman pumps are positioned between 219 THz and 238 THz, with none placed in the spectral gap between the C+L and E-bands to avoid E-band power depletion. This configuration follows the findings of [Sou25], which demonstrated that placing pumps in this intermediate region results in suboptimal system performance.

Table 5.8-1: Frequency bounds of each amplification band.

Band	Start Frequency [THz]	Stop Frequency [THz]
L	184.2	190.2
C	190.7	196.7
S	197.2	203.2
E	210.7	216.7

Optical fibers are characterized by a dispersion parameter of 16.7 ps/nm/km @ 1550 nm and a dispersion slope of 0.058 ps/nm^2/km. Additionally, the frequency-dependent loss and nonlinear coefficient of this fiber type are shown in Figure 5.8-1 and based on [Sou25-2]. We consider the normalized Raman gain profile of [Sou25-2] to calculate the SRS effect. Additionally, input and output connector losses of 0.25 dB and splice losses of 0.01 dB/km are assumed. After each fiber span, a band demultiplexer (with a 1 dB insertion loss) separates the transmitted bands and delivers them to the respective optical amplifier. We consider a band demultiplexer based on a band filter and assume its insertion loss will be slightly higher than current commercial C+L-band filters. The lumped optical amplifiers are modelled by a constant noise figure of [6, 6, 7, 7] dB for the L-, C-, S-, and E-bands for gain values higher than 20 dB. For gain values smaller than 14 dB, the amplifiers' NF is assumed to be 2 dB higher. The NF is linearly interpolated for gain values

ranging between 14 and 20 dB. Power losses are assumed to be perfectly compensated for in each fiber span (considering the impact of the SRS effect and the gain provided by the Raman amplifiers). Additional system parameters are transceiver OSNR of 38 dB, add/express OSNR of 38 dB/37 dB and a 0.05 dB GSNR penalty per in-line amplifier.

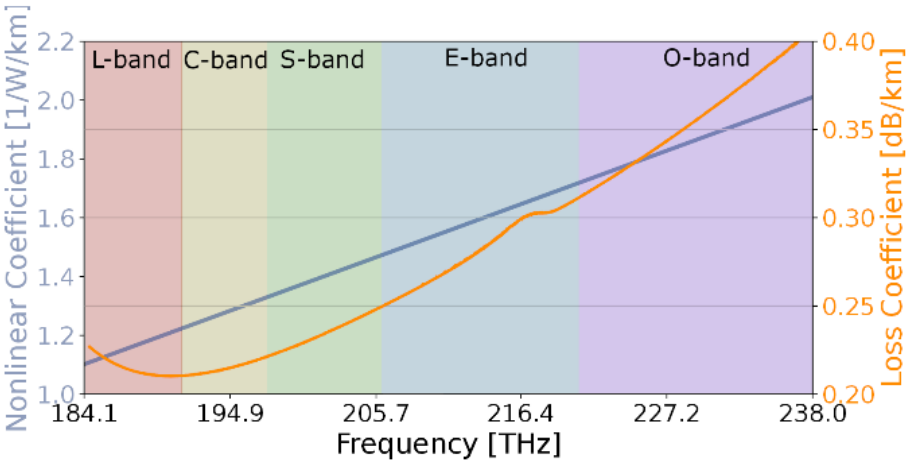

Figure 5.8-1: Frequency-dependent fiber loss and nonlinear coefficient.

5.8.2 Power Optimization

Effective optimization of launch power and Raman pump settings is essential for maximizing the performance, especially in MBT systems due to the frequency-dependent behavior of component characteristics and the impact of SRS. To assess transmission quality, we compute the Generalized Signal-to-Noise Ratio (GSNR) for each transmitted channel. The nonlinear interference component of the GSNR is estimated using the Generalized Gaussian Noise (GGN) model, as implemented in GNPy, which numerically solves the GGN integrals via the composite trapezoidal rule. SRS effects are evaluated by numerically solving the Raman equations (both algorithms are available in the open-source Python library GNPy [Cur22]).

We employ a multi-objective genetic algorithm to jointly optimize the launch power and design of the Raman amplifier [Sou25-2] in a single-span configuration ($L_S = 70$ km). The algorithm targets two simultaneous objectives: maximizing the ideal capacity of the single-span system and minimizing the total GSNR variation across bands. The ideal capacity is calculated as the sum of the capacities of all transmitted channels, where the capacity of channel i is given by $2\,R_S\,log_2(1 + GSNR_i)$, with R_S representing the symbol rate [Pog14].

5.8.3 Network Simulations

To estimate the network capacity of each transmission system, we perform simulations using the Spanish national reference network (Figure 5.8-2), as published by Telefónica in [IDEALIST-13]. For simplicity, all network spans are assumed to be 70 km in length.



Figure 5.8-2: Telefonica national reference network topology.

A basic sequential routing and wavelength assignment algorithm is employed. Traffic demands follow the pattern described in [IDEALIST-13], with payloads uniformly distributed between 200 and 800 Gbps. The algorithm first attempts to groom new connection requests into existing channels with the same source and destination, provided there is sufficient spare capacity. If grooming is not possible, the demand is routed along its shortest path, selecting the modulation format that minimizes the number of required lightpaths while remaining feasible. Among the available and optically feasible spectrum slots, the one with the smallest positive residual margin is chosen to reserve higher-quality slots for more demanding connections.

Five modulation formats are considered, ranging from 400 Gbps to 800 Gbps in 100 Gbps increments, based on [Sou25-2]. A modulation format is deemed feasible if its required SNR is below the GSNR. If no valid combination of route, modulation format, and spectrum slot is found, the connection is blocked, and the algorithm proceeds to the next request.

5.8.4 Results and Discussion

Figure 5.8-3 presents the non-dominated solutions computed by the optimization algorithm. When examining the capacity values for solutions with an average $\Delta\mathrm{GSNR}^{\mathrm{b}} = 0.5$ dB, the baseline C+L-band system is the least favorable in terms of total ideal capacity due to the smaller number of channels and the absence of Raman pumps.

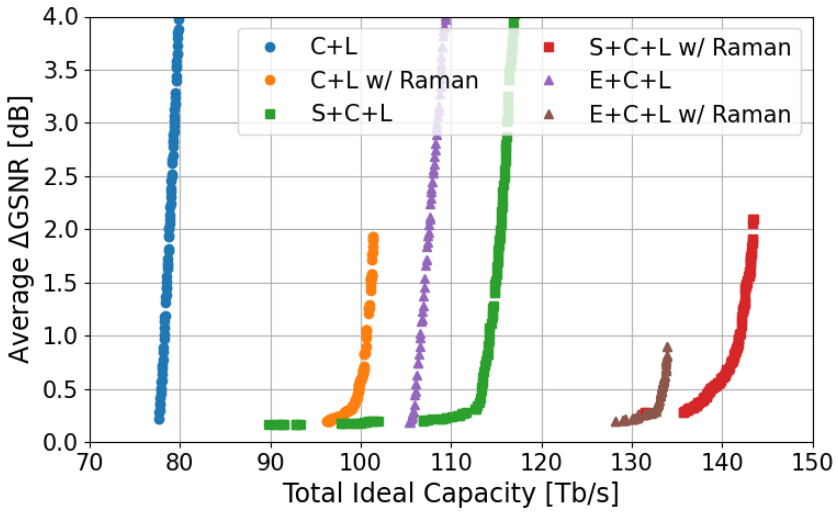

Figure 5.8-3: Final optimal non-dominated solutions for the various transmission systems obtained after the convergence of the multi-objective optimization algorithm.

We start by analyzing three upgrade options for the C+L-band system: incorporating Raman amplification, adding the S-band, and adding the E-band. Among these, the C+L-band system with Raman amplification yields the smallest capacity gain, offering a 29% increase over the baseline. The E+C+L-band configuration follows, achieving a 37% improvement. The highest capacity gain is observed with the S+C+L-band system (without Raman amplification), which delivers a 47% increase compared to the baseline.

Although Raman amplification is likely the most cost-effective upgrade, it yields the smallest capacity improvement. The E-band upgrade is generally less disruptive due to the 14-THz guard band between the C- and E-bands. Still, having a higher capacity than the C+L-band system with Raman amplification requires additional band filters at amplification stages and more interfaces, which increases overall cost. On the other hand, the S-band upgrade offers the highest capacity gain and may cost roughly the same as the E-band upgrade. However, it also expands the contiguous transmission bandwidth, which can complicate network management and exacerbate power transients in the event of link failures.

We then compare the optimized performance of systems incorporating Raman amplification. The S+C+L-band+Raman configuration delivers the highest total capacity, with a 39.5% increase over the C+L-band+Raman baseline whereas the E+C+L-band+Raman system offers a 32.8% capacity gain relative to the same reference. Notably, the capacity advantage of the S+C+L-band system over the E+C+L-band system is around 6% with or without Raman amplification.

Table 5.8-2 presents the average and standard variation of GSNR per band after a single 70-km span. These values serve as the basis for estimating the GSNR of each channel at the end of its lightpath. Figure 5.8-4 illustrates the average number of lightpaths operating at maximum data rate across all channels for each transmission scheme. Although the network contains 435 shortest paths (calculated as $\frac{N_n \cdot (N_n - 1)}{2}$, with N_n equal to the number of nodes of the network,

i.e., 30), the E+C+L-band system without Raman amplification cannot reach this number due to some channels being infeasible (insufficient GSNR).

Table 5.8-2: Per-band average and variation of the GSNR [in dB] for transmission in one 70-km span for the optimized solutions with $\Delta GSNR = 0.5$ dB.

	C+L	C+L w/ Raman	S+C+L	S+C+L w/ Raman	E+C+L	E+C+L w/ Raman
L	23.6 ± 0.6	32.5 ± 0.4	23.7 ± 1.0	28.8 ± 0.5	23.6 ± 0.6	28.2 ± 0.3
C	25.2 ± 0.5	30.4 ± 0.9	22.9 ± 0.2	30.7 ± 0.2	25.2 ± 0.5	27.4 ± 0.5
S	-	-	24.5 ± 0.4	27.7 ± 0.8	-	-
E	-	-	-	-	20.1 ± 0.3	28.2 ± 0.9

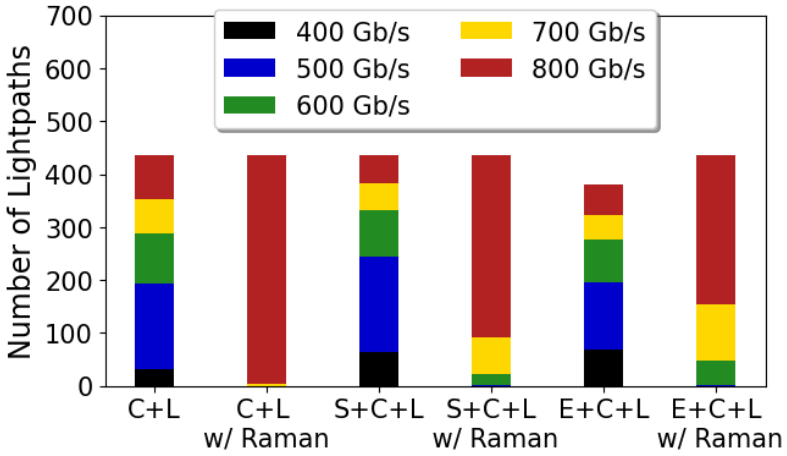

Figure 5.8-4: Number of lightpaths with a given maximum bitrate averaged over all transmission channels for different transmission systems for the optimized solutions with ΔGSNR=0.5 dB.

Among the evaluated systems, the C+L-band configuration (with and without Raman amplification) demonstrates the highest spectral efficiency. This is attributed to the higher number of lightpaths using higher bitrates. This result therefore confirms that using additional bands with less favorable fiber and amplifier characteristics negatively impacts the spectral efficiency.

Table 5.8-3 presents the network-wide average capacity for the Telefónica network [Clo16]. Compared to the single-span results, band upgrades without Raman amplification yield smaller capacity gains at the network level. For instance, adding the E-band increases average capacity by only 25% over the baseline (significantly less than the 37% gain observed in the single-span ideal capacity). In contrast, the S-band upgrade results in a 42% increase in network-wide average capacity.

Interestingly, enhancing the C+L-band system with Raman amplification leads to a 33% capacity improvement (higher than that achieved by adding the E-band without Raman). This outcome highlights the reduction in spectral efficiency resulting from integrating the S- or E-band into the C+L-band system. As a result, while additional bands increase the number of available channels,

their benefit diminishes over longer paths (i.e., multiple-span links), where spectral efficiency plays a more critical role.

Table 5.8-3: Network-wide average system capacity for the different transmission systems.

System	C+L	C+L w/ Raman	S+C+L	S+C+L w/ Raman	E+C+L	E+C+L w/ Raman
Capacity [Tb/s]	48	64	68	93	60	90

5.8.5 Conclusions

This section evaluated upgrade strategies for enhancing the capacity of C+L-band optical transmission systems, including the addition of Raman amplification, and the extension to the S-band or E-band. Comparative analysis with multi-band configurations incorporating Raman amplification (specifically S+C+L and E+C+L systems) revealed that Raman amplification plays a vital role in maintaining high spectral efficiency, particularly in large-scale network deployments. While the E+C+L-band system offers operational simplicity due to the guard band between the E- and C+L-bands, it achieves slightly lower total capacity than the S+C+L-band system. These findings highlight the trade-offs between capacity, spectral efficiency, and operational complexity when selecting an upgrade path for future optical networks.

These results are closely related to the KPIs 2.1 and 3.1 by helping to further understand the challenges and trade-offs involved in ultra-wideband transmission.

5.9 Simulation and Modeling of C+L+S Multiband Optical Transmission for SEASON OCATA Time Domain Digital Twin (related to C3.2)

5.9.1 Overview

This work focuses on modelling and simulation techniques for MB optical transmission to support the OCATA time-domain DT [Kha25]. The motivation stems from the increasing use of S, C, and L bands to meet the capacity needs of beyond-5G and 6G transport networks [Cis20, Rui23, Sou24, Cas25]. While MB operation significantly enlarges available spectrum, it also amplifies physical-layer complexity. Inter-channel stimulated Raman scattering (ISRS) introduces wavelength-dependent power transfer and modifies nonlinear interference across more than 14-15 THz of optical bandwidth [Sou23, Las23]. Accurately capturing these wideband effects is essential for predicting QoT and for enabling digital-twin-driven automation in modern optical networks [Cur22, Liu23, Yan24, Gha24].

The system that we considered consists of 337 channels, each spaced by 50 GHz and modulated at 32 GBd using 16 quadrature amplitude modulation (16QAM), and spanning the S, C and L

bands. We used a combination of TDFA and EDFA amplifiers. Such configurations are representative of current research on MB transmission over standard single-mode fiber [Fer20]. Simulating these systems with the traditional split-step Fourier method (SSFM) [Sin03] quickly becomes computationally prohibitive. Since the OCATA DT requires large amounts of high-fidelity data, the development of a more efficient and scalable simulation method becomes essential.

This solution provides a simulator to generate high-fidelity datasets for training ML models that can be used in the design of multi-band (C+L+S) optical systems. With respect to the literature, it overcomes the computational barrier for C+L+S simulation, providing the necessary foundation for the practical, data-driven implementation of the OCATA Digital Twin for autonomous control.

5.9.2 Efficient MB Simulation for Dataset Generation

To address the inefficiency of SSFM, we evaluate the Fourth-Order Runge–Kutta in the Interaction Picture (RK4IP) method [Agr95] as an alternative numerical solver for the nonlinear Schrödinger equation. The RK4IP formulation is implemented in both time and frequency domains, and its performance is enhanced through an adaptive step-size algorithm that modifies the propagation step based on local error estimation (see Algorithm 1 in [Kha25]). When the optical field evolves smoothly, propagation steps are enlarged, and they are reduced only in regions where nonlinear interactions intensify.

The adaptive RK4IP variants are benchmarked against a high-accuracy SSFM reference using a fully loaded MB configuration. All RK4IP versions achieve relative errors below 1% in reproducing the ISRS gain profile as shown in Figure 5.9-1 demonstrating that they preserve the accuracy needed for QOT-oriented modelling. Their computational benefits are substantial. The adaptive RG4IP reduces runtime by more than 90%, and the frequency-domain implementation (A-RKω) achieves an additional ~40% speed improvement over the time-domain version (see Figure 5.9-2). This efficiency gain makes A-RKω a suitable choice for generating the large datasets required for training ML models within OCATA.

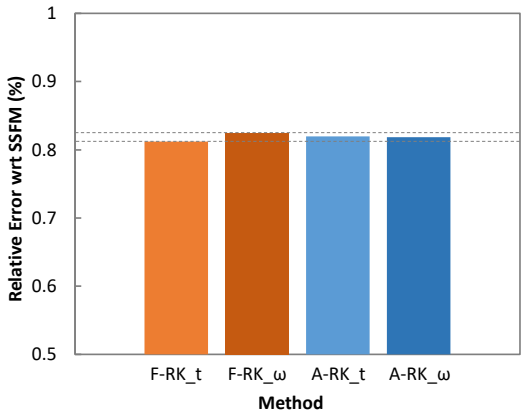

Figure 5.9-1: Relative error of RK4IP methods with respect to SSFM.

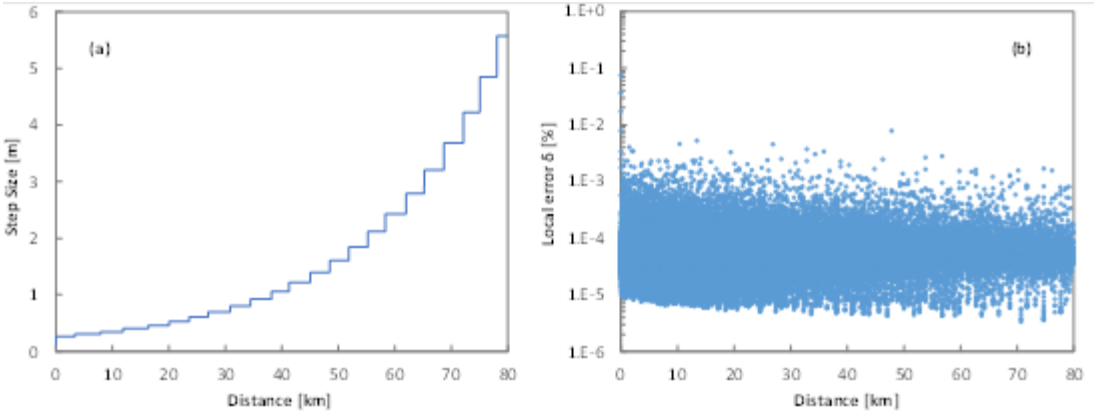

Figure 5.9-2: Evolution of the step size (a) and error (b) with propagation distance.

5.9.3 Machine-Learning Models for Constellation-Based QoT Prediction

Using the A-RKω solver, the study generates a dataset capturing the evolution of selected IQ constellation points (CPs) across transmission distances from 80 to 800 km. For each CP, the OCATA framework extracts statistical features using Gaussian Mixture Model (GMM) fitting, producing compact descriptors of constellation shape that reflect distortion and noise accumulation (see Algorithm 2 in [Kha25]). The OCATA-MB DT, illustrated in Figure 2 of [Kha25], reconstructs QoT estimates from these features.

Two complementary ML strategies are investigated.

The first employs Functional Link Artificial Neural Networks (FLANNs) [Mor18] to model the end-to-end evolution of constellation features for a specific total distance. FLANNs enhance their representational power by applying functional expansions to their inputs while remaining lightweight and easy to train. They provide accurate predictions but require different models for different propagation distances.

The second strategy develops per-span Deep Neural Networks (DNNs) that include the accumulated distance as an input feature. These DNNs can be concatenated to model arbitrary lightpath lengths (Figure 5 of [Kha25]), providing greater flexibility for operational contexts where span counts and configurations vary. While concatenation may introduce cumulative errors, this approach aligns naturally with digital-twin frameworks, which can periodically recalibrate models using live telemetry [Rui18].

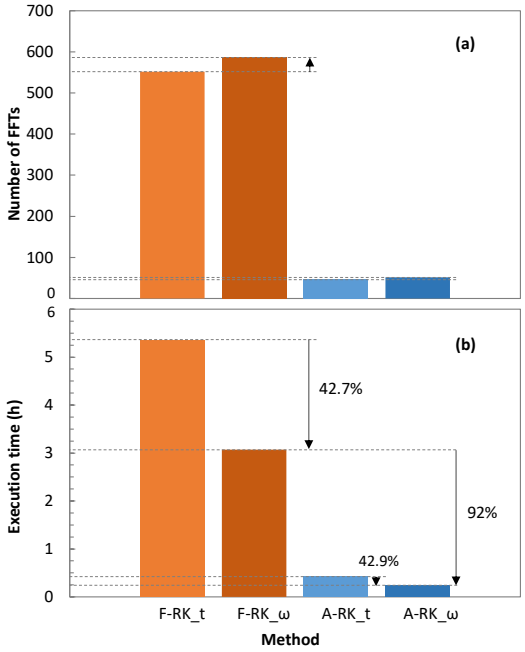

Figure 5.9-3: Number of FFTs required (a) and total computation time of RK4IP methods (b).

Both FLANN and per-span DNN models demonstrate strong predictive performance across representative channels from the S, C and L bands. Feature-prediction errors remain below 5%, see Figure 5.9-4, and constellation reconstructions closely match the simulated ones. The corresponding pre-FEC BER estimates (see Figure 5.9-5) are also accurate, with both ML strategies correctly identifying the reach associated with a BER threshold of 10^{-2}. For example, the S-band channel is shown to remain below threshold for up to three spans, while C- and L-band channels support slightly longer reach.

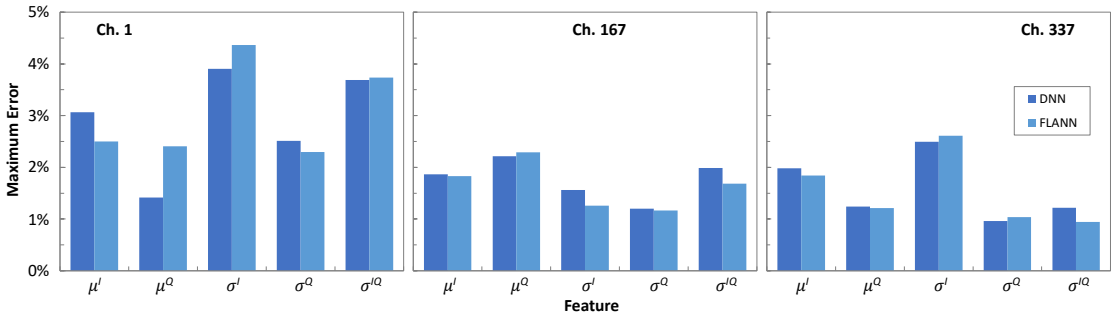

Figure 5.9-4: Maximum features error of ML models.

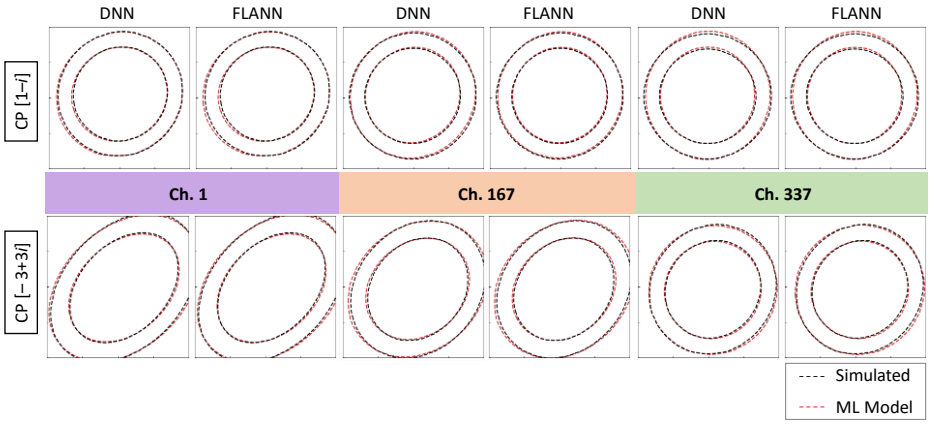

Figure 5.9-5: Contours of two CPs from the simulator and ML models.

5.9.4 Conclusions

The study presents a coherent methodology that enables scalable and accurate modelling of MB optical transmission for digital-twin-based network intelligence. The adaptive RK4IP solver reproduces SSFM-level accuracy at a fraction of the computational cost, making large-scale dataset generation feasible within project timelines and resource constraints. The ML models, comprising end-to-end FLANNs and modular per-span DNNs, accurately track constellation evolution and associated QoT metrics across the full S-C-L spectral range. This methodology directly supports the development of intelligent, data-driven, and automation-ready optical networks. It contributes to efficient spectrum use, improved QoT estimation, and enhanced resilience mechanisms such as soft-failure detection.

5.10 Creating and Tuning Multiband Optical Transmission Digital Twin Lightpath Models (related to C3.2)

5.10.1 Introduction

Based on the previous section, we investigate the construction and tuning of DT lightpath models for MB optical transmission. As mentioned, in MB networks using multiple bands, e.g., S, C, L-bands, ISRS significantly affects the QoT, making accurate pre-FEC BER estimation essential for both provisioning and failure management [Seq23, Dev24]. OCATA relies on pre-trained span DNNs stored in a model database; these must be concatenated into end-to-end (e2e) lightpath models and later tuned using telemetry to correct discrepancies arising from device variability, channel mismatch, and span-length differences. The key contribution of SEASON is the evaluation of strategies for composing accurate E2E models and the introduction of a model tuning block that updates these models once the lightpath is established. This framework can be used for composing and tuning models for DT lightpaths based on

Constellation Modelling. With respect to the state of the art, it achieves a higher accuracy of the QoT estimator thanks to the more granular constellation-based approach, which is essential for intelligent, autonomous, and self-managed multi-band networks

5.10.2 OCATA Constellation Modelling and QoT Estimation

OCATA represents received optical signals as IQ constellation samples X, reduced to per-CP feature vectors Yi = [μI, μQ, σI, σQ, σIQ] via Gaussian Mixture Models (GMM) [Bou20]. These features allow comparing samples using Euclidean distance and estimating pre-FEC BER using Φiout and its aggregation over all CPs (see Eq. (1-3) of eq. (3) of [Gha24-2]). This feature-based representation enables the DT to efficiently evaluate and compare QoT predictions from the concatenated span DNNs.

5.10.3 Lightpath Model Composition and Tuning

Two composition strategies are examined in [Gha24]:

Per-Span Composition (Algorithm 1). This method selects the span DNN whose training length most closely matches each physical span. While simple, it can produce substantial distance mismatch, which accumulates and degrades QoT accuracy, particularly in MB systems.

Distance-Based Composition (Algorithm 2). This strategy tracks accumulated distance and chooses a sequence of span models that minimizes the total length error. It better approximates the real optical path and significantly improves e2e estimation accuracy.

Since OCATA only trains span models for several reference channels (RChs) [Gha24-3], both algorithms operate on the two RChs closest to the allocated channel; QoT is then obtained via the original feature composition method and eq. (3) of [Gha24-2].

Once the lightpath is operational, discrepancies between model and telemetry require model tuning. Algorithm 3 proposed in [Gha24-2] periodically retrieves K telemetry samples, extracts features, and compares the observed BER with the modelled one. If the relative error exceeds a threshold, the concatenated DNN is updated using telemetry-derived features and written back to the model DB.

5.10.4 Results and Discussion

We used the MB simulator described in [Kha23], with 16QAM signals at 32 GBd and 50 GHz spacing, launched at 0 dBm. To highlight modelling inaccuracies, span models are pre-trained on 80 km spans, while lightpaths are evaluated on 50 km spans. Tests consider non-RCh channels 75 (S band), 170 (C), and 245 (L).

Before tuning, Figure 5.10-1(a) shows that the per-span method overestimates QoT, leading to incorrect rejections of lightpaths longer than ~4 spans. The distance-based approach performs

considerably better, though still affected by span-length mismatch. After tuning, Figure 5.10-1(b) demonstrates that e2e models achieve highly accurate QoT estimates for all evaluated channels. Figure 5.10-1(c) shows strong alignment between constellation contours after tuning and the true received distributions.

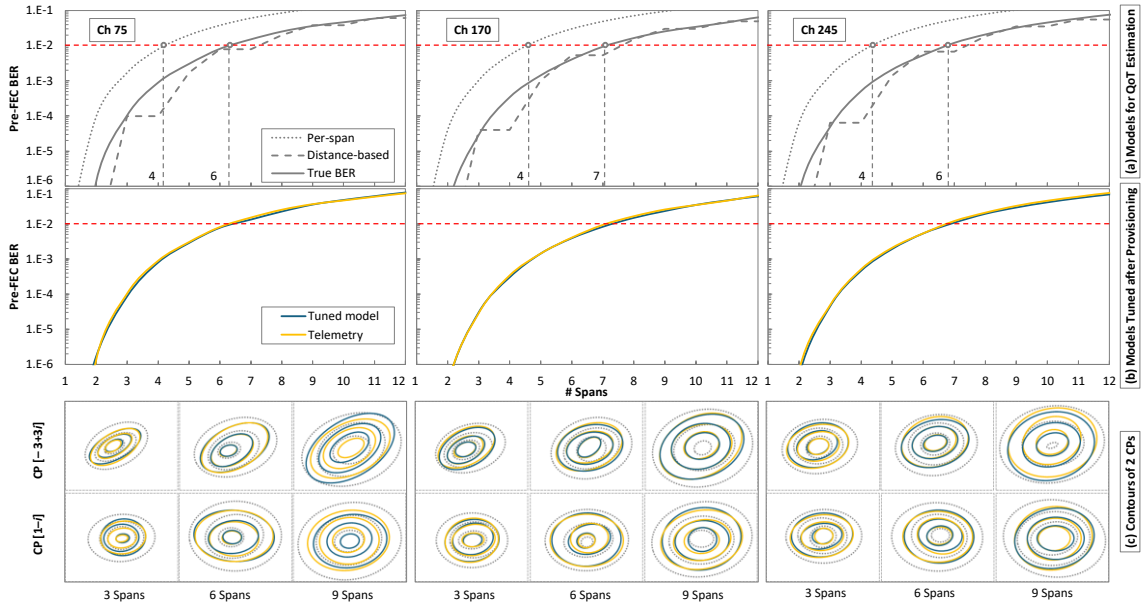

Figure 5.10-1: Pre-FEC BER vs # of spans (50 km) before (a) and after tuning (b). (c) Contours of bivariate Gaussian distribution for two CPs.

Figure 5.10-2 indicates that about 200 telemetry samples are sufficient to reduce the feature distance of eq. (1) in [Gha24-2] to very low values, confirming the efficiency of the tuning process. Overall, although span-length mismatches can severely degrade QoT prediction, distance-aware composition combined with telemetry-based tuning returns models to high accuracy, enabling both provisioning and degradation detection.

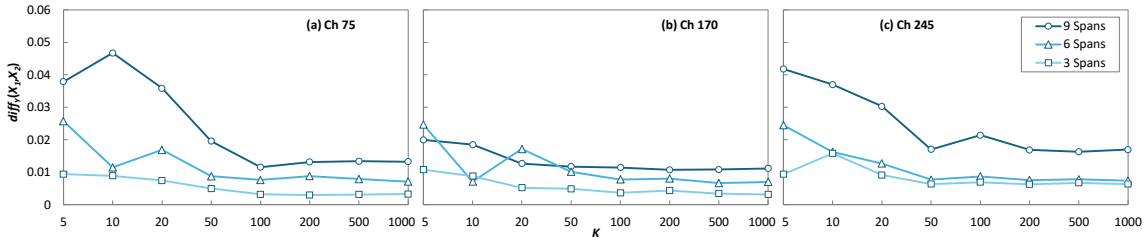

Figure 5.10-2: Average error between model and telemetry features vs number of samples K for three non-reference channels.

To conclude, this study provides a complete methodology for generating and maintaining accurate DT lightpath models in MB optical networks. Distance-aware composition reduces modelling error, and telemetry-driven tuning corrects remaining discrepancies, enabling precise pre-FEC BER prediction across the full S, C, and L spectrum.

5.11 Optical performance model of Multi-Band Transport Systems with up to 24 THz of Transmission Bandwidth (related to C3.2)

As already stated, one of the most promising strategies to address the anticipated capacity crunch in optical communication networks is to expand the transmission bandwidth of existing systems through multi-band (MB) transmission. Standard single-mode fiber, such as ITU-T G.652D, supports a broad low-loss transmission window spanning ≈54 THz across the O-, E-, S-, C-, and L-bands. Figure 5.11-1 illustrates the frequency-dependent attenuation across this spectrum, highlighting the low-loss transmission window. This spectrum offers the potential for more than a tenfold increase of usable bandwidth compared to conventional systems that operate solely within the C-band, which is limited to about 4.8 THz.

However, this theoretical gain is hampered by practical limitations. For instance, transmission bands outside the C-band typically exhibit inferior optical performance due to higher attenuation, increased nonlinearities (e.g., in O→S bands), and less mature amplification technologies. As a result, the full bandwidth expansion does not directly translate into a proportional increase in the total capacity of the system.

To mitigate these challenges, while still enhancing capacity, a more incremental approach has gained traction: extending the amplifier bandwidth within the C-band itself. Commercial systems are increasingly adopting amplifiers capable of operating over a 6 THz range (referred to as a "super C-band"), up from the traditional 4.8 THz. This strategy enables capacity scaling without the added complexity and cost of deploying additional amplification bands, band multiplexers, and demultiplexers required for full MB operation [Sho24]. MB transmission can then leverage the super bands (e.g., to realize a Super-C+L-band system [Ped24]).

For more substantial capacity gains, MB transmission can be combined with spatial-division multiplexing (SDM) techniques. These include the use of multiple fibers (MF), multi-core or multi-mode fibers (MCF/MMF), and few-mode fibers (FMF), which exploit parallel spatial paths to further increase throughput.

This section discusses the challenges of modelling wideband transmission and analyzes the optical performance and capacity of single- and multi-band transmission systems, ranging from a 6 THz single super band to a 24 THz four-super-band configuration. To limit the stimulated Raman scattering (SRS) effect and system complexity, contiguous spectral occupation is capped at 18 THz (equivalent to three super bands). Systems using all four bands include a 17 THz guard band between the super O-band and the others, effectively isolating it and minimizing any SRS-induced power transfer. Configurations include Super-C, Super-C+L, Super-S+C+L, and Super-S+C+L+O systems. A 4.8 THz C-band-only system is also evaluated for benchmarking. This framework enables comparison of the spectral efficiency, complexity, and capacity.

5.11.1 Simulation Setup

Table 5.11-1 summarizes the four configurations of the MBT system analyzed in this work. All systems include a minimum 500 GHz guardband between adjacent bands. As a reference, we first consider a C-band system spanning 191.3–196.1 THz. The Super-C system extends this to 190.8–196.8 THz. The Super-C+L system covers 184.3–196.8 THz (using the super C and super L bands), while the Super-S+C+L system spans 184.3–203.3 THz (using the super S, super C and super L bands). Finally, the Super-S+C+L+O configuration adds the Super O band (220.5–226.5 THz) to the three-band system, maintaining a guard band of over 17 THz from the S-band, as recommended in [Sam22, Sou25]. In this case, nonlinear interference (NLI) and the SRS-induced power transfer between the O-band and other bands are considered negligible. Although some transmission bands are formally defined with bandwidths exceeding 6 THz, we assume that the optical amplifiers used across these bands will have the same bandwidth as those in the super C-band, due to the challenges in extending amplifier bandwidth.

Table 5.11-1: Minimum and maximum frequencies of each amplification band.

Band	Start Frequency [THz]	Stop Frequency [THz]
Super L	184.3	190.3
C	191.3	196.1
Super C	190.8	196.8
Super S	197.3	203.3
Super O	220.5	226.5

A local span optimization approach is employed to determine the optimal launch power. The transmission system is modelled as a single optical fiber span followed by an optical amplifier. Each spectral band is supported by a dedicated amplifier with different doping materials for individual bands, necessitating the use of band-specific demultiplexers and multiplexers at each amplification site [Sou22].

The transmission system operates with 40 channels per super band and 32 channels within the C-band, all spaced on a 150 GHz channel grid. Each channel carries a 120 GBd signal shaped with a roll-off factor of 0.15.

The optical fiber is modelled according to the ITU-T G.652.D specification as specified in Section 3.8 The nonlinear coefficient and Raman gain characteristics are adopted from the model described in [Sou24]. The fiber attenuation profile is presented in Figure 5.11-1. Additional losses include 0.25 dB at both the input and output connectors, and splice losses of 0.01 dB/km.

Optical amplifiers are characterized by constant noise figures: 5 dB for the super L and super C/C bands, and 7 dB for the super S and super O bands. The total insertion loss introduced by the multiplexing and demultiplexing components is assumed to be 1.5 dB.

5.11.2 System Modelling and Power Optimization

We use the per-channel GSNR as the quality of transmission (QoT) estimation (considering the signal bandwidth as a reference). This QoT metric equation is shown below (Eq. 2), where P_i is the power of channel i and P_i^{ASE} and P_i^{NLI} are the power of the Gaussian noise corresponding to the amplified spontaneous emission (ASE) noise and the nonlinear interference due to the self- and cross-channel nonlinear crosstalk at channel i, respectively.

$$\mathrm{GSNR} = \frac{P_i}{P_i^{ASE} + P_i^{NLI}} \qquad \text{Eq. 2}$$

The NLI noise contribution is calculated using the GGN model [Can18] and the SRS is calculated by numerically solving the Raman equations that govern this effect [Chr96]. Both methods are available in the open-source python library GNPy [Cur22].

One of the most time-consuming parts when calculating the GSNR of a lightpath is the estimation of the nonlinear interference (NLI) power. Therefore, several extensions of the GN model that simplify the estimation of the NLI power, while aiming to assess it with reasonable accuracy when exploiting MBT systems, have been proposed in the literature. Each model makes different assumptions, which lead to different trade-offs between accuracy and computational complexity (analysed in [Sou23]).

The split-step Fourier method (SSFM)-based simulations, being the most accurate ones, should be used as references. However, they require an impractical amount of time to run in heavily loaded wideband transmission scenarios. The complexity of SSFM-based simulations depends on the step size and on the size of the discrete Fourier transforms (DFTs). With wider bands, the transmitted power within the fiber is higher, and therefore the step size must be reduced for an accurate estimation. Moreover, larger-sized DFTs are required, and their complexity depends quadratically on the size of the input. Consequently, the work in [Sou23] considers the numerical GGN implementation available on GNPy, as the most accurate because it is the one implementing fewer approximations and was already validated using SSFM simulations in a few wideband cases (up to S+C+L MBT systems [Dam22]) and also using data collected both from laboratory experiments and network field trials (using C-band only transmission) [Fer20, Dam22-2]. Additionally, the GNPy was adopted as the QoT estimation tool by the Telecom Infra Project (TIP), a global consortium of companies and organizations working together to accelerate the development and deployment of open, disaggregated, and standards-based technology solutions [TIP].

To limit the stimulated Raman scattering (SRS) effect and the complexity of accurately estimating the GSNR, contiguous spectral occupation is capped at 19 THz (equivalent to three super bands). The four-band system has a 17-THz guard band between the super O-band and the others, effectively isolating it and minimizing any SRS-induced power transfer. In this way, the GSNR of the O-band is estimated independently of the other bands.

The objective of launch power optimization is to maximize the overall system GSNR while minimizing GSNR fluctuations across each spectral band. Achieving a flatter QoT profile can simplify routing and spectrum assignment (RSA) algorithms and enhance channel availability, as discussed in [Men01].

The optimization parameters correspond to settings typically configurable on commercial optical amplifiers: the average channel power per band (P_x) and the power tilt (T_x). The power of a specific channel i in band x is defined as $P_i = (f_i - f_x)T_x$, where f_i and f_x are the channel frequency and the center frequency of band it belongs to, respectively.

To simplify the optimization process, the approach focuses on adjusting these band-level parameters rather than optimizing the power of each individual channel. This avoids the complexity of managing N_{ch}^x variables per band, where N_{ch}^x is the number of channels transmitted in that band.

Furthermore, the multivariate optimization problem is decomposed into a sequence of single-variable subproblems, which are solved iteratively until convergence is achieved. This method follows a similar strategy to the one proposed in [Sou22].

5.11.3 Optimization Results

Figure 5.11-1 and Figure 5.11-2 present the optimized launch power and GSNR profiles for a single 75-km span across various systems: C, Super-C, Super-C+L, Super-S+C+L, and Super-S+C+L+O. Among these, single-band systems exhibit the highest average GSNR (27.0 dB and 26.9 dB for the C and Super-C systems, respectively). This advantage stems from the absence of additional MUX/DEMUX losses, lower fiber attenuation, reduced nonlinear effects, and lower amplifier noise figures compared to MB systems.

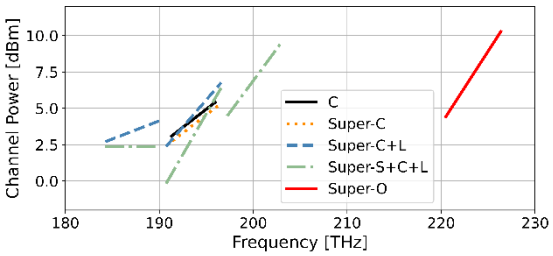

Figure 5.11-1: Optimized launch power for a 75-km span.

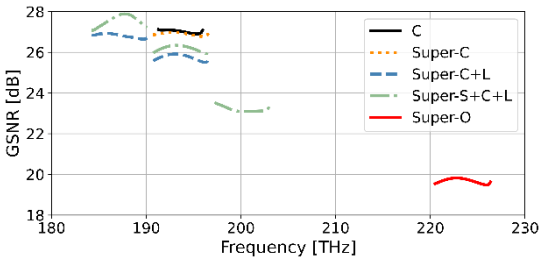

Figure 5.11-2: Optimized per-channel GSNR for a 75-km span.

The figures also reveal that incorporating the Super S-band into a Super-C+L system enhances GSNR in the super C- and super L-bands. This improvement is due to inter-band power transfer, where super S-band channels act as co-propagating Raman pumps, enhancing power transfer via the SRS effect. However, the super S and super O bands show significantly lower average GSNR, with the super O band performing the worst.

5.11.4 Conclusions

This section explored the challenges of accurately and efficiently estimating the GSNR of a lightpath in ultra-wideband transmission systems. Given the importance of precise and fast modeling, it discusses the applicability of GN models, emphasizing the transmission scenarios where the GGN model has been validated through SSFM simulations. It also comments on the performance of the ISRS-GN model for spectrum occupations up to 20 THz.

Recognizing the limitations of GN models and the impracticality of SSFM for performance estimation in ultra-wideband contexts, four MBT configurations were identified as promising candidates for future MBoSDM systems: SuperC+L, SuperC+L+S, and SuperC+L+S+O.

The performance of these configurations was optimized and compared. Results indicate that single-band systems achieve higher spectral efficiency, primarily due to lower losses from band MUX/DEMUX components, improved amplifier noise figures, and reduced fiber attenuation. These insights will support the techno-economic evaluation of the proposed systems in Deliverable 2.3.

6 SEASON OPTICAL SUBSYSTEMS DEVELOPED

6.1 PROGRAMMABLE MBOSDM TRANSCEIVER (RELATED TO C3.1 AND C3.3)

A MB(oSDM) S-BVT prototype has been developed and validated in the framework of SEASON towards supporting future network capacity requirements by the exploitation of multiple bands, beyond the C-band, and even multiple spatial channels (component 3.4). More details can be found in deliverable [D3.2-24]. Here, further transmission assessment has been performed in order to evaluate the transceiver scalability capabilities towards enabling multi Tb/s transmission [Nad25-2]. Suitable spectral spacing and power levels of transmitted channels are analyzed to limit the impact of inter-channel XT in a WDM scenario. The experimental setup of Figure 6.1-1 has been considered for the experimental assessment. By enabling additional bands beyond the C-band, with relatively low attenuation, and adopting SDM by means of including a MCF, improved network scalability is achieved.

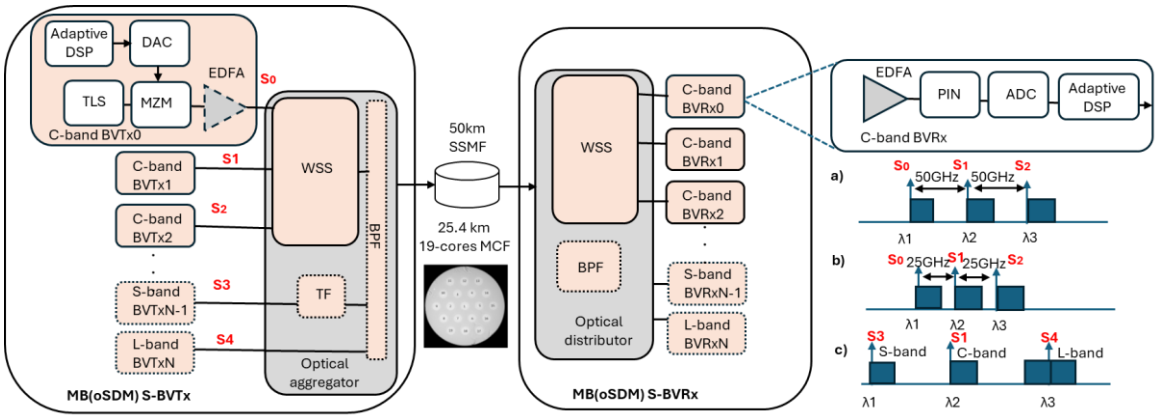

Figure 6.1-1: Experimental setup for scalability and MBoSDM assessment using a MB(oSDM) S-BVT.

Three different scenarios have been evaluated to assess transceiver scalability and MBoSDM operation. In particular, scenarios 1 and 2 evaluate the performance of three C-band slices (s0-s2) considering spectral spacing of 50 Ghz (Figure 6.1-1a) and 25 GHz (Figure 6.1-1b). In scenario 1, the TLSs are set to 1549.72 nm (s0), 1550.12 nm (s1), and 1550.52 nm (s2), each emitting at 14.5 dBm output power. In scenario 2, they are set to 1549.92 nm (s0), 1550.12 nm (s1), and 1550.32 nm (s2). Scenario 3 explores MB operation, where three S-BVT building blocks are enabled across different bands: S-band (1500 nm, s3), C-band (1550.12 nm, s1), and L-band (1600 nm, s4), as shown in Figure 6.1-1c. For Scenarios 1 and 2, an EDFA is used at the C-band bandwidth/bit rate variable transmitter (BVTx1) and BVTx2 to investigate how adjacent amplified channels with varying power levels affect transmission capacity. The three channels are combined using a wavelength selective switch (WSS) with a 25 GHz channel bandwidth, enabling single side band (SSB) modulation and improving resilience against chromatic dispersion (CD). At the receiver, a WSS-based optical distributor with a 25 GHz bandwidth is employed to separate the channels. In Scenario 3, the three S-BVT modules operate in the S, C,

and L bands to evaluate MBoSDM transmission over a 19-core MCF of 25.4 km. In this particular case, aggregation and distribution of the slices are performed with S+C+L band pass filters (BPFs). The S-band and C-band slices are filtered at the transmitter side to perform SSB with programmable filters of 25 GHz bandwidth. Due to laboratory constraints, the L-band slide is DSB modulated. A target bit error rate (BER) of 4.62e-3 is ensured.

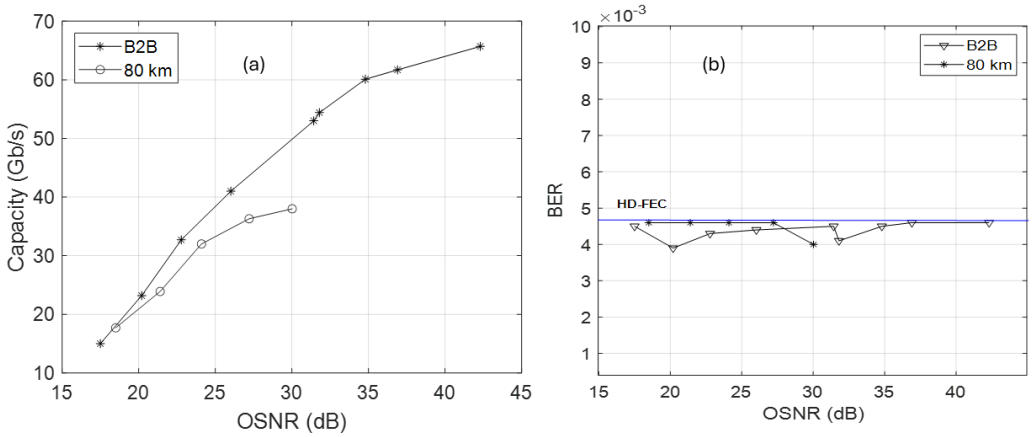

Figure 6.1-2: (a) Achieved experimental C-band capacity and (b) BER in B2B and after 50 km SSMF.

Experimental assessment of slice s1 (1550 nm) has been undertaken considering both a back-to-back (B2B) and transmission over 50 km path of standard single mode fiber (SSMF) scenarios, as depicted in Figure 6.1-2(a) and (b). According to the figure, a maximum capacity of 65.7 Gb/s is achieved at an optical signal to noise ratio (OSNR) of 42.3 dB, meeting the target BER. After 50 km of SSMF, the maxim capacity is 38 Gb/s at 30 dB OSNR due to fiber impairments.

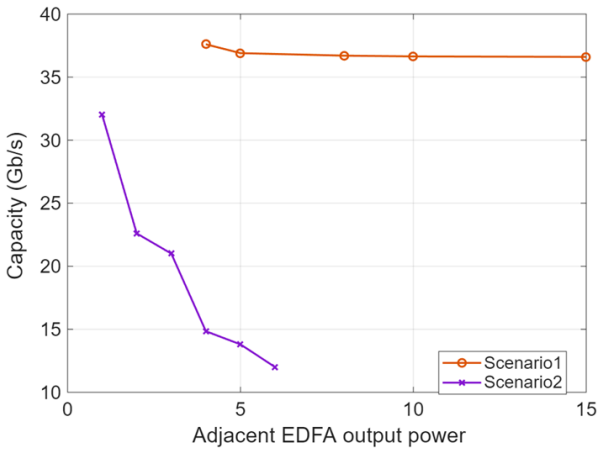

Figure 6.1-3: Achieved capacity of s1 after 50 km SSMF considering different spectral spacing (scenario 1 and 2).

Figure 6.1-3 shows the achieved capacity of s1 (1550.12 nm) considering different spectral spacing of the adjacent amplified channels (s0 and S2) after 50 km of SSMF. The EDFA output power at each BVTx block is adjusted to vary channel power, as shown in Figure 6.1-1. With a 100 GHz spectral spacing, the maximum capacity remains stable at around 37 Gb/s, even as adjacent channel power increases up to 15 dBm (an 11 dB power difference relative to s1). However, reducing the spacing to 50 GHz and maintaining equal power for all channels

introduces inter-channel crosstalk, resulting in a 6 Gb/s capacity drop at an OSNR of 25.8 dB (see Figure 6.1-2a). Further increasing the adjacent channel power introduces higher crosstalk, reducing the s1 capacity to 12 Gb/s at a 5 dB power difference.

This analysis offers insights into the scalability potential of the proposed MB(oSDM) prototype to enable multi Tb/s transmission. Considering a spectral spacing of 50 GHz (scenario 1) uniform capacity with negligible impact of the adjacent channels is enabled, but at the expense of reduced spectral efficiency and resource utilization. Reducing the channel grid slightly reduces the achievable capacity in an equal-power wavelength division WDM C-band transmission. The impact is more critical with adjacent channels at a higher power level than the channel of interest. Hence, by populating the whole C-band with equal-power channels with a 25 GHz channel grid, up to 175 channels can be allocated. This translates to a total transmission capacity of 5.6 Tb/s over a 50 km path.

By the exploitation of multiple bands beyond the C-band (MB) and spatial channels (SDM), further capacity increase can be envisioned, as demonstrated in scenario 3. In particular, the proposed transceiver solution enables MB operation in the S-, C- and L-bands, while the adoption of MCF fibers introduces the spatial dimension. A capacity of 60.5 Gb/s is obtained at 39 dB OSNR. Increasing the OSNR to 42.3 dB improves the capacity to 65.7 Gb/s in the B2B case at the target BER (see Figure 6.1-2). The S-band and L-band contributions achieve similar performance in B2B, enabling 60.4 Gb/s and 60 Gb/s capacities at 40 dB and 38.1 dB OSNR, respectively. By including the MCF, the MB flow is transmitted over core 1 and successfully received, achieving capacities of 45.4 Gb/s at 31.8 dB OSNR (S-band), 41.3 Gb/s at 32 dB OSNR (C-band), and 34 Gb/s at 34 dB OSNR (L-band). These results further demonstrate that the proposed approach can be further scaled by fully populating the available MB and spatial resources within the network towards meeting network requirements. In particular, **28.2 Tb/s** can be achieved by considering 350 SSB S-band channels, 175 SSB C-band channels and 150 DSB L-band channels transmitted over a single core of the MCF. This capacity can be further scaled considering the 19-cores of the MCF available.

Additional work has been performed towards the integration of the MB(oSDM) S-BVT prototype with an SDN control plane to foster network programmability and reconfiguration [Nad25-3]. Different transceiver programable parameters and components can be configured according to the network condition by means of the implementation of SDN agents. Specifically, the OpenConfig data model is adopted to promote network disaggregation. More details will also be included in SEASON deliverable D4.3. The wavelength and power of the TLS in each S-BVT building block can be configured to operate in a specific wavelength band, and the DAC and ADC output ports can also be enabled/disabled.

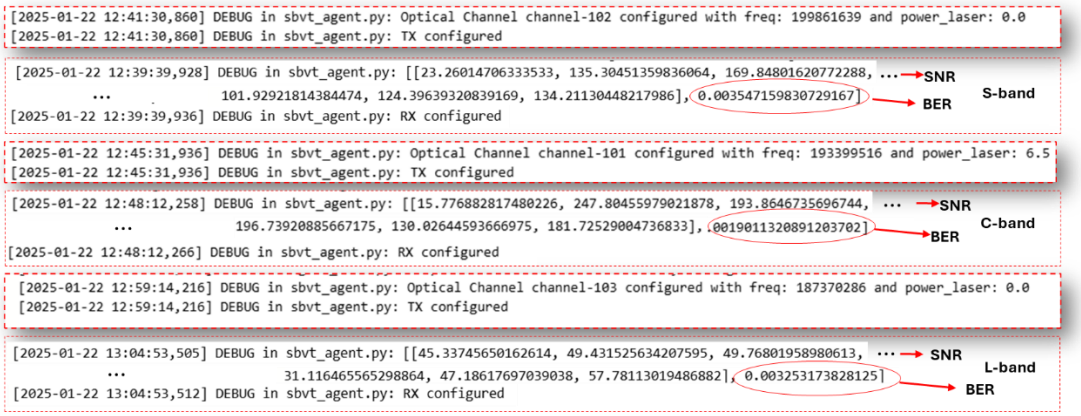

Figure 6.1-4: MBoSDM S-BVT configuration by means of SDN agents.

Figure 6.1-4 shows successful configuration of each MB(oSDM) building block. First the S-band slice is established, followed by the Cband and L-band transceivers. After configuring each receiver the signal to noise (SNR) per subcarrier vector and BER are calculated, ensuring the target FEC.

These results are closely related to the KPIs 3.1 and 3.2 by experimentally assessing MB transmission over MCF.

6.2 MBoSDM NODE PROTOTYPE (RELATED TO C3.1 AND C3.3)

In deliverable [D3.2-24] the assessment of the MBoSDM node prototype (component C3.1) has been performed. The developed prototype enables WDM (in the C-band), MB (S+C+L) and SDM (cores) exploitation. Further optimization of the switching device has been here implemented to include spectral switching granularity in the L-band.

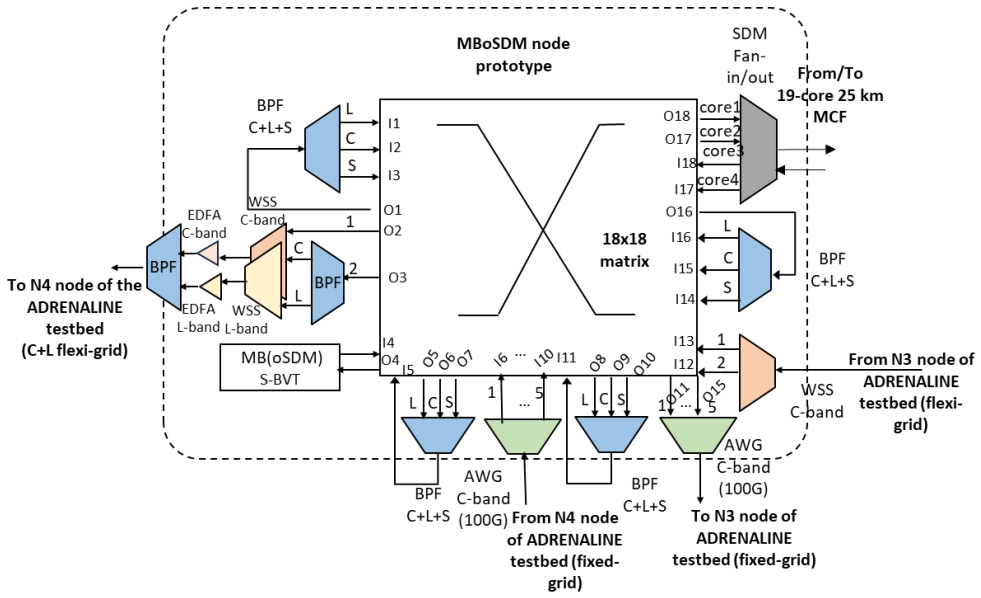

Figure 6.2-1: Enhanced MBoSDM node prototype architecture, with L-band spectral switching granularity.

Dissemination Level	Public

The node prototype is fully described in deliverable [D3.2-24]. The optimized node version is here reported and depicted in Figure 6.2-1 and Figure 6.2-2 to enable L-band spectral granularity. Specifically, a BPF is connected to node output O3, to disaggregate a MB signal (C+L). The MB signal can be generated by a MB(oSDM) S-BVT. The C- and L-band signals are each directed to dedicated WSS operating in a particular band. The appropriate number of slices around a central frequency and the switching port are programmed in both WSS subsystems. Then, each branch is amplified by its EDFA working at C- or L-band. Both contributions are finally aggregated by means of a BPF. The optimized node prototype is integrated in the ADRENALINE testbed [Vil25].

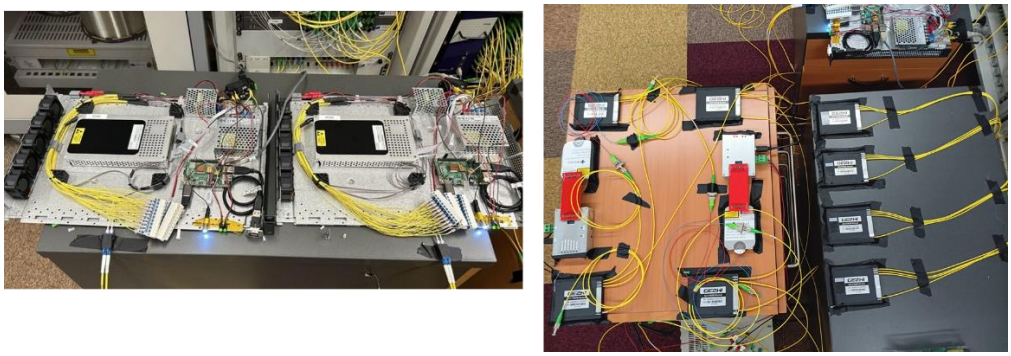

Figure 6.2-2: Optimized MBoSDM node prototype.

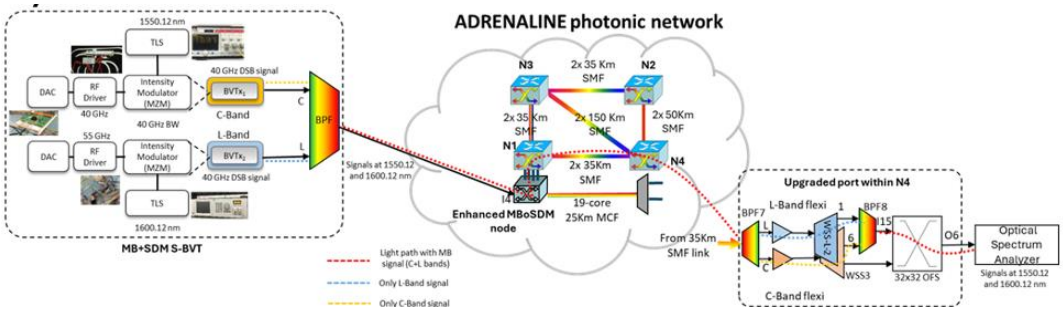

Figure 6.2-3: Experimental setup including MBoSDM node prototype with advanced capabilities.

Figure 6.2-3 show the experimental setup for the validation of the upgraded MBoSDM node prototype including advanced functionalities. In particular, the dashed red line represents the optical path established for MB transmission assessment. Figure 6.2-4(a) shows the optical spectra analyzed by connecting directly the OSA equipment to the output of the MB+SDM S-BVT. Peaks of -7.5 dBm and -7.4 dBm are detected for 1550.12 nm and 1600.12 nm signals, respectively. Figure 6.2-4(b) depicts the same signals after traversing the complete link established in the setup, at the O6 output of the 32x32 OFS in N4, depicted in Figure 6.2-3. Figure 6.2-4 (c) shows the C-band signal at this point, with around 0.3 dBm of peak power, and Figure 6.2-4 (d) presents the L-band signal at the same point of measurement, detecting a peak of around 2.5 dBm of power. OSA shows a deviation in the central wavelength, due to its limitation.

Dissemination Level	Public

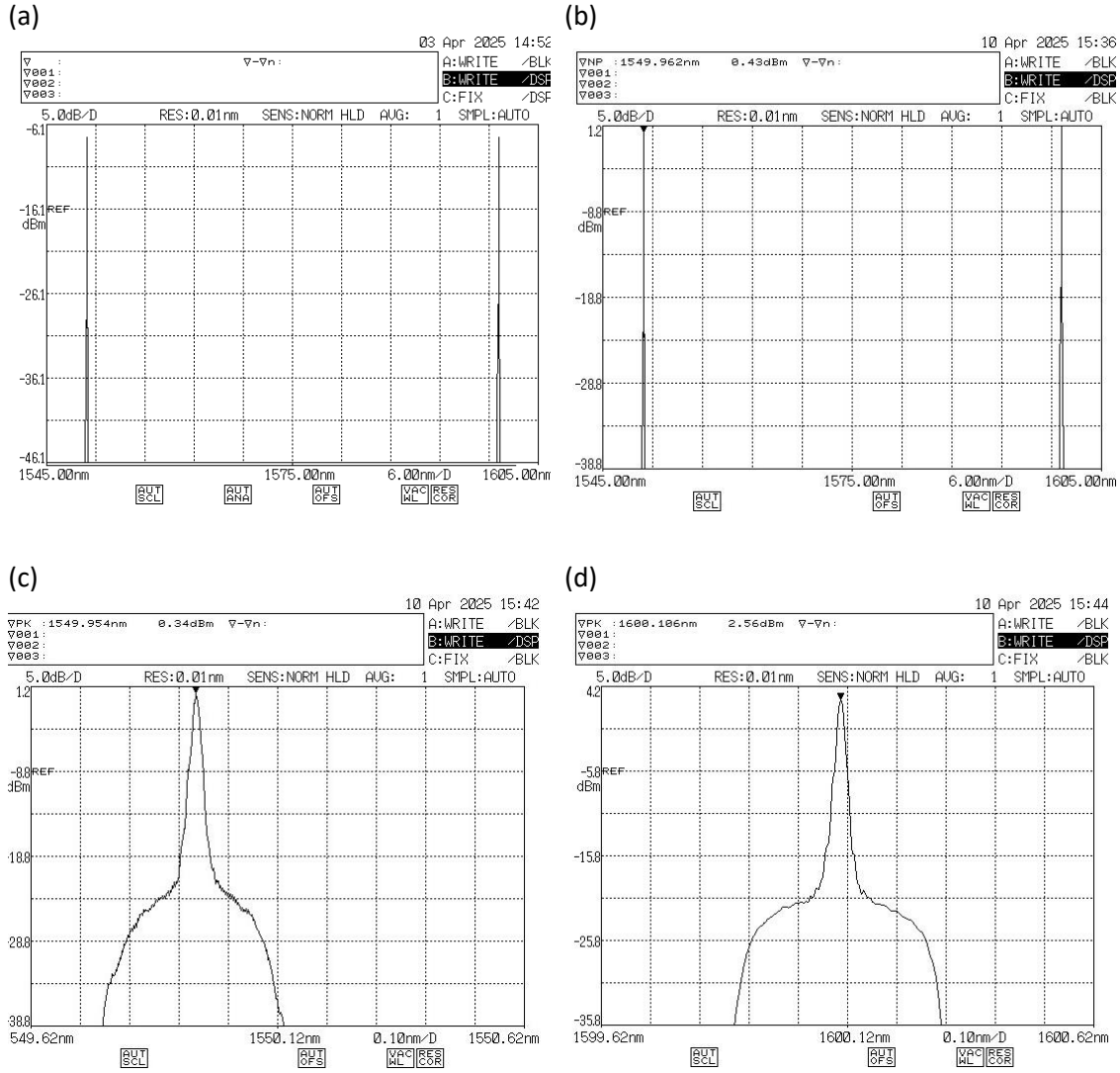

Figure 6.2-4: (a) C- and L-band signals generated by the MB(oSDM) S-BVT; (b) C+L signals at the O6 output of the OFS in N4; (c) C-band signal at the O6 output of the OFS in N4; (d) L-band signal at the same point.

These results are closely related to KPI 3.2 by extending the capabilities of the SEASON node prototype to include wavelength granularities in the C+L-bands.

6.3 NODE MULTI-BAND & SDM

In D3.2, the design, assembly, and assessment were reported. The node prototype is built on a fixed optical band-selective filter architecture, integrated with a fully reconfigurable optical cross-connect (i.e., an optical matrix switch). Operating as a hierarchical network node, it delivers a fast and efficient selective switching and add/drop capabilities for the S-, C-, and L-bands.

The design incorporates eight multiband multiplexers or splitters/combiners (MB Mux and MB Demux) and a 12×12 optical matrix switch that allows flexible band routing. This is shown in

Figure 6.3-1(a). Additionally, monitoring ports are integrated at each input and output port for measurement devices, such as Optical Spectrum Analyzers (OSA), to ensure effective monitoring throughout the validation and operational phases of the prototype, this is shown in the prototype layout Figure 6.3-1(c). The assembled prototype is shown in Figure 6.3-1(b). The node prototype is entirely controllable via a state-of-the-art SDN agent that includes a NETCONF server, more details on that can be found in the results from WP5.

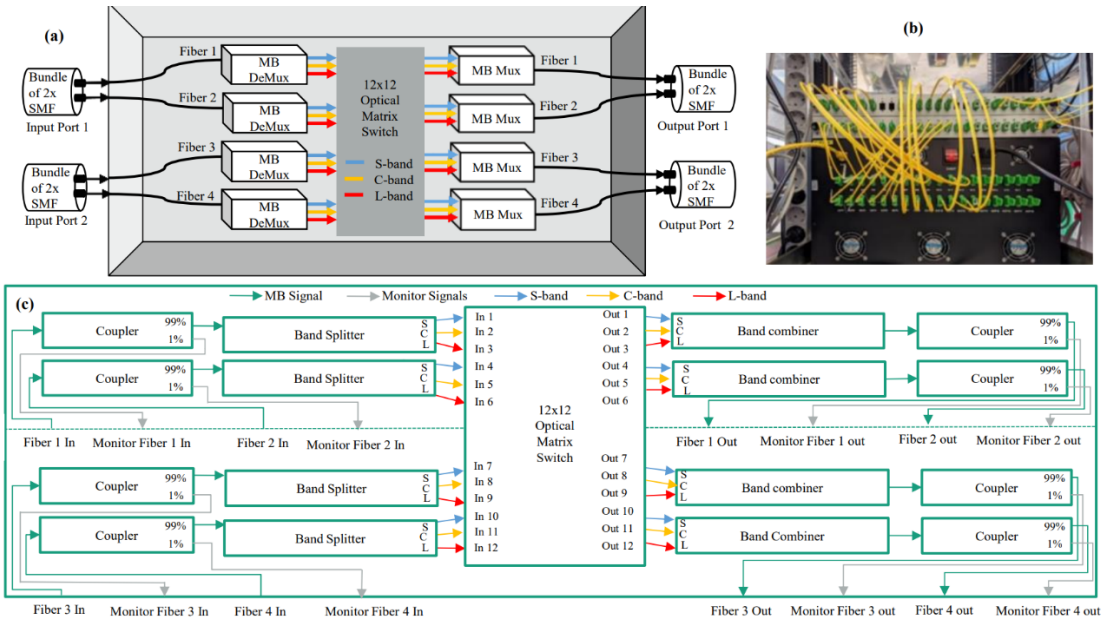

Figure 6.3-1: (a) Prototype design, (b) prototype after assembly, and (c) prototype layout.

To test and validate the node, Figure 6.3-2(a) shows the setup for the validation, the setup is physically deployed at the Fraunhofer HHI premises. Amplified Spontaneous Emissions (ASE) grid with a spacing of a 50 GHz were generated using a combination of band specific Wavelength Selective Switches (WSS) and noise sources. The grid is containing 125 S-band channels, 92 C-band channels and 80 L-band channels. The modulated signal will be loaded to one of the channels while the rest will be populated with ASE. The ASE grid is fed to the prototype input port 1 fiber 1, while input port 2 fiber 3, check Figure 6.3-1(a), will be fed a non-grid ASE profile.

The 4 monitoring input ports, the 4 output ports and the 4 monitoring output ports of the prototype will be connected to the 16x4 monitor switch using ports N5 up to N16, while N1 up to N4 of the monitor switch are connected to the setup as indicated in Figure 6.3-2(a). This allows to redirect any point of the setup, including the inputs and outputs of the prototype, to the 2 monitoring OSAs. The prototype is controlled through an SDN agent as stated above to make our life easier in testing, while the 16x4 monitor switch will be controlled through a local agent to show the routing and switching over the 2 OSAs.

This work was accepted and showed in OFC 2025 within the SEASON [Moa25], we fed the ASE grid to input fiber 4 while keeping the rest of the input fibers void to make the demo easier, then we switched them to output fiber 1. This can be seen in Figure 6.3-2(b) and Figure 6.3-2(c), respectively. The difference in the magnitude is due to the fact that we used a monitor port for

the input and the actual output port for the output powers to prove the monitoring couplers functionality also.

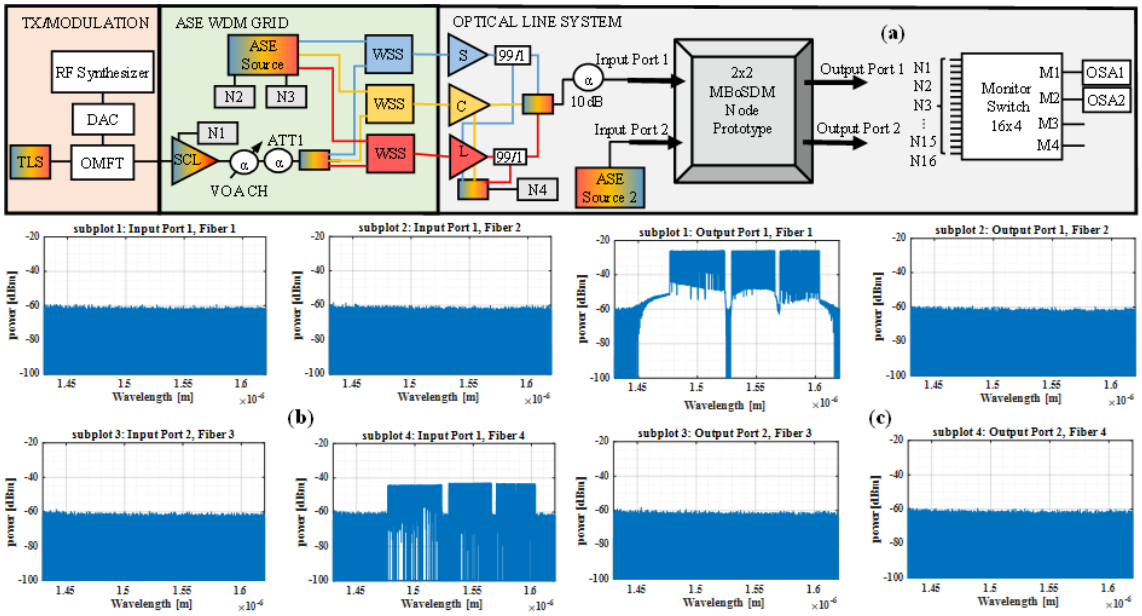

Figure 6.3-2: (a) Validation setup. (b, c) proof of concept, state of the input and output fibers, respectively.

These results are closely related to KPI 3.2.

7 SEASON OPTICAL TRANSPORT INFRASTRUCTURE FOR (BEYOND 5G) FRONT/MID-HAUL AND ACCESS

7.1 COST-EFFECTIVE OPTICAL RING ARCHITECTURE WITH AUTOMATED EDFA OPTIMIZATION (RELATED TO C3.8)

EDFAs represent a cost-effective and energy-efficient solution for extending optical signal reach in fixed-distance connections, particularly between datacenters and within fronthaul segments of next-generation networks. Although current deployments typically rely on fixed-gain designs, future generations of EDFAs are expected to incorporate variable-gain capabilities, unlocking additional flexibility in dynamic and heterogeneous environments. The proposed algorithm anticipates this evolution by introducing a framework capable of computing optimal gain settings based on real-time monitoring and traffic conditions, preparing the architecture for seamless adoption of next-generation amplifiers.

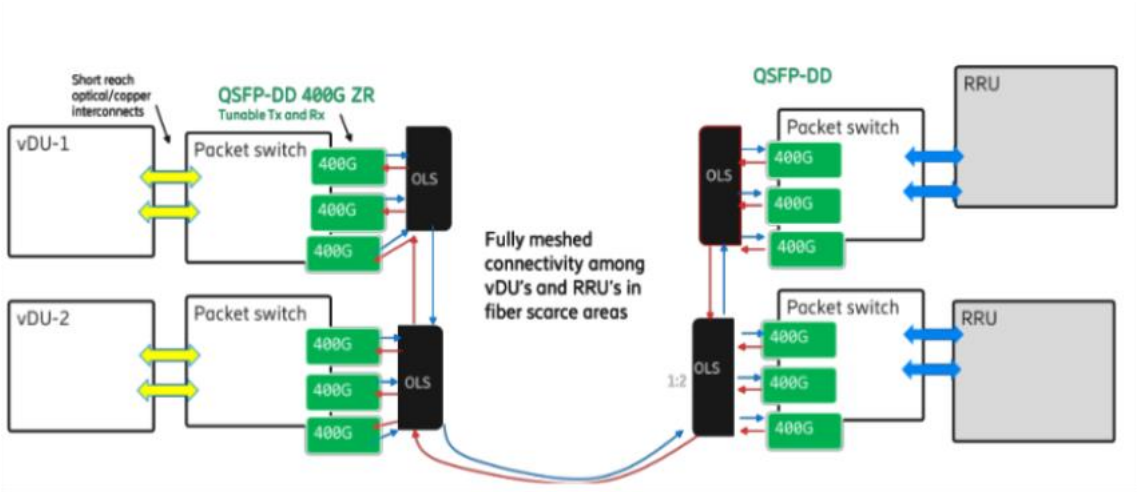

Figure 7.1-1: Optical network designed to handle the high-speed data transfer.

The proposed architecture, figure 7.11, implements an optical ring comprising four nodes and six WDM channels, allowing multiple signals to share a single fiber and maximizing infrastructure efficiency. This design integrates vDUs, RRUs, packet switches, and OLS equipped with QSFP-DD 400G transceivers, ensuring high bandwidth, scalability, and resilience even in fiber-constrained environments. The use of tunable transceivers and filterless OLS nodes with simple splitting mechanisms further enhances flexibility and adaptability, supporting advanced services such as 5G fronthaul and beyond.

A key innovation lies in the automation of EDFA configuration. OLCs, shown in Figure 7.12, combined with advanced algorithms, dynamically adjust amplifier settings to optimize performance, reduce manual intervention, and improve operational efficiency. The document examines EDFA operating modes—Constant-Power and Constant-Gain—highlighting their

respective advantages and challenges. By leveraging real-time power monitoring and traffic matrix data, the proposed approach computes gain values that keep received power and OSNR within design specifications across all network segments, ensuring optimal conditions even as amplifier technologies evolve.

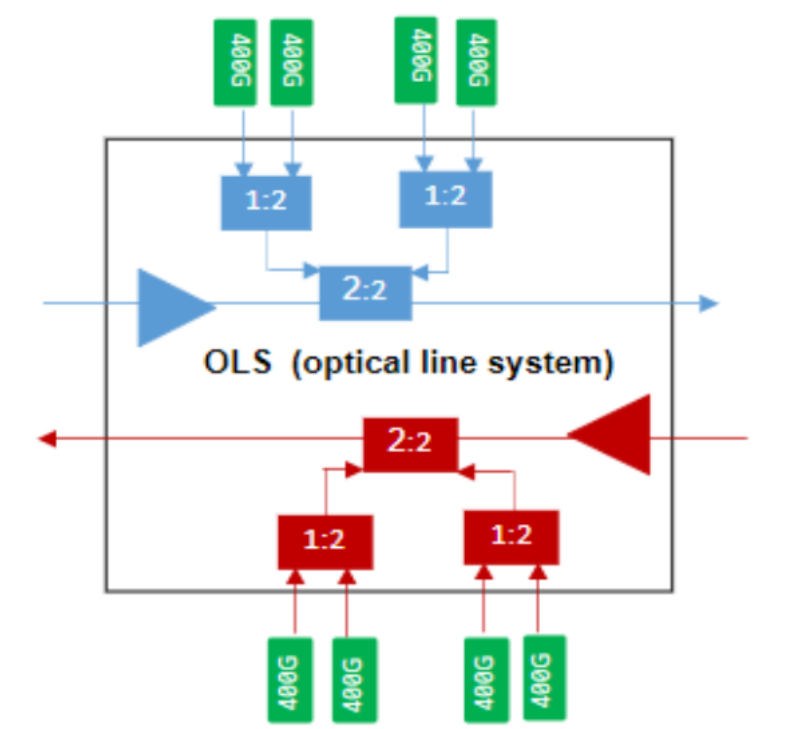

Figure 7.1-2: Optical Line System implementation.

This solution directly contributes to SEASON project objectives by enabling cost-effective scalability, energy efficiency, and operational automation in optical access and aggregation networks. It addresses key challenges in IP-over-WDM deployments where installing per-node monitoring equipment is impractical, offering a centralized and automated approach that improves reliability and reduces operational costs. Furthermore, the architecture supports sustainability goals by minimizing energy consumption through optimized amplifier operation.

7.1.1 P2MP Bidirectional Transmission

The physical layer of the RAN fronthaul is a cornerstone of high-performance and scalable 5G deployments. In disaggregated RAN architectures, it interconnects virtualized distributed units (vDUs) with remote radio units (RRUs), relying on a robust optical transport infrastructure to meet demanding requirements in bandwidth, latency, and synchronization. As depicted in Figure 7.13 this layer comprises transceivers, optical fibers, splitters, amplifiers, and optical line system (OLS) components. These elements enable bidirectional high-speed data transmission through technologies such as WDM and 400G optical modules.

With the ongoing evolution toward centralized and open RAN models (C-RAN, O-RAN), the physical layer must accommodate more complex and flexible architectures, including various functional splits and support for massive MIMO. Technologies like eCPRI, SDN, and NFV further push the need for adaptable, efficient, and power-conscious transport solutions. The illustrated network diagram highlights the orchestration of wavelength channels, signal integrity management, and the bi-directional flow of traffic, laying the groundwork for the enhanced architecture described in the next section.

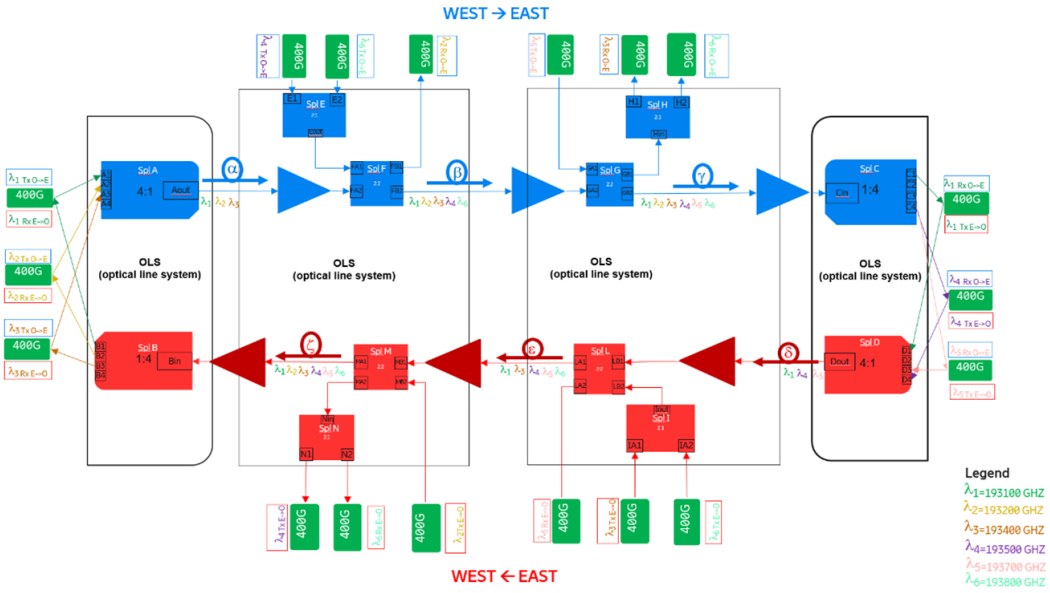

Figure 7.1-3: Optical network designed to handle the high-speed data transfer necessary for a RAN fronthaul.

As part of our activities on fronthaul network, we designed, implemented, and validated an upgraded optical network architecture that delivers significant gains in infrastructure efficiency and energy savings. This new setup (Figure 7.14) interconnects two hub nodes (HUB 1 and HUB 2) via two intermediate leaf sites (LEAF 1 and LEAF 2), forming a bidirectional ring topology using XR transceivers and 2×2 passive optical splitters. The network spans a total distance of 70 km (20 km + 15 km + 15 km + 20 km), with all links tested under realistic optical power conditions.

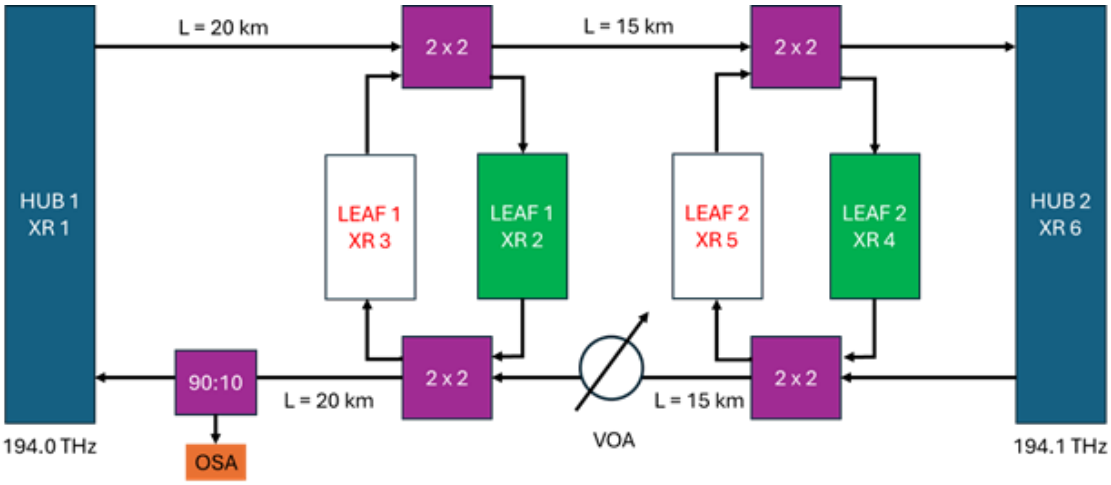

Figure 7.1-4: Optical network designed to handle the high-speed data transfer necessary for a RAN fronthaul using P2MP.

By adopting P2MP-capable XR pluggable modules, we successfully reduced the number of transceivers from 12 to 8—cutting the number of interfaces by one-third—while maintaining full bidirectional connectivity and redundancy. This modular design supports scalability, allowing the integration of up to 10 XR transceivers and additional leaf nodes with minimal architectural changes. The system is also amplifier-ready, though the current implementation operates entirely without EDFAs. The higher optical output of the XR modules (+0 dBm) enables extended reach—25 km more than the previous setup—while maintaining a balanced optical budget across all nodes. Additionally, the number of splitters was reduced by eight, further minimizing insertion losses and improving signal quality.

One of the most impactful outcomes is the substantial reduction in energy consumption. The XR-based design consumes 184 W (6 × 23 W + 2 standard XR), compared to 274 W in the earlier configuration (12 × 22 W plus 10 W for EDFA), achieving a 32.8% energy saving. This result demonstrates a tangible step toward sustainable and efficient transport design for next-generation mobile networks. The resulting network is not only fully operational and extensible but also sets a solid foundation for future deployments that prioritize energy efficiency, scalability, and advanced optical performance.

7.2 MID-HAUL FOR 6G RAILWAY AND HIGHWAY EXPLOITING SMART NIC (RELATED TO C3.9)

In Deliverable D2.3, a techno-economic use case is presented, focusing on providing high-bandwidth, low-latency, and highly reliable mobile radio connectivity along a railway line or motorway section. The study investigates the use of SmartNIC/Data Processing Unit (DPU) cards in servers—within the O-RAN and Cloud RAN perspectives—for a railway 5G/6G coverage scenario. This approach is explored as an alternative to traditional Radio Access Network (RAN) architectures that rely on legacy equipment for both RAN (e.g., aggregated BBUs) and transport

(e.g., cell-site routers). The overall objective is to analyze and assess the technical feasibility and potential economic benefits of deploying DPUs in this specific context.

This deliverable, which focuses on data plane solutions and prototypes, presents the experimental component of the study that demonstrates the viability of using a DPU-equipped server to handle mid-haul traffic in an O-RAN architecture. The goal is to show that the cell-site gateway (router) can be eliminated, as the two ports of a single DPU are sufficient to manage the traffic flows. Specifically, one port receives the traffic from the upstream station, the DPU terminates the traffic destined for the local RUs at the host and forwards the remaining traffic towards the downstream RUs through the second port. In this way, the cell-site router is no longer required, simplifying the architecture, the number of O/E/O conversions, and reducing equipment costs.

An experimental testbed, consisting of two commercial servers equipped with PCIe 5.0 buses and DPUs, was used to evaluate a 5G infrastructure scenario. Each DPU (NVIDIA Bluefield 2) includes 2 ports at 100Gb/s. This is visualized in Figure 7.2-1

Table 7.2-1: Offered and actual traffic throughput for both local RU termination and pass-through traffic across different packet sizes.

Pack size [bytes]	Offered - Local RUs [Gb/s]	Offered - Pass-through [Gb/s]	Actual - Local RUs [Gb/s]	Actual - Pass-through [Gb/s]	Actual - Total traffic [Gb/s]
1518	10	80	10	80	90
1518	80	10	80	10	90
512	10	80	10	80	90
512	80	10	80	10	90
128	10	80	10	70	80
128	80	10	80	10	90

The table compares the offered and actual traffic throughput for both local RU termination and pass-through traffic across different packet sizes. For large packet sizes (1518 bytes and 512 bytes), the system achieves full line-rate performance, matching the offered traffic for both local and pass-through flows. This confirms that the DPU can efficiently handle simultaneous local termination and forwarding at high aggregate rates (up to 90 Gb/s) without degradation.

However, for smaller packet sizes (128 bytes), a minor throughput drop is observed in the pass-through traffic, where the actual rate reaches 70 Gb/s instead of the offered 80 Gb/s. This reduction is due to the increased per-packet processing overhead associated with handling a higher packet rate at smaller sizes. Despite this, the DPU continues to sustain the full offered traffic for local RU termination, demonstrating its capability to maintain local processing performance.

Overall, the results validate the feasibility of using a DPU-based architecture to simultaneously terminate local RU traffic and forward downstream traffic without the need for a cell-site router, even under high-throughput conditions.

Beyond throughput, which was the main focus of this experiment, adopting a DPU-based architecture also enables the integration of additional network functions directly in hardware. These include enhanced security features (e.g., traffic filtering, encryption), traffic monitoring, and programmable offloading capabilities, which contribute to a more flexible, secure, and efficient RAN infrastructure.

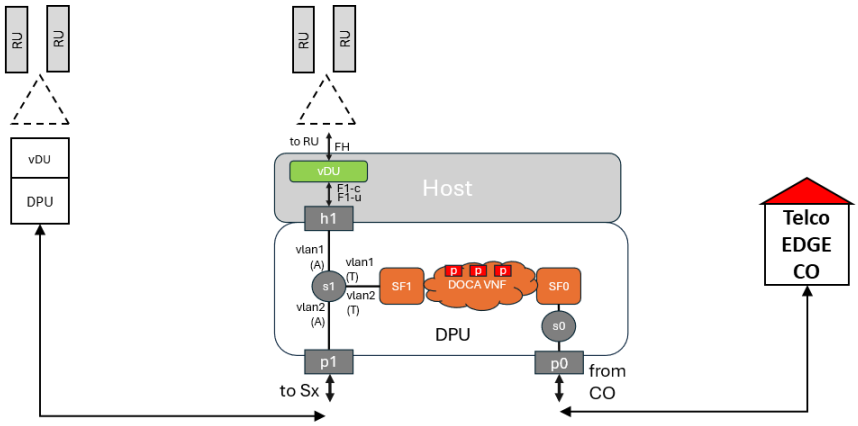

Figure 7.2-1: On the left the scheme of the proposed 5G infrastructure employing programmable DPUs as evaluated in CNIT experimental testbed, employing two commercially available servers equipped with PCIe 5.0 bus. On the right the bypass throughput n function of packet size.

Parallelly to the experimental activities on advanced transport architectures, a simulation-based study has been carried out focusing on the wireless performance of mobile access networks in high-mobility scenarios, with reference to the target railway environment. The goal of this effort is to quantify the bandwidth, and latency demands that next-generation mobile access networks impose on the underlying transport layers—particularly the fronthaul and midhaul segments—and to understand how different RAN configurations impact the overall system dimensioning and cost. The railway environment represents a particularly challenging use case, due to the combination of fast user mobility, strict coverage continuity requirements, and heterogeneous traffic patterns. Within this context, our simulation campaign focused on the evaluation of achievable data rates under different RAN deployment options, providing essential inputs for techno-economic trade-offs and infrastructure planning.

The simulation setup considers a linear railway topology, where Radio Units (RUs) are regularly spaced along the track and serve user equipment located onboard trains travelling at 300 km/h. Each RU is connected to a centralized or distributed DU node depending on the architecture under evaluation. Key parameters varied during the simulations include the channel bandwidth (20 MHz, 50 MHz, and 100 MHz), the MIMO configuration (SISO, 2×2, 4×4, 8×8), and the RU inter-site distance. The objective was to assess how these factors influence the achievable downlink throughput for a single train in motion, under realistic channel conditions that account for Doppler effects, path loss, and fading. The results demonstrate how increased spectral bandwidth and MIMO parallelism can compensate for the adverse propagation conditions typical of high-speed scenarios, albeit with diminishing returns at large inter-site distances.

The updated throughput curves, shown in Figure 7.2-2, reveal that with 100 MHz and 4×4 MIMO, the system can deliver downlink rates exceeding 500 Mbps per RU under optimal positioning, even in the presence of high-speed mobility. Conversely, with narrower bandwidths or simpler MIMO configurations, performance drops significantly, suggesting tighter site spacing or lower service guarantees. These results are critical for transport layer dimensioning: assuming O-RAN split 7.2, such throughput values translate into fronthaul requirements reaching up to 10 Gbps per site. This directly impacts the number and capacity of optical interfaces, the need for midhaul aggregation, and the potential benefits of employing advanced NIC/DPU platforms. Furthermore, the findings guide the identification of performance bottlenecks, resilience needs, and coverage vs. capacity trade-offs in real deployment environments, ultimately reinforcing the integration objectives of the SEASON architecture for high-mobility and infrastructure-constrained use cases.

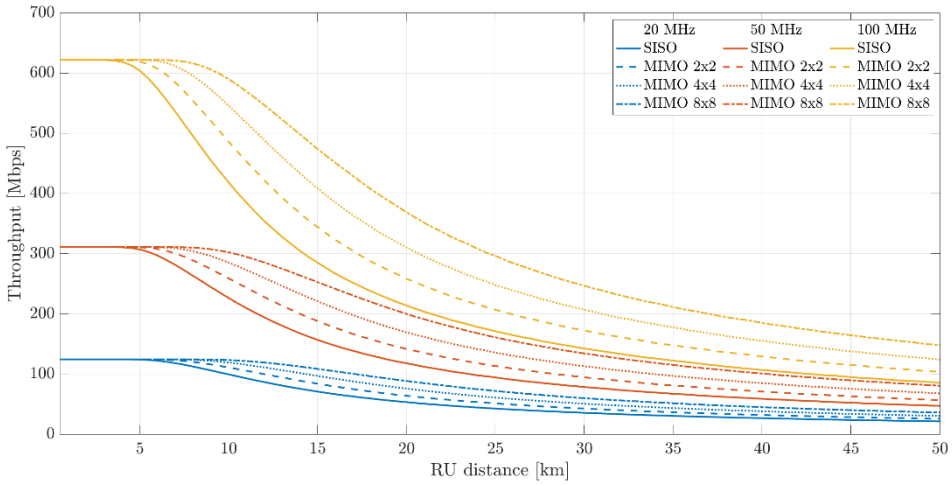

Figure 7.2-2: Analysis of radio performance for different Railway system configurations.

Dissemination Level	Public

8 OPTICAL MONITORING AND POWER EFFICIENCY IN SEASON NETWORK ARCHITECTURE

8.1 NEED FOR IMPROVED NETWORK MONITORING (RELATED TO C3.7)

Ongoing advancements in optical communication continue to focus on increasing transmission capacity per link. Key strategies include improving spectral efficiency, extending the usable wavelength range through multi-band transmission, and implementing space division multiplexing (SDM). These technological enhancements are now being complemented by initiatives aimed at optimizing the utilization of existing infrastructure. As illustrated in Figure 8.1-1, maximizing the efficiency of using the installed resources is becoming increasingly critical. Additionally, improving the availability of existing infrastructure significantly contributes to consistent and reliable network performance, thereby supporting the growing demand for data transmission.

Service flexibility is achieved through several core techniques. One such approach is the dynamic allocation of network resources, which enables energy-efficient operations and is facilitated by real-time adaptive routing to optimize performance. Furthermore, the concept of offering optical spectrum as a service introduces customizable bandwidth provisioning, allowing networks to meet diverse service requirements effectively.

The successful implementation of these improvements necessitates comprehensive monitoring of optical networks. Transparent transmission across multi-operator networks requires the ability to assess signal quality at transition points to ensure accountability for errors. Enhanced infrastructure availability also depends on sophisticated quality monitoring systems. This is equally important for the flexible provisioning of optical bandwidth, where compliance with interference-avoidance specifications must be continuously verified. Moreover, incorporating energy consumption into routing decisions demands the collection and analysis of additional physical parameters.

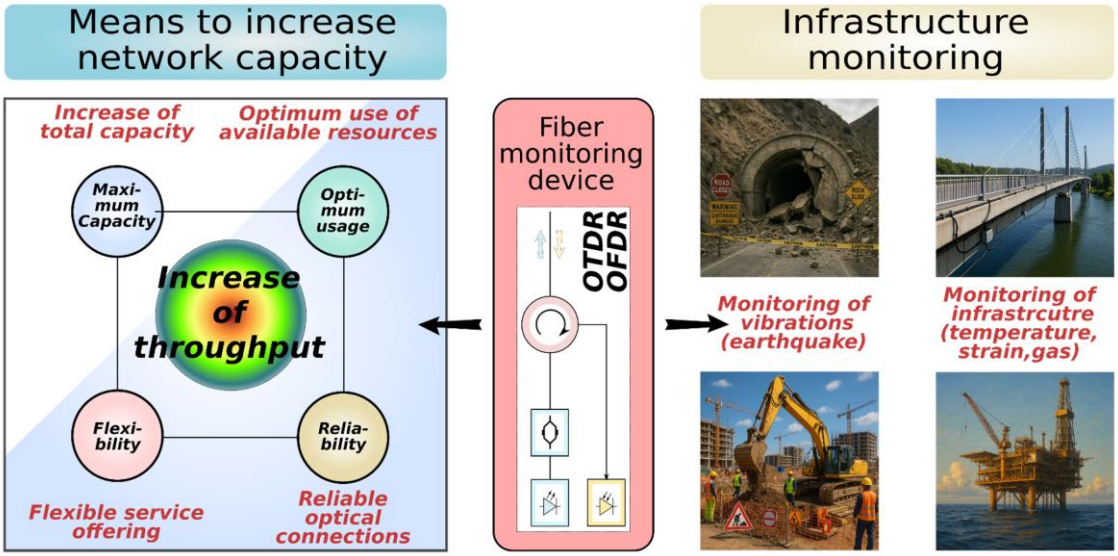

Figure 8.1-1: Dual use: Fiber sensing in the installed and depreciated fiber infrastructure is used for securing and optimizing data transmission and for infrastructure monitoring.

In addition to monitoring network performance and facilitating data transmission, network operators are increasingly recognizing a secondary application of fiber monitoring: the use of installed fiber infrastructure as a sensor system. Independent of its role in network operations, optical fibers can be utilized to gather environmental data—such as detecting seismic activity caused by earthquakes.

This capability opens new opportunities for network operators to generate revenue by offering the collected environmental data on the market. The dual use of fiber infrastructure not only enhances operational efficiency but also creates added value beyond traditional telecommunications services.

8.2 POWER EFFICIENCY ENABLED BY DSCM (RELATED TO C3.10 AND C3.11)

DSCM and P2MP enable all-optical traffic aggregation as shown in Section 5. This may result in huge benefits in terms of energy efficiency and, consequently, also on cost savings, as presented in [Cas25]. To evaluate the energy saving benefits of the proposed approach based on DSCM and P2MP (i.e., optical aggregation), we analyze the energy consumption of a router (handling up to 10 × 400G QSFP-DD service ports). In particular, power consumption measurements of an IPoWDM device are presented. The measurements were done every 15 seconds through command line interface. Note that the power consumption of the equipment without traffic and without any connected pluggable is ~226 W. Then, pluggables are connected: when a single 100G QSFP28 pluggable is connected, the energy consumption increases by ~4 W whereas adding one 400G CFP2 pluggable increases the energy consumption by ~22 W.

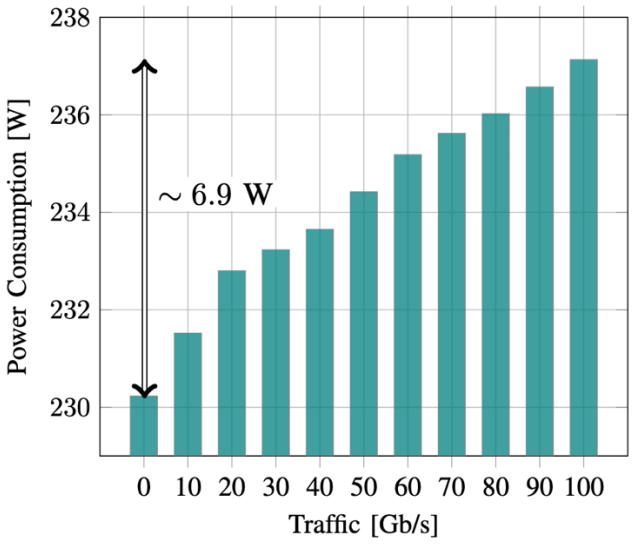

Figure 8.2-1: Router power consumption.

Then, tests have been done to assess energy consumption depending on traffic when the equipment is configured with 1×100G pluggable connected. Traffic has been increased by 10 Gb/s every 5 minutes. The energy consumption is reported in Figure 8.2-1. As it can be seen, by adopting optical aggregation and avoiding some of the edge routers, savings of > 230W can be achieved at each aggregator node. The impact is significant considering that, for example, in Italy there are ~3000 aggregation nodes [D2.1], each of them equipped with one or more routers.

The energy savings achieved by all-optical aggregation also reflect into cost savings: assuming 0.2€/kWh as the cost of energy and the (conservative) router power consumption of the idle case, an annual operational expense savings of 1.2M€ can be achieved.

8.3 ENHANCING MONITORING CAPABILITIES IN MB NETWORKS (RELATED TO C3.2, C3.6, AND C3.7)

One of the key elements in monitoring and optimizing network performance is tracking the communication signals across the various links in the network. As network infrastructures grow in complexity and scale, they are expected to dynamically adapt to changing traffic demands and network conditions. This requires a deep, continuous understanding of network performance. Therefore, robust performance monitoring is critical to maintaining service quality, optimizing resource allocation, and quickly addressing potential faults.

Traditional monitoring methods are often intrusive, relying on instrumentation that can disrupt network operations or limit flexibility. To overcome these challenges, non-intrusive performance monitoring solutions have emerged as a vital research area. These solutions allow network owners and operators to gain comprehensive insights into network behavior without compromising service integrity or increasing deployment costs [Fab18].

Within the SEASON project, we have developed tools that extract network performance knowledge from the optical spectrum, following the concept outlined in [Fab18]. We utilize performance monitoring probes that measure polarization-resolved spectra with high resolution (10 MHz), covering the S, C, and L bands.

After acquiring the polarization-resolved spectra, we apply signal processing algorithms to derive key performance indicators. Our focus is on estimating the optical signal-to-noise ratio (OSNR) for each signal present in the spectrum. This is done by combining the power values of each channel with corresponding noise power values in a common reference bandwidth (usually 0.1 nm).

Estimating noise power is challenging, as filtering effects can mask it, preventing direct measurement [Cha10]. To address this, we explore different methods:

1. Noise estimation at channel edges: We assume the space between the adjacent channels and the target channel reflects the noise. We calculate the overall power spectral density and estimate noise as the average of noise power at the channel's lower and upper edges.
2. Polarization null method: Implemented digitally, this method iteratively transforms the state of polarization to minimize one component that ideally contains only noise when the target channel has high polarization [Cha10].
3. Degree of polarization method: This method estimates OSNR based on polarization degree but was discarded due to poor accuracy for OSNRs above 10 dB.

We conducted studies using the experimental setup shown in Figure 8.3-1. An intensity-modulated OFDM signal is generated using a Mach-Zehnder modulator driven by a 64 GSa/s arbitrary waveform generator. The optical signal is attenuated with a variable optical attenuator and amplified by a doped fiber amplifier (DFA) operating in constant power mode. This setup allows varying OSNR from 10 dB to over 30 dB. An optical bandpass filter prevents saturation before signal input to the optical probe. With this, 128 spectra were recovered for different OSNR values and wavelengths; a sample spectrum is shown in Figure 8.3-2.

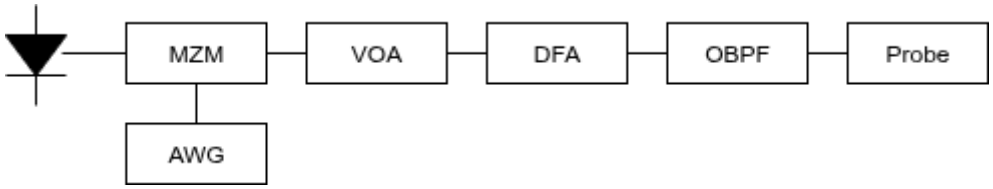

Figure 8.3-1: Experimental setup.

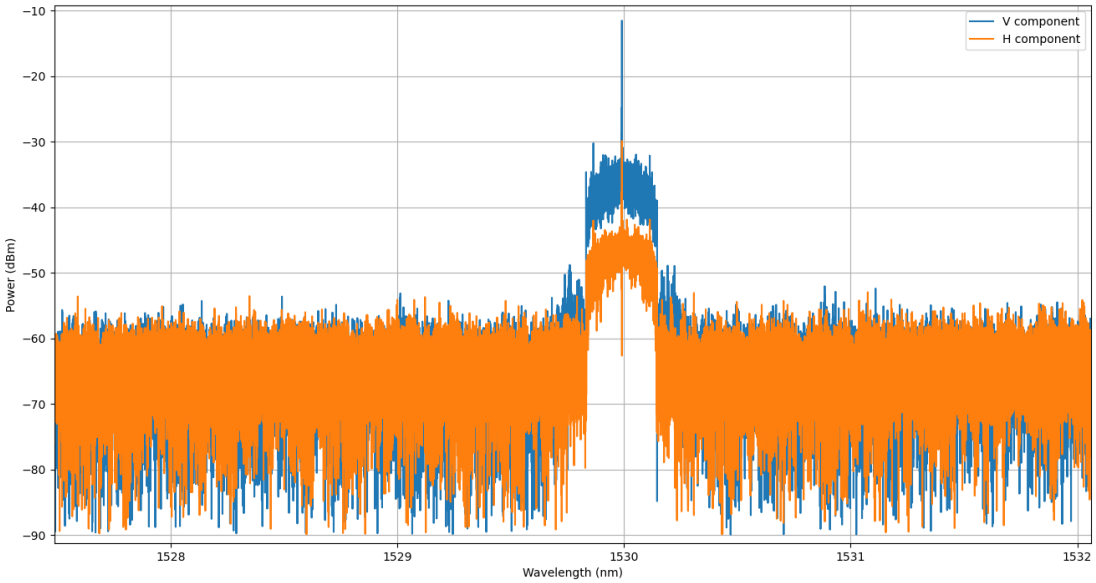

Figure 8.3-2: Sample optical spectrum recovered by the probe.

Results in Figure 8.3-3 show that the first method tends to overestimate OSNR in-band, while the second method may underestimate high OSNR values due to its iterative nature. Therefore, combining both methods might yield better performance.

Our baseline combination uses linear regression, as illustrated in Figure 8.3-3. While effective, this approach can exhibit variance and systematic bias. To improve it, we implemented iterative AI boosting with weighted Ridge regression [Tu05]. The objective was to minimize mean square error between base estimates and the boosted combination. After parameter optimization, results (Figure 8.3-3) indicate the boosted approach reduces variability, with mean error less than 2% compared to linear regression.

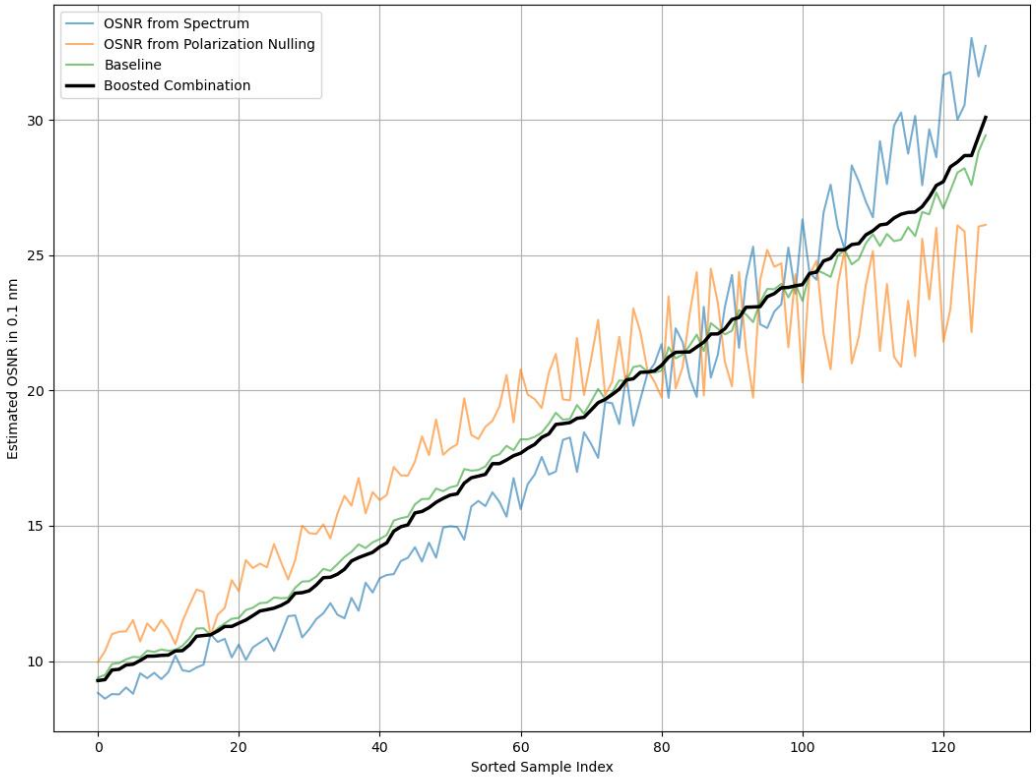

Figure 8.3-3: OSNR estimation results.

In conclusion, effective network performance monitoring is essential for maintaining service quality and adapting to dynamic traffic demands. Traditional intrusive methods limit flexibility, prompting the need for non-intrusive solutions. The SEASON project's approach, leveraging high-resolution polarization-resolved spectra, enables detailed OSNR estimation through advanced signal processing techniques. Among the methods explored, combining noise estimation at signal edges and polarization null approaches offers improved accuracy. Further refinement was achieved through AI boosting with weighted Ridge regression, reducing variability and bias in OSNR estimation. This hybrid method enhances monitoring precision, supporting better network optimization and fault management. Future work may explore additional algorithmic improvements and real-world deployment to further advance non-intrusive telecommunications performance monitoring.

8.4 LONGITUDINAL POWER MONITORING LPM (RELATED TO C3.5, C3.6 AND C3.7)

In modern optical networks, maintaining high service availability and rapid fault detection requires precise insight into the signal behavior along the fiber span. Traditional optical performance monitoring techniques often lack the resolution or sensitivity to detect subtle

impairments or localized power disturbances, especially in long-haul or access network environments. LPM allows accurate mapping of power variations along the transmission link — even for small disturbances below 1 dB. The SEASON project targets this capability by aiming to enhance optical network monitoring through improved resolution and accuracy in longitudinal power profile estimation.

The transmission model used in this work is based on simulating the propagation of an optical signal over a 200-km fiber link, as shown in Figure 8.4-1(a). The transmitter-side DSP generates four independent random sequences, which are then mapped to a dual-polarization (DP) 16-QAM format. Each tributary (XI, XQ, YI, and YQ; where X and Y represent the x- and y-polarization, and I and Q stand for the in-phase and quadrature components) carries $N = 2^{15}$ symbols. Pulse shaping is applied to each tributary using a root-raised cosine (RRC) filter with a roll-off factor of 0.2. The digitally processed signal is then passed to a digital-to-analog converter (DAC), operating at a fixed symbol rate of 128 GBd—except in subsection A, where different symbol rates ranging from 32 GBd to 128 GBd were explored. The four tributaries are subsequently used to drive a DP-IQ modulator. A continuous-wave (CW) laser with a linewidth of 100 kHz and a center frequency of 193.4 THz (approximately 1550 nm) provides the optical carrier, resulting in a modulated DP-QAM signal.

For fiber transmission simulation, the signal is oversampled at a factor of 8 relative to the symbol rate, and the split-step Fourier method (SSFM) is used to numerically model the fiber link. The SSFM simulation uses a spatial step size of 1 km to strike a balance between accuracy and computational efficiency. The optical link consists of a booster amplifier with an output power of 5 dBm per channel, followed by four 50-km spans of standard single-mode fiber (SMF). Each span includes an in-line optical amplifier. The fiber parameters used in the simulation are typical: an attenuation of 0.2 dB/km, chromatic dispersion of 16.47 ps/(nm·km), and a nonlinear coefficient of 1.1 $W^{-1}km^{-1}$. The amplifiers operate with a fixed output power of 5 dBm and a noise figure of 5 dB.

To model polarization effects commonly encountered in real systems, a random polarization rotation is applied to the optical signal at the end of the link. These effects, which include fiber bending, mechanical stress, and environmental influences, dynamically alter the state of polarization during transmission. On the receiver side, the signal is filtered using an optical bandpass filter (OBPF) centered at 193.4 THz with an 80 GHz bandwidth and then processed by an ideal coherent receiver front-end. Demodulation is carried out using a local oscillator with a 10 MHz frequency offset relative to the transmitter laser and a linewidth of 100 kHz. After that, the signal is resampled to 2 samples per symbol via the analog-to-digital converter (ADC) and forwarded to the receiver DSP for further processing.

Figure 8.4-1(b) shows the Rx-DSP chain used in this study. Following resampling, the signal is matched filtered and compensated for chromatic dispersion (CD). Polarization demultiplexing is then applied to correct for the random polarization rotation introduced during transmission. Carrier frequency recovery follows, correcting for any frequency offset between the transmitter laser and the local oscillator. Next, blind carrier phase recovery is performed using a blind phase search algorithm to mitigate phase noise due to the laser linewidth. Once this preprocessing is

complete, the signal is split into two branches, referred to as Tributary I and II in Figure 8.4-1(b), to be used for LPM computation.

In the implemented scheme, Tributary I is processed to make symbol decisions and generate a reference waveform A [0, n]. This reference is then used to calculate the regular perturbation coefficient vector G_k, representing how each fiber segment contributes to the received signal. Tributary II, on the other hand, is used to create an equivalent signal sequence A_1, which accounts for accumulated CD and nonlinear effects in the link. The power value associated with each fiber segment is estimated by minimizing a cost function involving G_k and A_1.

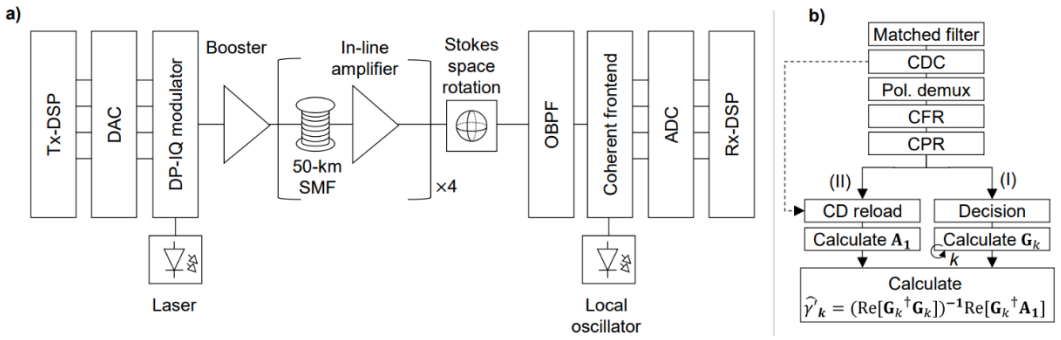

Figure 8.4-1: (a) Schematic of the transmission model used in the numerical simulations of this paper. (b) Rx-DSP structure based on the LLS method for estimating the LPM of the proposed transmission model. CD: chromatic dispersion. CDC: chromatic dispersion compensation. CFR: carrier frequency recovery. CPR: carrier phase recovery.

To demonstrate LPM's ability to detect physical-layer disturbances, Figure 8.4-2 presents simulation results showing how the LPM output changes in the presence of fiber taps, simulating also power drops across the optical line system, using standard optical couplers. In particular, the impact of 90:10, 75:25, and 50:50 couplers are studied, which introduce losses of 0.46 dB, 1.25 dB, and 3.00 dB, respectively. These values represent varying levels of stealth in a fiber-tapping scenario: from low-impact intrusions (0.46 dB) to blatant attacks (3 dB). It is important to note that inserting such couplers usually requires physical access and may interrupt transmission unless done during maintenance windows. However, an attacker could alternatively use a clip-on coupler based on micro-bending, which typically causes losses of around 0.8 dB without any service disruption.

Figure 8.4-2(a) shows the reference LPM power profile during normal system operation, which closely matches the actual simulated power, validating the LPM's accuracy in undisturbed conditions. Figure 8.4-2(b), (c), and (d) show how the LPM trace changes when 10%, 25%, and 50% of the light is tapped at the 75 km point. In each case, a visible drop in the LPM signal is observed, with greater tap ratios causing larger deviations. The figure includes a black dashed line indicating the expected LPM profile under normal conditions (extracted from Figure 8.4-2(a)), against which the distorted profiles are compared. Even in the 0.46 dB case (Figure 8.4-2(b)), the LPM deviates from the baseline, revealing a detectable gap.

To quantify these observations, Figure 8.4-2(e) compares the relative loss from each attack case to the baseline LPM trace. Both the actual loss and the Rx-based estimation are plotted, with solid lines (LPM-based) closely following the dashed lines (actual loss). While the LPM-based

estimates are slightly smoother, they show a clear trend and converge to the expected loss levels. For example, the red solid line shows that even the subtle 0.46 dB drop is accurately captured from 76 km onward.

Finally, Figure 8.4-2(f) presents the first-order derivative of the relative loss, showing where the most significant deviations occur along the fiber. In all three attack scenarios, the peak derivative values are either exactly at or very near the actual tap location, demonstrating LPM's ability not only to detect fiber taps, but also to localize them with high accuracy (sub-km). This further confirms the technique's suitability for real-time physical-layer monitoring, intrusion detection or any various power drop cases.

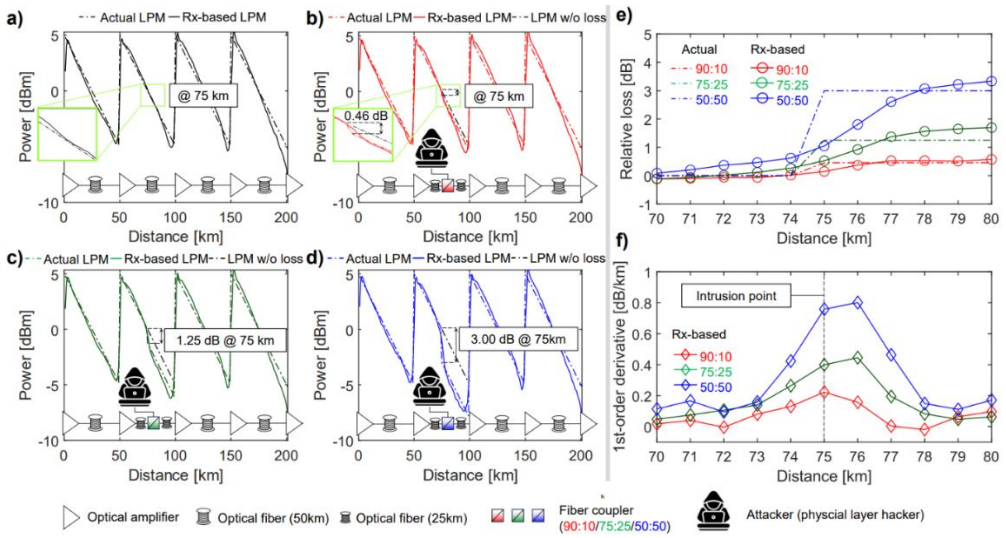

Figure 8.4-2: (a) Actual LPM vs estimated LPM. Actual LPM vs estimated LPM with emulated power drop at 75 km with values of (b) 0.46 dB, (c) 1.25 dB, and (d) 3 dB. (e) Zoomed-in LPM tracking the emulated relative loss (power drop) in the vicinity of 75 km. (f) Anomaly tracker through 1st-order derivative of (e).

8.5 DIGITAL SIGNAL PROCESSING – GROUP VELOCITY DISPERSION (RELATED TO C3.5)

The current work on optimized DSP for metro and core coherent applications is making strides toward supporting up to 1.6 Tb/s per port, aligning with the demands for future pluggable modules under the emerging 1600ZR standard. A key focus is the integration of novel low-power DSP architectures, specifically those employing frequency domain (FD) filtering for first order and second order group velocity dispersion (GVD) compensation—a computationally intense task within DSP.

In Section 6.4 from D3.2, the FD filter architecture uses FFT and IFFT to facilitate GVD compensation by handling signal processing in the frequency domain. However, as symbol rates increase, the complexity and power demands of these DSP operations grow significantly, especially for symbol rates of 120 GBd and higher, due to the substantial increase in taps needed to manage accumulated GVD across longer fiber spans. Testing reveals that for high symbol

rates, such as 240 GBd, complexity rises sharply beyond 100 km, underscoring the need for low-power designs capable of mitigating this power burden.

The CD (Chromatic dispersion) compensator filter complexity scales with the CD impulse response length. For the GVD, this length grows quadratically with the symbol-rate and linear with the total link length. Additionally, second order GVD (SO-GVD) starts to have a relevant impact into the system performance at long link length or high symbol-rates. This can be approximately seen using the dispersion length. The GVD (β_2) dispersion length is defined as the distance where a Gaussian pulse of width (T_0) is broadened by a factor of √2 and is equal to $L_D = {}^{1}/_{R_s^2|\beta_2|}$, where R_s is the symbol rate. Also, the dispersion length associated with the SO-GVD (β_3) is defined as $L_D = {}^{1}/_{R_s^3|\beta_3|}$. Figure 8.5-1 shows GVD and SO-GVD L_Ds as a function of the wavelength (λ) for a measured ITU-T G.652D fiber.

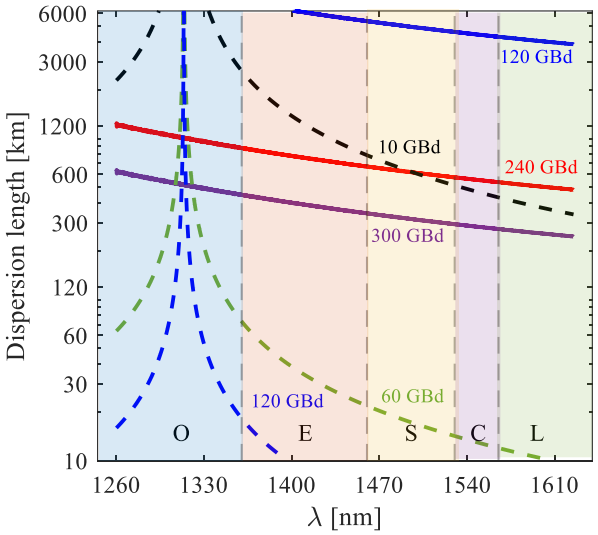

Figure 8.5-1: GVD and SO-GVD dispersion lengths at different λ. Dashed ∠D for GVD, solid ∠D for SO-GVD.

We can see that the L_D decreases as the symbol rate increases. For 240 GBd we can observe SO-GVD L_D comparable to the GVD L_D of legacy 10 GBd generations. Since for next-generation coherent transceivers the target symbol-rate is potentially 240 GBd single carrier, we studied the complexity impact of SO-GVD for next generation coherent transceivers. From Figure 8.5-1 we can also expect a higher SO-GVD impact at higher wavelengths. As an example, this implies that the SO-GVD impact is higher in the L-Band than in the O-Band.

We developed a formula to approximate the total memory in samples required by a SO-GVD compensation filter (K). As mentioned, the complexity of the CD compensator scales with the impulse response length. We calculated the impulse response associated to the SO-GVD as shown in Eq. 3, where Ai(k) = 1/(2π) $\int_{-\infty}^{\infty} \exp\left(j(x^3/3 + xk)\right) dx$ is the Airy function.

$$H_3(t, L) = \sqrt[3]{2/(|\beta_3|L)}\, \mathrm{Ai}(-\sqrt[3]{2/(\beta_3 L)}\, t) \qquad \text{Eq. 3}$$

Sampling at a sampling frequency f_s, such as k=t*f_s, we obtain the approximated memory in samples occupied by the SO-GVD impulse response given by Eq. 4 with $K^+ = 3.5053\sqrt[3]{|\beta_3|L/2}\, f_s$ and $K^- = |\beta_3|L\pi 2 f_s^3/2$.

$$K = |K^+ + K^- + 1| \qquad \text{Eq. 4}$$

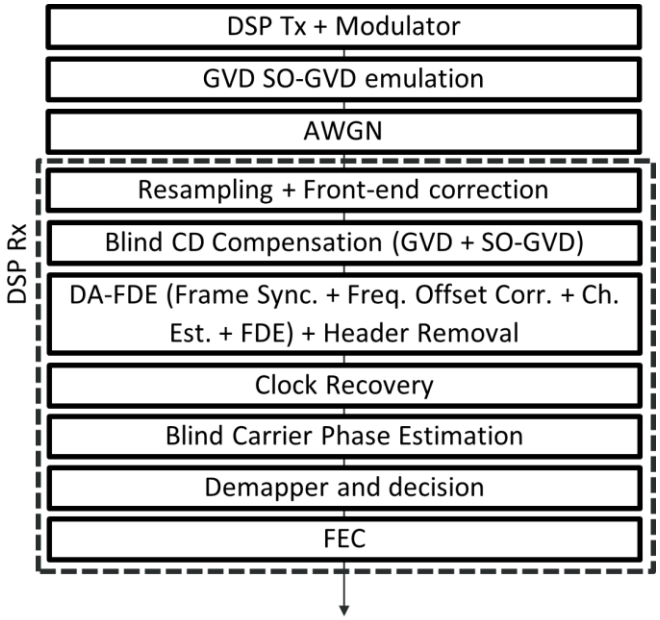

Figure 8.5-2: Block diagram of the considered setup.

Figure 8.5-2 presents a simplified block diagram of a data-aided (DA) coherent optical communications system considering a transmitter DSP (DSP Tx), a channel (Modulator, GVD and SO-GVD emulation, AWGN and resampling) and a receiver DSP (DSP Rx). A blind chromatic dispersion (CD) compensator compensates for the GVD and potentially for the SO-GVD. A dynamic data-aided frequency domain equalizer (DA-FDE) compensates the impact of the PMD and other channel impairments. It also corrects for the frequency offset. When the blind CD compensator compensates only for the GVD, then the DA-FDE compensates for the SO-GVD with enough memory (Number of taps). On the other hand, when the blind CD compensator compensates for the GVD and the SO-GVD, the DA-FDE can be designed with a lower number of taps, what translates in a lower complexity.

Figure 8.5-3 shows complexity—quantified by non-trivial complex multiplications—as a function of R_s in the L band (λ = 1600 nm), comparing static SO-GVD compensation disabled (dashed) versus enabled (solid). We considered a mean DGD of 10 ps, fs=1.5Rs and 3% of header overhead. For the DA-FDE and the CD compensator, overlap-save method with 6% and 50% respectively are considered. The figure shows that for R_s higher or equal than 120 GBd, a static SO-GVD compensator can significantly reduce the complexity compared to dynamic (DA-FDE) compensation.

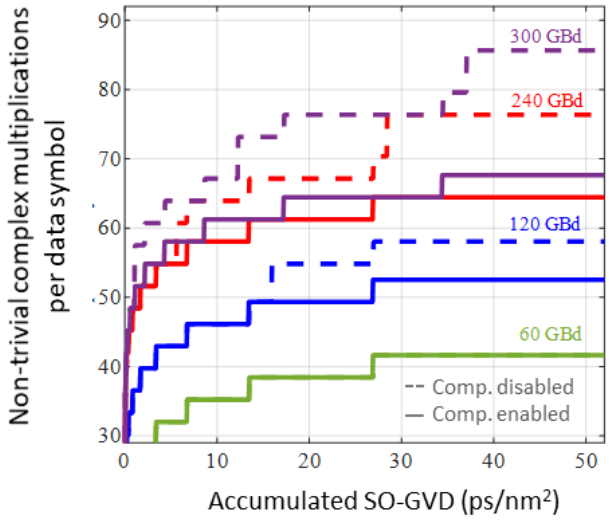

Figure 8.5-3: Complexity, measured by the number of non-trivial complex multiplications, versus R_s for the L band (λ = 1600 nm), with static SO-GVD compensation off (dashed) and on (solid).

8.6 Transceiver Count Reduction in Filterless Metro-Aggregation Networks Using DSCM (related to C3.11)

The capability of DSCM to combine traffic and aggregate leaf nodes in a P2MP configuration can be exploited by network operators to design networks that are not only flexible in terms of dynamic operation, but also efficient with respect to the hardware (e.g., transceivers, amplifiers, etc.) that would need to be used for greenfield or brownfield deployments. Following this, being mindful about the devices and the dimensioning of the deployment, we can reduce the capital expenditures (CAPEX) across the network.

To draw general conclusions about the conditions and eventual deployment implications in the metro-regional domain of the network, we have developed a numerical tool that generates network scenarios based on a filterless architecture and random topological data [D2.2] such as number of horseshoes, number of leaf nodes, distances between nodes, traffic volume, growth rate and/or fluctuations of the traffic demands over time [Cas24, Cas25-2].

The objective of our present study is to quantify the impact that optical aggregation and changes in traffic have on the overall system performance and on the corresponding amount of necessary pluggable transceivers according to a pay-as-you-grow approach. Furthermore, by comparing to more traditional single-carrier point-to-point (P2P) coherent solutions, we give insights into the required costs of DSCM-based transceivers to produce cost-efficient deployments. In this regard, Figure 8.6-1 summarizes the operation on a filterless optical system in a P2P and in a P2MP configuration. In the former, the transceivers at the leaf nodes communicate with book-ended counterparts at the hub node. In the illustration, this is highlighted by different transceivers being represented as different colours. On the other hand, in a P2MP scheme, a single source can communicate with multiple endpoints simultaneously.



Figure 8.6-1: Simplified diagrams for a horseshoe network topology (disregarding the protection hub node) in a (a) P2P and (b) P2MP operation.

The implication behind this technique is that a hub node transceiver not only can communicate with multiple leaf nodes within a single horseshoe, but also with leaf nodes across different horseshoes provided that the bandwidth is sufficiently large to establish a link [Cas23]. Previously, to quantify how bandwidth resources (i.e., digital subcarriers (DSCs)) are allocated to the various leaf nodes across the available horseshoes, we introduced a metric called 'aggregation level' to covey the degree of connectivity in the network in relation to the transceiver(s) at the hub node.

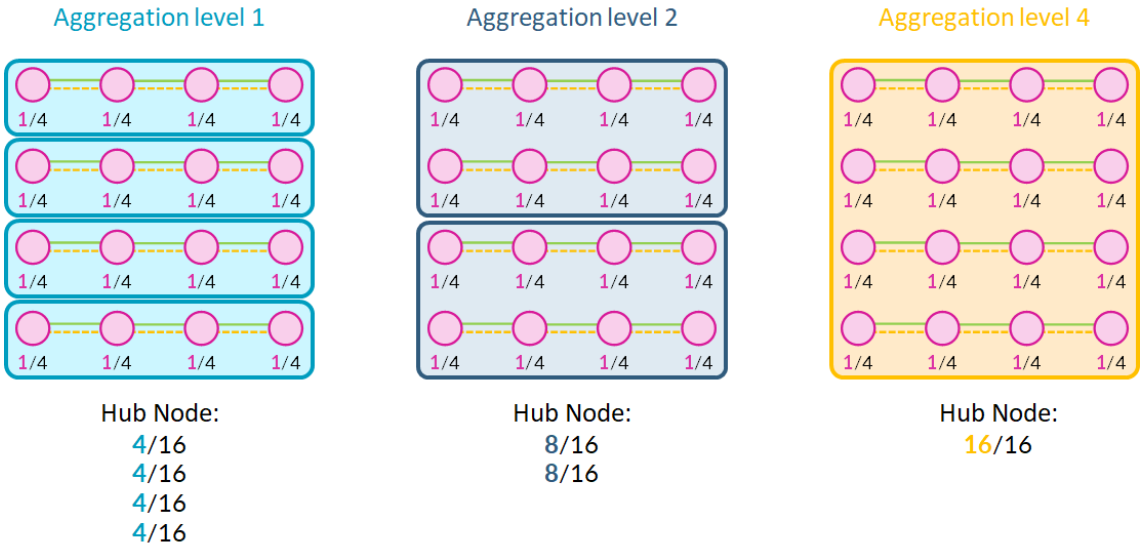

Figure 8.6-2: Visual representation of aggregation levels in a four-horseshoe network. For simplification, the hub node has been removed from this figure, and the traffic demands of each leaf node ( ) can be addressed by the bandwidth provided by a single DSC (i.e., 25 Gb/s).

In the scenario we investigate, the DSCs exhibit a capacity of 25 Gb/s (i.e., 4 GBd dual-polarized 16-QAM). While the hub node houses a high-speed unit with a total capacity of 400 Gb/s (i.e., 16 DSCs), at the leaf nodes we would deploy lower-speed units; these transceivers would have a capacity of 100 Gb/s (i.e., 4 DSCs). Figure 8.6-2 illustrates how traffic can be combined and served by a single unit at the hub node. For example, with an aggregation level of 1, each horseshoe connects to a 400G unit at the hub node, causing each of these units to be used at 25% of their total capacity (i.e., 4 out of the 16 available DSCs). As we have available bandwidth, we can funnel more traffic to the same unit at the Hub node; this increases the aggregation level to 2 or even 4, which further reduces the number of units required at the hub node to fully address the traffic demands of the network.

Before carrying out a techno-economic analysis, it is necessary to evaluate the operating conditions of the network. With this in mind, we looked at the OSNR margin, a metric that relates the OSNR conditions of a given optical transmission to the minimum required OSNR of a transceiver for error-free operation, a requirement typically stated in the device specifications. Figure 8.6-3 shows the OSNR margin conditions of a network based on the size of the network and aggregation level as a function of traffic growth (10% and 40% for (a) and (b), respectively). In these graphics, we observe how, as time goes on and traffic increases (i.e., causing us to deploy additional passive components such as splitters and couplers, and transceivers, and to adjust the operating condition of the modules in terms of subcarrier activation), the overall optical performance degrades. Hence, with a larger traffic growth rate, the degradation is more noticeable earlier (see Figure 8.6-3 (b)).

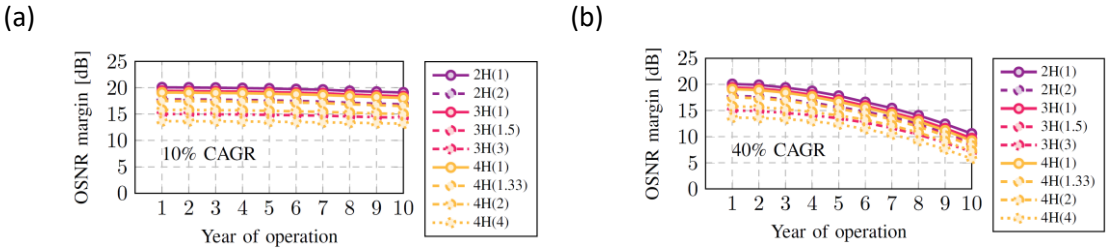

Figure 8.6-3: Average OSNR margin displaying the effects of traffic growth across the years as a function of the size of the network and corresponding aggregation level. The number that precedes the 'H' indicates the number of horseshows in a network and the number in parenthesis, the aggregation level.

In pay-as-you-grow provisioning scenarios, operators decide to deploy new hardware in a network when the need arises; in this case, it would be as the traffic growth approaches within a certain margin of the nominal maximum capacity of the devices. Figure 8.6-4 illustrates the average rate at which transceivers would have to be deployed in the network for both P2P and P2MP deployments under different traffic conditions and aggregation levels.

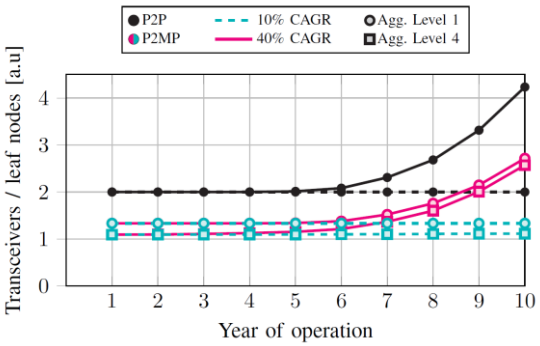

Figure 8.6-4: Transceiver units per leaf node as a function of aggregation level and traffic growth rate.

In this example, we have normalized the number of transceivers to the amount of leaf nodes in the network to allow for networks of different sizes to be compared directly. With single-carrier P2P solutions, at start-of-life conditions, we require an average of two pluggables per leaf node, indicating that one unit is to be deployed at the leaf node and the other one, at the hub; whereas by implementing a P2MP communication scheme, we can reduce this value, as the modules at

the hub node can serve multiple units at the leaf nodes simultaneously. Subsequently, by comparing the colored data (i.e., P2MP) with respect to the data in black (i.e., P2P), we can determine a transceiver reduction rate.

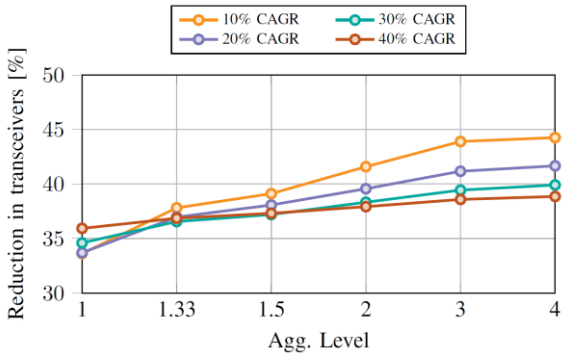

Figure 8.6-5: Reduction percentage in terms of transceivers based on level of aggregation and traffic growth rate.

This so-called reduction rate is displayed in Figure 8.6-5 for the traffic conditions in year 10. Here, the curves reveal that the larges potential for savings is tied to the lower traffic conditions, since we are able to maximize the sharing of bandwidth resources. Conversely, if the volume of traffic increases, the effectiveness of the optical aggregation decreases, as the units at the hub are addressing a smaller subset of leaf nodes.

At this point, we need to highlight that the number of pluggables is not the only metric to consider; we should also focus on technological enhancements (i.e., increased/enhanced functionalities across the network) and development cost of the modules. For this reason, we motivate the consideration of a more tangible hardware acquisition cost, as a metric to compare P2P and P2MP. Now, based on the knowledge regarding the required type and number of transceiver units, we can define Eq. 5, where *N* refers to the deployed number of units of a given transceiver type and *Cost* refers to the corresponding acquisition cost of the unit.

$$N_{P2MP-400G} \cdot Cost_{P2MP-400G} + N_{P2MP-100G} \cdot Cost_{P2MP-100G} \leq N_{P2P-100G} \cdot Cost_{P2P-100G} \quad \text{Eq. 5}$$

Then, to simplify the function even further, we can set the $Cost_{P2P\text{-}100G}$ to 1 and relate all *Cost* variables concerning P2MP to that value, leading to Eq. 6.

$$N_{P2MP-400G} \cdot \alpha + N_{P2MP-100G} \cdot \beta \leq N_{P2P-100G} \quad \text{Eq. 6}$$

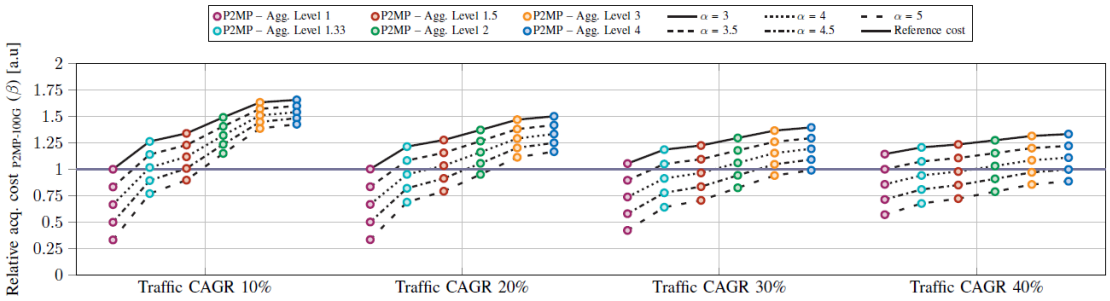

Figure 8.6-6: Average maximum possible relative cost for a DSCM-capable 100 Gb/s transceiver to guarantee cost-efficiency with respect to single-carrier 100 Gb/s coherent solutions. Relative unit costs are presented with respect to the cost of a single-carrier 100 Gb/s transceiver (solid line at value of 1), as a function of the scenario's traffic growth rate and the cost of a 400 Gb/s DSCM-capable module.

After carrying out calculations according to the previous equations, we have summarized the results in Figure 8.6-6. This graph provides us with the necessary guidelines to deploy cost-effective P2MP networks, since the datapoints indicate the necessary cost of P2MP transceivers (for both 400 Gb/s and 100 Gb/s) so that the implementation costs the same as designing the network to use single-carrier 100 Gb/s units. Therefore, cost values below these thresholds would lead to more cost-effective network deployments [Cas25-3]. Interestingly, this is even possible with DSCM-capable modules that are more expensive than their P2P counterparts due to the reduced number of transceivers thanks to the ability to share the total module capacity (i.e., DSCs) among multiple leaf nodes/clients.

8.7 Power Consumption Considerations of Coherent Transceivers in Filterless Point-to-Multipoint Metro-Aggregation Networks with Digital Subcarrier Multiplexing (related to C3.10 and C3.11)

Building on the study presented in previous sections, we refocused our target to understand the implications of the flexibility aspects of DSCM on the power consumption of the network. More specifically, we investigate the flexibility in terms of operational conditions thanks to DSCM and relate it to how much power the pluggable units would consume [Cas24].

Similarly to the CAPEX analysis conducted in previous sections, we generate network scenarios randomly according to general topological characteristics of metro-regional networks. The data corresponds to horseshoe networks and was provided in the form of realistic network examples by Telecom Italia (TIM) [Cas23].

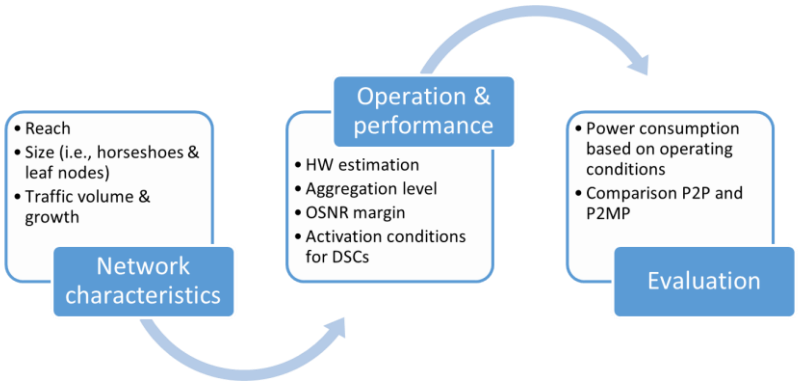

Figure 8.7-1: General concept for the evaluation of the operating conditions of metro-regional network scenarios.

Figure 8.7-1 describes the concept for the network evaluation in terms of power consumption, which is to serve as a proxy for the Operational Expenses (OPEX) of the network scenarios in the simulations. For this study, we begin by extracting the network characteristics and we build a model to determine the necessary hardware (HW), the OSNR margin, and the operating conditions of the transceivers (i.e., dynamic activation of DSCs) for filterless network deployments. Based on these conditions and performance values, we can estimate the number and type of transceiver units for the deployments and by combining this with traffic-dependent operating conditions, we can estimate the power consumption of the modules in the network.

For the analysis, base assumptions are that 100 Gb/s and 400 Gb/s DSCM-capable transceivers will be used to address traffic demands in P2MP configuration for the leaf nodes and the hub node, respectively. For a P2P deployment, on the other hand, we'll exclusively be using single-carrier 100 Gb/s coherent transceivers. In addition, our study presumes that a network will be operational for a given number of years, experiencing traffic increments defined by a compound average growth rate. Then, in accordance with a pay-as-you-grow model for deploying HW, we analyze the traffic demands of the network on a yearly basis and deploy additional transceivers when required. To illustrate this methodology, let is consider the simplified scenario in Figure 8.7-2: a three-horseshoe network without protection path. Here, by having fully flexible DSCM-capable transceivers, we can adjust the bandwidth resources (i.e., DSCs) with a granularity of 25 Gb/s. This leads to a situation at the start of the analysis, in which the HW at the hub node must be able to address a total of eight DSCs divided among eight leaf nodes. Therefore, a single high-speed 400 Gb/s DSCM pluggable at the hub is enough to guarantee connectivity across the complete network.

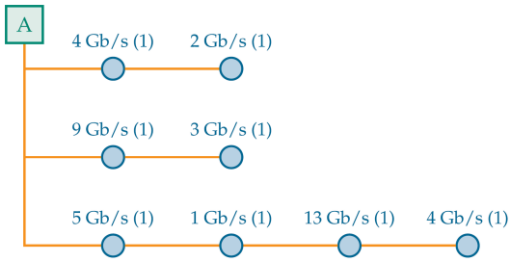

Figure 8.7-2: Model network to illustrate the HW estimation methodology. The text on top of the nodes indicates their traffic demands and the number in parentheses, the required DSCs.

Table 8.7-1: Hardware estimation for simplified model network.

Year	Traffic – (DSCs)	Leaf node transceiver(s)	Hub transceiver(s)
1	41 Gb/s – (8)	8 x 100 Gb/s	1 x 400 Gb/s
2	57 Gb/s – (8)	8 x 100 Gb/s	1 x 400 Gb/s
3	80 Gb/s – (9)	8 x 100 Gb/s	1 x 400 Gb/s
4	113 Gb/s – (9)	8 x 100 Gb/s	1 x 400 Gb/s
5	158 Gb/s – (10)	8 x 100 Gb/s	1 x 400 Gb/s
6	221 Gb/s – (12)	8 x 100 Gb/s	1 x 400 Gb/s
7	309 Gb/s – (16)	8 x 100 Gb/s	1 x 400 Gb/s
8	432 Gb/s – (21)	9 x 100 Gb/s	2 x 400 Gb/s
9	605 Gb/s – (28)	10 x 100 Gb/s	2 x 400 Gb/s
10	847 Gb/s – (38)	12 x 100 Gb/s	3 x 400 Gb/s

Table 8.7-1 expands the HW estimation analysis over a period of 10 years for the model network in Figure 8.7-2. By observing the data, we can see how additional resources must be enabled/deployed at the different nodes in the network as traffic increases. For example, in the third year of operation, an additional DSC must be activated on one of the DSCM-capable transceivers to match the growing traffic. At this point, however, it is important to notice that this does not require additional hardware, since 'new' DSCs can be activated to keep ahead of the traffic demands in terms of bandwidth. Nevertheless, in years 8 and 10, it is no longer possible; here, the growth in traffic causes the required number of DSCs to exceed the capacity of the 100 Gb/s and 400 Gb/s modules. Therefore, additional transceivers must be deployed at the corresponding nodes. Knowing the type of modules and their operating conditions, we can use the measurements of manufactured DSCM transceivers in Figure 8.7-3 (a) and (b) to estimate the energy consumed by the pluggable modules. Figure 8.7-3 (a) shows the normalized power consumption of various probed modules operating at full capacity for different operation modes, while Figure 8.7-3 (b) indicates how the modules' consumption decreases as fewer DSCs are active. The reason behind this dependency is that in the transceiver design, there are elements that could be turned off or that could be working at limited capacity (e.g., FEC, equalizers, clock recovery, among others) when not needed.

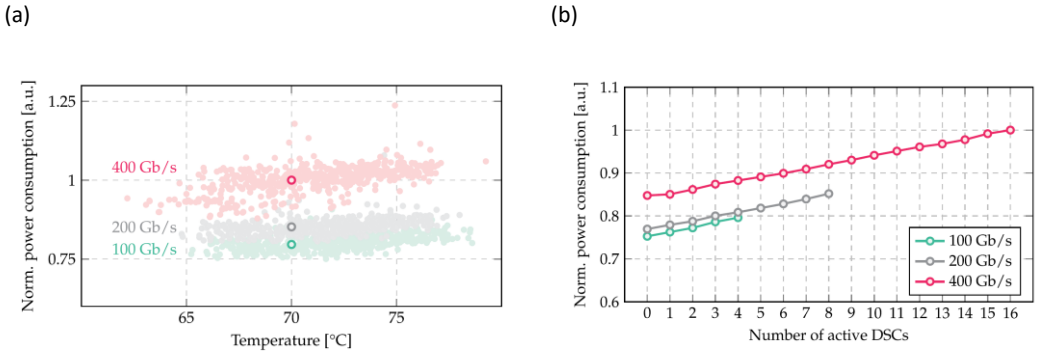

Figure 8.7-3: (a) Measurements from manufactured DSCM-capable coherent transceivers for various operating conditions as a function of the case temperature. (b) Normalized overall power consumption of a DSCM-capable transceiver for different operating conditions as a function of the number of active DSCs.

Before calculating the power consumption of the transceivers in the network, it is important to evaluate the optical performance of the scenario to determine whether the deployment can be realized from an OSNR perspective. The reason for this is the broad subset of network conditions: aggregation level (with their corresponding losses), number of horseshoes, number of leaf nodes, transmitted distance, and number and type of transceiver units, among others. Figure 8.7-4 (a) and (b) illustrate the statistical nature of our analysis by depicting the histogram of OSNR margin values as a function of the year-in-operation; in this depiction, brighter values correspond to more network scenarios that match those OSNR margin values. Our results show the time-dependency of the overall performance: the longer a filterless network remains in operation, due to the increasing traffic demands and the corresponding deployment of new optical devices such as transceivers and splitters/couplers, the more the OSNR of the network degrades. However, please keep in mind that this does not imply that all individual leaf nodes will experience the same level of degradation, but rather that, as more connections experience lower OSNR levels, it is more likely that the limiting OSNR value (i.e., the worst-performing signal in terms of OSNR) is worse than that of a previous point in time. Furthermore, by comparing different aggregation levels, we observe how the OSNR performance is affected by passively combining more horseshoes. For the OSNR margin calculation, we based the requirements for the DSCM-capable units on the specifications published by the Open XR Optics Forum [XR-24].

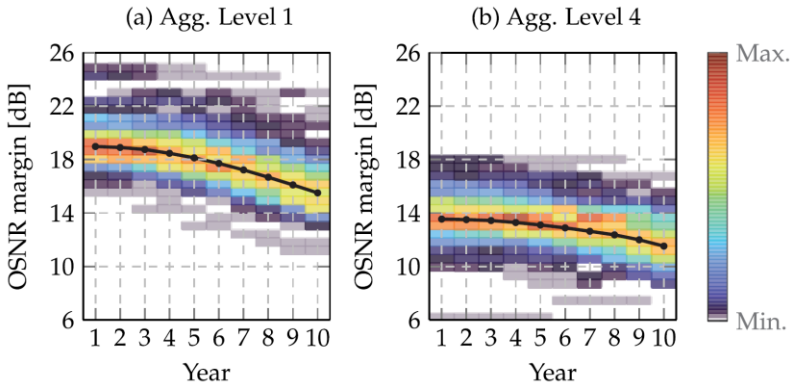

Figure 8.7-4: OSNR margin of four-horseshoe network scenarios as a function of the year-in-operation and aggregation level for a traffic growth of 20% per year. Color mapping has been normalized to the maximum value of occurrences, and the solid line highlights the mean OSNR margin value.

If we then establish a relation between reach, which is denoted as $\overline{D}$, and the corresponding optical performance (i.e., OSNR margin), we can better understand the reaction of the system with respect to the traffic demands' compound average growth rate (CAGR). The thorough evaluation of a three-horseshoe scenario has been summarized below, where the results reveal that, as the aggregation level increases, not only the optical performance degrades, but the reach is effectively reduced; this is evidenced by the progressive shift of the data points toward the left. Moreover, besides the degradation due to optical aggregation, the performance also worsens when the traffic volume increases. This can be observed by comparing the results of year 1 and year 10 as a consequence of needing new transceivers and supporting passive optical components. Now, as the changes occur faster in the network, the compounding effect on the overall performance and reach are more pronounced than in scenarios with less traffic.

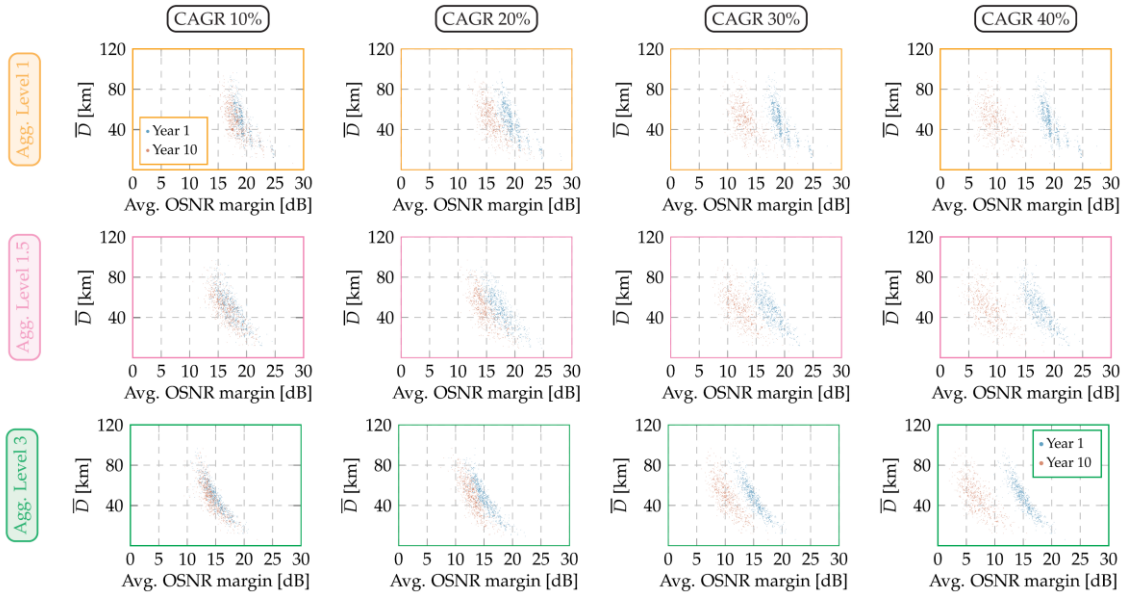

Figure 8.7-5: Relation between average link distance (i.e., from the hub node to the last leaf node of a horseshoe) and OSNR margin in a three0horseshoe network scenario at years 1 and 10. Results have been grouped according to the network traffic's CAGR conditions.

Dissemination Level	Public

Assuming that the OSNR margin value fulfils the requirements set by the operators, we can then compute the power consumption of the DSCM-capable pluggable transceivers that are needed to construct and operate the network. In a similar vein to how we described the hardware estimation in Figure 8.7-2, Figure 8.7-6 depicts a simplified network scenario with two horseshoes and certain operating conditions (e.g., traffic volume and aggregation level).

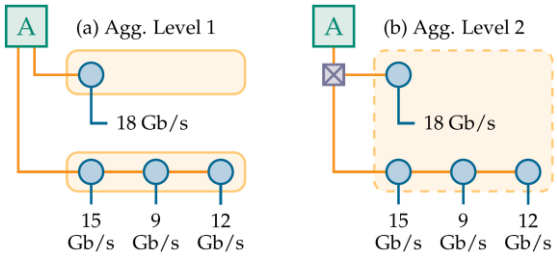

Figure 8.7-6: Two-horseshoe network scenario in configurations corresponding to an (a) aggregation level of 1 and an (b) aggregation level of 2.The coupler/splitter has an equal ration among its inputs/outputs, respectively.

In Figure 8.7-6, even though a single DSC per leaf node is sufficient to provide connectivity agrees the network the implications for the actual settings of the transceivers depend on how the network is configured to operate. Table 8.7-2 provides a detailed summary of the logic behind our estimate of power consumption, where we define the conditions of the networks as well as the necessary HW and bandwidth resources for a given operation and the corresponding overall consumption of these devices.

Table 8.7-2: Example of the normalized power consumption calculation for a two-horseshoe network scenario.

Operation	Horseshoes (Leaf nodes)	Agg. Level	Hub node units	Leaf node units	Norm. consumption [a.u.]
Full/P2P	2 (1;3)	N/A	4 x 100G (4 x 4 DSC)	4 x 100G (4 x 4 DSC)	6.4
Adj./P2P	2 (1;3)	N/A	4 x 100G (4 x 1 DSC)	4 x 100G (4 x 1 DSC)	6.08
Adj./P2MP	2 (1;3)	1	2 x 400G (1 x 1 DSC; 1 x 3 DSC)	4 x 100G (4 x 1 DSC)	4.76
Adj./P2MP	2 (1;3)	2	4 x 100G (1 x 4 DSC)	4 x 100G (4 x 1 DSC)	3.92

The first few of columns in the table provide the general operating conditions: adjustability of DSCs (i.e., full operation or adjusted operation), communication scheme (i.e., P2P or P2MP), and aggregation level. Based on this abstraction, we can determine the number of units and settings of the pluggable transceivers at the leaf nodes and, in turn, of their bookended counterparts at the hub node. In this example, the transceivers at the leaf nodes will produce either a four-subcarrier or a one-subcarrier signal depending on whether the units are able to freely adjust the number of DSCs according to the network traffic. The situation of the hub node, on the other hand, is not as straightforward, as the communication scheme enables the use of different types of transceivers in addition to considering (de)activating DSCs and the degree of optical

aggregation. In Table 8.7-2, we report the various conditions for the provisioning of the hub node and, next to them, the required DSCs to establish connections with the leaf node units. Finally, we can calculate a normalized power consumption value with respect to that of a 400 Gb/s DSCM-capable transceiver module operating at maximum capacity. For instance, according to Figure 8.7-6 (b), a transceiver operating at 100 Gb/s would consume 0.8 arbitrary units. Therefore, the arrangement needed in P2P configuration, with the pluggable modules working at full capacity, would require as much power as 6.4 of the 400 Gb/s DSCM-capable units. Then, by turning off the unnecessary DSCs, we can slightly reduce power consumption. In the case of freely adjustable modules and P2MP with maximum aggregation, the 400 Gb/s transceiver with four DSCs and each of the four 100 Gb/s transceivers with one DSC would consume 0.88 and 0.74 arbitrary units, respectively. This leads to an arrangement that equates the consumption of 3.92 of the 400 Gb/s DSCM-capable units. By combining the flexible adjustment of DSCs with optical aggregation, we manage to obtain considerable operational savings: around 25% and 39% for aggregation levels of 1 and 2, respectively, compared to the P2P implementation of the network using DSCM-based transceiver units operating at full capacity.

We have to keep in mind that despite talking about P2P and P2MP, all the network deployments concern the utilization of DSCM-capable transceivers. In this regard, the comparison shown in Figure 8.7-7 allows us to quantify the advantages of flexibly operating DSCs in the transceiver modules as well as implementing a P2MP communication scheme.

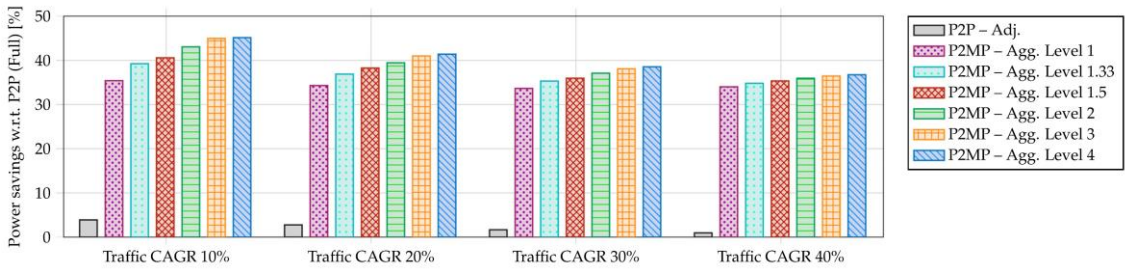

Figure 8.7-7: Average operative savings regarding the pluggables' power consumption with respect to a P2P (full) scenario as a function of the traffic demands' CAGR at year 10.

From Figure 8.7-7 we can conclude that the largest improvement regarding the power consumption across a network would be achieved by connecting multiple leaf nodes to the same transceiver at the hub. As a consequence, the higher the aggregation level, the more efficient the network deployment. However, as the volume of traffic grows, the hub transceiver(s) will progressively use more of their available bandwidth in communications with fewer leaf nodes and leaf node units. For this reason, aggregating traffic seems to be less effective in improving the power savings under high traffic conditions.

To compare single-carrier and DSCM-based technologies and provide design guidelines, we carried out an analysis similar to the relative acquisition cost of the units in section 0. In this case, we phrase our objective as follows: how much should a native, DSCM-capable 100 Gb/s

consume in terms of power to realize P2MP deployments that match the consumption of traditional single-carrier P2P networks?

Without loss of generality, we can represent the posed questions mathematically by Eq. 7, where *P* denotes the power consumed by the transceiver units, and *HN* and *LN* indicate the hub node and leaf node locations, respectively.

$$P_{P2MP-HN} + P_{P2MP-LN} \leq P_{P2P-HN} + P_{P2P-LN} \quad \text{Eq. 7}$$

Using exclusively 100 Gb/s transceivers at the leaf nodes and 400 Gb/s units at the hub node, we can rewrite Eq. 7 as Eq. 8.

$$P_{P2MP-400G} + P_{P2MP-100G} \leq P_{P2P-100G} \quad \text{Eq. 8}$$

Now, Eq. 8 is the basis for our subsequent analysis, since from specifications, data sheets, and device measurements, both $P_{P2MP\text{-}400G}$ and $P_{P2P\text{-}100G}$ are known quantities, provided that we know the number of required transceivers for a given network deployment.

Up until this point, for DSCM transceivers, we have been considering the power consumption of a 400 Gb/s unit that is capable of operating at different capacity values. This, however, presents a contention point, since the power consumption of a 100 Gb/s pluggable in these conditions (according to Figure 8.7-8 (a)) would be around 75% of a 400 Gb/s unit. When compared to single-carrier solutions, which exhibit power consumption values between 5 and 6 W, this value complicates deploying DSCM-based technologies in an energy-efficient manner. For this reason, we are interested in determining the requirements for a native, DSCM-capable 100 Gb/s transceivers.

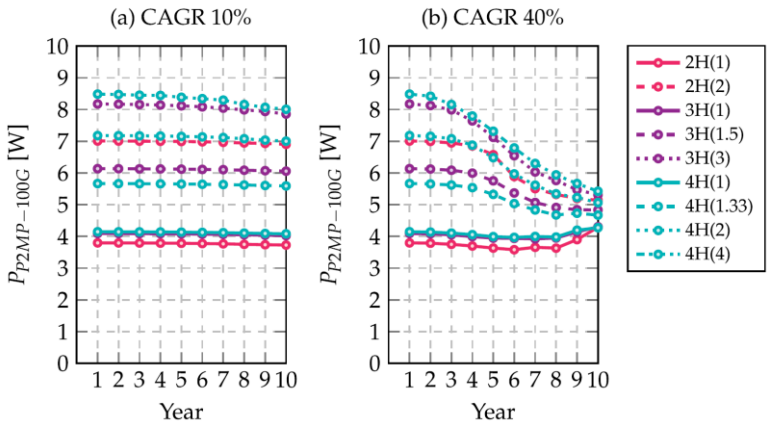

Figure 8.7-8: Average maximum possible power consumption for a DSCM-capable 100 Gb/s transceiver to ensure a DSCM network deployment as power-efficient as one utilizing traditional single-carrier 100 Gb/s coherent pluggable transceivers. The reference P2P 100 Gb/s units are assumed to exhibit a power consumption of 5 W [Adt, Cis].

Calculating the required power consumption of the lower-speed DSCM transceivers according to the previous equations provides us with an upper boundary for the development of competitive 100 Gb/s solutions with DSCM capabilities. In this regard, Figure 8.7-8 shows a side-by-side comparison between the scenarios with 10% CAGR (a) and 40% CAGR (b), assuming that the single-carrier transceivers consume 5 W [Adt, Cis] per unit. Our results indicate that not maximizing optical aggregation results in very stringent power consumption requirements (below the consumption of traditional P2P modules) on the P2MP transceivers. On the other hand, by aggregating multiple horseshoes and connecting multiple leaf nodes to the pluggables at the hub node, we observe some degree of margin for the transceiver design; showing that DSCM-capable 100 Gb/s transceivers could consume more than their P2P counterparts and still be competitive when we look at the network deployment as a whole.

8.8 Resilient Anomaly Detection in Fiber Networks: ML for Multi-Threat Identification via Polarization Monitoring (related to C3.6 and C3.7)

This section provides a comprehensive framework for anomaly detection in optical fiber networks based on the analysis of the State of Polarization (SOP) and associated temporal fingerprints. Fiber infrastructures, increasingly used in sensing applications such as railway monitoring [Bao15], avalanche detection [Edm23], and earthquake early warning [Awa24], are exposed to both environmental disturbances and malicious intrusions such as eavesdropping attacks. Previous studies have shown that polarization-based sensing enables the identification of bending events, acoustic vibrations, and tapping activities along existing telecom fibers [Sif15, Pen22]. Building on this background, the authors propose a ML-based system capable of distinguishing multiple threat scenarios through SOP monitoring alone, without requiring specialized sensing fiber or intrusive hardware. The study examines three representative anomaly categories: (i) eavesdropping attacks, typically produced via macro-bending [Zaf11, Son23]; (ii) simultaneous disruptive events, such as coordinated shaking and tapping [Mal25] and (iii) vibration-based disturbances of varying severity, which emulate realistic environmental or accidental stresses. All experiments employ SOP time series collected from a polarimeter attached to a fiber network and are processed using ML classifiers, including Random Forest (RF), XGBoost, k-Nearest Neighbor (k-NN), and decision trees.

8.8.1 Sensing Mechanism and Experimental Setup

The sensing method is rooted in the principle that any external perturbation modifies the polarization state of light propagating in a standard single-mode fiber [Tos22]. SOP variations were retrieved through the Stokes parameters (S1, S2, S3) and the State-of-Polarization Angular Speed (SOPAS), which is known to be strongly correlated with vibration strength. Using these measurements, we demonstrate how rich temporal signatures can be extracted and used to detect mechanical stress or malicious activity.

Eavesdropping Detection. To emulate a tapping attack, the authors used an optical fiber identifier (OFI) device clamped onto a 13-km metropolitan fiber. The induced macro-bend causes measurable changes in the Stokes parameters that clearly deviate from the fiber's undisturbed state. Figure 8.8-1 illustrates the characteristic polarization distortions associated with bending events. Repetitive experiments confirmed that even short-duration clampings produce distinctive SOP transitions, consistent with findings in earlier fiber-security studies [Mec21].

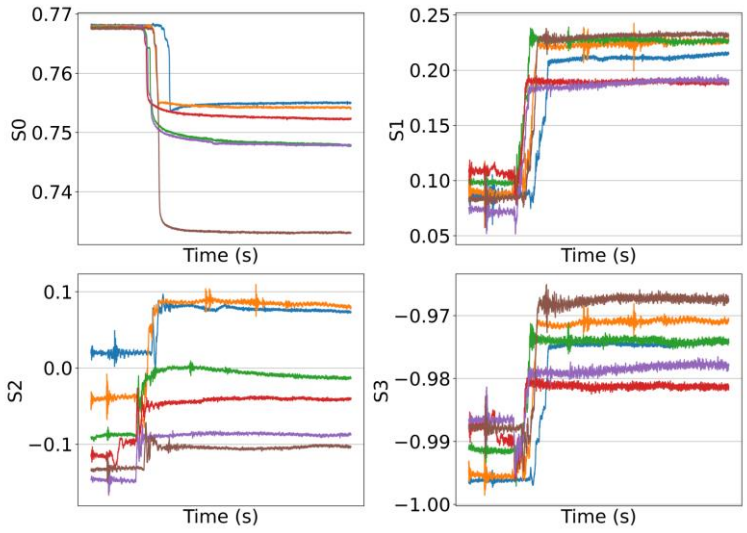

Figure 8.8-1: Bending for various experiments using OFI.

8.8.2 Simultaneous Events

In the presence of overlapping disturbances – such as shaking plus tapping – the signatures become more complex. In this case, we generated such events using a robotic arm oscillating at 3 Hz combined with manual tapping once per second. The resulting mixed fingerprints are reported in Figure 8.8-2, reveal identifiable tapping peaks superimposed on slower polarization oscillations. An XGBoost classifier successfully distinguished these compound events with 98% accuracy and only 2.06% misclassification, confirming previous work that ML approaches outperform traditional threshold-based detection [Mal25].

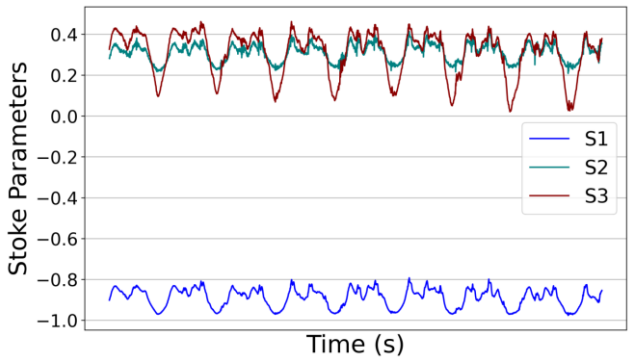

Figure 8.8-2: Simultaneous occurrence of bending and tapping.

8.8.3 Vibration Monitoring

To characterize vibration severity, shaking frequencies of 1, 3, 5, and 10 Hz were applied to a fiber testbed composed of 8 km and 5 km SMF segments attached to a continuous-wave laser source. A polarimeter sampled SOP variations at 1500 samples/s. Figure 8.8-3 shows how shaking frequency influences the temporal evolution of the Stokes parameters; higher-frequency vibrations compress polarization excursions, while lower frequencies result in wider spreads.

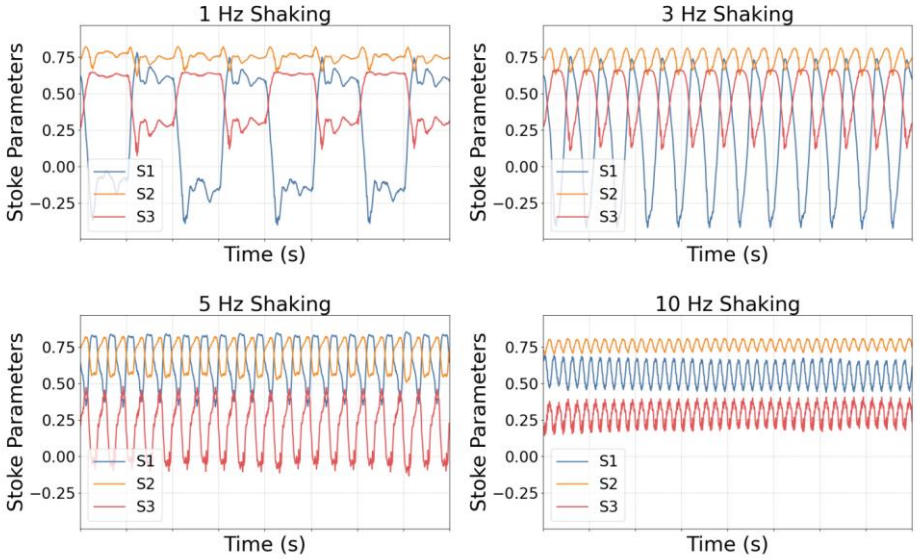

Figure 8.8-3: Stoke parameters plot for the clean dataset.

When noise was artificially added, the polarization fingerprints shifted noticeably, as seen in Figure 4 of [Mal25-2], underscoring the need for robust classification techniques.

8.8.4 Machine-Learning Framework

The ML architecture receives time-series data of Stokes parameters and SOPAS and enriches them through lagged features and rolling statistics (mean and standard deviation over windows of 500 and 1000 samples). These features improve the classifier's ability to capture short-term temporal dependencies and mitigate noise effects. The dataset contains five classes: No Event, and Shaking at 1, 3, 5, or 10 Hz. An 80:20 train-test split is used. The full processing chain – including feature generation, classifier training, and real-time decision logic – is summarized in Figure 8.8-4. Four ML models were evaluated: RF, XGBoost, k-NN, and decision tree, consistent with established ML practices in fiber anomaly detection [Nat19] and cybersecurity applications [Zha21].

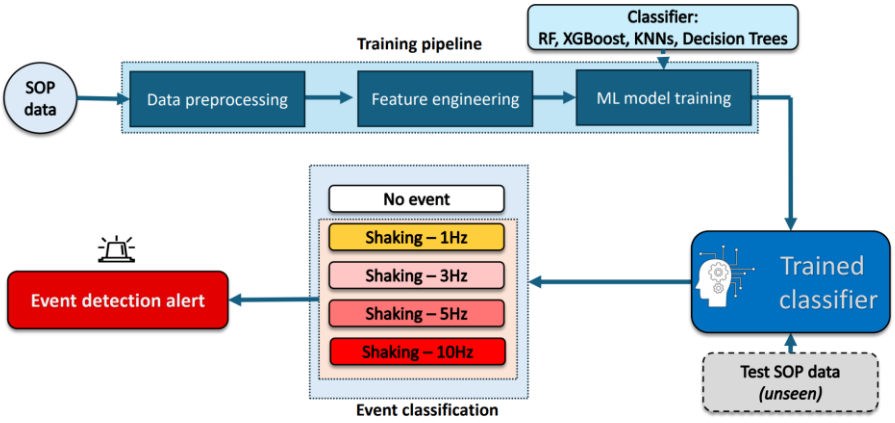

Figure 8.8-4: Flowchart of the machine learning framework for predictive modelling.

8.8.5 Results and Performance Evaluation

In this section, we will assess model performance using accuracy, precision, recall, F1-score, and AUC-ROC curves (definitions provided in Section 4.2 of [Mal25-2]).

Classification on Clean Data. Figure 8.8-5 shows that RF and XGBoost achieve the highest performance, with accuracy exceeding 99%. ROC curves in Figure 8.8-6 indicate AUC = 1.00 for all tree-based models, with RF slightly surpassing the others in discriminating adjacent vibration frequencies. The confusion matrices also confirmed the superior precision of RF, particularly in distinguishing 3 Hz from 5 Hz vibrations – an essential capability for real-world monitoring.

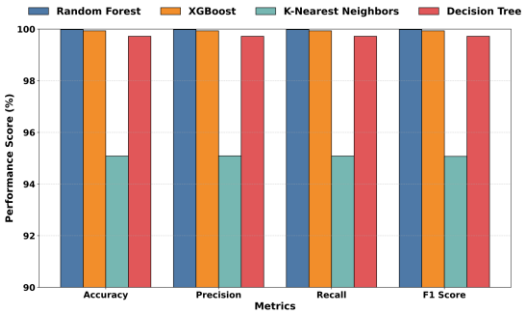

Figure 8.8-5: Comparison of metrics of the models trained on the clean dataset.

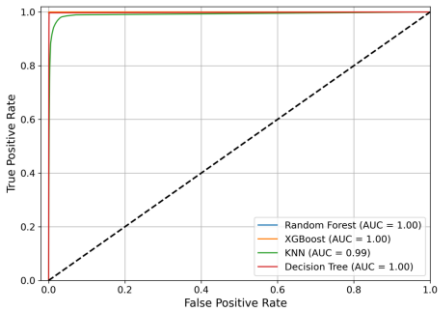

Figure 8.8-6: AUC-ROC curves of the different models on clean dataset.

8.8.6 Robustness to Noise

Noise robustness is examined by superimposing 1, 3, and 5 Hz noise onto the SOP data. As expected, classification becomes more challenging as noise increases; nonetheless, RF maintains respectable accuracy levels of 87.41%, 70.50%, and 58.99%, respectively (Figure 9 of [Mal25-2]). The ROC curves in Figure 8.8-7 reveal that even under severe noise, high-risk events such as 10 Hz shaking remain reliably detectable, with AUC values remaining above 0.90. Confusion matrices for noisy datasets (Figure 11 in [Mal25-2]) further demonstrate that although low-frequency events become harder to separate under noise, critical anomalies remain highly identifiable.

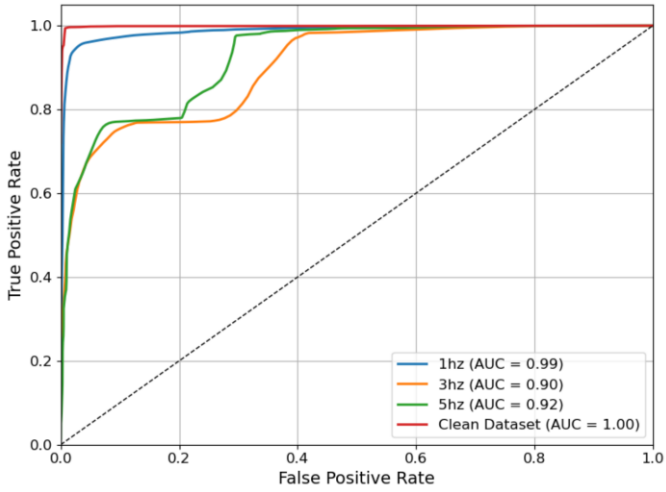

Figure 8.8-7: AUC-ROC curves of the random forest model on clean and noisy datasets.

Overall, the results indicate that tree-based models – especially RF – provide the most reliable and noise-resilient classification, fully supporting earlier findings on the efficiency of ensemble-learning approaches for physical-layer anomaly detection in optical networks.

8.8.7 Conclusions

In section 8.8 is described the introduction of an effective and computationally efficient ML framework for detecting multiple categories of anomalies in optical fiber networks based solely on SOP monitoring. The system demonstrates strong capability in identifying eavesdropping attempts, overlapping disturbances, and vibration events of different frequencies, achieving near-perfect accuracy on clean data and maintaining robustness against environmental noise. By leveraging SOP fingerprints, the method avoids intrusive sensing hardware and is compatible with existing telecom fibers, offering a promising solution for real-time network security and diagnostic applications. Future improvements envisaged by the authors include noise-aware feature extraction, adaptive filtering, and lightweight model optimization for deployment in latency-sensitive environments.

9 CONCLUSIONS

Deliverable D3.3 concludes the activities of WP3, which has been dedicated to the definition, development, implementation, and validation of SEASON's data plane technologies and subsystems. Building upon the foundations laid in D3.1 ("End-to-end design of next generation smart optical networks") and D3.2 ("Optical systems enabling ultra-high-capacity access/metro networks"), this final document consolidates the technological outcomes, experimental validations, and integration achievements that together form the SEASON data plane solution.

Over the course of the project, WP3 has transitioned from theoretical modelling and architectural definition to the realization and demonstration of tangible prototypes and experimental platforms. The technologies developed within this work package address the dual challenge of scaling optical network capacity while simultaneously improving sustainability and operational efficiency. Through a coherent sequence of design, implementation, and testing, SEASON has delivered a set of innovative data plane solutions that advance the state of the art in terms of capacity, energy efficiency, cost effectiveness, and self-management.

The deliverable presents the final suite of SEASON data plane prototypes and subsystems, developed and validated by the consortium partners. These include MBoSDM transmission systems, programmable and filterless node architectures, advanced DSCM, P2MP transceivers, spatial PON solutions, and integrated monitoring and telemetry components. Together, these elements form a coherent technological ecosystem supporting the SEASON architecture as defined in WP2, and they enable a flexible, future-proof network infrastructure capable of meeting the demands of 6G-era applications and services.

Beyond the individual components, WP3 has also provided the modelling frameworks and optimization tools required for efficient network design and operation. The studies on robust optimization, end-to-end latency, energy and cost trade-offs, and crosstalk analysis have supported the architectural choices made throughout the project and ensured that the developed solutions are grounded in both theoretical soundness and practical feasibility. Furthermore, the integration of these models into SEASON's digital twin and network planning workflows paves the way for automated, intelligent, and adaptive network management, which will be fully realized in the subsequent work packages.

A central outcome of WP3 has been the validation of SEASON technologies in multiple experimental demonstrations. The demonstrations conducted in Berlin, L'Aquila, and with the operator testbeds (Telefonica and Fibercop) have proven the functional maturity and interoperability of the developed prototypes. They have shown that the proposed SEASON solutions can operate seamlessly within realistic network environments, delivering high throughput, low latency, and enhanced power efficiency across the access, metro, and backbone segments. These experiments provide the essential bridge between laboratory innovation and field deployment, confirming that SEASON's data plane is ready for integration into the project's final demonstrators.

From a broader perspective, the results of WP3 represent a major step toward the realization of self-managed, sustainable, and scalable optical networks. The project's innovations contribute directly to the SEASON KPIs – enhancing fiber capacity through multiband and SDM technologies, reducing power consumption via DSCM-based aggregation and pluggable optics, improving scalability through modular and open architectures, and enabling pervasive monitoring for autonomous operation. These achievements align with the overarching objectives of the Smart Networks and Services Joint Undertaking (SNS JU) and the Horizon Europe framework, addressing the urgent need for greener, more adaptive, and more efficient network infrastructures. It is worth mentioning that some of the results described in Section 5 led to prestigious recognition among the top 10 achievements. In fact, the work published in [Fer25] was selected as one of the most significant accomplishments within the SNS project in 2025.

With this deliverable, WP3 successfully completes its mission within SEASON. The data plane subsystems and models developed here constitute the technological foundation upon which the next stages of the project will build. WP4 will further integrate these solutions into programmable control and telemetry frameworks, while WP5 will focus on their large-scale demonstration and performance evaluation in realistic end-to-end network scenarios. Together, these activities will realize the full SEASON vision: a self-managed, sustainable, and high-capacity optical network architecture capable of supporting the next generation of digital services and applications.

In summary, Deliverable D3.3 marks the culmination of an extensive collaborative effort that has translated ambitious research concepts into validated technological solutions. The outcomes achieved under WP3 demonstrate SEASON's capacity to bridge the gap between research and deployment, laying the groundwork for future innovation in optical networking and contributing significantly to Europe's leadership in sustainable 6G infrastructure development.

10 GLOSSARY

Acronym	Description
ADC	Analog-to-Digital Converter
ADSL	Asymmetric Digital Subscriber Line
AL	Ambitious Level
AR	Augmented Reality
ASE	Amplified Spontaneous Emission
ASIC	Application-Specific Integrated Circuit
AWG	Arrayed-Waveguide Grating
b2b	Back-to-Back
BNG	Broadband Network Gateway
BOL	Begin of Life
BVT	Bandwidth/bit rate Variable Transponder
CC-MCF	Coupled-Core Multi-Core Fiber
CD	Colorless Directionless
CDC	Colorless Directionless Contentionless
CDF	Change Detection Framework
CDN	Content Delivery Network
CM	Confusion Matrix
CO	Central Office
CSG	Cell Site Gateway
DAC	Digital-to-Analog Converter
DC	Data Center
DCM	Dispersion Compensation Modules
DD	Direct Detection
DPU	Data Processing Unit
DSB	Double Sideband
DSCM	Digital Supply Chain Management
DSP	Digital Signal Processor/Processing
DWDM	Dense Wavelength Division Multiplexing
E2E	End-to-End
EA	Entropy Analysis
ECL	External-Cavity Laser
EDFA	Erbium-Doped Fiber Amplifier
EON	Elastic Optical Networks
FC	Fault Case
FEC	Forward Error Correction

FIFO	First In First Out
FMF	Few-Mode Fiber
FOADM	Fixed Filter Optical Add-Drop Multiplexer
FTTH	Fiber-To-The-Home
FTTx	Fiber-To-The-x
GE	Gigabit Ethernet
GGN	Generalized Gaussian noise
GN	Gaussian Noise
GPON	Gigabyte Passive Optical Network
GPU	Graphics Processing Unit
GSNR	Generalized Signal-To-Noise Ratio
HLx	Hierarchical Level X
IM	Intensity Modulation
ISP	Internet Service Provider
ISRSGN	Inter-Channel Stimulated Raman Scattering
ITST	Inverse Triple-Aspect Self-Attention Transformer
KPI	Key Performance Indicator
MAN	Metropolitan Area Network
MB	Multiband
MBoSDM	Multiband over Space Division Multiplexing
MBT	Multiband Transmission
MC	Multi-Core
MCF	Multi-Core Fiber
MCS	MultiCast Switch
MDL	Mode-dependent loss
MIMO	Multi-input-multi-output
MMF	Multimode fiber
MPF	Multi-parallel fiber
MPLS	Multi-Protocol Label Switching
MW	Microwave
MZM	Mach-Zehnder Modulator
NIC	Network Interface Card
NLI	Nonlinear interference
NN	Neural Network
NOS	Network Operating System
O/E/O	Optical to Electrical to Optical
ODE	Ordinary differential equations
ODN	Optical Distribution Network
OFDM	Orthogonal Frequency Division Multiplexing
OLT	Optical Line Terminal

ONT	Optical Network Terminal
OPC	Optical Packet Core
O-RAN	Optical Radio Access Network
OSA	Optical Spectrum Analyzer
OSC	Optical Supervisory Channel
OSFP	Optical Small Factor Pluggable
OSNR	Optical Signal-to-Noise Ratio
OTDR	Optical Time Domain Reflectometer
OTN	Optical Transport Network
P2MP	Point-to-Multipoint
P2P	Point-to-Point
PCA	Principal Component Analysis
PdM	Predictive Maintenance
PGW	Packet Data Network Gateway
PON	Passive Optical Network
QoT	Quality of Transmission
QSFP	Quad Small Factor Pluggable
RAN	Radio Access Network
RMA	Return Merchandise Authorization
ROADM	Reconfigurable Optical Add-Drop Multiplexer
RTF	Run-To-Failure
RUL	Remaining Useful Lifetime
S-BVT	Sliceable Bandwidth Variable Transceiver
SDM	Spatial division multiplexing
SE	Spectral Efficiency
SLAT	Sparse Low-Ranked Self-Attention Transformer
SMF	Single-Mode Fiber
SNR	Signal-To-Noise Ratio
SoA/SotA	State of the Art
SOP	State of Polarization
S-OXC	Spatial Optical Cross Connect
SRS	Stimulated Raman Scattering
SSB	Single Sideband
SSMF	Standard Single Mode Fiber
TDFA	Thulium-Doped Fiber Amplifier
TF	Tunable Filter
TLS	Tunable Laser Source
UC-MCF	Uncoupled-Core Multi-Core Fiber
URLLC	Ultra-Reliable and Low-Latency Communications
VPN	Virtual Private Network

VR	Virtual Reality
WC-MCF	Weakly-Coupled Multi-Core Fiber
WDM	Wavelength Division Multiplexed
WSS	Wavelength Selective Switch
XGS-PON	10Gb Symmetric Passive Optical Network

11 REFERENCES

[Abr65] M. Abramowitz, Handbook of Mathematical Functions, 9th ed., Dover Publications, 1965.

[Aca24] Acacia, Coherent bidi for edge and access network applications, [Online]. (visited on 05/16/2

[Adt] "Coherent 100ZR," https://www.adva.com/.

[Agr95] G. Agrawal, Nonlinear Fiber Optics, 2nd ed. London, U.K., Academic, 1995

[Ala21] M. Alasmar, R. Clegg, N. Zakhleniuk, and G. Parisis, "Internet traffic volumes are not gaussian—they are log-normal: An 18-year longitudinal study with implications for modelling and prediction," IEEE/ACM Transactions on Netw. 29, 1266–1279 (2021).

[Awa24]. Awad, H.; Usmani, F.; Virgillito, E.; Bratovich, R.; Proietti, R.; Straullu, S.; Pastorelli, R.; Curri, V. A Machine Learning-Driven Smart Optical Network Grid for Earthquake Early Warning. In Proceedings of the 2024, ICTON, Bari, Italy, 14–18 July 2024; pp. 1–6.

[Bao15] Bao, Y.; Chen, G.; Meng, W.; Tang, F.; Chen, Y. Kilometer-Long Optical Fiber Sensor for Real-Time Railroad Infrastructure Monitoring to Ensure Safe Train Operation. In Proceedings of the 2015 Joint Rail Conference, San Jose, CA, USA, 23–26 March 2015; ASME/IEEE Joint Rail Conference.

[Ber03] Bertsimas, Dimitris, and Melvyn Sim. "Robust discrete optimization and network flows." *Mathematical programming* 98.1 (2003): 49-71.

[Bha08] U. N. Bhat, "The general queue G/G/1 and approximations," in An Introduction to Queueing Theory, (Birkhäuser, 2008), pp. 169–183.

[Bou20] N. Bouguila and W. Fao, "Mixture Models and Applications", Springer, 2020

[Can18] M. Cantono, D. Pilori, A. Ferrari, C. Catanese, J. Thouras, J.-L. Auge, and V. Curri, "On the interplay of nonlinear interference generation with stimulated Raman scattering for QoT estimation," Journal of Lightwave Technology, vol. 36, p. 3131–3141, Aug. 2018.

[Cas23] C. Castro et al., "Scalable filterless coherent point-to-multipoint metro network architecture", IEEE/Optica JOCN, Vol. 15, no. 5, B53—B66, 2023.

[Cas23] C. Castro, A. Napoli, et al., "Scalable filterless coherent point-to-multipoint metro network architecture", Journal of Optical Communications and Networking, vol. 15, no. 5, B53–B66, 2023.

[Cas24] C. Castro et al., "Power and Spectral Savings in Metro-Aggregation Networks Exploiting Coherent Point-to-Multipoint Transceivers", in proc. ECOC, Tu4E.3, 2024.

[Cas24] Castro, Carlos, et al. "Power and spectral savings in metro-aggregation networks exploiting coherent point-to-multipoint transceivers." *ECOC 2024*

[Cas25] P. Castoldi, "Energy-efficient Optical Aggregation Enabled by Digital Sub-Carriers", ICTON 2025.

[Cas25] Castro, Carlos, et al. "Power consumption considerations of coherent transceivers in filterless point-to-multipoint metro-aggregation networks with digital subcarrier multiplexing." Journal of Optical Communications and Networking 17.6 (2025): 526-542.

[Cas25-2] C. Castro, et al., "Power consumption considerations of coherent transceivers in filterless point-to-multipoint metro-aggregation networks with digital subcarrier multiplexing", IEEE/Optica JOCN, Vol. 17, no. 6, pp 526—542, 2025.

[Cas25-3] C. Castro, et al., "Transceiver Count Reduction in Filterless Metro-Aggregation Networks Using DSCM", in proc. 2025 International Conference on Optical Network Design and Modeling (ONDM).

[Case25] R. Casellas, R. Martinez, R. Vilalta, and R. Muñoz, "Overview of SDN control of multiband over SDM optical networks with physical layer impairments [Invited Tutorial]," J. Opt. Commun. Netw., vol. 17, pp. A165-A177, 2025.

[Cast25] Castoldi, P., et al. "Energy-efficient Optical Aggregation Enabled by Digital Sub-Carriers.", ICTON. IEEE, 2025.

[Cav24] F. Cavaliere, G. Sarlet, and M. Distefano. "Mobile Optical Pluggables Alliance (MOPA), Technical paper on Coherent lite for mobile networks". (2024), [Online]. Available: https://mopa-alliance.org/wp-content/uploads/2024/03/MOPA_Coherent_Lite_paper-v1.0.pdf.

[Cha10] C. C. K. Chan, ed., Optical performance monitoring: advanced techniques for next-generation photonic networks. Burlington, MA: Academic Press/Elsevier, 2010. OCLC: ocn470818731.

[Chr19] K. Christodoulopoulos and et al., "Toward efficient, reliable, and autonomous optical networks: the orchestra solution [invited]," IEEE/Optica JOCN, vol. 11, no. 9, pp. C10–C24, 2019.

[Chr96] D. Christodoulides and R. Jander, “Evolution of stimulated Raman crosstalk in wavelength division multiplexed systems,” IEEE Photonics Technology Letters, vol. 8, no. 12, pp. 1722–1724, 1996.

[Cis] “Cisco QSFP28 100ZR,” https://www.cisco.com/

[Cis20] Cisco annual Internet report (2018–2023), White paper, 2020.

[Clo16] B. Clouet, J. Pedro, N. Costa, M. Kuschnerov, A. Schex, J. Slovak, D. Rafique, and A. Napoli, “Networking aspects for next-generation elastic optical interfaces,” Journal of Optical Communications and Networking, vol. 8, no. 7, pp. A116–A125, 2016.

[Cug20] F. Cugini et al., “Coherent pluggable optical transceivers: Performance versus standardization trade-offs,” J. Light. Technol. 38, 1071–1079 (2020).

[Cug20-2] F. Cugini et al., “Coherent pluggable optical transceivers: Performance versus standardization trade-offs in optical transport networks,” J. Opt. Commun. Netw. 12, 194–203 (2020).

[Cur22] V. Curri, “GNPy model of the physical layer for open and disaggregated optical networking [Invited],” J. Opt. Commun. Netw. vol. 14, pp. C92-C104, 2022.

[D2.1-24] D2.1, EU Project SEASON. (2024) Definition of Use Cases, Requirements and Reference Network Architecture.

[D2.2-25] D2.2, EU Project SEASON. (2025) Self-Managed Sustainable High-Capacity Optical Networks, February 2025.

[D2.3-25] D2.3, EU Project SEASON. (2025) Techno-economic Analysis.

[D3.2-24] SEASON deliverable D3.2, ‘Optical systems enabling ultra-high-capacity access/metro networks’, December 2024.

[Dam22] A. D’Amico, B. Correia, E. London, E. Virgillito, G. Borraccini, A. Napoli, and V. Curri, “Scalable and disaggregated GGN approximation applied to a C+L+S optical network,” J. Light. Technol. 40, 3499–3511 (2022).

[Dam22-2] A. D’Amico, E. London, B. L. Guyader, F. Frank, E. L. Rouzic, E. Pincemin, N. Brochier, and V. Curri, “Experimental validation of GNPy in a multi-vendor flex-grid flex-rate WDM optical transport scenario,” J. Opt. Commun. Netw. 14, 79–88 (2022).

[Dev24] M. Devigili et al., “Applications of the OCATA Time Domain Digital Twin: from QoT Estimation to Failure Management,” JOCN, vol. 16, 2024.

[Dic24] T. Dicorato, “Enabling IP-optical integration in core and metro networks [invited],” J. Opt. Commun. Netw. 16, C121–C132 (2024).

[Edm23] Edme, P.; Paitz, P.; Walter, F.; van Herwijnen, A.; Fichtner, A. Fiber-optic detection of snow avalanches using telecommunication infrastructure. arXiv 2023, arXiv:2302.12649.

[Eur23] European Commission, “Report on the state of the digital decade”,Report, 2023. [Online]. Available: https: //digital- strategy.ec.europa.eu/en/library/2023-report-state-digital-decade.

[Fab18] J. M. Fabrega, M. Svaluto Moreolo, and L. Nadal, “Optical performance monitoring systems in disaggregated optical networks,” in 2018 20th International Conference on Transparent Optical Networks (ICTON), pp. 1–4, 2018.

[Fei14] Feihong Ye, et al., ”Simple analytical expression for crosstalk estimation in homogeneous trench-assisted multi-core fibers,” Opt. Express 22, 23007-23018 (2014).

[Fer20] A. Ferrari, A. Napoli, J. Fischer, N. Costa, A. D’Amico, J. Pedro, W. Forysiak, E. Pincemin, A. Lord, A. Stavdas, J. Fernandez-Palacios, G. Roelkens, N. Calabretta, S. Abrate, B. Sommerkorn-Krombholz, and V. Curri, “Assessment on the Achievable Throughput of Multi-Band ITU-T G.652.D Fiber Transmission Systems,” J. Lightwave Technology, vol. 38, pp. 4279-4291, 2020.

[Fer20] A. Ferrari, M. Filer, K. Balasubramanian, Y. Yin, E. Le Rouzic, J. Kundrat, G. Grammel, G. Galimberti, and V. Curri, “GNPy: an open source application for physical layer aware open optical networks,” IEEE/OSA J. Opt. Commun. Netw. 12, C31–C40 (2020).

[Fer24] P. Torres-Ferrera et al., “Single-fiber bidirectional transmission using 400G coherent digital subcarrier transceivers”, in OFC, 2024, Tu3E–5

[Fer25] P. Torres-Ferrera et al., “Single-Fiber Single-Wavelength Bidirectional Digital Subcarrier Point-to-Multipoint Coherent Systems for Beyond 5G Transport”, ECOC 2025

[Fuj01] Alcoa Fujikura, “Alcoa Fujikura annual internet report (2001)”, 1–5–1, Kiba, Kouto–ku, Tokyo 135-8512, Japan, White paper, 2001. [Online]. Available: https://www.southern-telecom.com/content/dam/southern-telecom/pdfs/AFL-Reliability.pdf.

[Gha24] S. Ghasrizadeh, P. Khare, N. Costa, M. Ruiz, A. Napoli, J. Pedro, and L. Velasco, "Digital Twin - Assisted Lightpath Provi-sioning and Nonlinear Mitigation in C+L+S Multiband Optical Networks," MDPI Sensors, vol. 24, pp. 1-21, 2024.

[Gha24-2] Sadegh Ghasrizadeh et al, "Creating and Tuning Multiband Optical Transmission Digital Twin Lightpath Models"

[Gha24-3] S. Ghasrizadeh et al., "DT-Assisted Lightpath Provisioning and Nonlinear Mitigation in C+L+S MB Optical Networks," Sensors, vol. 24, 2024

[Gio23] A. Giorgetti, D. Scano, A. Sgambelluri, F. Paolucci, E. Riccardi, R. Morro, P. Castoldi, and F. Cugini, "Enabling hierarchical control of coherent pluggable transceivers in sonic packet–optical nodes," J. Opt. Commun. Netw. 15, 163–173 (2023).

[Ham19] F. Hamaoka, M. Nakamura, S. Okamoto, K. Minoguchi, T. Sasai, A. Matsushita, E. Yamazaki, and Y. Kisaka, "Ultra-wideband WDM transmission in S-, C-, and L-bands using signal power optimization scheme," Journal of Lightwave Technology, vol. 37, no. 8, pp. 1764–1771, 2019.

[Han24] S. J. Hand, D. F. Welch, V. Bhaskara, D. Naik, A. Wikman, M. Silvola, H. Su, T. Monteiro, F. Marques, P. Santos, N. Swenson, A. Napoli, D. Hillerkuss, and H. Bock, "A new operational paradigm for IPoWDM networks," IEEE Access 12, 56050–56061 (2024).

[Her23] J. A. Hernández et al., "On clustering coherent optics point-to-multipoint trees for cost-effective bandwidth assignment in MANs", Journal of Optical Communications and Networking, vol. 15, no. 12, pp. 999–1007, 2023.

[IDEALIST-13] FP7 IDEALIST Project Deliverable D1.1, June 2013 "Elastic optical network architecture: Reference scenario, cost and planning." [On-line]. Available: https://cordis.europa.eu/docs/projects/cnect/9/317999/080/deliverables/001-D11ElasticOpticalNetworkArchitecture.doc.

[Kha23] P. Khare et al., "SSMS: A Split Step MB Simulation Software," ICTON, 2023.

[Kha25] Prasunika Khare et al., "Simulation and Modeling of C+L+S Multiband Optical Trans-mission for the OCATA Time Domain Digital Twin", MDPI, March 2015.

[Kin61] J. F. C. Kingman, "The single server queue in heavy traffic," Math. Proc. Camb. Philos. Soc. 57, 902 (1961).

[Kum12] V. Kumar and D. Rajouria, "Fault detection technique by using OTDR: Limitations and drawbacks on practical approach of measurement", Intern. Journ. of Emerging Technol. and Advanced Engineering, vol. 2, no. 6, pp. 283–287, 2012.

[Las23] C. Lasagni, P. Serena, A. Bononi, and J. Antona, "A Generalized Raman Scattering Model for Real-Time SNR Estimation of Multi-Band Systems," J. Lightwave Technol., vol. 41, pp. 3407-3416, 2023.

[Liu23] Y. Liu, X. Liu, Y. Zhang, M. Cai, M. Fu, X. Zhong, L. Yi, W. Hu, and Q. Zhuge, "Building a digital twin of an EDFA for optical networks: a gray-box modeling approach," J. Opt. Commun. Netw. vol. 15, pp. 830-838, 2023.

[Lug19] E. Lughofer, M. Sayed-Mouchaweh, "Prologue: Predictive Maintenance in Dynamic Systems", Predictive Maintenance in Dynamic Systems: Advanced Methods, Decision Support Tools and Real-World Applications, pp. 1-23, 2019.

[Mal25] Malik, G.; Masood, M.U.; Dipto, I.C.; Mohamed, M.C.; Straullu, S.; Bhyri, S.K.; Galembirti, G.M.; Pedro, J.; Napoli, A.; Wakim, W.; et al. Intelligent Detection of Overlapping Fiber Anomalies in Optical Networks Using Machine Learning. In Proceedings of the IEEE Summer Topicals, 2025

[Mal25-2] Gulmina Malik et al., "Resilient Anomaly Detection in Fiber-Optic Networks: A Machine Learning Framework for Multi-Threat Identification Using State-of-Polarization Monitoring", MDPI, 2025

[Mec21] Mecozzi, A.; Cantono, M.; Castellanos, J.C.; Kamalov, V.; Muller, R.; Zhan, Z. Polarization sensing using submarine optical cables. Optica 2021, 8, 788–795.

[Men01] M. Menif, L. Rusch, and M. Karasek, "Application of preemphasis to achieve flat output OSNR in time-varying channels in cascaded EDFAs without equalization," Journal of Lightwave Technology, vol. 19, no. 10, pp. 1440–1452, 2001.

[Moa25] Abdelrahmane Moawad, Robert Emmerich, Hussein Zaid, Caio Santos, Alessio Giorgetti, Roberto Morro, Colja Schubert, Behnam Shariati, Johannes Karl Fischer. Demonstration of a Programmable Node Prototype for Spatial Lane Switching and Band Switching. In OFC 2025.

[Moh25] Hosseini, Mohammad M., João Pedro, and Antonio Napoli. "Robust Optimization of Filterless Optical Networks with Physical Layer Uncertainties." *OFC*. Optica Publishing Group, 2025.

[Mor18] R. Morais and J. Pedro, "Machine learning models for estimating quality of transmission in DWDM networks," J. Opt. Commun. Netw., vol. 10, pp. D84–D99. 2018.

[Nad23] Nadal, Laia, Fàbrega, Josep Ma, Vílchez, Francisco, Svaluto Moreolo, Michela. (2023). Next-Generation Optical Transceiver and Switching Solutions Exploiting MB and SDM. 13-15. 10.1109/IMOC57131.2023.10379777.

[Nad24] Nadal, et al., "The Multiband over Spatial Division Multiplexing Sliceable Transceiver for Future Optical Networks." Future Internet 2023, 15, 381.

[Nad25] L. Nadal, et al., 'Crosstalk Analysis in MBoSDM Optical Networks with Programmable Transceiver and Switching Solutions', invited talk in Optica APC, 13 - 17 July 2025, Marseille.

[Nad25-2] L. Nadal, et al., invited talk, 'Innovative Transmission Systems for Capacity Scaling in 6G Optical Networks', ICTON, Barcelona, 6-10 July, 2025.

[Nad25-3] L. Nadal, et al., invited talk 'Addressing Capacity Scaling and Programmability in Future Optical Networks', ONDM, Pisa, 6-9 May (2025).

[Nap25] Antonio Napoli et al., "Towards Truly Scalable Sustainable Flexible Optical Networks", ECOC 2025

[Nat19] Natalino, C.; Schiano, M.; Di Giglio, A.; Wosinska, L.; Furdek, M. Experimental Study of Machine-Learning-Based Detection and Identification of Physical-Layer Attacks in Optical Networks. J. Light. Technol. 2019, 37, 4173–4182.

[Ped24] J. Pedro and A. Souza, "Impact of channel provisioning strategies in the transient resiliency of SuperC+L-band networks," in 2024 14th International Workshop on Resilient Networks Design and Modeling (RNDM), pp. 1–7, 2024.

[Pen22] Pendão, C.; Silva, I. Optical Fiber Sensors and Sensing Networks: Overview of the Main Principles and Applications. Sensors 2022, 22, 7554

[Pog14] P. Poggiolini, G. Bosco, A. Carena, V. Curri, Y. Jiang, and F. Forghieri, "The GN-model of fiber non-linear propagation and its applications," Journal of Lightwave Technology, vol. 32, no. 4, pp. 694–721, 2014.

[Rad19] A. Rashidinejad et al., "Real-time demonstration of 2.4 Tbps (200Gbps/λ) bidirectional coherent DWDM-PON enabled by coherent nyquist subcarriers", in OFC, IEEE, 2020, pp. 1–3

[Rap23] Rapp, Lutz. "Amplifiers in multi–band scenarios—output power requirements, control and performance characteristics." *Journal of Lightwave Technology* 42.6 (2023): 1991-1999.

[Rap25] Lutz Rapp et al., "Impact of Inter-Core Loss and Gain Equalization on Transmission Performance in Multi-Core Systems", vol. 37, issue 13, 2025

[Rui23] M. Ruiz, J. A. Hernandez, M. Quagliotti, E. Hugues-Salas, E. Riccardi, A. Rafel, L. Velasco, and O. Gonzalez de Dios, "Network Traffic Analysis under Emerging Beyond-5G Scenarios for Multi-Band Optical Technology Adoption," J. Opt. Commun. Netw., vol. 15, pp. F36-F47, 2023.

[Sam22] N. Sambo, B. Correia, A. Napoli, J. Pedro, L. Kiani, P. Castoldi, and V. Curri, "Network upgrade exploiting multi band: S- or E-band?," Journal of Optical Communications and Networking, vol. 14, no. 9, pp. 749–756, 2022.

[Sas22] Sasai, Takeo. "Digital longitudinal monitoring of optical transmission link." *2022 European Conference on Optical Communication (ECOC)*. IEEE, 2022..

[Sch24] D. Schneider, L. Rapp, C. Ament, "Anomaly Detection in Time-Series of EDFA Pump Currents to Monitor Degeneration Processes using Fuzzy Clustering", 2024 IEEE International Conference on Machine Learning for Communication and Networking (ICMLCN), pp. 454-459, 2024.

[Sch25] D. Schneider, L. Rapp, C. Ament, “A Transformer-based Approach for Diagnosing Fault Cases in Optical Fiber Amplifiers”, 2025 25th Anniversary International Conference on Transparent Optical Networks (ICTON), pp. 1-4, 2025.

[Sch26] D. Schneider, L. Rapp, C. Ament, “Transformer-based Prognostics: Enhancing Network Availability by Improved Monitoring of Optical Fiber Amplifiers”, 2026 Optical Fiber Communication Conference and Exhibition (OFC), accepted for publication, 2026.

[Sem20] D. Semrau, E. Sillekens, R. I. Killey, and P. Bayvel, “The benefits of using the S-band in optical fiber communications and how to get there,” in 2020 IEEE Photonics Conference (IPC), pp. 1–2, 2020.

[Sen22] Sena, Matheus, et al. "DSP-based link tomography for amplifier gain estimation and anomaly detection in C+ L-band systems." *Journal of Lightwave Technology* 40.11 (2022): 3395-3405.

[Sen25] Sena, Matheus, et al. "Exploring the potential of longitudinal power monitoring for detecting physical-layer attacks." *Journal of Optical Communications and Networking* 17.7 (2025): C30-C40.

[Seq23] D. Sequeira et al., “OCATA: A Deep Learning-based Digital Twin for the Optical Time Domain,” JOCN, vol. 15, pp. 87-97, 2023.

[Sho24] Rob Shore, “Optical networking in 2024 - lighting the way forward.”[Online]. Available: https://www.thefastmode.com/expert-opinion/34436-optical-networking-in-2024-lighting-the-way-forward.

[Sif15] Sifta, R.; Munster, P.; Sysel, P.; Horvath, T.; Novotny, V.; Krajsa, O.; Filka, M. Distributed fiber-optic sensor for detection and localization of acoustic vibrations. Metrol. Meas. Syst. 2015, 22, 111–118.

[Sin03] O. Sinkin, R. Holzlohner, J. Zweck and C. R. Menyuk, “Optimization of the split-step Fourier method in modeling optical-fiber communications systems,” J. of Lightwave Technology, vol. 21, pp. 61-68, 2003.

[Son23] Song, H.; Lin, R.; Li, Y.; Lei, Q.; Zhao, Y.; Wosinska, L.; Monti, P.; Zhang, J. Machine-learning-based method for fiber-bending eavesdropping detection. Opt. Lett. 2023, 48, 3183–3186.

[Sou22] A. Souza, N. Costa, J. Pedro, and J. Pires, “Benefits of counterpropagating Raman amplification for multiband optical networks,” Journal of Optical Communications and Networking, vol. 14, no. 7, pp. 562–571, 2022.

[Sou23] A. Souza, N. Costa, J. Pedro and J. Pires, “Comparison of fast quality of transmission estimation methods for C+L+S optical systems,” J. Opt. Commun. Netw., vol. 15, pp. F1-F12, 2023.

[Sou24] A. Souza, B. Correia, A. Napoli, V. Curri, N. Costa, J. Pedro, and J. Pires, “Cost analysis of ultrawideband transmission in optical networks,” Journal of Optical Communications and Networking, vol. 16, no. 2, pp. 81–93, 2024

[Sou25] A. Souza, N. Costa, and J. Pedro, “Performance and transient-resiliency of S- and E-band upgrades of a C+L-band system,” in Optical Fiber Communication Conference (OFC) 2025, p. M4G.6, Optica Publishing Group, 2025.

[Sou25-2] A. Souza, N. Costa, J. Pedro, and J. Pires, “Raman amplifier design and launch power optimization in multi-band optical systems,” Journal of Optical Communications and Networking, vol. 17, no. 1, pp. A13–A22, 2025.

[Tal04] Ben-Tal, Aharon, et al. "Adjustable robust solutions of uncertain linear programs." *Mathematical programming* 99.2 (2004): 351-376.

[Tar24] A. Tartaglia, F. Fredricx, K. Jackson, et al. “Mobile Optical Pluggables Alliance (MOPA), Technical paper on Optical pluggable performance for tight synchronization”. (2024), [Online]. Available: https://mopa-alliance.org/wp-content/uploads/2024/03/MOPA_Tight-Sync_Paper-v1.0.pdf.

[TIP] “Telecom infra project (TIP),” [Online]. Available: https://telecominfraproject.com/

[Tos22] Tosi, D.; Sypabekova, M.; Bekmurzayeva, A.; Molardi, C.; Dukenbayev, K. 2—Principles of fiber optic sensors. In Optical Fiber Biosensors; Tosi, D., Sypabekova, M., Bekmurzayeva, A., Molardi, C., Dukenbayev, K., Eds.; Academic Press: Cambridge, MA, USA, 2022; pp. 19–78

[Tu05] G. Tutz and H. Binder "Boosting ridge regression," Discussion Paper, No. 418, Ludwig-Maximilians-Universität München, Sonderforschungsbereich 386 - Statistische Analyse diskreter Strukturen, München, https://doi.org/10.5282/ubm/epub.1787

[Vil25] F. Javier Vílchez, et al., 'Introducing L-band Spectral Switching Granularity in Programmable MBoSDM Node Prototype', ICTON, Barcelona, 6-10 July, 2025.

[Wel21] D. Welch and et al., "Point-to-multipoint optical networks using coherent digital subcarriers," JLT, 2021.

[Win18] P. J. Winzer, D. T. Neilson, and A. R. Chraplyvy, "Fiber-optic transmission and networking: the previous 20 and the next 20 years [invited]," Opt. Express, vol. 26, no. 18, pp. 24190–24239, 2018.

[XR-24] Open XR forum Optics. (2024) Open XR Optics Transceiver Optical and Client Interface Specification. OXR.TCVROPTCLI.01.0, https://www.openxrforum.org/.

[Yan24] X. Yang, Ch. Sun, G. Charlet, M. Tornatore, and Y. Pointurier, "Digital-twin-based active input refinement for insertion loss estimation and QoT optimization in C and C+L networks," J. Opt. Commun. Netw. vol. 16, pp. 1261-1274, 2024.

[Zaf11] Zafar Iqbal, M.; Fathallah, H.; Belhadj, N. Optical fiber tapping: Methods and precautions. In Proceedings of the 8th International Conference on High-Capacity Optical Networks and Emerging Technologies, Riyadh, Saudi Arabia, 19–21 December 2011; pp. 164–168

[Zha21] Zhang, C.; Wang, D.; Wang, L.; Guan, L.; Yang, H.; Zhang, Z.; Chen, X.; Zhang, M. Cause-aware failure detection using an interpretable XGBoost for optical networks. Opt. Express 2021, 29, 31974–31992.